ESPOO 2008 VTT RESEARCH NOTES 2428

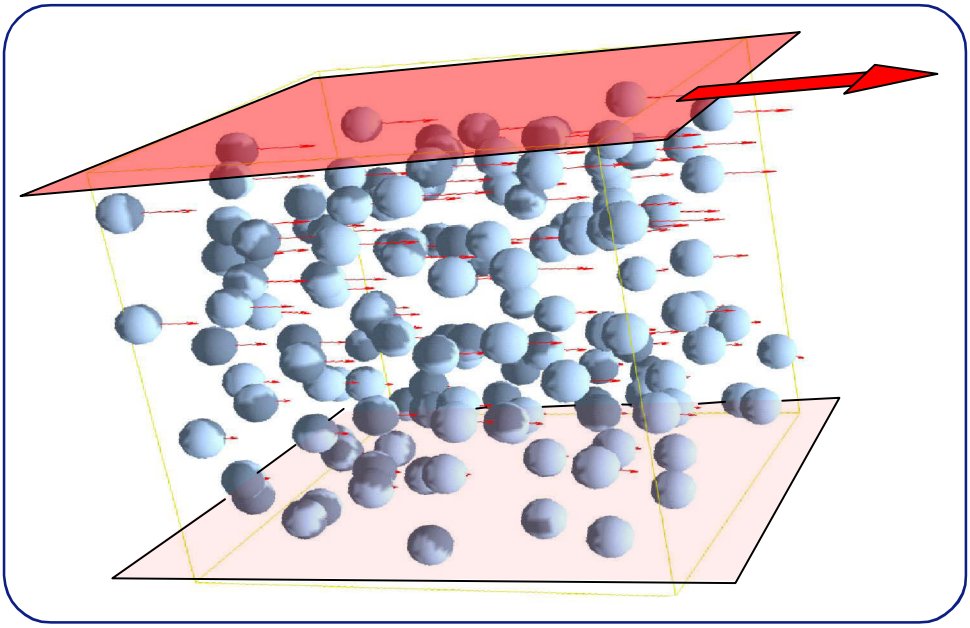

Rheological materials in process industry

ReoMaT Final Report

VTT TIEDOTTEITA – RESEARCH NOTES 2428

Rheological materials in process industry

ReoMaT Final Report

Markku Kataja (ed.), Ari Jäsberg, Sanna Haavisto, Antti Koponen, Vesa Kunnari, Heikki Parviainen, Tero Ponkkala, Pasi Raiskinmäki, Elias Retulainen & Kristian Salminen

VTT

Seppo Syrjälä & Johanna Aho

Tampere University of Technology, Laboratory of Plastics and Elastomer Technology

Jari Hyväluoma, Tomi Kemppinen, Viivi Koivu, Tuomas Turpeinen, Markko Myllys & Jussi Timonen

University of Jyväskylä, Department of Physics

Martti Toivakka & Jan Gustafsson

Åbo Akademi University, Laboratory of Paper Coating and Converting

Jouni Karhu & Kari K. Koskinen

Outokumpu Research Oy, Pori, Finland

ISBN 978-951-38-7200-7 (soft back ed.)
ISSN 1235-0605 (soft back ed.)

ISBN 978-951-38-7201-4 (URL: http://www.vtt.fi/publications/index.jsp)
ISSN 1455-0865 (URL: http://www.vtt.fi/publications/index.jsp)

JULKAISIJA – UTGIVARE – PUBLISHER

VTT, Vuorimiehentie 3, PL 1000, 02044 VTT
puh. vaihde 020 722 111, faksi 020 722 4374

VTT, Bergsmansvägen 3, PB 1000, 02044 VTT
tel. växel 020 722 111, fax 020 722 4374

VTT Technical Research Centre of Finland, Vuorimiehentie 3, P.O. Box 1000, FI-02044 VTT, Finland
phone internat. +358 20 722 111, fax +358 20 722 4374

VTT, Koivurannantie 1, PL 1603, 40101 JYVÄSKYLÄ
puh. vaihde 020 722 111, faksi 020 722 2596

VTT, Koivurannantie 1, PB 1603, 40101 JYVÄSKYLÄ
tel. växel 020 722 111, fax 020 722 2596

VTT Technical Research Centre of Finland, Koivurannantie 1, P.O. Box 1603,
FI-40101 JYVÄSKYLÄ, Finland
phone internat. +358 20 722 111, fax +358 20 722 2596

Technical editing Leena Ukskoski

Edita Prima Oy, Helsinki 2008

Kataja, Markku (ed.) Rheological materials in process industry. ReoMaT Final Report. Espoo 2008. VTT Tiedotteita – Research Notes 2428. 172 p.

Keywords rheology, rheological materials, rheometry, porous material, particulate suspension, momentum transfer, fibre suspension, pressure loss, polymers, fibrous materials, x-ray tomography, lattice-Boltzmann flow simulation, ultrasound Doppler velocimetry

Abstract

'Rheological materials in process industry (ReoMaT)', was a three-year research project started 1.2.2003 and funded mainly by Tekes and industry. It was carried out as a joint effort of five research groups from VTT, University of Jyväskylä, Tampere University of Technology and Åbo Akademi University. The participating companies were Metso Paper Oy, Outokumpu Research Oy, M-real Oyj, Stora Enso Oyj, Kemira Chemicals Oy and Premix Oy. The project was devoted to the study of properties and dynamics of rheological and porous materials found in industrial processes. The general goal of the project part was to support the related industrial research by methods development, research networking and technology transfer. The research included three main topical areas: experimental rheology, development of experimental techniques and numerical analysis. In addition to conventional methods, the projected research utilized several novel techniques, both experimental and numerical, that have only recently become available in other disciplines of materials science and flow mechanics. The results of the first project year were reported separately in: *M. Kataja (ed.), Rheological materials in process industry. ReoMaT Project Report 2003, VTT Project Report, 15.3.2004.* This reports covers the results of ReoMaT consortium for its latter two-year funding period 1.1.2004–30.4.2006.

The results of the project are prolific ranging from direct numerical simulation results on elementary dynamics of momentum transfer in particulate suspensions to new semiempirical pressure loss correlations in fibre suspension flows, rheological characterization of polymer-based and fibrous materials, and to new measurement methods for sedimenting suspensions. Results of general interest have been published in international conferences and journals.

The main results of the project, readily applicable in industrial research and development are:

- A new measurement technique based on helical-flow modified rotational rheometer was developed. The measurement allows for characterization of strongly sedimenting suspensions, which has not been possible previously. The measurement will be offered to industry as a research service.

- The research has enabled to better identify and account for various factors related to the rheometry of polymer melts. The consequent improved accuracy of the rheological characterization of polymeric materials is of great practical importance for example when solving the processability problems in existing processes or when developing new materials.
- The research has led to several new innovations in experimental techniques for finding the relevant material properties of liquid-particle suspensions. In particular, methods based on ultrasound Doppler velocimetry are now being utilized in industrial research by the participating groups. Further development and possible commercialisation of some of the methods is projected.
- New improved semiempirical correlation model for estimating losses for fibre suspension flows was developed. The model and the related measurement techniques is adopted by the participating research groups as a new supplement in their research service potential, and is thereby available for the industry.
- New research method based on using x-ray tomography and numerical lattice-Boltzmann flow simulation has been employed and validated. The techniques is now available for the industry and has already been used in analysing *e.g.* structure and transport properties of paper-making fabrics.
- The in-plane mechanical properties of wet web were found to be strongly affected by furnish, chemicals and DCSs (dissolved and colloidal substances). This offers new possibilities for controlling rheology, stiffness and runnability of wet webs. The results have led to applications and applied research projects in the industry.
- The improved z-directional compression tester proved to be a valuable tool in studying the out-of-plane behaviour of paper under short compressive pulses. The instrument and the generated knowledge is applicable, and has been applied, in industrial cases for solving problems related to paper deformations and processability under z directional stresses.

Many of these results now make an important contribution to the present capabilities of the participating groups and have already been successfully utilized in industrial research carried out parallel to the present project. Some of the results are expected to make similar contribution and benefit research and applications in the near future.

Based on the results and their estimated impact, we conclude that the general goal of the ReoMaT project, namely “to support the related industrial research by methods development, research networking and technology transfer”, has been met.

Contents

1. Introduction

Rheological condensed materials, both fluids and solids, are crucial in many important industrial processes. The properties and behaviour of many rheological materials are, however, still quite poorly known, and this condition clearly hinders effective design and control of these processes. The basic problems involved seem to be common to many, seemingly different industries. A prerequisite for solving these long-standing problems is continuous and active research which, in particular, involves introducing new research techniques that may help to reveal phenomena that has not been tractable with previous methods.

The rheological materials include, except of non-Newtonian fluids, also 'soft' solid and porous materials with non-linear deformation properties. Typical for these materials is their complex structure either in microscopic (molecular) or mesoscopic (constituent particle) scale. They may consist of large molecules or complexes, fibrous particles, or they may be inhomogeneous mixtures of several, intrinsicly simple materials. The properties of such materials have been extensively studied, but they still possess many features that are not understood adequately. The general cause for this is that the microscopic or mesoscopic processes underlying the apparent macroscopic properties are difficult to scrutinize. These properties are mostly strongly non-linear and evade both analytical solution and direct experimental observation. During last few years, new numerical and experimental techniques have, however, been developed. Examples of these new prospects include direct numerical simulations, x-ray microtomography and some recent developments in multiphase flow measurements. Combined with conventional rheological methods, these novel techniques will contribute in solving many fundamental and practical problems of rheology in the future. Many of the particular objectives projected in the ReoMaT consortium share this common feature of combining novel and traditional methods of rheological research.

2. Project overview

The project started at 1.2.2003 and ended 30.4.2006. It was carried out as a joint effort of the following five research groups at three research institutes.

1. Multiphase flows (project coordination)
   VTT Processes, Pulp and paper industry
2. Papermaking
   VTT Processes, Pulp and paper industry
3. Plastic materials development
   VTT Processes, Materials and chemicals
4. Disordered materials
   University of Jyväskylä, Department of physics
5. Pigment coating, suspension flow
   Åbo Akademi University, Laboratory of Paper Coating and Converting.

The projected research included three main topical areas, namely experimental rheology, development of experimental techniques and numerical analysis. These main topics are divided into a number of subtopics as follows.

I EXPERIMENTAL RHEOLOGY

- I.1 Rheology of liquid-particle suspensions
  - I.1.1 Influence of particle size distribution and colloidal forces and sedimentation.
  - I.1.3 Boundary layer phenomena
- I.2 Rheological characterization of polymer materials
- I.3 Rheological measurements using ultrasound Doppler techniques
  - I.3.1 Yield stress of fibre network in fibre suspension flows
  - I.3.2 Properties of filtrating fibre suspension
- I.4 Rheology of consolidating fibre network
  - I.4.1 In-plane rheology of wet fibre network
  - I.4.2 Rheological properties of paper in out-of-plane direction.

II DEVELOPMENT EXPERIMENTAL TECHNIQUES

II.1 Ultrasound Doppler rheometry

II.2 Experimental techniques for magnetorheological fluids

II.3 Fibre suspension filtration measurement.

III NUMERICAL ANALYSIS

III.1 Direct numerical simulation of flows
- III.1.1 Development of numerical methods
- III.1.2 Numerical data analysis
- III.1.3 Flow in porous medium

III.2 Numerical simulation of polymer melt flows

III.3 Numerical modelling of magnetorheological fluids.

During the first project year 2003, emphasis was put on development of new numerical and experimental methods for rheological research. The latter two years were spent mainly on applying the methods in numerical and experimental research and to adapting selected methods in industrial applications.

3. Results

3.1 Rheology of the particulate model suspensions

Tomi Kemppinen* and Martti Toivakka**

(*) University of Jyväskylä, Department of Physics P.O. Box 35, 40014 Jyväskylä, Finland

(**) Åbo Akademi University, Laboratory of Paper Coating and Converting, Porthansgatan 3, 20500 Åbo/Turku, Finland

Abstract

Rheological properties of model colloidal and non-colloidal suspensions were investigated. Colloidal bidisperse suspensions were studied with rotational rheometry and monodisperse suspensions studied with Stokesian dynamics simulations at high volume concentrations. Capillary and rotational rheometry was used in non-colloidal suspensions studies. Viscosity minimum for bidisperse suspensions was found when fraction of small particles was 40%. Numerical simulations show that increasing electrolyte concentration decreases the viscosity of the suspension, which was contributed to the reduction of the hydrodynamic radius of the particles. Non-colloidal hollow glass sphere suspensions were measured with the rotational rheometry and data could be fitted with Krieger-Dougherty model. Capillary rheometry results showed apparent shear thinning behavior.

3.1.1 Introduction

The rheology of particulate suspensions is determined mainly by the particle size and shape distributions, interparticulate forces, the type of deformation and liquid phase properties. Here, especially the influence of particle size and shape distributions, and colloidal forces on rheology is currently not well understood. The role of particle size distribution has been investigated experimentally in e.g. Tekes-financed project *Pigmentit paperin raaka-aineena (1998–2002)*. The experimental work concentrated on characterization of commercial pigment coating suspensions but the results could not be explained satisfactorily with existing empirical models. It seems obvious that the suspensions that were used were too complex to make it possible to understand fundamental mechanisms controlling the rheological behavior. Therefore, the current work approached the problem by using well-characterized model suspensions, for which both particle size distributions and interparticle forces are known and controllable.

In order to understand the role of colloidal interaction for suspension behavior, both colloidal and non-colloidal suspensions need to be studied. In colloidal suspensions (particle sizes < 1 μm) surface chemical and Brownian forces dominate the system behaviour [1, 2]. If particle sizes are larger that 1 μm, hydrodynamic interactions prevail. By studying both suspensions the influence of colloidal forces can be separated from that of hydrodynamics. The results of the model suspension experiments are analyzed with particle dynamics simulations in cooperation with other consortium partners. The main objective of the project is to clarify the fundamental mechanisms that control rheological behaviour of particulate suspensions at high particle volume concentrations. Below, results are reported on influence of particle size, particle concentration and colloidal forces on suspension rheology. The viscosity of three model suspensions with different particle sizes was measured at different particle concentrations. In addition, the effect of colloidal forces on viscosity was studied by varying concentration of an electrolyte added in suspension. The effect of the electrolyte additive is to decrease thickness of the electric double layer on the surface of suspended particles, and thereby to decrease repulsive forces between particles.

3.1.2 Theory

Several theoretical models for the dependence on volume fraction of particles of relative viscosity of liquid-particle suspension have been presented in literature. The results by Mooney, Eiler and Krieger-Dougherty are given in equations (1), (2) and (3), respectively [1–7].

$$\frac{\eta}{\eta_s} = \exp\left(\frac{[\eta]\phi}{1-\phi/\phi_{max}}\right), \tag{1}$$

$$\frac{\eta}{\eta_s} = \left(1+\frac{[\eta]\phi}{2(1-\phi/\phi_{max})}\right)^2, \tag{2}$$

$$\frac{\eta}{\eta_s} = \left(1-\frac{\phi}{\phi_{max}}\right)^{-[\eta]\phi_{max}}. \tag{3}$$

Here, η is the viscosity of the suspension, η_s is the viscosity of the suspending liquid and ϕ is the volume fraction. All these formulas contain two unknown parameters, the intrinsic viscosity $[\eta]$ and the maximum packing fraction ϕ_{max}. Notice that equations (1)–(3) are generalizations to Einstein linear relation $\eta/\eta_s = 1 + [\eta]\phi$, where $[\eta] = 2.5$ is the intrinsic viscosity of the monodisperse suspension [8]. Typical experimental results for the value of the maximum packing fraction for suspensions containing monodisperse

spheres range from $\phi_{max} \approx 0.64$ at low shear rates to $\phi_{max} \approx 0.70$ at high shear rates [1, 2, 5]. Krieger-Dougherty model (Eq. 3) was used in this study.

When using capillary rheometer in measurements, the applied shear to the sample is not uniform and measurements have to be corrected [5]. The shear rate correction (Rabinowitsch equation [9]) for non-Newtonian fluids is

$$\dot{\gamma}_w = \frac{1}{4}\dot{\gamma}_{wall}\left(3 + \frac{d\log Q}{d\log \tau_w}\right), \tag{4}$$

where $\dot{\gamma}_{wall}$ is the shear rate at the capillary wall, Q is the flow rate and τ_w is the shear stress at the capillary wall. End effects are corrected with Bagley method [10]. Here pressure difference is plotted as a function of L/R where L is the length and R is the radius of the capillary. Length is the variable and radius is constant. Capillary is extrapolated to zero length and the intercept of the y-axes will be taken as the entrance pressure.

For numerical studies, a modification of the Stokesian dynamics method was used. The method can be described by the motion of a diffusing particle

$$m\dot{v} = B(t) - \alpha v, \tag{5}$$

where B(t) is a Brownian component, e.g., random force and αv is the average viscous force [11]. This Langevin equation can be written in the N-body form which is usually used in the Stokesian dynamics [12]

$$m \cdot \dot{U} = F^B + F^H + F^P, \tag{6}$$

where m is a generalized mass or moment of inertia matrix of dimension 6N × 6N, U is the 6N dimensional translational and rotational velocity vector of particle and the 6N dimensional force vectors (F) are Brownian motion, hydrodynamic forces and non-hydrodynamic forces, respectively. Here non-hydrodynamic forces can be either interparticle or external forces. More details of the simulation approach can be found in e.g. [13].

3.1.3 Experimental

Colloidal model suspensions were polystyrene latices (for details see Ref. [7]). Suspensions were mixed as bimodal mixtures at the volume concentration of $\phi = 0.35$. Mixing ratios of the bimodal suspensions were 0:100, 20:80, 40:60, 60:40, 80:20 and

100:0. Electrolyte concentrations were 0, 4.2 and 5.9 mmol/l and $CaCl_2$, was used as the electrolyte. Initial approach to use $CaSO_4$ was abandoned, due its limited solubility. Electrolyte was added as a water solution into the suspension. Since the initial volume concentrations of the monosize suspensions were approximately 0.40, the samples were diluted with distilled water. Measurements were carried out with Paar Physica MCR 300 rotational rheometer using a concentric cylinder (bob in cup) measuring system. Samples were presheared at shear rate 0.1 1/s for 30 seconds prior to each measurement, in order to homogenize the samples. Shear viscosities were then measured by increasing the shear rate linearly from 5 1/s to 100 1/s and back down to 5 1/s. Measurement temperature was 20.0 ± 0.1°C.

Non-colloidal suspensions were formulated from Newtonian oil and glass spheres. Measurements were carried out both with Paar Physica MCR 300 and capillary rheometer. In MCR 300 measurements hollow glass spheres (D = 10 μm, $\rho = 1.15$ g/cm^3) and highly viscous Newtonian oil ($\rho = 0.960$ g/cm^3, $\eta = 0.380$ Pa·s) were used. Measurement systems were concentric cylinder (bob-in-cup), cone-plate and parallel plate. The shear rate ramp was from 1 1/s to 60 1/s and back down to 1 1/s. This loop was run two times during each measurement. The gap between bob and cup was 1.1 mm and the height of the bob was 46.0 mm. The plate diameter was 50.0 mm for cone-plate and parallel plate systems. The gap between cut cone and plate was 50.0 μm and in parallel plate setup three gap widths 0.1 mm, 0.5 mm and 1.0 mm were used. These samples were also presheared at shear rate 0.1 1/s for 30 s. Suspensions were diluted in 9 different volume concentrations in the range $\phi = 0.10$–0.55. Measurement temperatures were 20.0 ± 0.1°C and 40.0 ± 0.1°C.

Capillary rheometer measurements used solid glass spheres (D = 10 μm, $\rho = 2.5$ g/cm^3) and low viscous Newtonian oil ($\eta = 0.094$ Pa·s, $\rho = 0.940$ g/cm^3). Diameters of capillaries were 0.735 mm, 0.525 mm and 0.292 mm. Length and diameter ratios (L/D) were approximately 170, 120 and 90. Pressure was raised to 200 bar in the suspension chamber. Maximum shear rate was in the order of 10^6 1/s corresponding to a pressure of 200 bar. Volume concentrations of the samples were $\phi = 0.20$, 0.35 and 0.45. Measurement temperature was approximately 20°C. However, some heat generation in the measurement is inevitable, which should be kept in mind when drawing conclusions.

Stokesian dynamics was used to simulate the flow of model suspensions. The number of particles in a simulation was chosen as 150, which is enough to reproduce the statistical behavior of a system with a large number of particles but saves computational resources [14, 15]. Four different random initial particle positions were generated for each simulation. Particles were placed between two parallel wall boundaries that move in opposite directions during the simulation, thus creating a linear shear flow between them. All the other boundaries use periodic boundary conditions. The viscosity from a simulation can

be calculated from the forces that resist the predefined motion of the wall boundaries. Variables in simulations were electric double layer thickness ($1/\kappa$ = 1.0–6.7 nm), dimensionless shear rate (0.001–100) and particle volume fraction (ϕ = 0.4 and 0.5). Surface potential was set at ζ = -71 mV which is the same as in the model suspension GK404/49 [7]. Simulations were run until the viscosity reached a plateau level, which usually took approximately 2000 dimensionless units of time.

3.1.4 Results and discussion

Viscosity of colloidal bidisperse suspensions were studied in varying electrolyte concentration. Many studies have been seen viscosity minimum in fraction of 0.4 of small particles [16–20]. This effect was not seen clearly in the present study as shown in Figures 1 and 2. Only for the mixture GK404/39 and GK404/49 a clear local minimum was found at the fraction of 0.4 small particles as shown in figure 1a. The ratio of the particle radii for GK404/39 and GK404/49 is 1:6, which allows smaller particles to fit in between the larger ones [7]. The minimum in viscosity becomes deeper as the shear rate is increased. At high shear rates the hydrodynamic interactions between particles become more dominant in comparison to the colloidal forces, and the geometric effect of the more efficient packing for the particle mixture causes the reduction in viscosity when compared to the monodisperse systems.

When electrolyte is added to the system, it is more difficult to locate the minimum as function of added fraction small particles. The added electrolyte will compress the electric double layer on particle surfaces and increase the interparticle hydrodynamic forces. The increased dissipation of energy results in increased viscosities, as shown in Figures 1b and 2b. A side effect of the electrolyte addition is particle aggregation, which effectively determines the particle packing efficiency, and thereby, seems to decouple the viscosity from the particle geometries. For aggregated systems the rheological properties such as viscosity cannot be predicted from the particle size alone. The high electrolyte concentration increases variation of the measured viscosities, which reflects the complexity of the model systems. One source of variability in the measurements that cannot be ruled out is boundary slip.

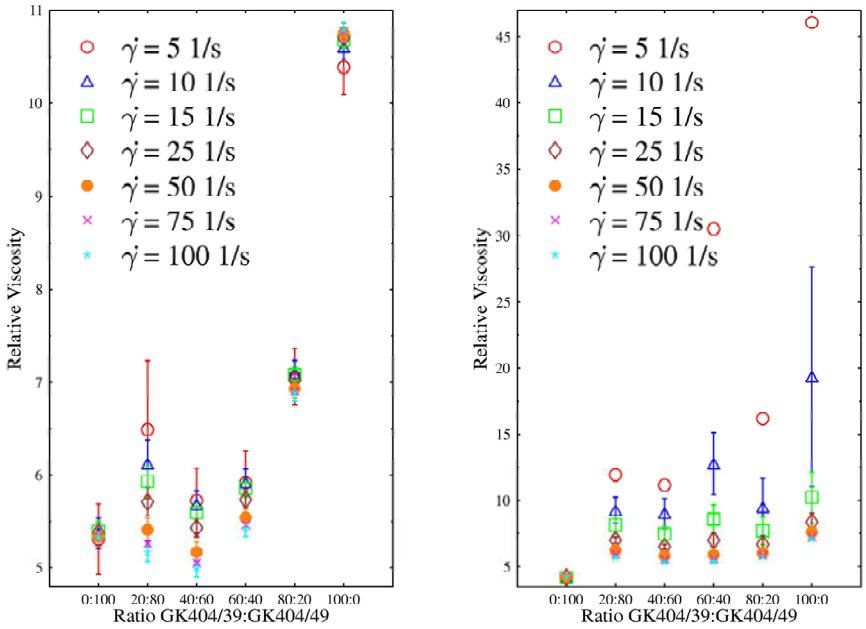

Figure 1. Relative viscosity in bidisperse suspension (GK404/39:GK404/49) at various particle mixing ratios: (a) electrolyte concentration 0 mmol/l and (b) electrolyte concentration 5.8 mmol/l, at $\dot{\gamma}$ = 5 1/s errors were too large to be included in the plot. Here $\dot{\gamma}$ is the shear rate.

Results of numerical simulations are shown in Figure 3, where the reduced viscosity is plotted as a function of shear rate for the monodisperse model suspension GK404/49. Simulations predict shear thinning behavior that can be contributed to breakdown of aggregates as the shear rate is increased. Similarly to the experiments, the viscosity increases as the electric double layer thickness is decreased (corresponding to an electrolyte addition). Further simulations and analysis of the experimental results is needed in order to fully understand the behavior of the system.

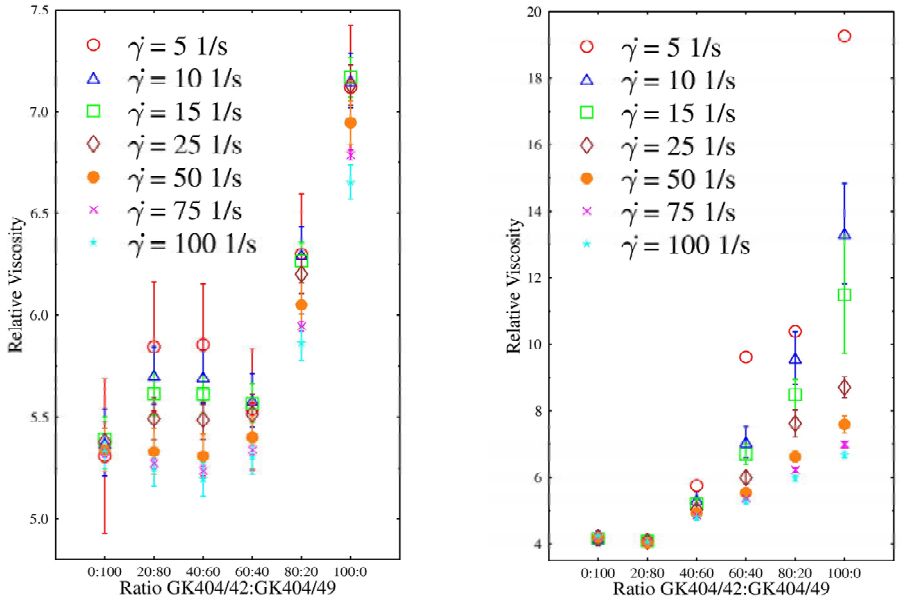

(a) (b)

Figure 2. Relative viscosity in bidisperse suspension (GK404/42:GK404/49) at various particle mixing ratios: (a) electrolyte concentration 0 mmol/l and (b) electrolyte concentr ation 5.8 mmol/l, at $\dot{\gamma}$ = 5 1/s errors were too large to be included in the plot. Here $\dot{\gamma}$ is shear rate.

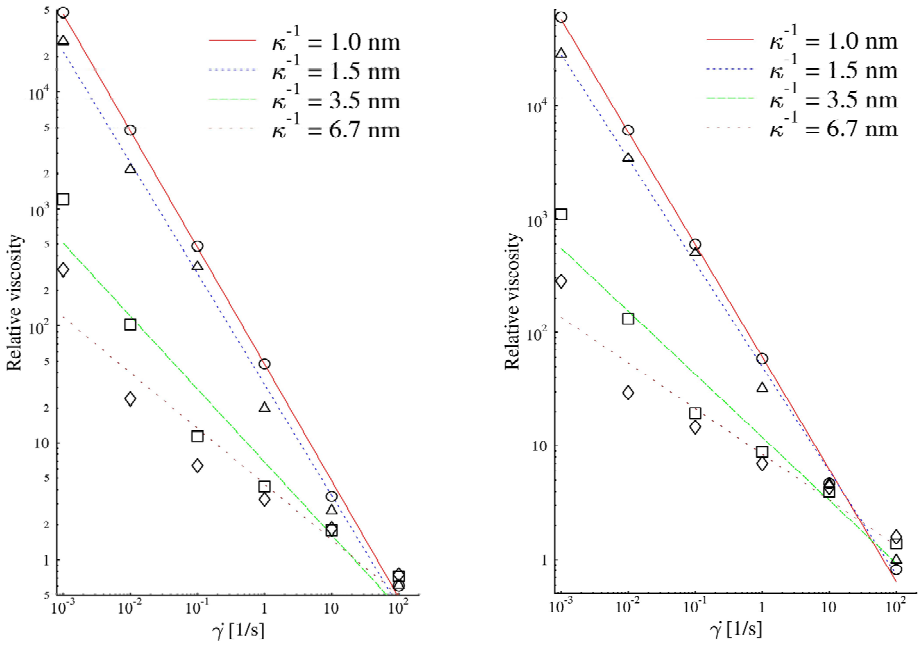

(a) (b)

Figure 3. Simulation results at volume concentration (a) ϕ = 0.4 and (b) ϕ = 0.5. Here surface potential is ς = -71 mV, κ-1 is the electric double layer and $\dot{\gamma}$ is the dimensionless shear rate 49.

Selected results for non-colloidal suspensions that were measured with rotational rheometry are shown in Fig. 4. The results fit the Krieger-Dougherty equation and the calculated intrinsic viscosities and maximum packing densities are given in Table 1. The results are similar across the used measurement geometries, with a notable exception of cone-and-plate geometry. The maximum packing fraction values are larger than the face centered cubic (FCC) lattice ($\phi = 0.74$) which is the most dense structure for rigid spheres. The maximum packing density compares favorably with theoretical values that vary from 63% of random packing to 74% of hexagonal close packing [1, 2, 5]. According to the measurements a decrease of the measurement gap in the parallel plate geometry increases the maximum particle packing density. The same phenomenon has been seen elsewhere for fiber suspensions [21]. This effect can also be a result of increased slip in the narrow gap. The clearly different results with the cone-and-plate geometry can be contributed to the extremely small gap (50 μm) between the cone and plate in relation to the sample particle size (10 μm) i.e. particles will stuck in the gap.

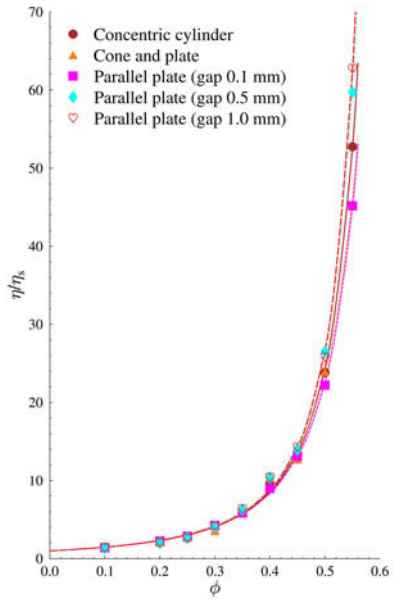

Figure 4. MCR 300 experiment results for non-colloidal suspensions and fits by Krieger–Dougherty model (Eq. 3 and Table 1), where η/η_s s is the relative viscosity and ϕ is the volume fraction.

An example of capillary rheometer results is shown in Fig. 5, which plots the shear stress as a function of shear rate for the non-colloidal suspension at 20 vol-% concentration using three different capillary diameters. The plots include the non-corrected raw data, as well as the data that is corrected for Non-newtonian and end effects. The results indicate shear-thinning behavior also after the corrections are applied. However, it is expected that the true material property for a monodisperse non-

colloidal suspension in a Newtonian liquid is either Newtonian or even dilatant in the high shear rate region. This has also been shown by numerical simulations [22]. A detailed analysis of the suspension behavior in a capillary is done in cooperation with other consortium partners.

Table 1. Non-colloidal suspensions fitting parameters in Krieger-Dougherty model (Eq. 3) measured with MCR 300. Here $[\eta]$ is intrinsic viscosity and ϕ_{max} is maximum packing fraction.

Measurement system	$[\eta]$	ϕ_{max}
Concentric cylinder	3.58	0.68
Cone-plate	5.33	2.47
Parallel plate (0.1 mm)	3.72	0.72
Parallel plate (0.5 mm)	3.85	0.70
Parallel plate (1.0 mm)	3.71	0.68

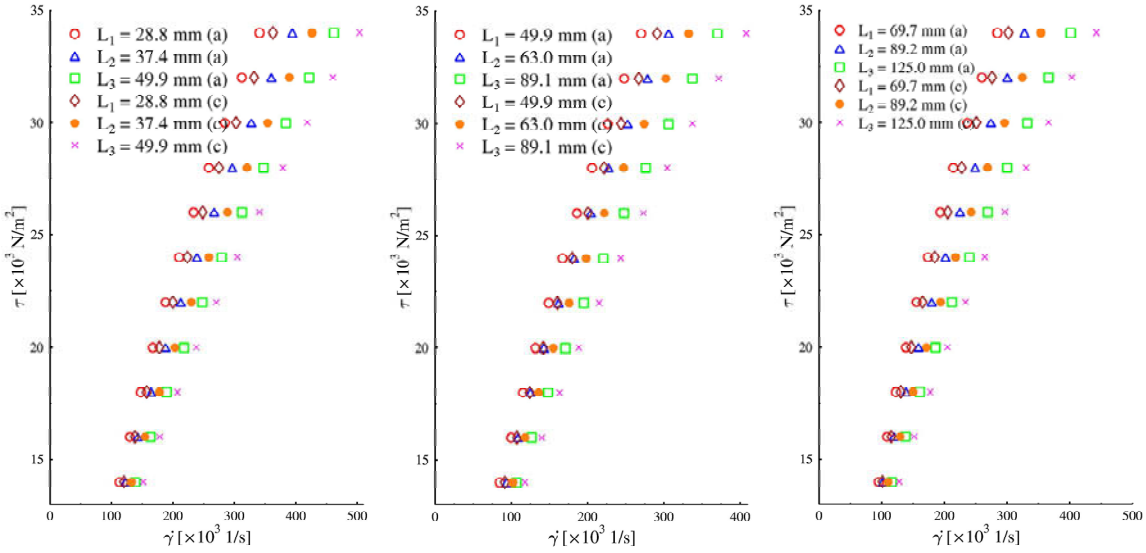

(a) (b) (c)

Figure 5. Non-colloidal suspension data (ϕ = 0.2) in capillary diameter (a) 0.292 mm, (b) 0.525 mm and (c) 0.735 mm. Here $\dot{\gamma}$ is shear rate, τ is shear stress, L_N is the length of the N^{th} capillary, (a) is the apparent measurement data and (c) is flow and entrance corrected data.

3.1.5 Conclusions

Colloidal bidisperse model suspensions were studied with rotational rheometry and monodisperse suspensions with numerical simulations. Bidisperse suspensions reached a minimum in viscosity when fraction of small particles was 40% and when the diameter ratio of the small and the large particles was 1:6. The behavior was attributed to the geometric effects, i.e. more efficient packing of particle mixtures when compared to pure monodisperse systems. This was especially true at high shear rates that accentuate hydrodynamic interactions in comparison to colloidal behavior. The addition of electrolyte compressed the electrical double layer and lead to increased viscosities and aggregation of particles. The results indicate that the aggregation decouples the geometry-viscosity relationship, and it is more difficult to predict the system behavior with on models based on packing efficiency considerations.

Numerical simulations show similar qualitative behavior to experiments reported earlier. However, the simulations did not predict as rapid viscosity increase in viscosity as experiments due to irreversible aggregation. A reason for this might be slip at the smooth wall boundaries. Non-colloidal suspensions results, measured with rotational rheometry, were fitted in Krieger-Dougherty model. A decrease in the gap between parallel plates increase the maximum packing fraction as calculated with the model above. This can also be an artifact of slip, which should be investigated further. The capillary rheometer results indicate shear thinning behavior for the non-colloidal model suspensions, while Newtonian or shear-thickening results were expected. Further analyses regarding this will be done.

References

[1] Barnes, H.A., Hutton, J.F. and Walters, K. An Introduction to Rheology. Elsevier Science Publishers, 1993.

[2] Carreau, P.J. and Cotton, F. Rheological Properties of Concentrated Suspensions Transport Processes. In: Bubbles, Drops and Particles. 2nd ed. Ed. by De Kee, D. and Chhabra, R.P. Taylor and Francis, 2002. Ch. 16.

[3] Macosko, C.W. Rheology Principles, Measurements and Applications. Wiley-VCH, 1994.

[4] Lindhjem, C.E. Particle Packing and Shape Effects on the Rheological Characteristics of Paper Coating Pigments. TAPPI Proceedings, Coating Conference 1991. Pp. 131–141.

[5] Roper, J. Rheology of Pigment Slurries and Coating Formulations. Pigment Coating and Surface Sizing of Paper. Ed. by Lehtinen, E. Fapet Oy, 2000. Ch. 31.

[6] Nommensen, P.A. et al. Steady shear behaviour of polymerically stabilized suspensions: Experiments and lubrication based modeling. *Phys. Rev. E* **59**, 3147 (1999).

[7] Kataja, M. (ed.). Rheological materials in process industry. ReoMaT Project Report 2003. VTT Project Report, 15.3.2004.

[8] Einstein, A. Eine neue Bestimmung der Molekuldimensionen. *Ann. d. Phys.* **19**, 289 (1906).

[9] Rabinowitsch, B.Z. Physik. *Chem. Leipzig* **145A**, 1 (1929).

[10] Bagley, E. End Corrections in the Capillary Flow of Polyethylene. *J. Appl. Physics* **28**, 624 (1957).

[11] Chaikin, P.M. and Lubensky, T.C. Principles of Condensed Matter Physics. Cambridge University Press, 2000.

[12] Deryaguin, B.V. and Landau, L. *Acta Physicochim USSR* **14**, 633 (1941).

[13] Nopola, T. Simulation of particle motion in concentrated colloidal suspensions. Licenciate thesis, Turku University, 2002.

[14] Brady, J.F. and Bossis, G. The Rheology of Concentrated Suspensions of Spheres in Simple Shear Flow by Numerical Simulation. *J. Fluid Mech.* **155**, 105 (1985).

[15] Brady, J.F. and Bossis, G. Stokesian Dynamics. *Ann. Rev. Fluid Mech.* **20**, 111 (1988).

[16] Shapiro, A.P. and Probstein, R.F. Random Packings of Spheres and Fluidity Limits of Monodisperse and Bidisperse Suspensions. *Phys. Rev. Lett.* **68**, 1422 (1992).

[17] Chang, C. and Powell, R.L. Dynamic simulation of bimodal suspensions of hydrodynamically interacting spherical particles. *J. Fluid Mech.* **253**, 1 (1993).

[18] He, D. and Ekere, N.N. Viscosity of concentrated noncolloidal bidisperse suspensions. *Rheol. Acta* **40**, 591 (2001).

[19] Wagner, N.J. and Woutersen, A.T.J. The viscosity of bimodal and polydisperse suspensions of hard spheres in the dilute limit. *J. Fluid Mech.* **278**, 267 (1994).

[20] Zaman, A.A. and Moudgil, B.M. Role of Electrostatic Repulsion on the Viscosity of Bidisperse Silica Suspensions. *J. Colloid Interface Sci.* **212**, 167 (1999).

[21] Djalili-Moghaddam. M. et al. Study of geometry effects in torsional rheometry of fibre suspensions. *Rheol. Acta* **44**, 29 (2004).

[22] Toivakka, M. and Eklund, D. Prediction of suspension rheology through particle motion simulation. *Tappi Journal* **79**, 1 (1996), pp. 211–222.

3.2 Rheology of settling suspensions

Jan Gustafsson*, Martti Toivakka*, Jouni Karhu** and Kari K. Koskinen**

(*) Åbo Akademi University, Laboratory of Paper Coating and Converting, Porthansgatan 3, 20500 Åbo/Turku, Finland

(**)Outokumpu Research Oy, Pori, Finland

Abstract

The flow properties of suspensions of industrial grade magnetite, as well as spherical model samples of ceramic beads and glass beads have been investigated with a modified Couette rheometer. The suspensions exhibited instability to sedimentation due to their high density and large particle size. In order to homogenise the suspension for rheological measurements, an additional upward force was applied by pumping the stirred suspensions through the measuring cell. Due to the difference in density between the materials, it was possible to analyse the impact of different settling properties on the suspension rheology. It was found that the shear stress increased with increasing density for samples of the same size and at the same solids contents. For magnetite suspensions, the shear stress decreased with increasing size, but for ceramic and glass beads the influence of size on the shear stress remained unclear, due to small absolute shear stresses and small variations between the samples. However, the measuring system was found to be useful for determining the flow properties of settling samples.

3.2.1 Introduction

Processing of dense medium mineral suspensions involves various sub-processes such as grinding, flotation, filtration and pumping [1]. The wide range of particle concentrations that are used, lead to variable flow properties and makes it challenging to control and dimension the processing apparatus. Typical particle concentrations for e.g., magnetite-processing can be up to 15% by volume [2].

Measuring rheological properties of sedimenting suspensions are of great interest for many process applications where a solid is handled as a suspension, i.e. a particulate fluid. Many pigment suspensions, e.g. paper coatings colours, possess short-term stability from several hours up to several days. Minerals from the mining and metal recovery industries, on the other hand, may have such a high density and large particle size that the sedimentation rate is up to several centimetres per second. Measuring the flow properties of such particle suspensions by conventional rotational shearing techniques is hence more or less impossible.

For colloidal particles (< 1 μm) it is possible to stabilize the suspension, i.e. diminish the sedimentation tendencies by addition of polymers (sterically), by increasing the surface charge (electrostatically) or in combination. These interactions of colloidal particles can be estimated with the so called DLVO-theory (from Derjaguin-Landau and Verwey-Overbeek) [3]. The magnitude of the stabilizing repulsive interaction diminishes with increasing particle size and the sedimentation velocity increases with increasing size and density [3]. Due to their high density, the viscosity of magnetite suspensions was mainly governed by surface friction and inter-particle collisions [2].

Several attempts have been made to measure the rheology of settling suspensions. Sarmiento et al. [4] used in their study a capillary rheometer with different tube lengths and tube diameters in combination with a with parallel plate geometry. Their particle size was relatively small (d_{50} = 2.5 μm) and of average density (3.0 kg dm^{-3}), which made it possible to measure the rheological properties with this setup.

Kawatra et al. [5–6] combined a vibrating sphere viscometer and a rotational viscometer. They used silica slurries (d_{50} = 30 μm, density not mentioned) as model sample. The viscometer had a high shear rate due to the oscillation at 750 Hz. It also had the suspension continuously circulated from a tank to the measuring cell in order to maintain homogeneity of the dispersion. By plotting the apparent viscosity from the two independent methods against each other, they were able to determine the viscosity and also the flow type, i.e. Newtonian or non-Newtonian.

He and Laskowski [2] as well as Klein et al. [7] used a double gap system to investigate the flow properties of magnetite suspensions (density 4.8 kg dm^{-3}, size: 24 μm). The purpose was to place the inner cylinder in the hindered settling zone, below the transition zone. This setup would ensure that the concentration around the bob (the inner cylinder) would remain known and constant and hence not affect the measuring result. A limitation of the approach was that the settling rate of the particles needed to be known and be relatively low. The Casson model was found to best describe the flow properties of the magnetite suspensions [2]. Furthermore, it was concluded that the Casson yield stress was dependent on the size distribution and the solids content of the suspensions.

By taking advantage of the helical flow that arises when the suspension is pumped upwards through a measuring cell, most of the settling problems can minimized. The theory for the approach and a practical implementation has been developed by Akroyd and Nguyen [8–9]. The theory takes into account both the tangential (around the center) and axial (upward) flow components. With their instrument they were also able to determine the yield stress. They tested their instrument on e.g. fly ash (size 50 μm, settling rate 0.2 mm h^{-1}) and diamond (size 10 μm, settling rate 13 mm h^{-1}) slurries.

The aim of the current work was to clarify the influence of particle size, density as well as solids content on the measured shear stress of settling suspensions of magnetite, solids ceramic beads and solid glass beads.

3.2.2 Experimental

The magnetite (Fe_3O_4) samples were of industrial grade and fractionated by sieving. Five size (diameter) fractions have been investigated, namely "< 30 μm", "30–146 μm", "43–63 μm", "63–146 μm", and "> 146 μm". The density of the magnetite particles was 5.2 g cm^{-3}. The range between the lowest and the highest settling rate in water (23 °C) is shown in Table 2.

Table 2. The range of the settling rate for the different size fractions of magnetite.

Size fraction	**Settling rate mm s^{-1}**
"< 30 μm"	8.2–32.1
"30–146 μm"	10.4–29.8
"43–63 μm"	8.7–31.0
"63–146 μm"	17.4–40.5
"> 146 μm"	29.3–77.2

The spherical ceramic beads (Zirblast from Saint-Gobain ZirPro) consisted of a mixture of ZrO_2 and SiO_2. The material had a density of 3.8 g cm^{-3} and had two size (diameter) fractions, namely 63–125 and 125–250 μm.

The spherical glass beads (Spheriglass 2024, Spheriglass 2429 and Spheriglass 5000 from Potters Industries Inc.) were a soda lime glass composition. The material had a density of 2.5 g cm^{-3} and had three size (diameter) fractions: 0.5–19, 63–106 and 106–212 μm.

The shear stress was measured with a modified Haake RV-2, with a concentric Couette system. The cup (outer cylinder) and bob (inner cylinder) diameters were 42 mm 38.6 mm, respectively. Data of the torque was gathered as voltage on a PC through a data card (Pico Technology Ltd.). The setup, which was modified according to Akroyd and Nguyen [9], is shown in Fig. 6.

The suspension was heavily stirred in a separate vessel and pumped with a peristaltic pump from the vessel upwards through the measuring cell. The drain was thereafter led back to the vessel. The axial volume flow rate was kept constant at approximately 1 l min^{-1}. The shear stress was measured at varying shear rates in 10 steps between 11 and 976 s^{-1}.

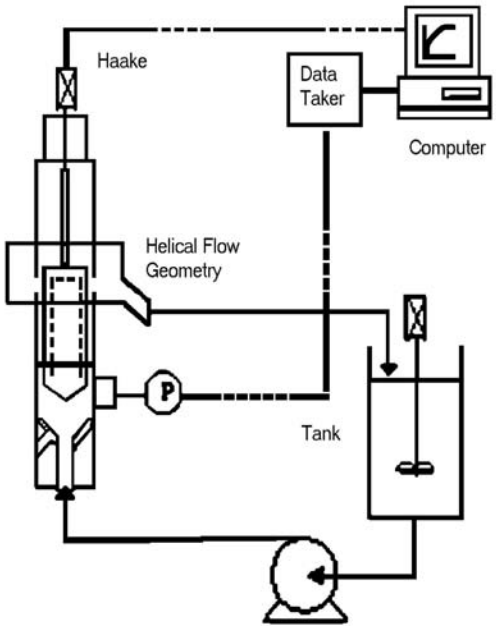

Figure 6. Setup of the modified Haake rheometer [9].

Calibration

The shear rate ($\dot{\gamma}$) was calculated from the rotational speed and the dimensions of the Couette measuring cell by using the following equation:

$$\dot{\gamma} = (2\Omega)\left(\frac{\alpha^2}{\alpha^2 - 1}\right) \tag{7}$$

where Ω is the angular speed, defined as

$$\Omega = (2\pi)\mathrm{RPS} \tag{8}$$

and α is the ratio between the radii of the cup and the bob:

$$\alpha = R_{cup} / R_{bob} \tag{9}$$

The shear stress, σ, was calculated from:

$$\sigma = \eta_{known} \times \dot{\gamma}_{set} \quad (10)$$

The rheometer was calibrated with three Newtonian liquids with known viscosities. The voltage was then related to the calculated shear stress, σ, at all 10 preset shear rates, of which the two highest, i.e. 690 s^{-1} and 976 s^{-1}, are illustrated in Fig. 7.

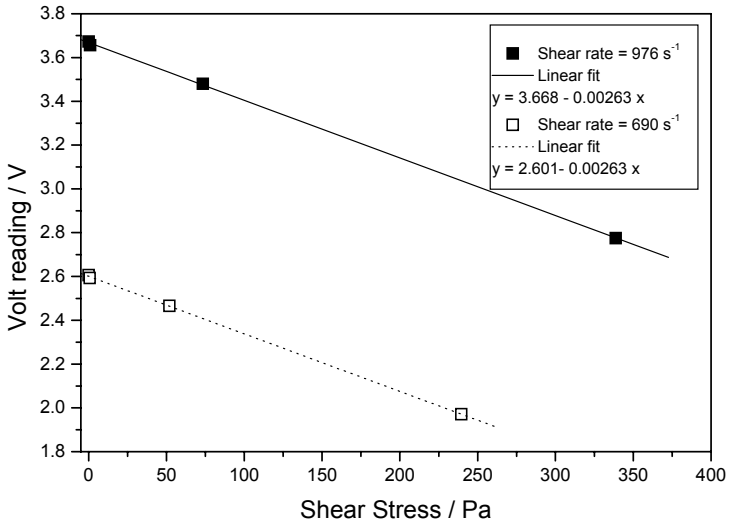

Figure 7. Calibration curves.

The linear dependencies could be expressed for the shear rates 690 s^{-1} and 976 s^{-1}, respectively.

$$(V) = 2.601 – 0.00263\ (\sigma) \quad (11)$$

$$(V) = 3.668 – 0.00263\ (\sigma) \quad (12)$$

The other eight shear rates were calibrated accordingly.

3.2.3 Results

Magnetite

The measured shear stress for the "< 30 μm" fraction is shown in Fig. 8. Each measuring point is a mean value of 100 data points, which were recorded at 1 Hz. The shear stress increased with increasing shear rate, with a small plateau between shear rates 200–500 s-1. At higher shear rates the tendency for turbulence in the measuring cell increased. On the other hand, the lower sensitivity limit of the measuring device was approached at low shear stresses, which were found at below shear rates

approximately 50 s^{-1}. Therefore, the optimal shear rates for the samples investigated were between 100–500 s^{-1}. The measured shear stress increased systematically with increasing volume fraction, due to higher number of inter-particle collisions. The magnitude of the shear stress was in the same range as that of Ref. [2].

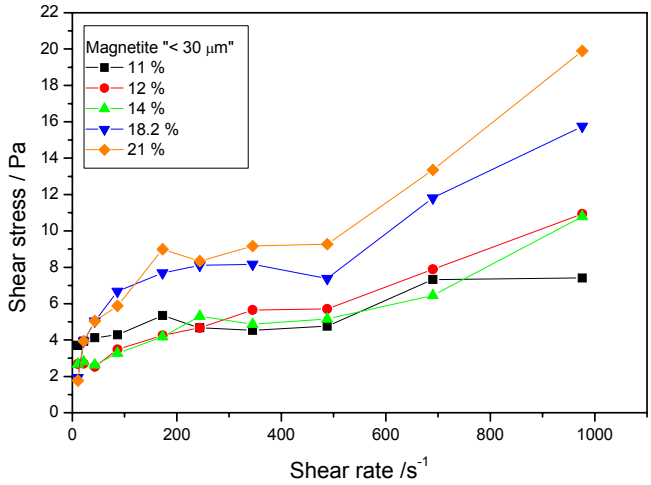

Figure 8. Shear stress as a function of shear rate for different solids contents of the "< 30 μm" magnetite fraction.

The apparent viscosity of magnetite suspensions of the "< 30 μm" fraction was calculated from the data in Fig. 8 and is shown in Fig. 9. The shear thinning behaviour is obvious, except for the two highest shear rates, where the viscosity appear to flatten out to a constant value. This behaviour is probably due to the turbulence occurring at high shear rates. The apparent viscosity was found to be approximately 10–100 times the viscosity of water, which is indicated with a solid line in the figure.

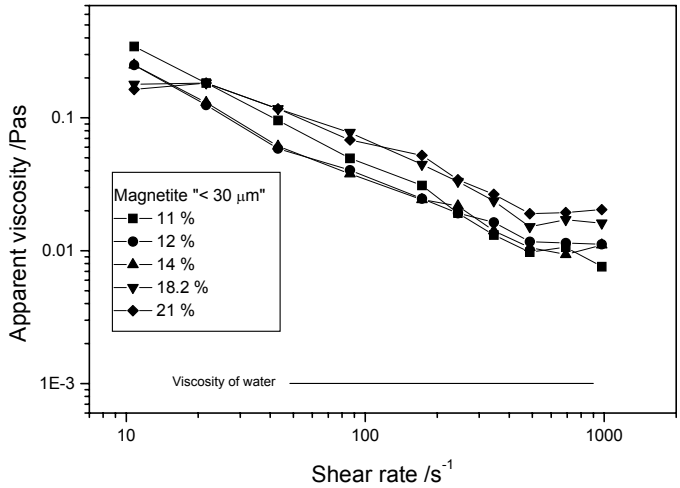

Figure 9. The apparent viscosity as a function of shear rate for different solids contents of the "< 30 μm" magnetite fraction.

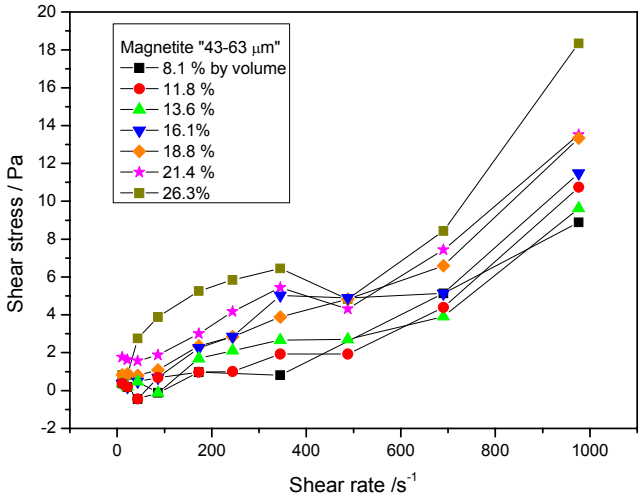

Figure 10. Shear stress as a function of shear rate for different solids contents of the "43–63 μm" magnetite fraction.

The shear stress of the other size fractions of magnetite, i.e. "43–63 μm", "63–146 μm" and "30–146 μm" can be seen in Fig. 10, Fig. 11 and Fig. 12, respectively. The shear stress for these fractions all followed the same pattern as described above for the "< 30 μm" fraction in Fig. 8. However, the magnitude of the shear stress was lower due to the larger particles size, and hence fewer particles at the same solids content, resulting in fewer inter-particle collisions.

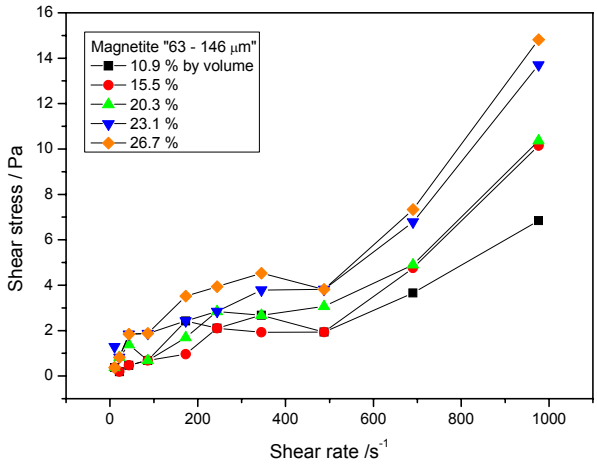

Figure 11. Shear stress as a function of shear rate for different solids contents of the "63–146 μm" magnetite fraction.

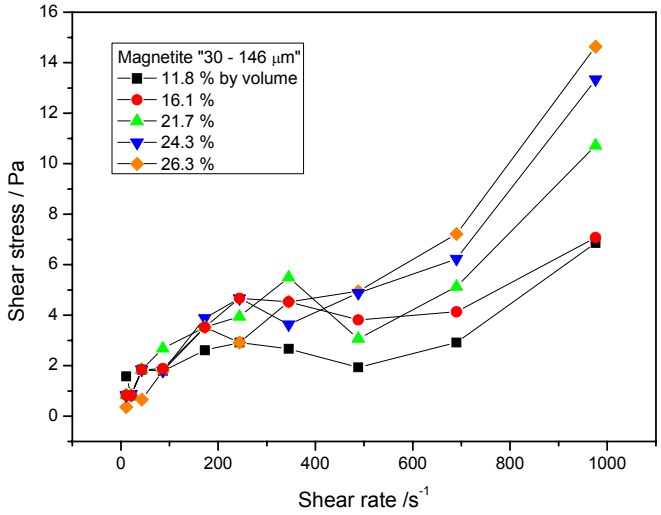

Figure 12. Shear stress as a function of shear rate for different solids contents of the "30–146 μm" magnetite fraction.

Comparing the shear stress of the different size fractions at constant solids content, which is shown in Figure 13, gives at hand that the highest shear stress is obtained for the smallest size fraction, < 30 μm. Since the "63–146 μm" fraction had a slightly higher solids fraction and the shear stress therefore should in comparison be slightly lower, the conclusion can be drawn that the "43–63 μm" had a higher shear stress than the "63–146 μm" fraction. These three fractions follow the logic of decreasing shear stress with increasing size. Theoretically, the "30–146 μm" fraction should have the lowest shear stress, due to the widest size range, and hence best (tightest) packing abilities, but that could not be clearly found from the results, probably due to the low magnitude of the shear stress.

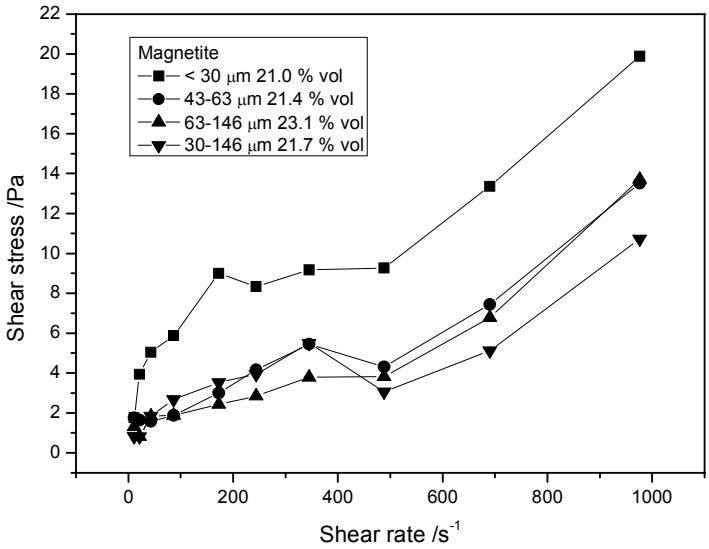

Figure 13. Shear stress as a function of shear rate for different size fractions of magnetite at constant solids content.

Solid Ceramic beads

The shear stress of the solid ceramic beads are shown for the "63–125 μm" and "125–250 μm" fractions in Fig. 14 and Fig. 15, respectively. The magnitude of the shear stress in Fig. 14 was quite low over the whole range of shear rate and solids content investigated. Therefore, no significant difference can be seen between the different solids contents. For the larger particles (see Fig. 15) a clearer trend was found. In the shear rate range above 200 s^{-1}, the shear stress increased with increasing solids content, which was most clearly found for the two highest solids contents, i.e. higher than 23.3 volume -%. The shear stress values of the "125–250 μm" suspensions were slightly higher than for "63–125 μm" suspensions at the same solids content, which is somewhat contradictory. This might be due to the large particles compared to the measuring gap of the instrument (1.7 mm). The largest particles should be less than approximately 200 μm in order for the particles to flow freely in the gap. Too large particles in the gap may create a change in the velocity profile of the particles and change the active (effective) solids content in the measuring gap, e.g. due to plugging of the flow. This results in a higher torque reading, which consequently leads to a higher shear stress value than the actual based on the true material property.

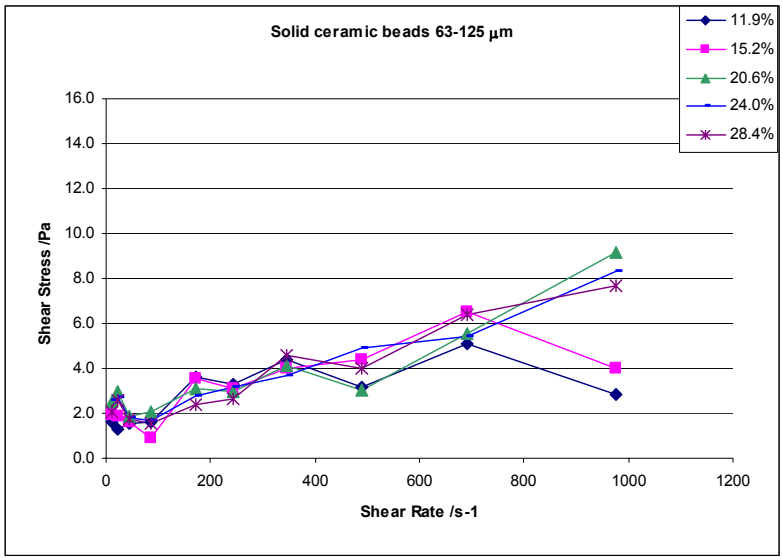

Figure 14. Shear stress as a function of shear rate for different solids contents of the "63–125 μm" fraction of ceramic beads.

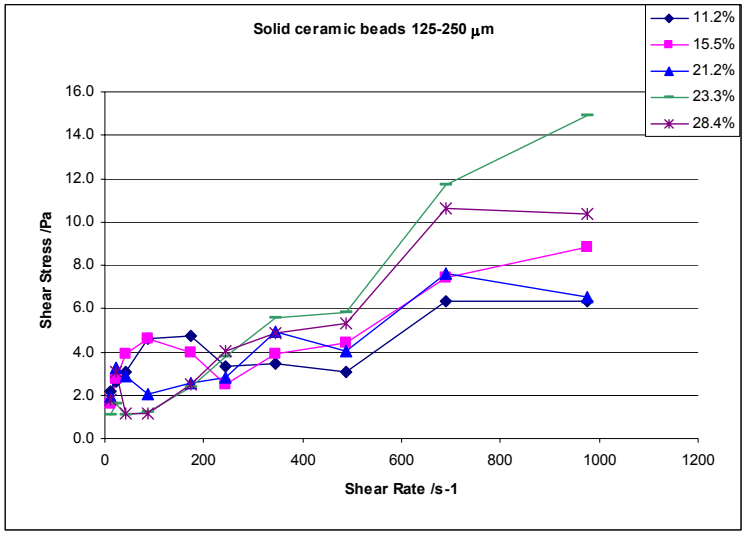

Figure 15. Shear stress as a function of shear rate for different solids contents of the "125–250 µm" fraction of ceramic beads.

Solid Glass beads

The shear stress of the solid glass beads are shown in Fig. 16, Fig. 17 and Fig. 18. The shear stress of the smallest glass beads, i.e. the "0.5–19 µm" fraction in Fig. 16 was very low, probably due to the low density, which resulted in that particles started to float on the surface of the liquid. This led to an uneven distribution of the particles in the measuring cell. A low density also creates a low pressure against the bob, and since small differences at low magnitude of shear stress were difficult to detect by the instrument, no trends were found for these size fractions.

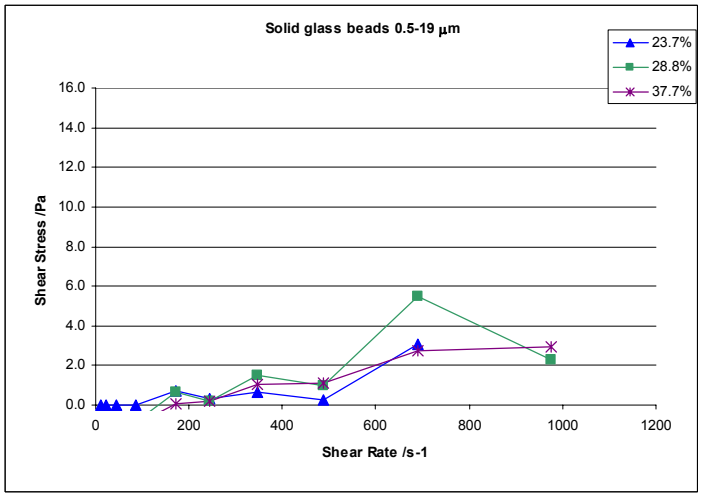

Figure 16. Shear stress as a function of shear rate for different solids contents of the "0.5–19 µm" fraction of glass beads.

Larger size fractions of the glass beads (in Fig. 17 and 18) resulted in slightly higher but on an absolute scale still quite low shear stresses. The most reliable results of the glass beads are those in Fig. 17 (the "53–106 µm" fraction), since the large particle size of the suspensions in Fig. 18 might cause erroneous results for the same reason as discussed for the "125–250 µm" fraction of ceramic beads in Fig. 15. The increasing shear stress with increasing solids content in Fig. 17, was most clearly found for the two highest solids content, above 33.7 volume-%. Below that value the shear stress values were not very different from each other.

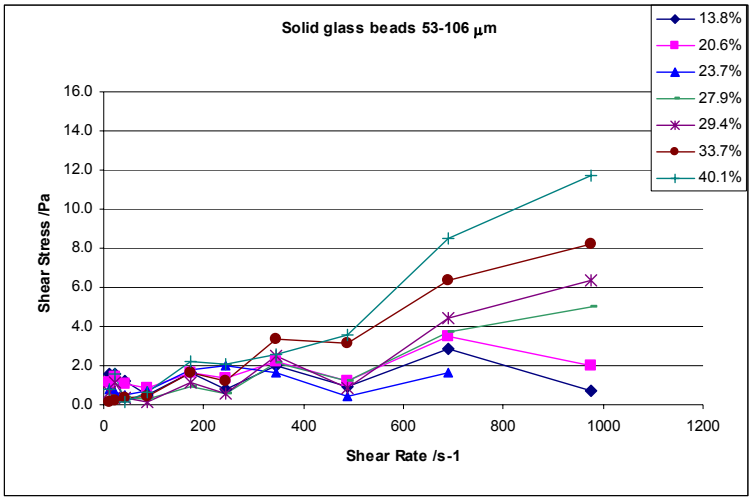

Figure 17. Shear stress as a function of shear rate for different solids contents of the "53–106 µm" fraction of glass beads.

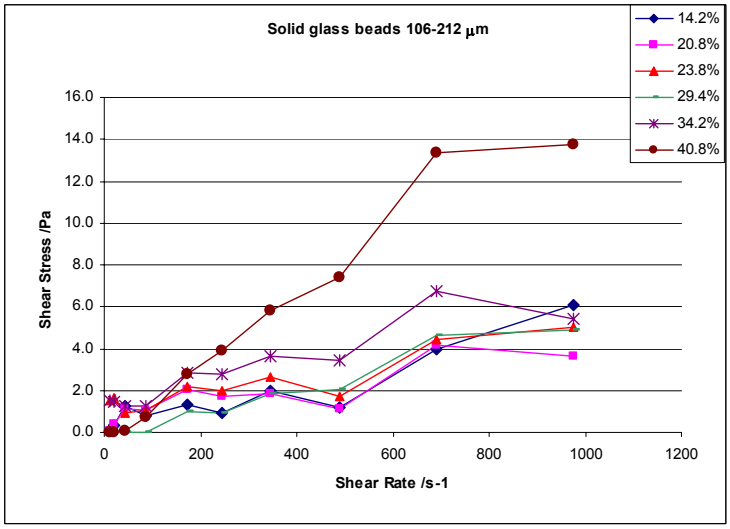

Figure 18. Shear stress as a function of shear rate for different solids contents of the "106–212 µm" fraction of glass beads.

Influence of density

The influence of density for the suspension with the same size distribution (63–146, 63–125 and 53–106 for magnetite, ceramic beads and glass beads, respectively) and at constant solids content is shown in Fig. 19. The shear stress increased with increasing density over the whole shear rate range investigated, but was most evident at high shear rates. Magnetite which had the highest density resulted in the heaviest impacts during collisions with the bob. The glass beads, on the other hand, had a low effect on the shear stress, due to its low density.

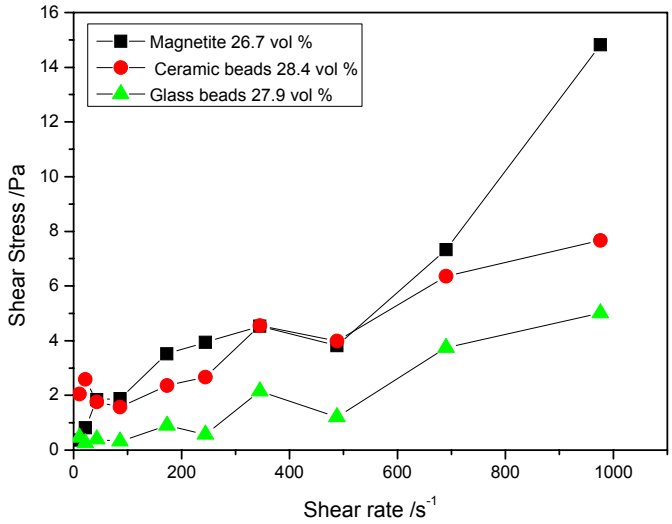

Figure 19. Shear stress as a function of shear rate for different materials of at constant size fractions (63–146, 63–125 and 53–106) and constant solids content.

3.2.4 Conclusions

The flow properties of sedimenting particle suspensions with different densities have been investigated with a modified Couette rheometer in which axial flow was used to enable measurements at high volume concentrations and to minimize the effects of sedimentation. The materials used were magnetite, ceramic beads and glass beads, with different size fractions. It was shown that the measured shear stress increased with increasing density of the particles in suspension at the same solids content and size fraction. The shear stress increased systematically as a function of increasing solids content. Smaller size of the particles resulted in higher shear stresses at constant solids content, but this was only clearly found for magnetite, which had the highest density. For the ceramic and glass beads a smaller size resulted in overall very low stress values and small differences between the different samples, leading to difficulties of interpretation of the influence of size. The technique could be useful in determining the rheology of sedimenting suspensions on an absolute scale, but further development is still needed.

References

[1] Shi, F.N., Napier-Munn, T.J. Measuring the rheology of slurries using an on-line viscometer. *Int. J. Miner. Process.* **47**, (1996), pp. 153–176.

[2] He, Y.B. and Laskowski, J.S. Rheological properties of magnetite suspensions. *Miner. Process. Extract. Metall. Rev.*, **20**, (1999), pp. 167–182.

[3] Shaw, D.J. Introduction to Colloid and Surface Chemistry. 4th ed., Butterworth-Heinemann, London, 1992. Pp. 21–32, pp. 210–234.

[4] Sarmiento, G., Crabbe, P.G., Boger, D.V. and Uhlherr, P.H.T. Measurement of the rheological characteristics of slowly settling flocculated suspensions. *Ind. Eng. Chem. Process Des. Dev.*, **18**, (1979), pp. 746–51.

[5] Kawatra, S.K., Bakshi, A.K. and Miller, T.E. Jr. Rheological characterization of mineral suspensions using a vibrating sphere and a rotational viscometer. *Int. J. Miner. Process.*, **44–45**, (1996), pp. 55–165.

[6] Kawatra, S.K. and Bakshi, A.K. Online measurement of viscosity and determination of flow types for mineral suspensions. *Int. J. Miner. Process*. **47**, (1996), pp. 275–283.

[7] Klein, B., Laskowski, J.S. and Partridge, S.J. A new viscometer for rheological measurements on settling suspensions. *J. Rheol.*, **39**, (1995), pp. 827–840.

[8] Akroyd, T.J. and Nguyen, Q.D. Continuous rheometry for industrial slurries. *Exp. Therm. Fluid Sci.* **27**, **(**2003), pp. 507–514.

[9] Akroyd, T.J. and Nguyen, Q.D. Continuous on-line rheological measurements for rapid settling slurries. *Minerals Engineering* **16**, (2003), pp. 731–738.

[10] Steffe, J.F. Rheological methods in food process engineering. 2nd ed. Freeman press, East Lansing, 1996. Pp. 115–139.

[11] He, Y.B., Laskowski, J.S. and Klein, B. Particle movement in non-Newtonian slurries: the effect of yield stress on dense medium separation. *Chem. Eng. Sci.* **56**, (2001), pp. 2991–2998.

3.3 Rheological characterization of polymeric materials

Seppo Syrjälä*, Johanna Aho* and Heikki Parviainen**

(*) Tampere University of Technology, Laboratory of Plastics and Elastomer Technology, P.O. Box 589, FIN-33101 Tampere, Finland

(**) VTT, Advanced Materials, P.O. Box 1300, FIN-33101 Tampere, Finland

3.3.1 Introduction

Reliable characterization of the rheological behaviour of polymer melts is of significant practical importance. It is well known that the rheological properties of polymers depend strongly on the underlying molecular structure such as molecular mass, molecular mass distribution and degree of long-chain branching. The data from the rheological measurements can therefore provide the link between molecular structure, processability, and end-use properties of polymers. Accurate rheological data are also needed for the numerical simulations of polymer processing flows.

In industrial practice, some kinds of fillers are frequently added into polymers. Most frequently used fillers are inorganic in nature; examples include calcium carbonate, mica, talc, kaolin, wollastonite, glass bead and glass fibre. One of the original aims of introducing fillers was simply to reduce the cost of the polymers by using inexpensive fillers. At present, however, fillers are generally employed to improve the properties of polymer products. It is obvious that the addition of particulate fillers into polymers changes the rheology of the material, which in turn influences the processing behaviour. The presence of fillers can complicate the measurement and modelling of the flow behaviour of the material due to the onset of phenomena not necessarily seen in the unfilled material, for example wall slip and yield behaviour.

Even though polymer melts are known to exhibit both viscous and elastic response, the key rheological property in most situations is the shear viscosity and its dependence on shear rate and temperature and possibly on pressure. The effect of pressure on the viscosity of polymer melts is quite often completely neglected, which obviously does not always reflect the reality. The assumption of pressure-independent viscosity can be justified for most extrusion operations, whereas in the case of injection moulding this assumption is much more questionable. Especially in thin-wall injection moulding applications pressures in excess of 100 MPa frequently occur, which can cause a significant increase in the polymer viscosity. For example, in the simulations of the injection moulding process the omission of these pressure effects may lead to largely inaccurate predictions of pressure and other variables.

Instruments that are generally used to characterize the rheological properties of polymeric materials are the capillary rheometer and the rotational rheometer. The former is primarily intended for the measurement of shear viscosity, while most of the latter types of equipments are capable of yielding both the viscous and elastic properties of the material. As is well known, several corrections have often to be applied to the measured raw data, if the true rheological values are desired. This is especially the case in capillary rheometry; for details see [1–5].

This report covers the following topics, which constitute the essence of the research activity in this project directed to the rheological characterization of polymeric materials (some other more industrially-oriented subjects were also considered, but the results are not included in this report):

– Bagley and Rabinowitch corrections in capillary rheometry
– Slip on the capillary wall with a highly filled thermoplastic elastomer
– Flow instability in the capillary flow of a HDPE melt
– Pressure dependence of viscosity of polymer melts
– Yield stress phenomenon with filled polymers
– Effect of molecular mass distribution on the polymer viscosity
– Cox–Merz rule.

3.3.2 Measurement methods

In this investigation, the rheological measurements were conducted using the Göttfert Rheograph 6000 capillary rheometer and the Anton-Paar Physica MCR-301 rotational rheometer shown in Fig. 20. The principles and theoretical bases of these equipments are briefly outlined next; more detailed discussions are available in textbooks on rheology and rheometry [1–6].

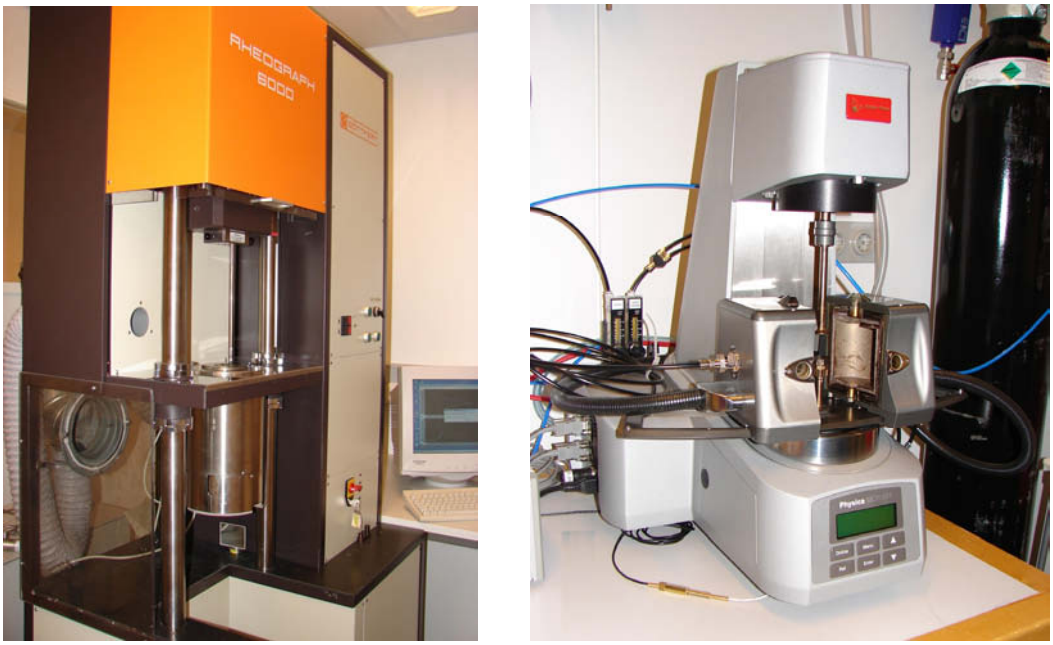

Figure 20. Capillary and rotational rheometers used in the measurements.

Capillary rheometer

Figure 21 gives a schematic view of the capillary rheometer having a barrel of diameter $2R_p$, and a capillary die of diameter D (= $2R$) and length L. To conduct the experiment, the test material is first put into the barrel, where it is melted and heated. The barrel usually contains several heating zones, which can be individually controlled to create and maintain a uniform temperature. Thermal equilibrium is typically reached within 5–15 minutes, depending on the diameter of the barrel and the material under test, after which the actual measurement can be started.

In the rate-controlled mode of operation considered here, the piston is moved downwards at constant speed to drive the test material through the capillary. The raw data of capillary rheometry consist of the volumetric flow rate, Q, and the pressure drop across the capillary, Δp. The volumetric flow rate is directly proportional to the piston speed, V_p, that is

$$Q = \pi R_p^2 V_p \tag{13}$$

To determine the pressure drop across the capillary, the pressure in the barrel just above the capillary is measured by means of a transducer. This measurement gives Δp, since the ambient pressure generally remains constant.

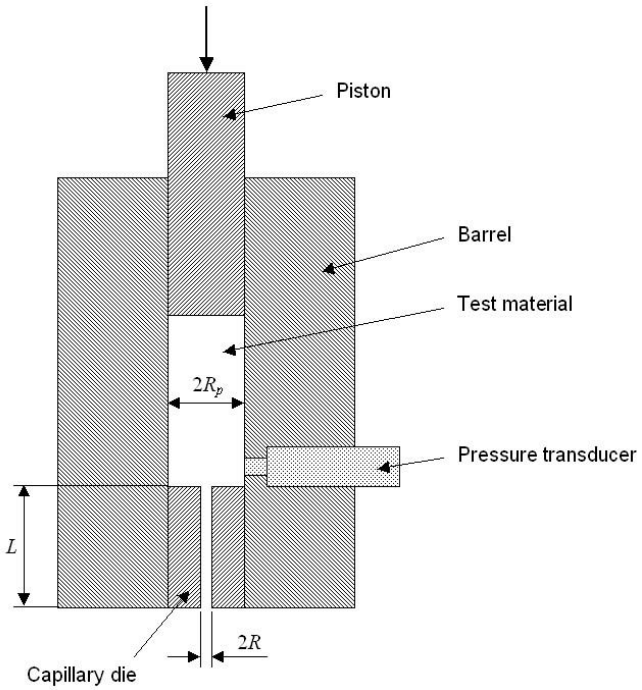

Figure 21. Schematic drawing of the capillary rheometer.

The analysis for determining the viscosity from the values of Q and Δp includes the following simplifying assumptions: (i) the flow is time-independent, (ii) the flow is isothermal, (iii) there is no slip at the capillary wall, (iv) the test fluid is incompressible, (v) the viscosity is independent of pressure, and (vi) the flow is fully developed all along the capillary. With these assumptions, the expressions for the apparent wall shear stress τ_{wa}, apparent wall shear rate $\dot{\gamma}_{wa}$ and apparent viscosity η_a can be written as follows [1–5]:

$$\tau_{wa} = \frac{\Delta p}{2L/R}; \qquad \dot{\gamma}_{wa} = \frac{4Q}{\pi R^3}; \qquad \eta_a = \frac{\tau_{wa}}{\dot{\gamma}_{wa}} \tag{14}$$

The quantities calculated on the basis of Eq. (14) are called apparent, because for non-Newtonian fluids they more or less deviate from the true values. To obtain the true values of viscosity and shear rate, the Bagley and Rabinowitsch corrections are typically applied to the measured data. The Bagley correction accounts for the excess pressure drop in the entrance to the capillary, where the fluid element undergoes strong stretching. The application of the Bagley correction requires the measurements to be conducted with at least two (preferably three or four) capillaries of the same diameter, but different lengths. For each value of the apparent shear rate, a plot of the total pressure drop against the length-to-diameter ratio (L/D) of the capillary, the Bagley plot, can then be constructed and the entrance pressure drop, Δp_e, is obtained by extrapolation to zero L/D. Consequently, the true wall shear stress can be calculated as follows:

$$\tau_w = \frac{\Delta p - \Delta p_e}{2L/R} \tag{15}$$

Another way of determining Δp_e is to measure it directly by using the orifice die, i.e., the capillary with nominally zero length.

The Rabinowitsch correction is a way of determining the actual shear rate at the capillary wall for non-Newtonian fluids exhibiting a non-parabolic velocity profile. Namely, for shear-thinning fluids like polymer melts the velocity profile in the capillary is more plug-like than that for Newtonian fluids, which implies that the shear rate at the capillary wall is higher for shear-thinning fluids. The Rabinowitsch correction can be expressed as

$$\dot{\gamma}_w = \frac{4Q}{\pi R^3}\left(\frac{3n'+1}{4n'}\right) = \dot{\gamma}_{wa}\left(\frac{3n'+1}{4n'}\right) \tag{16}$$

where

$$n' = \frac{d(\log \tau_w)}{d(\log \dot{\gamma}_{wa})} \tag{17}$$

It is worth noting that there are some other factors, which may also affect the accuracy of the measurement results. For example, there is ample evidence that at least certain polymers are prone to wall slip above a critical wall shear stress, which may in some circumstances lead to the instability and time-dependent evolution of the flow in the capillary. The effect of viscous heating may also become significant, particularly when very high viscosity melts are driven at high speeds, which results in a non-isothermal flow. The pressure dependence of viscosity is also likely to play some role at high speeds, where high pressures are to be expected.

Capillary rheometer with a pressure chamber

It is possible to use the standard capillary rheometer to study indirectly the influence of pressure on the viscosity. Namely, the pressure dependence can be inferred from the non-linearities in the pressure profiles observed during the flow through the capillary. This technique, however, suffers from a scarce sensitivity and is useful only for materials, which exhibit a large effect of pressure on viscosity. Moreover, as pointed out in [7], temperature and slip effects may also contribute to the non-linearity of the pressure profile and it is difficult to separate these from pressure effects. In this work, the capillary rheometer modified with a pressure chamber was used to investigate the pressure dependence of polymer melt viscosity. The pressure chamber surrounded by a

heating element is mounted below the rheometer barrel and capillary die. An adjustable conical valve downstream of the chamber enables one to constrict the flow and thereby increase the pressure level in the capillary. The construction of the pressure chamber is presented in Fig. 22.

During the experiment with pressure chamber, the pressure is monitored at two locations by transducers: in the barrel just above the capillary and in the pressure chamber right below the capillary. The test is started by selecting the desired valve position and piston speed, which determines the apparent shear rate at the capillary wall. The piston speed is kept constant throughout a single test run, whereas the valve is always adjusted (tightened) once the pressures for the current valve position have stabilized, i.e., the flow has reached a steady state. This procedure is continued until the barrel gets empty or the maximum capacity of either pressure transducer is reached. The recommended maximum operating (mean) pressure for the device is 120 MPa.

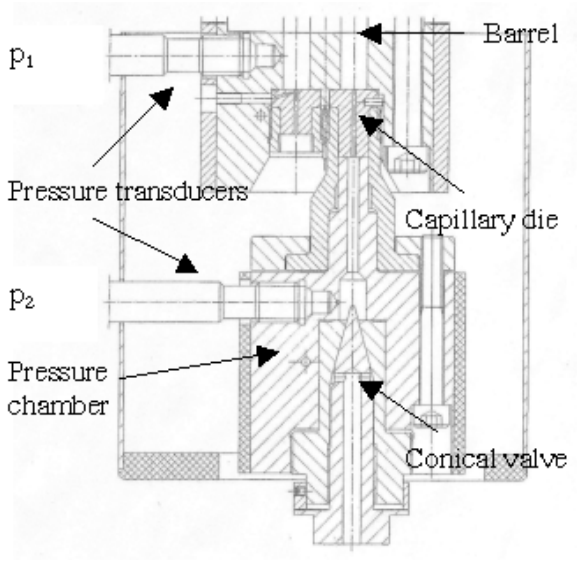

Figure 22. Pressure chamber used in conjunction with capillary rheometer.

Rotational rheometer

With rotational rheometers, cone-and-plate and plate-and-plate geometries shown in Fig. 23 are typically used for polymer melts. Most of the rotational rheometers are capable of operating in both steady and dynamic modes. In steady mode, the shear viscosity can be measured as a function of shear rate. In this type of measurement the cone-and-plate configuration has the advantage of providing a uniform shear rate throughout the sample. With the cone-and-plate geometry, the equations for calculating the shear rate and viscosity take the following forms [1–6]:

$$\dot{\gamma} = \frac{\Omega}{\tan\theta} \approx \frac{\Omega}{\theta}; \qquad \eta = \frac{3M\theta}{2\pi R^3 \Omega}. \tag{18}$$

Here, the radius of the plates, R, and the cone angle, θ, are the geometrical quantities and the angular velocity, Ω, and the torque, M, are the measured quantities. The plate-and-plate geometry, on the other hand, imposes a non-uniform shear rate in the sample; zero at the centre and maximum at the edge. Accordingly, the cone-and-plate configuration is usually preferred over the plate-and-plate configuration for the shear viscosity measurements. The equations applicable to the plate-and-plate geometry can be found in [1–6].

In rotational rheometry, dynamic small amplitude oscillatory shear measurements are also widely used to determine the linear viscoelastic properties of polymeric materials. For these measurements, the plate-and-plate geometry is most commonly employed. In this case the components of the complex viscosity in terms of the measured torque amplitude M_o and phase shift δ can be written as

$$\eta' = \frac{2M_o h}{\pi R^4 \omega \phi_o} \sin\delta; \qquad \eta'' = \frac{2M_o h}{\pi R^4 \omega \phi_o} \cos\delta, \tag{19}$$

where ϕ_o is the angular amplitude and ω is the angular frequency (note that ϕ_o must be sufficiently small in order to keep the deformation in the linear region). The magnitude of the complex viscosity is the quantity, which is often of significant practical interest. This is because of the observation that for many materials (especially for polymer melts) the steady shear viscosity versus shear rate curve has the same shape and values as the magnitude of the complex viscosity versus angular frequency curve. This empirical relation was originally proposed by Cox and Merz [8] and it is presently known as the Cox–Merz rule. It can be expressed as

$$\eta(\dot{\gamma}) = \left|\eta^*(\omega)\right|_{\dot{\gamma}=\omega} \tag{20}$$

where

$$\left|\eta^*\right| = \sqrt{\eta'^2 + \eta''^2} \tag{21}$$

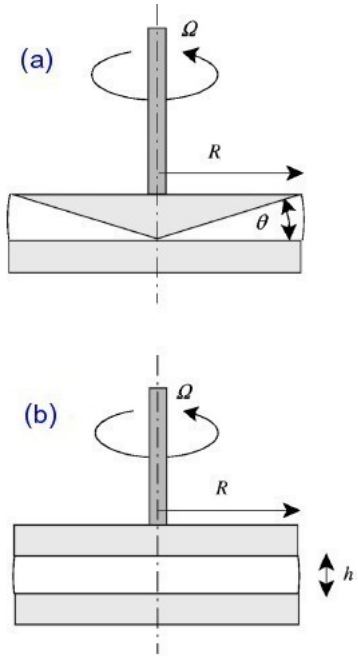

Figure 23. Cone-and-plate and plate-and-plate geometries used in rotational rheometers.

3.3.3 Results

Bagley and Rabinowitsch corrections in capillary rheometry

In this section, a practical application of the Bagley and Rabinowitsch corrections in capillary rheometry is illustrated for LDPE Lupolen 1840H (manufactured by Basell). The experiments were performed with capillaries having D = 1 mm and L/D = 5, 10, 20 and 30. In addition, the orifice die having nominally a zero length (actually L = 0.2 mm) was used. The Bagley plots with linear extrapolations to zero L/D are shown in Fig. 24. It can be seen that the data from different capillaries nicely fall on straight lines. The use of the orifice die, instead, appears to result in a systematic over-estimation of the entrance pressure drop. More details about the measurements can be found in [9].

In performing the Rabinowitch correction, the key issue is the estimation of Eq. (17) for each data pair (τ_w , $\dot{\gamma}_{wa}$). Probably the most convenient way to calculate the derivative in Eq. (17) is to fit the test data to the 2nd-order polynomial according to

$$y = c_0 + c_1 x + c_2 x^2 \tag{22}$$

in which $y = \log(\tau_w)$, $x = \log(\dot{\gamma}_{wa})$ and c_o, c_1 and c_2 are the fitting constants. Now, Eq. (17) can be written simply in the form $n' = c_1 + 2c_2$. Following this procedure, a perfect curve fit is obtained for the present measurements, as revealed by Fig. 25. When both the Bagley and Rabinowitch corrections are applied to the test data, the true viscosity

values shown in Fig. 26 are obtained. For comparison purposes, the uncorrected results are also given in this figure.

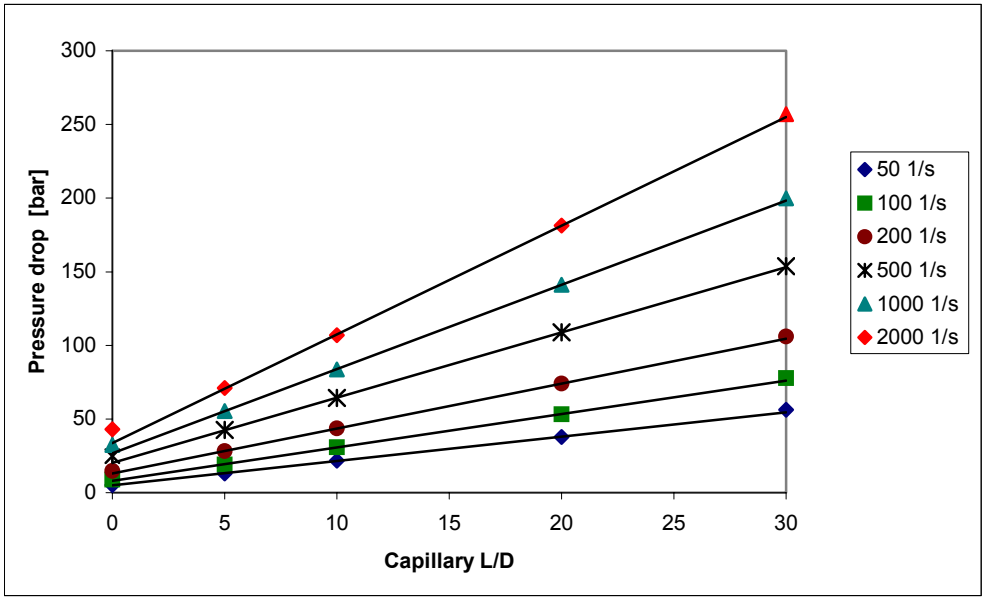

Figure 24. Bagley plot for LDPE Lupolen 1840H; the linear fit is based on the capillaries with L/D = 5, 10 and 20.

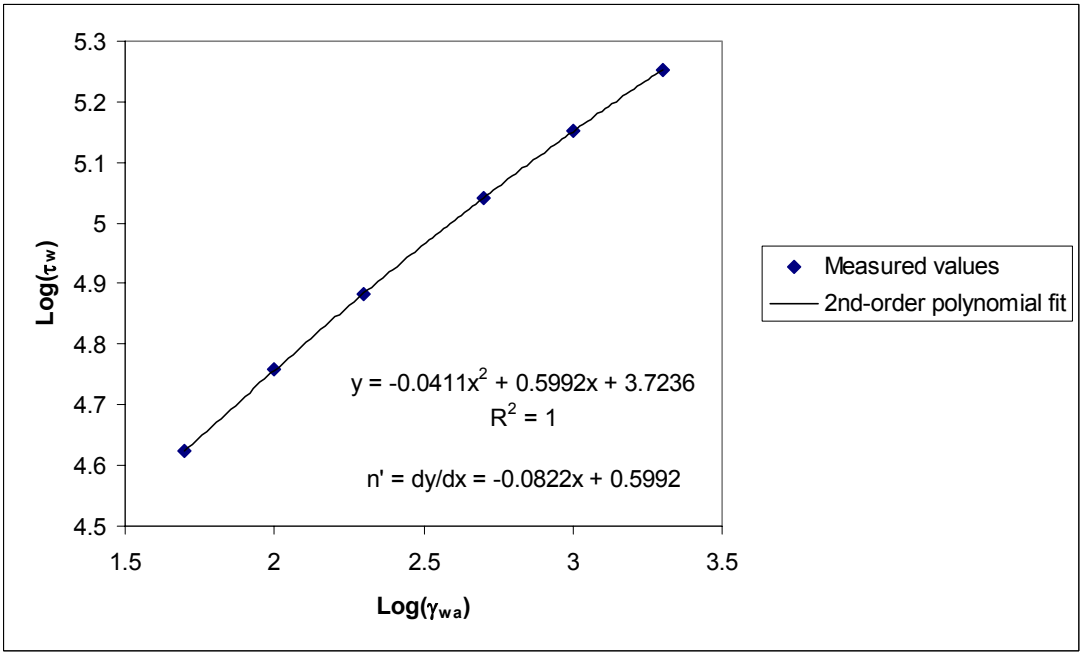

Figure 25. Determination of the Rabinowitch correction term in Eq. (17) by means of the 2nd-order polynomial fit (LDPE Lupolen 1840H).

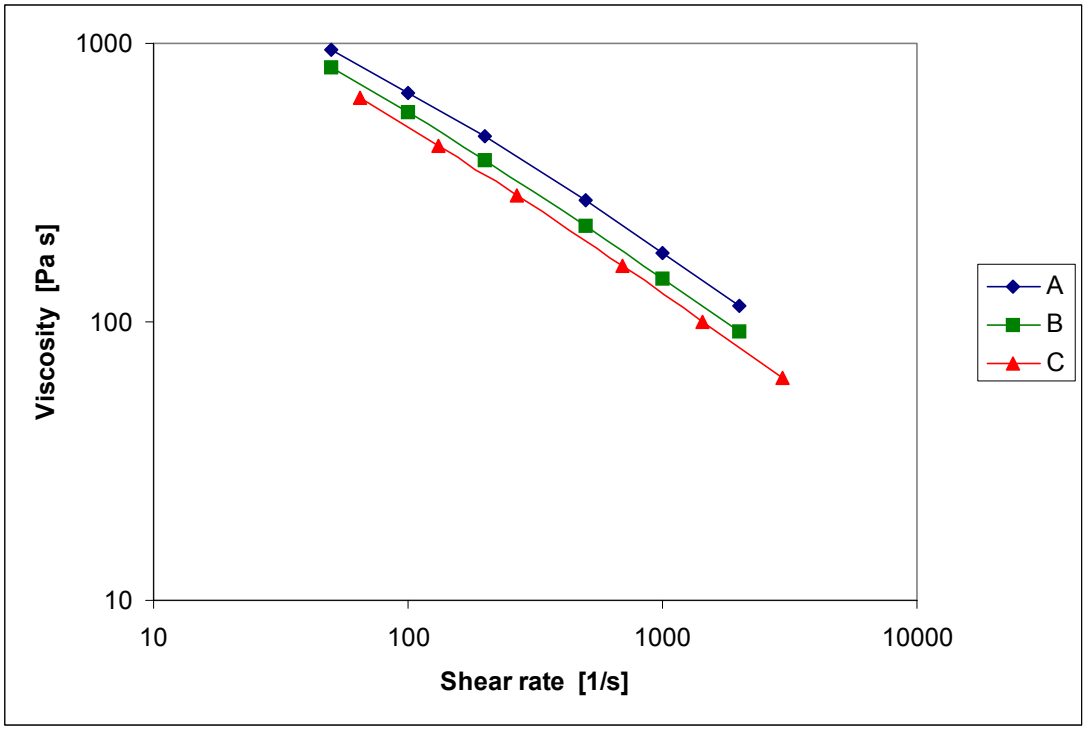

Figure 26. Corrected and uncorrected viscosity versus shear rate data for LDPE Lupolen 1840H: (A) Uncorrected; (B) Bagley-corrected; (C) Bagley and Rabinowitch corrected.

Determination of slip velocity with the Mooney method

As was mentioned above, the usual assumption in the viscosity measurements is that the no-slip condition at the capillary wall is valid. It is obvious, however, that this condition is occasionally violated. Whether or not slip occurs can be inferred by performing measurements with several capillaries having different diameters, but the same L/D ratios, as first suggested by Mooney [10]. If appreciable slip does not occur, the plots of the apparent shear stress, τ_{wa}, against the apparent shear rate, $\dot{\gamma}_{wa}$, with different capillaries coincide with each, as illustrated in Fig. 27 for a PP melt. In the presence of slip, however, these plots exhibit dependence on capillary diameter; the smaller diameter produces lower values of τ_{wa} at equivalent values of $\dot{\gamma}_{wa}$.

It is quite common that highly filled materials are prone to slip. To illustrate this, capillary rheometer measurements were carried out for highly filled thermoplastic elastomer (TPE); the filler particles in the material are approximately spherical in shape and the filler content is about 50 vol.%. The measurements were carried out using four different capillaries with D = 0.6, 0.8, 1.0 and 1.5, and L/D = 20. In this case, as indicated by Fig. 28, the data points obtained with different capillaries do not coincide with each other, suggesting the presence of slip. According to Mooney, a plot of $\dot{\gamma}_{wa}$ as

a function of $1/R$, for a fixed value of τ_{wa}, will be a straight line with a slope of $4V_s$, with V_s being the slip velocity. In order to construct such a Mooney plot, the data shown in Fig. 28 were fitted using the 2nd-order polynomials. As depicted in Fig. 29, fairly straight lines are obtained in accordance with the suggestion of Mooney. The slip-corrected shear rate is now obtainable as [10]

$$\dot{\gamma}_{slip-corrected} = \frac{4Q}{\pi R^3} - \frac{4V_s}{R} \tag{23}$$

It is often observed that the slip velocity is proportional to the wall shear stress. This was examined for the present measurements by fitting the data to the following power-law type equation

$$V_s = a\tau_w^b \tag{24}$$

where a and b are constants. As shown in Fig. 30, an excellent fit was achieved.

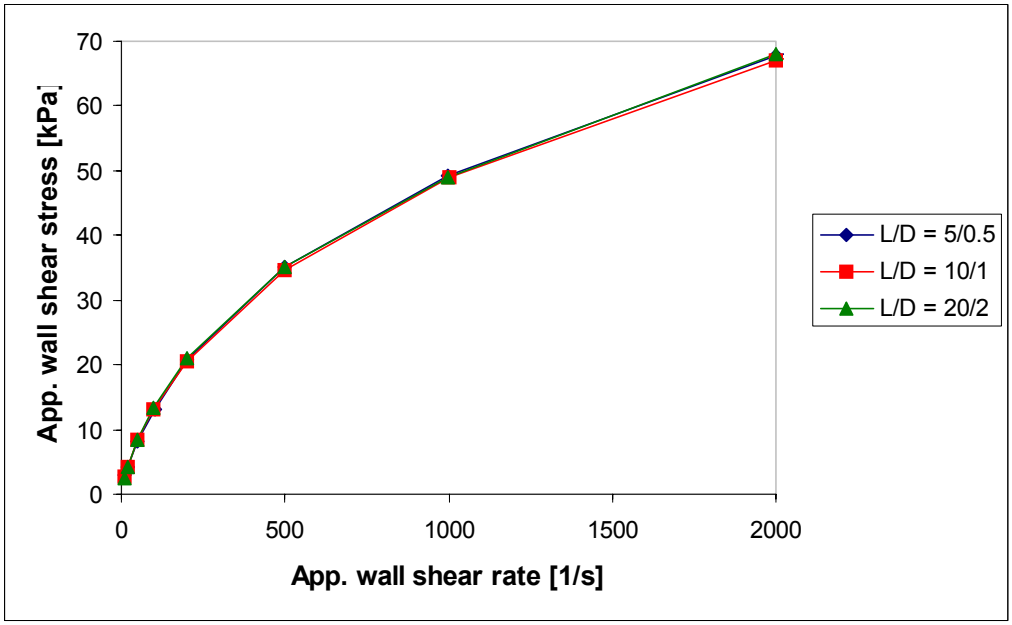

Figure 27. Apparent shear stress versus apparent shear rate for PP (Borealis BH345MO).

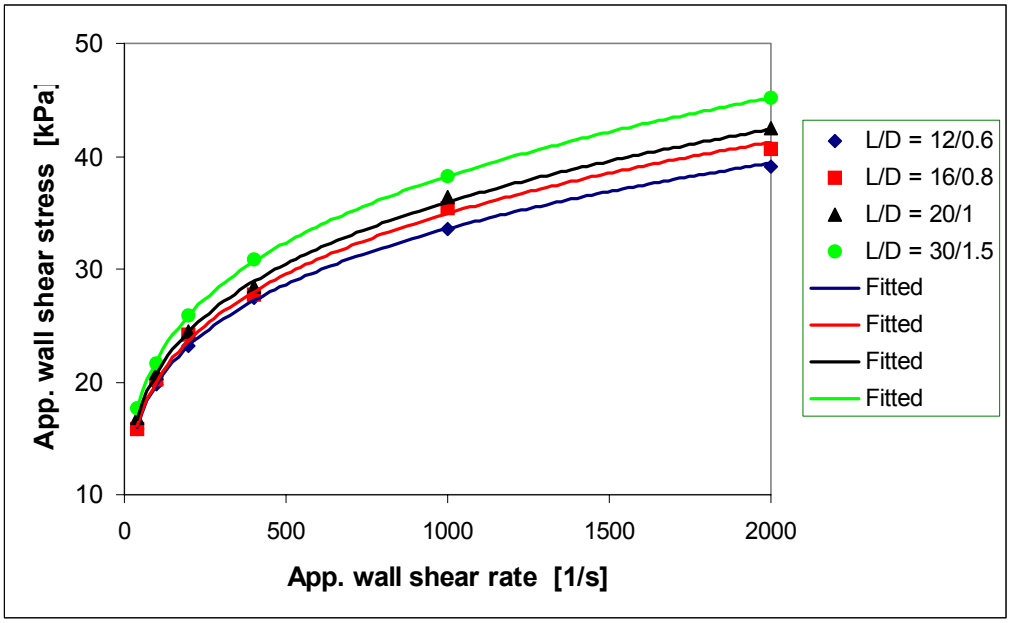

Figure 28. Apparent shear stress versus apparent shear rate for filled TPE with four different capillaries.

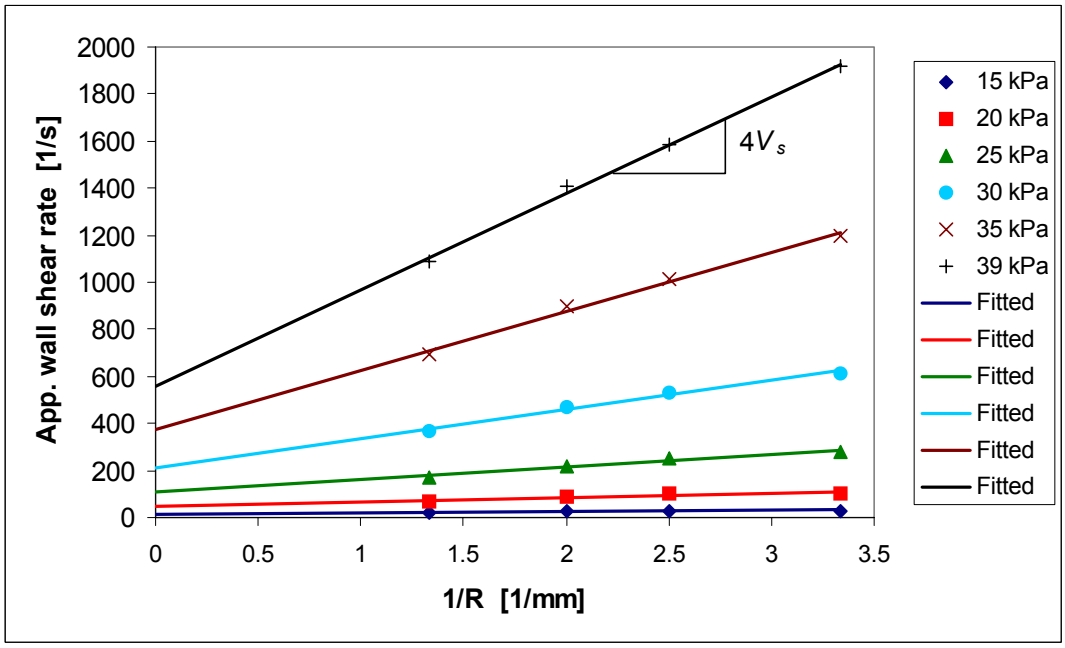

Figure 29. Mooney plot for filled TPE melt.

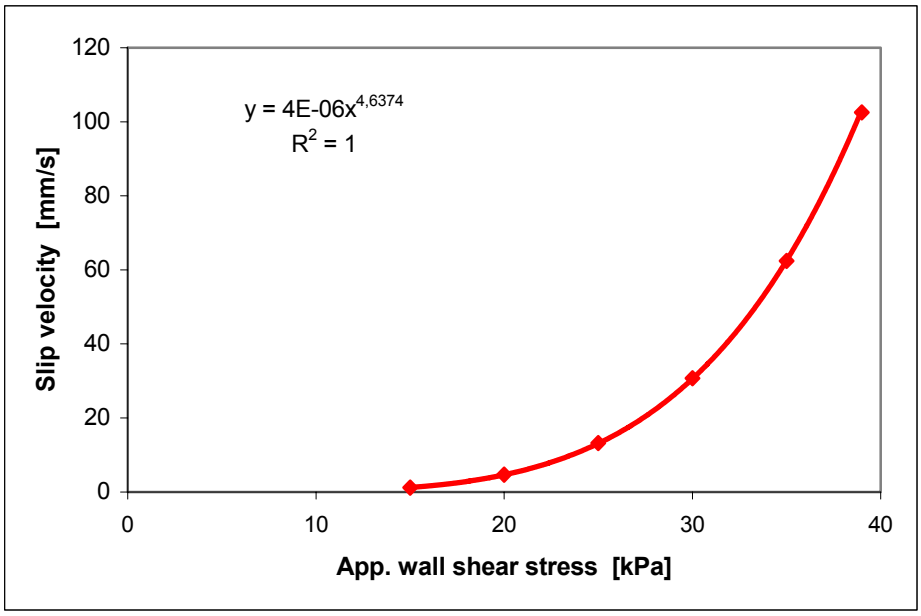

Figure 30. Measured wall slip velocity against apparent shear rate for filled TPE and fitting to a power-law.

Flow instability in the capillary flow

It is worth noting that slip may also occur with pure polymers; notably with linear polyethylenes like LLDPE and HDPE. For these polymers, the slip phenomenon often results in flow instability. The instability phenomenon may also be present in industrial extrusion processes limiting the production rates and influencing the appearance and quality of end-products.

In order to illustrate the potential of the capillary rheometer as a tool to examine the polymer flow instability phenomenon, experiments were performed for HDPE 53050E (manufactured by Dow Chemicals). The measurements were made at a temperature of 190°C in such a way that the piston speed was increased step-by-step so that the apparent wall shear rates were 200, 250, 300 1/s and so on. The pressure variation with time during the test is shown in Fig. 31. It can be observed that the pressure oscillations appear at a certain speed. This phenomenon is generally attributed to a periodic transition of no wall slip and pronounced wall slip (the phenomenon is often referred to as slip-stick effect or spurt flow). It has been observed that the critical shear stress for the appearance of pressure oscillations is of the order of 0.3 MPa [11]. For the present measurements the oscillations appear at the pressure level of 28 MPa, which corresponds to the apparent wall shear stress of about 0.24 MPa. It can also be seen that at sufficiently high piston speeds the oscillations disappear and the pressure level settles at a significantly lower value than before the appearance of oscillations. It is apparent that full slip occurs in this region. The distortions in the material coming out of the capillary rheometer can be seen Fig. 32.

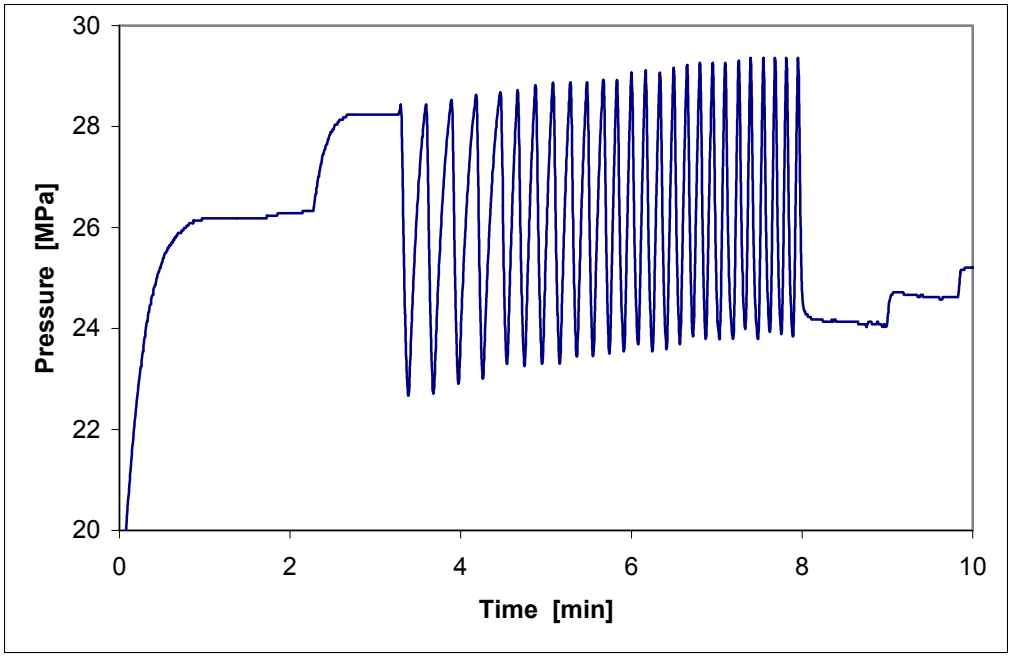

Figure 31. Time dependence of the pressure of a HDPE melt for a stepwise increase of the flow rate.

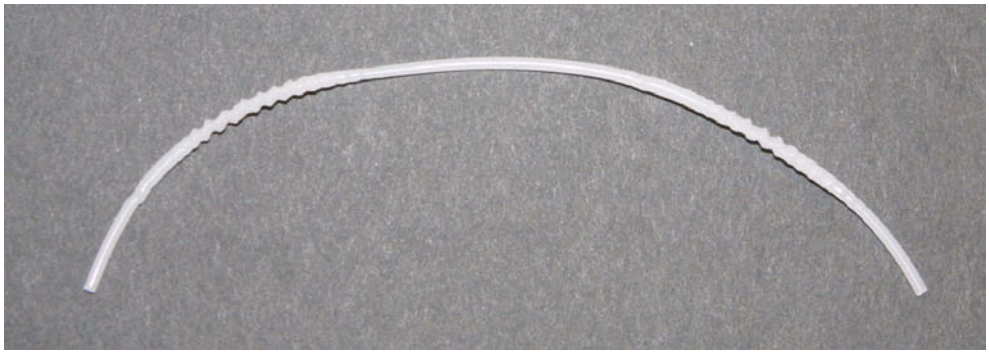

Figure 32. Distortions in the material after capillary rheometer experiment.

Pressure dependence of viscosity of polymer melts

To study the pressure dependence of polymer melt viscosity, the tests with the capillary rheometer and pressure chamber were conducted for several polymers including ABS, PS, POM, LDPE, PC and PP. In this paper, only the results for LDPE Lupolen 1840H are provided, more extensive presentation of results are given elsewhere [12, 13].

To enable the Bagley correction to be made, measurements were performed using two capillaries having a diameter of 1 mm and length-to-diameter ratios (L/D) of 10 and 20. Pressure transducers with maximum capacities of 140 and 100 MPa were employed for upstream and downstream pressure recordings, respectively.

As was described above, pressure chamber experiments were carried out in such a way that the piston speed, which corresponds to a specific apparent wall shear rate, was remained constant throughout a single test run. The pressure level in the barrel as well as in the pressure chamber were increased step-by-step by turning the valve once the pressures corresponding to an existing valve position were stabilized. For each data point, the pressure drop across the capillary (Δp) and the mean pressure in the capillary (p_m) are defined as follows:

$$\Delta p = p_1 - p_2 \tag{25}$$

$$p_m = (p_1 + p_2)/2 \tag{26}$$

Here, p_1 and p_2 are the pressures recorded before and after the capillary, respectively.

In the pressure chamber tests, the analysis of the experimental data is complicated by the fact that the data for different capillaries and apparent shear rates are not attainable with the same mean pressures. In principle, this could be achieved by suitable valve adjustments, but such a procedure would become extremely time-consuming, because the mean pressure within the capillary cannot be controlled directly. To facilitate the analysis, the experimental data points for each capillary and apparent shear rate were fitted to the equation of the form

$$\ln \Delta p = c_o + c_1 p_m + c_2 p_m^2 \tag{27}$$

Here, c_o, c_1 and c_2 are the fitting constants. This type of equation was chosen, because it was observed that the measured $\ln(\Delta p)$ versus p_m did not always exhibit a straight line. The measured data and the fitted curves are shown in Fig. 33 for apparent shear rates of 50, 200 and 500 1/s.

After the fitting, the Bagley correction can be made for an arbitrary value of p_m. The pressure drops associated with the capillaries of L/D = 10/1 and 20/1 are denoted as $(\Delta p)_{10}$ and $(\Delta p)_{20}$, respectively. Assuming a linear extrapolation to zero capillary length, the entrance pressure drop, Δp_e, can be calculated from the capillaries of 10/1 and 20/1 as follows:

$$\Delta p_e = 2(\Delta p)_{10} - (\Delta p)_{20} \tag{28}$$

The Bagley corrected viscosity for a given apparent wall shear rate, $\dot{\gamma}_a$ (= $32Q/\pi D^3$), can now be written as

$$\eta_a = \frac{\Delta p - \Delta p_e}{4(L/D)\,\dot{\gamma}_a} \tag{29}$$

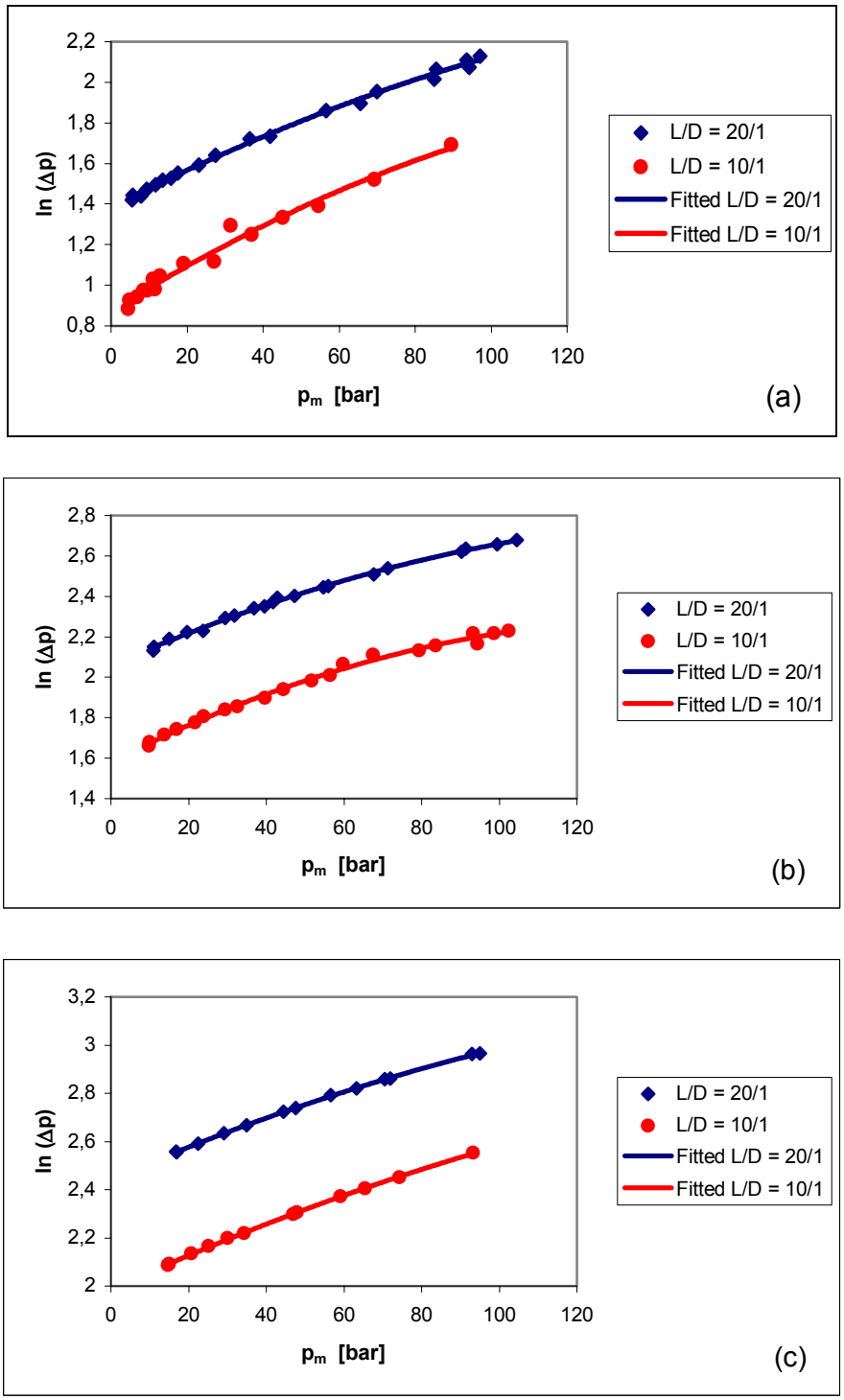

Figure 33. Semi-log plot of measured pressure drop (Δp) against mean pressure in the capillary (p_m) at apparent shear rates of (a) 50 1/s, (b) 200 1/s and (c) 500 1/s. Lines represent corresponding fits according to Eq. (27) (LDPE Lupolen 1840H).

Note that Δp in Eq. (29) is $(\Delta p)_{10}$ or $(\Delta p)_{20}$ depending on whether the L/D value of 10 or 20 is used (both yield the same result). The resulting apparent viscosity versus apparent shear rate data at different pressures are shown in Fig. 34 for LDPE Lupolen 1840H.

The curves shown in this figure were obtained by fitting the measured data to the Carreau-Yasuda model of the form

$$\eta = \alpha_p \eta_o \left[1 + (\alpha_p \lambda \dot{\gamma})^a \right]^{(n-1)/a} \tag{30}$$

where the pressure-shift factor was obtained by

$$\alpha_p = \exp(\beta p) \tag{31}$$

with β being the pressure coefficient. The values of the fitting parameters obtained are as follows: η_o = 9100 Pa·s, n = 0.21, a = 0.31, λ = 0.089 s and β = 0.012 1/MPa. It is worth noting that for semi-crystalline polymers like LDPE the effect of pressure on the viscosity is not so important as with amorphous polymers like PS and PC (see [13]).

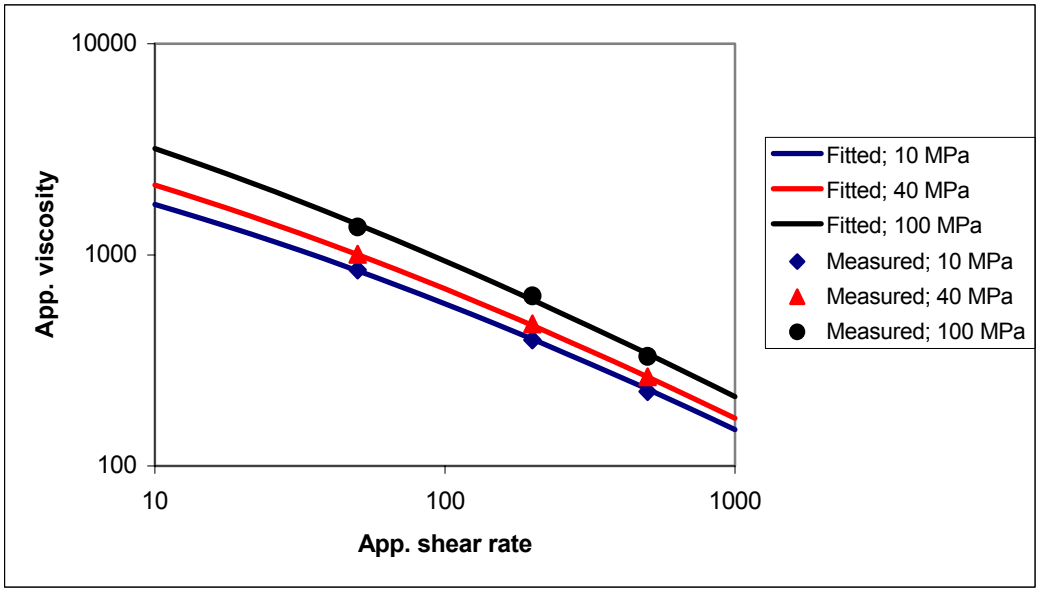

Figure 34. Measured apparent viscosity against apparent shear rate at different pressures for LDPE Lupolen 1840H. Lines represent fits according to Carreau-Yasuda model with exponential pressure dependence (Eqs. (30) and (31)).

Yield-stress with filled polymers

It is known that the influence of fillers on the polymer viscosity is often considerable at low shear rates, but much smaller at high shear rates [14]. Moreover, the viscosity of filled polymers may increase strongly with decreasing shear rate when the filler content becomes sufficiently high. This kind of behaviour is an indication of a yield stress, a stress below which the material behaves as a solid and does not flow any more. A

possible explanation for the existence of a yield stress is that the suspended particles form a strongly interacting network, which must be disrupted before flow can occur.

To exemplify the effect of filler content on the rheology of polymer melts, the measured results for the shear viscosity against the shear rate are presented in Fig. 35 for a glass-fibre-filled POM with three different fibre contents (0, 10 and 20%). The measurements were performed using the rotational rheometer with cone-and-plate configuration (low shear rates) and capillary rheometer (high shear rates). The impact of the fibres is clearly observable at low shear rates, where the Newtonian plateau does not appear at all within the range covered by the present measurements. At high shear rates, on the other hand, the viscosity is only moderately affected by fibres.

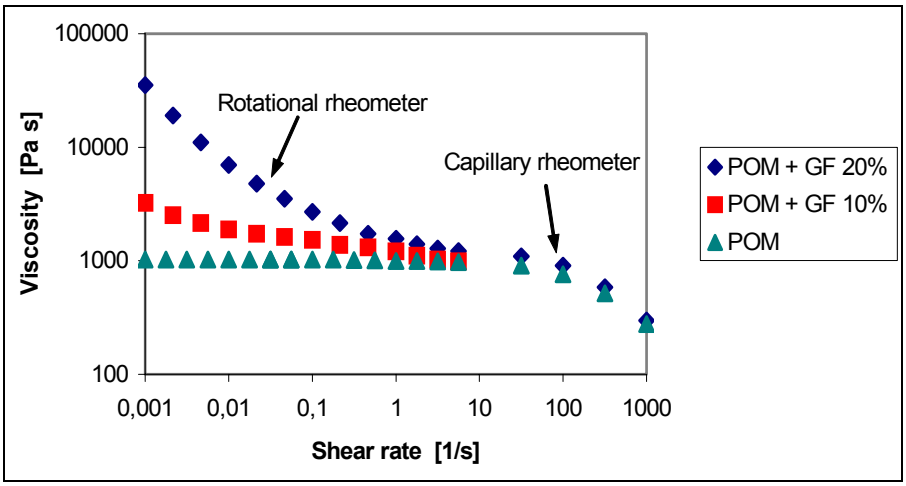

Figure 35. Measured viscosity against shear rate for glass-fibre-filled POM with fibre contents of 0, 10 and 20%.

Effect of molecular mass distribution on the polymer viscosity

As is generally known, the rheological behaviour of polymeric materials is directly controlled by their molecular structure. In order to demonstrate the effect of molecular mass distribution (MMD) on the rheology, dynamic oscillatory measurements using the rotational rheometer with plate-and-plate geometry were performed for two polymers showing distinctly different MMDs. The polymers studied were a standard LDPE with a broad MMD and a metallocene polyethylene (mPE) with a narrow MMD; for details see Table 3. The dependence on MMD can be clearly seen in Fig. 36, where the magnitude of the complex viscosity is plotted against the angular frequency. The trend in this figure is indeed generally observed for polymers, that is, the onset of the shear-thinning behaviour of the (shear or complex) viscosity shifts to lower shear rates when the MMD becomes broader. Furthermore, the degree of shear-thinning typically increases with increasing breadth of the MMD. For more details, see [15].

Table 3. Molecular data of the two polymers.

	mPE Affinity PL1850	LDPE Lupolen 1840 H
M_w [kg/kmol]	77 100	258 000
M_w / M_n	2.31	16.6

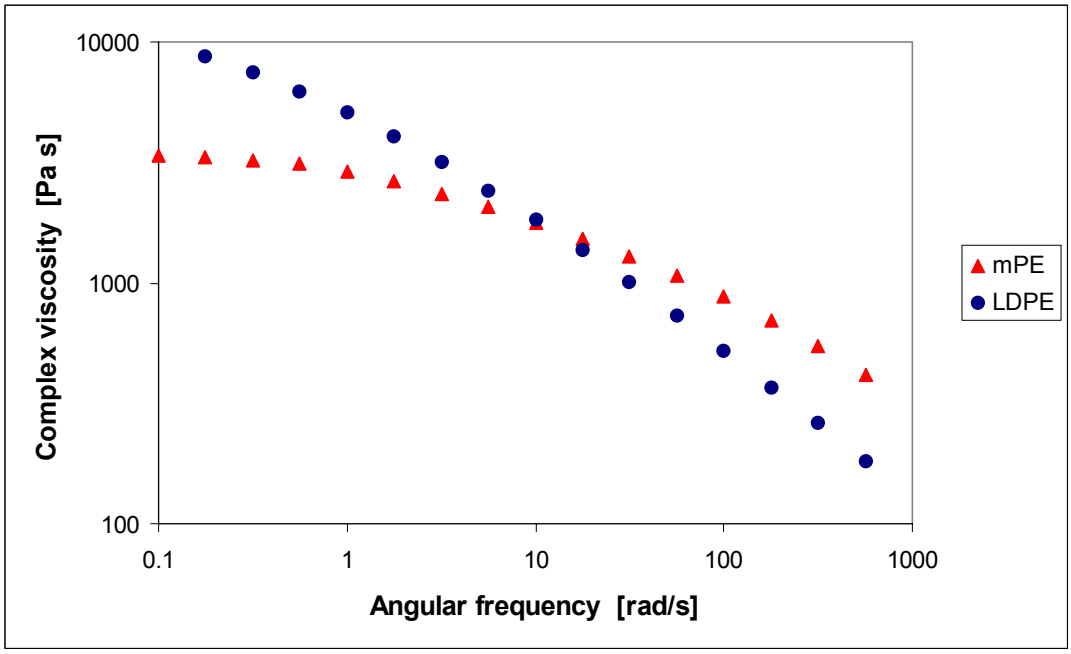

Fig. 36. Measured amplitude of complex viscosity against angular frequency for LDPE (Lupolen 1840H) and mPE (Affinity PL1850).

Cox-Merz rule

A well-known empiricism in the rheology of polymer melts is the Cox–Merz rule, which relates the magnitude of the complex viscosity as a function of angular frequency to the steady shear viscosity as a function of shear rate, as stated by Eq. (20). This relationship is very useful because it allows the estimation of the shear viscosity curves from the more readily obtainable dynamic oscillatory measurements. The Cox–Merz rule is indeed a very interesting relationship, because there are no theoretical reasons for such a correspondence to exist, since the rheological responses of polymer melts in dynamic and steady measurements are quite different. The former is carried out in the linear viscoelastic regime and the latter in the non-linear regime.

To demonstrate the validity of the Cox–Merz rule, experiments were carried out for a metallocene polyethylene (mPE) Affinity PL1850 (manufactured by Dow Chemicals). The steady shear viscosity versus shear rate was measured by means of the capillary

rheometer and rotational rheometer with cone-and-plate geometry. Dynamic tests were conducted using the rotational rheometer with plate-and-plate geometry. According to the results displayed in Fig. 37 the Cox-Merz rule appears to hold fairly well. It is worth pointing out that even though most pure polymers seem to obey the Cox–Merz rule, this is not necessarily the case with filled polymers and polymer blends [1–3].

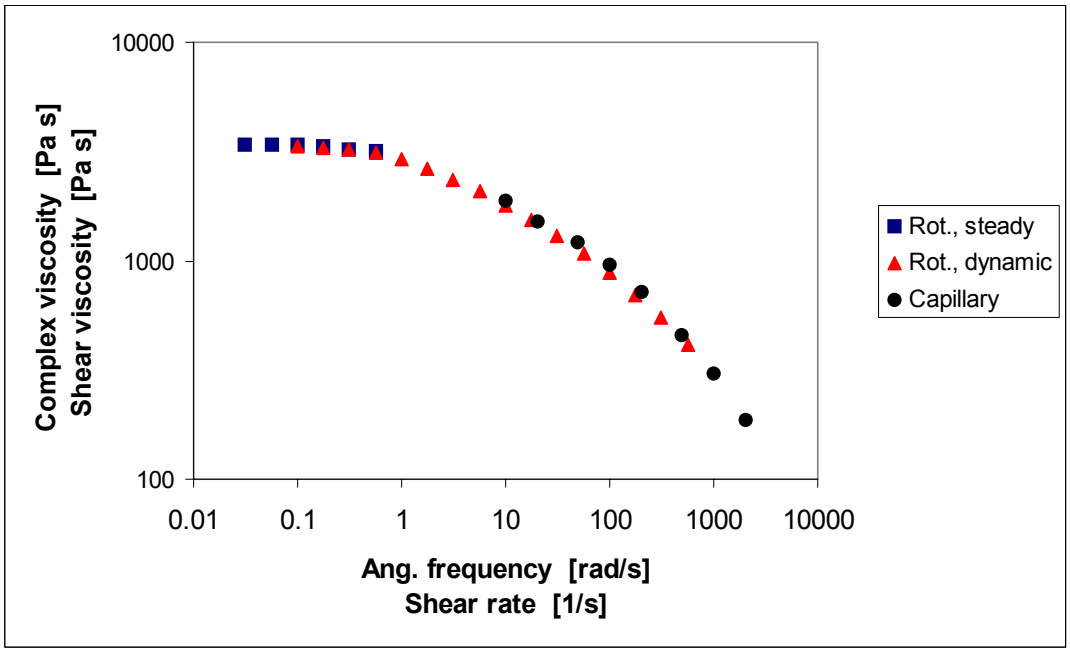

Fig. 37. Validity of Cox–Merz rule for mPE Affinity PL1850.

3.3.4 Conclusions

In this work, many aspects of the rheological behaviour of polymeric materials were experimentally studied using capillary and rotational rheometers. In particular, the work focused on various phenomena affecting the accuracy of the capillary rheometer measurements. In addition to standard Bagley and Rabinowitch corrections, the correction due to wall slip effect was explored. It was found that for the highly filled material studied the slip at the wall plays a significant role. The omission of the wall slip in the analysis of the experimental data may result in a largely inaccurate viscosity results. For example, the slip-corrected shear rates appeared to be of the order of one-third of the uncorrected values. It was also demonstrated how the capillary rheometer can be exploited in the investigation of flow instability often occurring with linear polymers like HDPE and LLDPE. The data obtained can be utilized in the actual extrusion processes, where similar instabilities may appear. Considerable efforts have also been directed to the measurement of the pressure-dependent viscosity of polymer melts using the capillary rheometer modified with a pressure chamber. The importance of pressure effects is clearly revealed by the results obtained. It is obvious that the

inclusion of the pressure-dependent viscosity is essentially important for the accuracy of the injection moulding simulations. In addition, some other aspects of polymer rheology, such as the yield stress phenomenon, the effect of molecular mass distribution on the viscosity and the Cox–Merz rule, were briefly discussed in this report.

References

1. Morrison, F. Understanding Rheology. Oxford University Press, 2001.
2. Dealy, J.M. and Wissbrun, K.F. Melt Rheology and its Role in Plastics Processing. Kluwer Academic Publishers, 1999.
3. Macosko, C.W. Rheology: Principles, Measurements and Applications. Wiley-VCH, Inc., 1994.
4. Whorlow, R.W. Rheological Techniques. Ellis Horwood, 1992.
5. Collier, A.A. and Clegg, D.W. (eds). Rheological Measurements. Chapman and Hall, 1998.
6. Mezger, T.G. The Rheology Handbook. Vincentz Verlag, 2002.
7. Goubert, A., Vermant, J., Moldenaers, P., Göttfert, A. and Ernst, B. Comparison of measurement techniques for evaluating the pressure dependence of viscosity. *Appl. Rheol.* **11** (2001), pp. 26–37
8. Cox, W.P. and Merz, E.H. Correlation of dynamic and steady flow viscosities. *J. Polym. Sci.* **28** (1958), pp. 619–622.
9. Aho, J. and Syrjälä, S. Determination of the entrance pressure drop in capillary rheometry using Bagley correction and zero-length capillary. *Annual Transactions of the Nordic Rheology Society* **14** (2006), pp. 143–147.
10. Mooney, M. Explicit formulas for slip and fluidity. *J. Rheol.* **2** (1931), pp. 210–222.
11. Denn, M.M. Extrusion instabilities and wall slip. Ann. Rev. Fluid Mech. **33** (2001), pp. 265–287.
12. Aho, J. and Syrjälä, S. Evaluation of pressure dependence of viscosity for some polymers using capillary rheometer. *Annual Transactions of the Nordic Rheology Society* **13** (2005), pp. 55–59.
13. Aho, J. and Syrjälä, S. Pressure dependence of viscosity of polymer melts. Submitted for publication in Polymer Testing.
14. Hornsby, P.R. Rheology, compounding and processing of filled thermoplastics. *Adv. Polym. Sci.* **139** (1999), pp. 155–217.
15. Dealy, J.M. and Larsson, R.G. Structure and Rheology of Molten Polymers. Hanser, 2006.

3.4 Rheology and flow behaviour of fibre suspensions

Ari Jäsberg*, Pasi Raiskinmäki** and Markku Kataja*

(*) Department of Physics, P.O. Box 35 (YFL), FI-40014 Universtiy of Jyväskylä, Finland

(**) VTT, P.O. Box 1603, FI-40101 JYVÄSKYLÄ, Finland

The central issue in many engineering problems involving fluid flow is estimating frictional losses. For simple Newtonian fluids, loss in a fully developed flow in a straight tube is relatively accurately given by the famous Moody's diagram, or the related correlation formulas, which summarize the existing (yet incomplete) theoretical understanding on frictional flow in closed channels and a vast amount of carefully measured and analyzed experimental data. Although the qualitative flow behaviour of wood fibre suspensions in straight tubes is relatively well known, this general knowledge is not sufficient for providing us with similar loss correlations for these complex fluids. The practical design equations used in the industry are based on experimental correlations utilizing a large amount of data but relatively vague theoretical reasoning. The design principles are thus quite conservative and omit many fine details of the flow behaviour. For a review on the topic, see Ref. [1] and references therein. In this work, we utilize new experimental methods that have only recently become available, in order to gain more detailed understanding on the flow behaviour and the relevant rheological material properties of wood fibre suspensions. This information is then utilized in an effort to develop improved methods for predicting frictional losses in straight tube flow of fibre suspensions.

Below, we will first give a short summary of the well known qualitative features of fibre suspension flow in a straight tube. We then shortly review the experimental methods used, including the ultrasound Doppler method and the optical method for measuring wall layer thickness. Next, we apply these methods to study the transient behaviour of the flow after a tubulence generator (sudden step), approach to steady state flow, and the main features of fully developed flow. In particular, we seek to identify various dynamically different flow regimes on the basis of direct measurements. The observed results are summarized to yield a more detailed qualitative description of the flow behaviour. Guided by the experimental observation, we then introduce a two-phase laminar flow model for the fully developed plug flow regime. In the turbulent regime, we seek to find a empirical correlation model for the measured mean flow velocity profiles. Finally, we utilize the two-phase model and the velocity correlation formulas to derive general expressions for predicting frictional losses for plug flow and turbulent regimes.

3.4.1 Background

We consider here the behaviour of wood fibre suspension with fibre concentration above the sedimentation concentration, that is typically of the order of 0.5–1% by weight, in a pressure driven flow in a straight tube with smooth walls. According to Duffy [1], the flow behaviour can be roughly divided in two main regimes: the plug flow regime that occurs at low flow rates and the drag reduction regime that occurs at high flow rates [2]. Within the plug flow regime the fibre phase moves as a continuous fibre network with solid like properties and with no shearing motion. In this regime, the frictional loss is high compared to that of the carrier fluid (usually water) at the same flow rate. Furthermore, the dependence on flow rate of loss can be quite complicated. In some cases the loss may degrease with increasing flow rate. In the drag reduction regime, the fibre network is partly or entirely broken into flocs that undergo turbulent and shearing motion. Characteristic to this region is that the frictional loss may be below that of a pure carrier fluid. These qualitatively different main regimes can be divided into several subregimes. If the pressure gradient applied to the tube is below some threshold value that depends on fibre type and concentration the fibre plug does not move at all and the motion of the carrier fluid is described as a flow through porous medium. Above the threshold pressure, also the fibre plug is set into motion. The fibres are first in a direct contact with the wall inducing high shear stress (high loss). As the flow rate is increased, a plug flow behaviour is preserved, but a thin layer of pure water (a 'lubrication' layer) is created next to the wall. Characteristic to this flow regime is that the wall friction is approximately constant, and may even degrease with increasing flow velocity. As the flow rate increases further, turbulent flow appears near the walls and the fibre plug begins to break from its outer surface. Thus, in this mixed flow regime a turbulent fibre annulus surrounds a rigid fibre plug in the middle of the tube. At some point, frictional loss falls below that of the carrier liquid and drag reduction regime is obtained. As the flow rate is still increased, the solid fibre core gradually vanishes indicating fully turbulent or 'fluidized' flow regime. Here, the loss typically approaches the pure fluid curve asymptotically as the flow rate is increased.

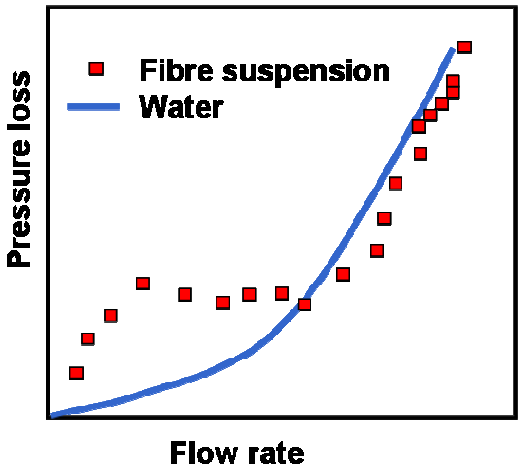

Figure 38. Qualitative behaviour of pressure loss as a function of flow rate for a fully developed flow of fibre suspension in straight smooth tube. The solid line indicates the standard pressure loss behaviour of water.

This quite generally accepted view on the different flow domains was originally based on pressure loss measurements, visual observations of the flow near the tube wall and on velocity profile measurements made at turbulent region using a specific annular-purge impact probe [1]. We now wish to investigate this qualitative general flow behaviour in more detail using the new experimental methods that allow direct measurement of fibre velocity field at all flow situations and of thickness of the fibre free lubrication layer near the wall.

3.4.2 Experimental methods and set-up

The experiments were made in an acrylic flow loop with tube diameter 40 mm for birch and pine fibre suspensions. The volume flow rate in the tube was controlled by adjusting the rotation speed of the centrifugal pump and measured using a magnetic flow meter. The flow line was equipped with differential pressure transducer for loss measurement.

The velocity profile across the tube was measured using pulsed ultrasound velocimetry (PUDV) techniques illustrated in Fig. 39. The measurement is based on using a transmitter to send short ultrasound bursts through the tube wall and into the flow. Target particles (fibres) moving with the flow scatter the sound which is detected by the transmitter. The distance of the particle is found by the time-of-flight method using the known velocity of sound, and the velocity of the particle from the measured Doppler shift of the echoed sound. (The device thus measures the velocity component in the direction of the ultrasound beam.) Within the present measurement, 32 pulse emissions were used to construct a single velocity profile, and 3000 profiles were collected during

20 seconds. The mean velocity profile was calculated as the average of these 3000 individual profiles, and the fluctuating velocity component was determined as the deviation of each individual velocity value from the mean velocity at a given position across the tube. The individual velocity profiles given by the PUDV method suffer from a noise intrinsic to the measuring principle. The measured absolute value of the fluctuating velocity may thus not be very accurate. For the present purpose we are, however, only interested in relative values of fluctuations at different parts of the tube. In addition, the intrinsic noise is highly uncorrelated, and can thus be eliminated from the measured spatial velocity correlations.

The thickness of the lubrication layer was measured optically using a collimated laser beam guided inside the flow channel (see Fig. 40). The horizontal position of the vertical beam could be controlled such that the focal point remained at the horizontal tube diameter. The accuracy of the beam position as well as the diameter of the focal waist of the beam were approximately 10 μm. The light scattered from fibres traversing the beam was detected by an optical sensor placed just outside the tube wall and having a narrow horizontal field of view through the tube wall into the focal point of the beam. The straight tube sections upstream and downstream of the measuring point were approximately 2.7 m and 0.5 m, respectively. For each flow rate, 1000 light intensity values were collected at a sampling rate adjusted according to the mean flow velocity such that the distance between consequent measuring points in the moving fibre plug was approximately 1 mm. Notice, that this method is applicable in the plug flow regimes (regions I and II), where the velocity of the fibre plug is very close to the measured mean velocity. The pressure loss in the tube was measured simultaneously with the lubrication layer thickness.

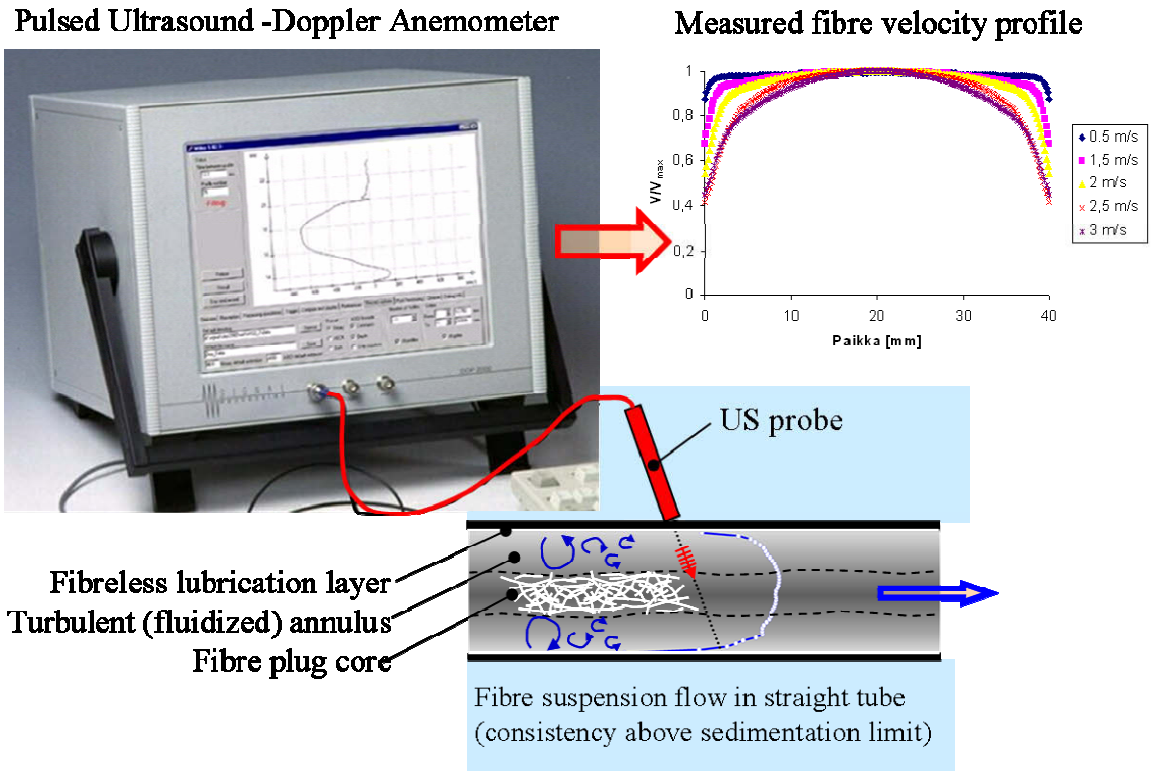

Figure 39. The pulsed ultrasound Doppler velocimeter (Signal Processing-DOP2000) applied in fibre suspension flow measurements. In each measurement 3000 individual flow profiles are collected to find the mean velocity profile and velocity fluctuation profile. The latter was used to identify the fibre plug core and turbulent annulus in the mixed flow region.

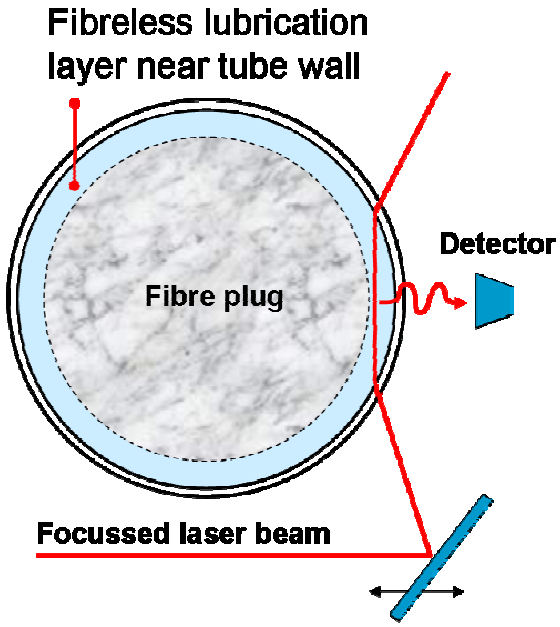

Figure 40. The principle of the laser-optical measurement of the lubrication layer thickness.

3.4.3 Developing flow

We first apply the PUDV -method to study the flow in a straight tube of diameter is D = 40 mm and length L = 3 m with a constriction block of inner diameter 20 mm and length 0.25 m placed inside the entrance part of the tube. The resulting forward facing sudden step provided by the exit end of the constriction block generates a recirculation zone and a strong turbulent field in the downstream part of the tube. The velocity and fluctuation profiles through the tube diameter (see Fig. 41) were measured at 18 fixed locations after the constriction block for different flow rates varied between 0.7 and 3.5 l/s. The first measuring point was located at distance 0.2 m and the last point at distance 2.6 m from the step. The measurement zone thus includes portion of the tube, downstream of the recirculation zone, where the flow is already reattached to the tube walls, takes place in a decaying turbulent field and approaches a fully developed condition towards the end of the tube. In this experiment birch/pine fibre suspension at consistency 0.5–2% were used.

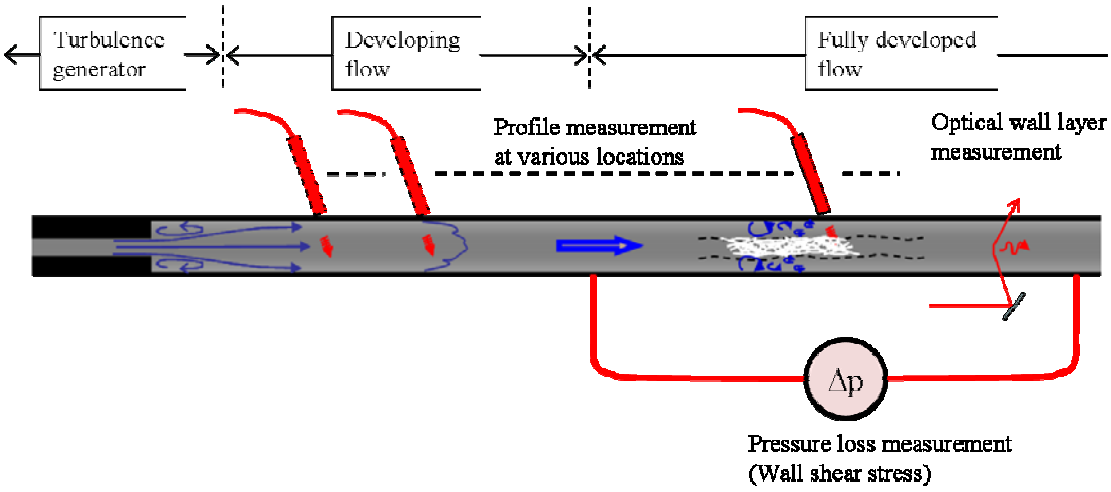

Figure 41. Schematic illustration of the experimental arrangement for fibre suspension flow in a straight tube after a turbulence generator.

Figures 42, 43 and 44 show the mean velocity and turbulent intensity profiles at various locations along the tube for flow rates 0.7 l/s, 1.9 l/s and 3.5 l/s, respectively. The turbulent intensity is defined as $I_T = <\delta u^2>/2$, where δu is the fluctuation velocity (deviation from time mean velocity) and < > denotes average over the 3000 individual velocity profile measurements.

At all flow rates used, the turbulent intensity immediately after the sudden expansion is very high indicating that the suspension is in a fluidized state where the fibre phase is broken into small flocs that undergo turbulent motion. The turbulent intensity is highest in the middle of the tube and degreases rapidly with distance x as the fluctuations of the fibre phase cease. At low flow rate (see Fig. 42), the fibre phase finally forms a

continuous network that spans through the tube, except of a thin fibre free lubrication layer that may be formed at the walls (but can not be observed with the PUDV techniques). The shape of the mean velocity profile undergoes only minor change along the tube, being plug-like turbulent profile immediately after the recirculation zone and turning into a plug-like steady profile further downstream where the flow approaches fully developed condition. The developed profiles shown in Fig. 42 are typical to plug flow regime.

At moderate flow rate (see Fig. 43) the behaviour is similar to that shown in Fig. 42. However, the overall turbulent intensity is higher and the high intensity region extends further downstream. In addition, the increased wall friction now prevents fibres from forming continuous network near the walls. Instead, a turbulent annulus remains near the walls and a continuous network is formed only at the core. This is seen as the turbulent intensity maxima near the walls and a slightly more rounded mean flow profile in the developed flow region. Here, the developed flow is typical to the mixed flow regime.

At the highest flow rate (see Fig. 44), the initial turbulent intensity is still higher and extends still further downstream. The turbulence induced by strong wall friction now prevents formation of continuous fibre network throughout the tube. The suspension remains fully fluidized also in the developed flow and is thus in the turbulent flow regime. Although the mean velocity and turbulent intensity profiles in the developed flow region appear quite similar to those for ordinary turbulent flow of simple fluids, a closer examination of the mean velocity profile reveals marked differences to the conventional logarithmic law behaviour (see below).

In this experiment we used a forward facing step to induce transient flow in decaying turbulence field and the resulting approach to fully developed flow. In practical applications, turbulent flow may be generated by other devices such as pumps, mixers and valves. We can, however, expect the qualitative features of the flow remain the same irrespective of the way in which the turbulence was generated.

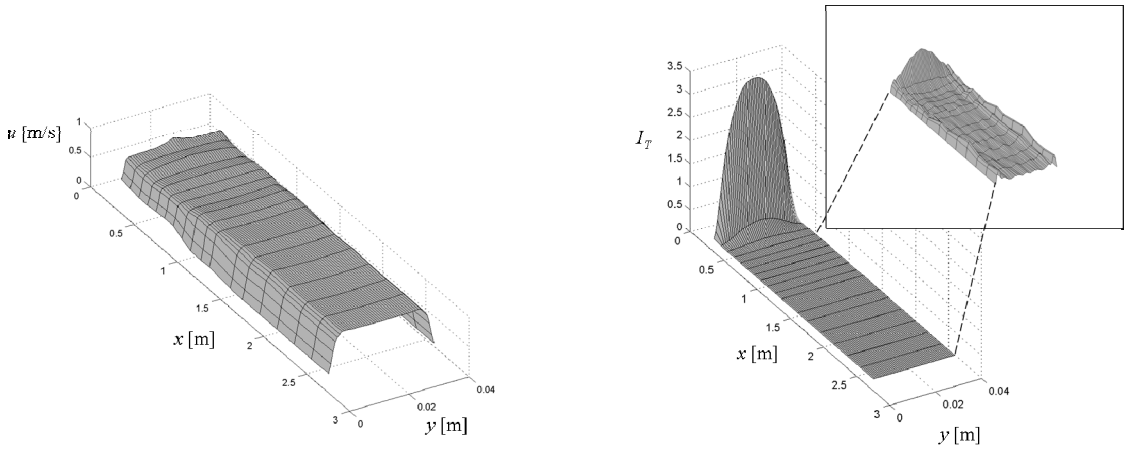

(a) (b)

Figure 42. The measured mean velocity profile (a) and turbulent intensity profile (b) after the recirculation zone created by a sudden expansion with area ratio 1:4 for flow rate Q = 0.7 l/s. The insert in (b) shows the measured turbulent intensity in the latter part of the tube, multiplied by a factor 100 for clarity.

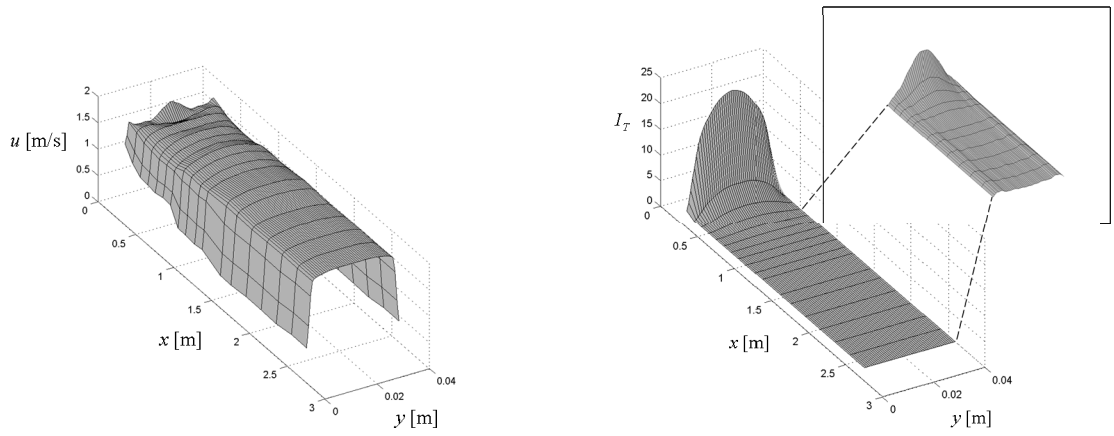

(a) (b)

Figure 43. Same as Fig. 42 but for flow rate Q = 1.9 l/s.

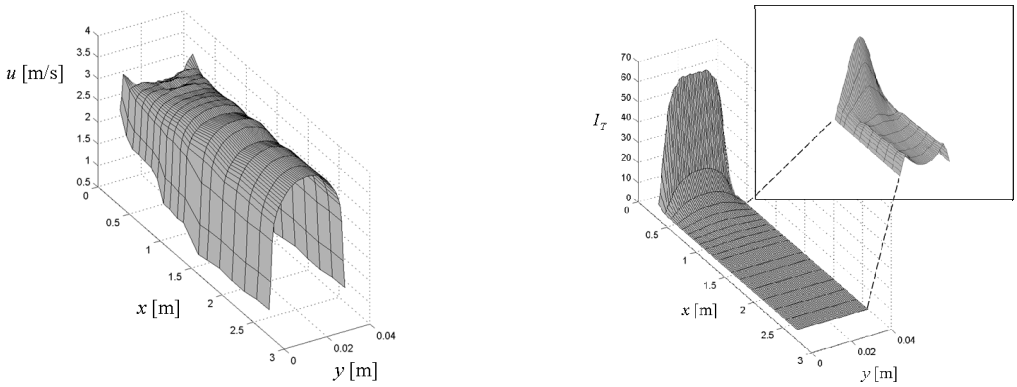

(a) (b)

Figure 44. Same as Fig. 42 but for flow rate Q = 3.5 l/s.

Although the results shown above may not seem to add much to the qualitative understanding of the developing flow of fibre suspension in decaying turbulence, they do indicate that the new experimental method utilized here can be used to gain much more detailed information on the flow behaviour as has been previously possible. This point will be further confirmed below. However, based on already these results, even the qualitative behaviour of the tube flow can be further specified at least in two respects. Firstly, unlike often phrased, for a tube flow in mixed or turbulent flow regions (after a pump, say) the wall friction does not *break* the continuous fibre network. Instead, wall friction prevents such a network from ever forming within an annulus of some thickness or in the entire tube. (Actual breaking of fibre network would only take place if the flow was first stopped to allow the continuous network to form, and then resumed.) Even though this difference may appear quite superficial, it can have some significance in *e.g.* when using the measured values of disruptive shear stress of the fibre network in predicting tube flow behaviour. It is not clear, without further investigation, that the value of disruptive shear stress measured by actually breaking an existing network by applied shear stress is the proper value to be used *e.g.* in predicting the transition from plug flow to mixed and turbulent flow regions in conventional tube flows. Secondly, the appearance of the fibre free lubrication layer in the plug flow regime is often explained by mechanical models based on shear deformation of the network induced by the wall stress, and the resulting reduction of plug diameter [1]. For a tube flow brought about by a pump, such a model is unphysical simply because the undeformed state of the network never existed. Instead, the fibre plug formed from the fluidized state in decaying turbulence after a pump or any fluidizing device is originally of diameter slightly less than that of the tube. The existence of lubrication layer is more likely due to inertial lift force that acts on particles moving near the wall. This phenomenon leads to a tubular pinch effect where the fibres are repelled from the wall and the fibre plug is formed in a state where the lift force is balanced by the elastic force of the network. The elastic force, in turn, is affected by the turbulent energy of fibres, partially stored as the elastic energy of the forming network.

3.4.4 Thickness of the lubrication layer. Dynamical regimes of tube flow

Figure 45 shows an example of results obtained by the laser optical lubrication layer thickness measuring device discussed above. In the figure, shown is the mean intensity of scattered light as a function of the laser beam position inside the tube of diameter 40 mm near the tube wall. The measurement is for pine fibre suspension at consistency 0.5% and flow rate 0.5 l/s, where the flow is well in the plug flow region. The pure water layer is indicated by the constant intensity region next to the wall. As the beam enters the fibre plug, the intensity starts to increase with the beam position more or less linearly. The thickness of the lubrication layer is defined as the crossing point of the two straight lines fitted to the data points in the constant intensity region and in the increasing intensity region as indicated in Fig. 45. In the flow condition shown, the thickness of the lubrication layer is thus estimated to be 0.32 mm. In Fig. 46 shown are the measured values of layer thickness as a function of mean flow velocity for various consistencies. The layer thickness h and mean flow velocity u are given in dimensionless form such that $u^+ = u/u^*$ and $h^+ = u^*h/\nu$, where $u^*=(\tau_w/\rho)^{1/2}$ is the friction velocity, ν and ρ are the kinematic viscosity and density of the carrier fluid (water) and τ_w is the wall stress (given by the measured pressure loss at each flow rate).

The measured layer thickness is shown in Fig. 46 only for those flow velocities at which a well defined finite thickness value could be found. Especially, with the present measuring techniques, the lubrication layer could not be observed at very low flow rates. Fig. 47 shows the measured pressure loss curves as a function of flow rate for pine fibre suspension at different consistencies. It appears that in each case, the region where the lubrication layer was not found coincides with the low flow rate domain where the pressure loss increases with flow rate. That domain is indicated in the figure as region I, and we naturally identify it as the plug flow region with direct fibre-wall contact.

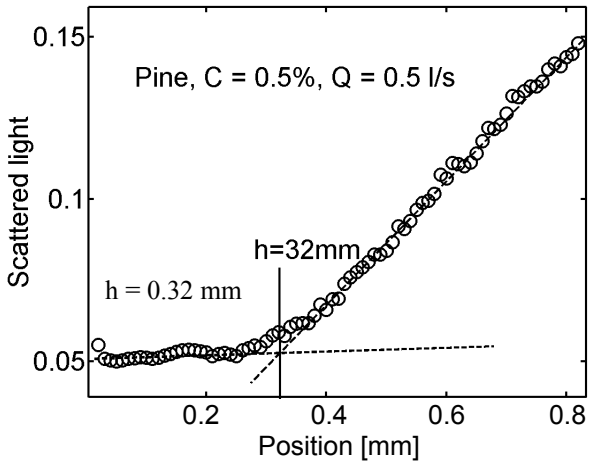

Figure 45. Intensity of the laser light scattered by fibres, as measured by the laser-optical device, as a function of distance from the tube wall. The crossing point of two fitted lines indicates the thickness of the fibre free lubrication layer.

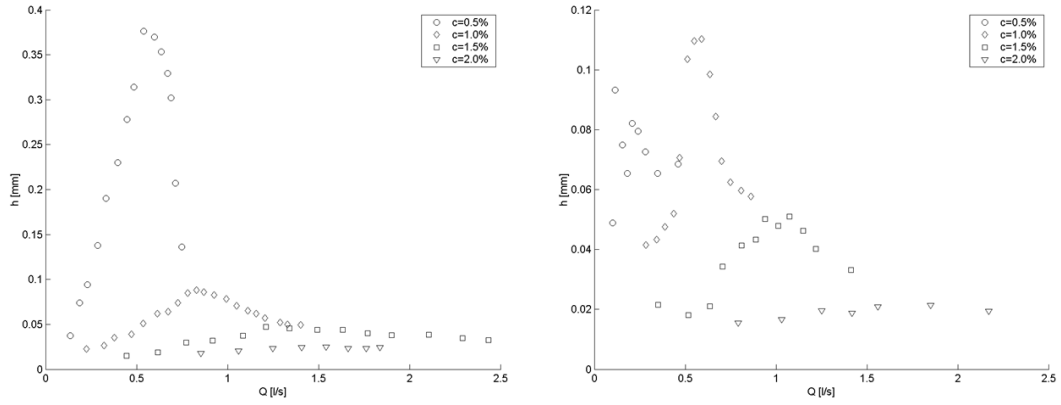

(a) (b)

Figure 46. The measured dimensionless thickness of the lubrication layer vs. dimensionless mean flow velocity for pine (a) and birch (b) fibre suspensions at various consistencies. The solid lines indicate the approximate position of the maximum layer thickness for different consistencies.

An observable lubrication layer appears at the flow rate corresponding to the local maximum in the loss curve (birch) or to the point where the loss curve levels off (pine). Above that flow rate, the thickness of the lubrication layer first grows with flow rate, reaches a maximum and starts to decrease. In general, the thickness degreases with consistency and the location of maximum point becomes less definite. The flow rate corresponding to the maximum layer thickness (where observable in the data) falls approximately at the same point, where the loss curve again starts to grow. The region where the lubrication layer thickness increases is indicated as regime II in Fig. 47 and we identify it as the plug flow regime with lubrication layer. The observed degrease of the layer thickness after the maximum is most likely due to incipient turbulence, *i.e.* turbulence in the fluid phase (that we do not observe with the present methods). This turbulence is not yet strong enough to cause macroscopic breakage of the fibre network, but only to bend and dislodge individual fibres that are loosely bound to the fibre plug surface. These fibres can then be randomly displaced towards the tube wall by fluctuations of fluid velocity, and thereby cause increased light scattering as they traverse the laser beam. The apparent decrease of lubrication layer thickness may thus be explained by dispersion of the fibre plug surface layer due to fluid phase turbulence. This region, where the measured lubrication layer thickness decreases and pressure loss increases but where macroscopic rupture of fibre plug is not yet observed, is indicated as regime III in Fig. 47.

As the flow rate is still increased, interpretation of the light scattering data becomes uncertain, most likely due to increased dispersion of the fibre plug. As discussed above, however, we can effectively use the PUDV data to identify the various regimes of fully developed flow in this region. The onset of fibre phase turbulence near the wall takes place approximately at flow rate, where the dependence of pressure loss on flow rate

also seems to undergo a rather subtle yet observable change. In regime III the dependence is approximately linear and turns into approximately quadratic dependence at the region where the turbulent annulus first becomes observable. This mixed flow regime is indicated as region IV in Fig. 47. The transition from mixed flow regime into fully turbulent regime V is gradual and no sharp change in loss behaviour can be observed. The exact flow rate at which the fibre plug core disappears can not be identified from pressure loss data. We will discuss this topic in greater detail below utilizing the results from velocity profile measurements. At very high flow rates, the pressure loss behaviour approaches that of pure fluid.

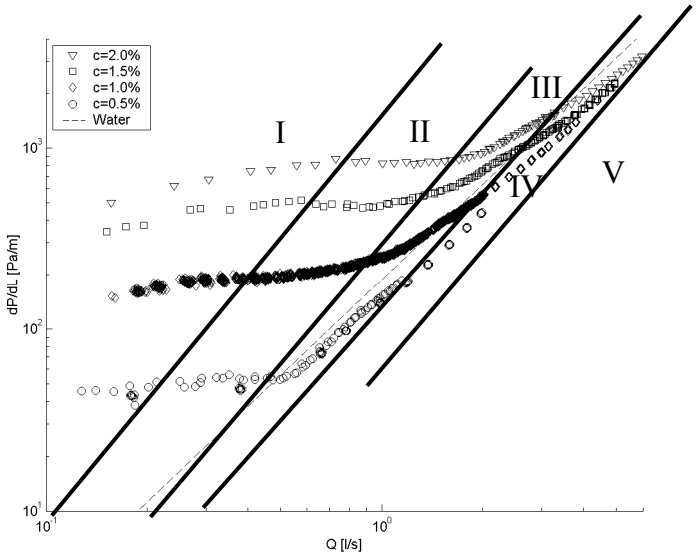

Figure 47. Measured loss vs. flow rate for pine fibre suspension in a D = 40 mm flow channel for various consistencies (by weight). Dashed line is the standard curve for pure water in a hydraulically smooth pipe, and solid lines divide the flow domain into five main regimes (labelled I–V) based on the flow behaviour (see Fig. 48).

Figure 48 illustrates the five qualitatively different flow regimes discussed above. The numbering coincides with that shown in the context of pressure loss data, Fig. 47. Although this classification is very similar to those presented previously (see e.g. Ref. [1]), there are some subtle differences. In particular, the existence and nature of regime III and identification of the different flow regimes in the pressure loss data are now more precisely defined. Notice also, that the present classification is based on direct experimental evidence on various features of the flow.

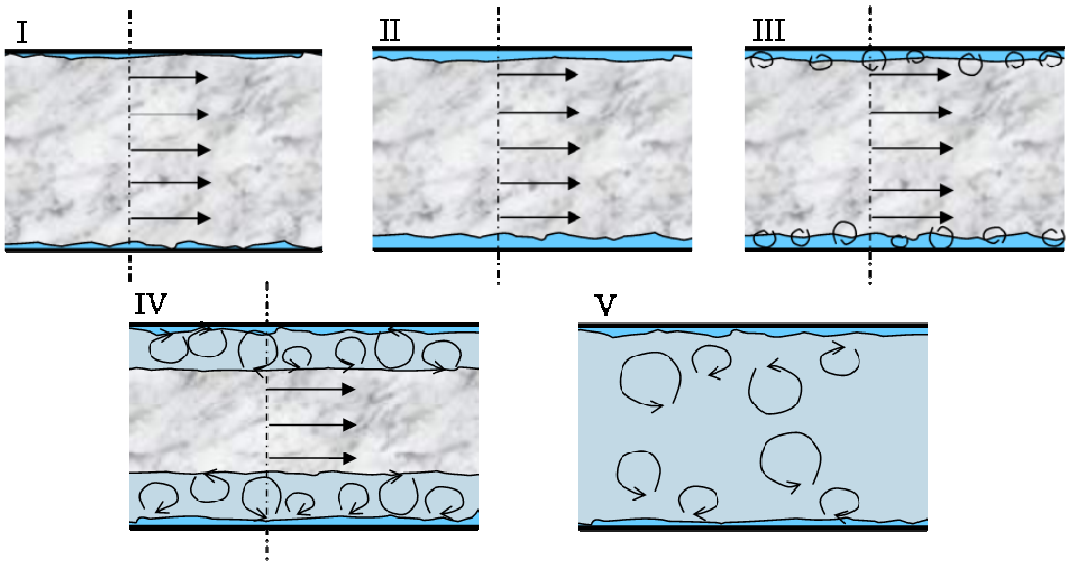

Figure 48. The main flow regimes of fibre suspensions. (I) Plug flow regime with direct fibre-wall contact, (II) plug flow regime with lubrication layer, (III) plug flow regime with incipient (fluid phase) turbulence, (IV) mixed flow regime and (V) fully turbulent flow regime

3.4.5 Velocity profiles

We consider here the flow velocity profiles separately for plug flow regimes I and II and for turbulent regimes III–IV for fibre suspensions of concentration exceeding the sedimentation. The plug flow regime profile is based on a theoretical two-phase continuum model while the turbulent profiles are given by empirical correlations based on PUDV measurements.

a) Plug flow regime

We consider here a laminar two-phase flow model that takes into account the direct contact friction between fibres and tube wall at low flow rates and existence of lubrication layer at higher flow rates (see Fig. 49). Within the model, lubrication layer is formed due to repulsive inertial lift force that is known to act on particles moving near a solid wall. The averaged fluid flow is assumed to be steady and fully developed, and the mean fluid velocity is longitudinal, $\bar{v}_f = v_f(r)\hat{e}_z$. Fibres move as a rigid plug with a constant velocity $\bar{v}_s = v_s\hat{e}_z$. At very low flow rates the fibre plug is in direct contact with the pipe wall. As the flow rate increases a lubrication layer of pure carrier fluid occurs next to the pipe wall. The width h of the lubrication layer is small compared to the pipe radius R.

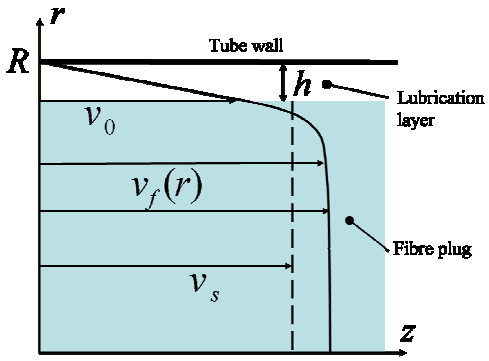

Figure 49. Schematic view of the plug flow of fibre suspension with lubrication layer.

In the case where lubrication layer exists, the velocity of the fluid within the thin layer is given by the quadratic Hagen-Poiseuille profile that can here be approximated by the linear expression

$$v_f(r) \cong -\frac{R}{\mu}\frac{\partial}{\partial z}\tilde{p}_f\left(R-r\right) = \frac{\tau_w}{\mu}y\,, \tag{32}$$

where r and z is the radial and axial coordinates, respectively, μ is the dynamic viscosity of the fluid, $\tilde{p}_f$ is the fluid pressure, R is the tube radius, y is the distance from the wall and $\tau_w = -\frac{R}{2}\frac{\partial}{\partial z}\tilde{p}_f$ is the wall shear stress. The fluid velocity at the surface of the fibre plug is thus given by

$$v_0 \cong \frac{\tau_w}{\mu}h \tag{33}$$

Inside the fibre core, the system is modelled as two interacting continua, and the governing two-phase equations for momentum are obtained by (volume) averaging the corresponding equation for each phase. The flow inside the core is thus described by a set of coupled equations

$$\begin{cases} \overline{\nabla}\cdot\overline{\overline{\sigma}}_f - D\hat{e}_z - L\hat{e}_r = 0 \\ \overline{\nabla}\cdot\overline{\overline{\sigma}}_s + D\hat{e}_z + L\hat{e}_r = 0 \end{cases}, \tag{34}$$

where $\overline{\overline{\sigma}}_f$ and $\overline{\overline{\sigma}}_s$ are the stress tensor of the carrier fluid and the fibre plug, respectively. The force applied on the unit volume of the fibre plug by the carrier fluid consist of the longitudinal drag force D and the transverse lift force L. The drag force is modeled by Darcy's law as

$$D = \frac{\mu}{k}(v_f - v_s)\,, \tag{35}$$

where k is the permeability of the fibre plug. The stress tensor of the fluid phase is

$$\bar{\bar{\sigma}}_f = -\phi \tilde{p}_f \bar{\bar{\mathrm{I}}} + \phi\mu\left(\overline{\nabla}\bar{v}_f + (\overline{\nabla}\bar{v}_f)^T\right). \tag{36}$$

Here ϕ is the porosity of the fibre plug.

The longitudinal component of the equation for the carrier fluid can now be written in the form

$$-\phi\frac{\partial}{\partial z}\tilde{p}_f + \phi\mu\left(\frac{d^2}{dr^2}v_f + \frac{1}{r}\frac{d}{dr}v_f\right) - \frac{\mu}{k}(v_f - v_s) = 0\,. \tag{37}$$

The proper boundary conditions for this equation are the velocity at the plug surface given by Eq. (33), and zero velocity gradient at the pipe axis. The solution of Eq. (37) is

$$v_f(r) = \left(v_s - v_0 - \frac{\phi k}{\mu}\frac{\partial}{\partial z}\tilde{p}_f\right)\left[1 - \frac{I_0(r/\sqrt{\phi k})}{I_0((R-h)/\sqrt{\phi k})}\right] + v_0\,, \tag{38}$$

where $I_0(x)$ is the modified Bessel function of the first kind of order zero. The length scale $\sqrt{k}$ of the velocity profile is typically of the order of 10^{-3}m – 10^{-5}m so that the arguments of the Bessel functions in Eq. (38) are large. The velocity can thus be approximated by an exponential profile:

$$v_f(r) = \left(v_s - v_0 - \frac{\phi k}{\mu}\frac{\partial}{\partial z}\tilde{p}_f\right)\left[1 - \exp\left(-\frac{y}{\sqrt{\phi k}}\right)\right] + v_0\,, \tag{39}$$

where $y = (R-h) - r$ is the distance from the plug surface.

The velocity of the fibre plug can be solved from the condition that the sum of the forces acting on the plug is zero in the steady state. The forces acting on the plug can be identified by integrating the equation for the longitudinal momentum over the cross-section of the fibre core. The resulting equation manifests a balance between two forces, namely the total Darcy's drag applied by the carrier fluid and the extra mechanical friction with the pipe wall (present in the case where lubrication layer does not exist, *i.e.* h = 0). Darcy's drag can be obtained by integrating the velocity profile for the carrier fluid, Eq. (39). Combining these two results and replacing wall shear stress for pressure gradient yields the plug velocity in a form

$$v_s = \frac{1}{\mu}\sqrt{\frac{k}{\phi}}\left((1-\frac{h}{R})\tau_w - \tau_s\right) - \frac{2\phi k}{\mu R}\tau_w + v_0\,. \tag{40}$$

Here the shear stress at the plug surface τ_s is the (yet unknown) mechanical wall friction per unit area. Finally, combining Eqns. (39) and (41) gives the velocity profile of the carrier fluid in the form

$$v_f(r) = \frac{1}{\mu}\sqrt{\frac{k}{\phi}}\left((1-\frac{h}{R})\tau_w - \tau_s\right)\left[1-\exp\left(-\frac{y}{\sqrt{\phi k}}\right)\right] + v_0 \,. \tag{41}$$

Notice that equations (40) and (41) are valid for both plug flow regimes I and II and even for the regime, where the fibre plug is stagnant and only fluid flow occurs. It now remains to develop an appropriate model for the shear stress at the plug surface τ_s and for the thickness of the lubrication layer *h*. Clearly, τ_s must depend on the radial structural stress of the fibre network at tube wall. We thus start with the radial stress balance equation of the fibre plug, namely

$$-\frac{\partial}{\partial r}P_S + L = 0 \,. \tag{42}$$

Here, L (≤ 0) is the inertial lift force per unit volume acting on the fibres and P_s is the radial normal stress of the fibre network. In what follows we shall call it simply the structural stress. (Notice that the structural stress arises originally from turbulent energy partially converted into elastic energy of the network that forms in the decaying turbulent flow field). The lift force decays rapidly with the distance from the pipe wall – typically within a few fibre diameters – and is thus significant only in a thin layer near the plug surface. Integration of Eq. (42) gives the structural stress at the surface of the fibre plug

$$P_S(R-h) = P_S(0)\big|_h + \int_0^{R-h} L\,dr \equiv P_S(0)\big|_h - P_L \tag{43}$$

where $P_S(0)\big|_h$ is the structural stress at the centre of the tube. (The notation is chosen to emphasize that the stress in the centre may depend on the lubrication layer thickness *h*.) The quantity P_L (≥ 0) gives the integrated contribution of lift force on structural stress and depends on flow rate. We choose to model the integrated lift force as

$$P_L = \frac{1}{2}\rho_f {v_s}^2 C_L \,\mathrm{Re}_s{}^{\beta-2} \,, \tag{44}$$

where ρ_f is the density of the carrier fluid, C_L is the lift force coefficient and $\mathrm{Re}_s = v_s\sqrt{k}/\nu$ is the fibre Reynolds number. It is obvious from the experimental

results discussed above that the lift force must increase with velocity of the fibre plug whereby the constant β must be positive.

In the case of vanishing lubrication layer thickness, the structural stress at the surface of the fibre plug is positive, *i.e.*, $P_S(R) \geq 0$. We assume that the mechanical frictional stress between the plug surface and the pipe wall is then proportional to that stress, *i.e.*, $\tau_S = C_S P_S(R)$, where C_S is a friction coefficient. This frictional stress decreases with increasing plug velocity (flow rate), and eventually becomes zero. A lubrication layer then develops at the pipe wall. In that case the structural stress at plug surface must vanish, *i.e.*, $P_S(R-h) = 0$ for all $h > 0$. Denoting $P_S(0)\big|_{h=0} = P_{S0}$ we can define the excess stress at tube centre ΔP_S at finite value of h such that

$$P_S(0)\big|_h \equiv P_{S0} + \Delta P_S(\mathrm{h}). \tag{45}$$

For small values of h, we may write $\Delta P_S \cong \frac{1}{\Gamma} h$ where Γ is a constant. This relation gives a natural constitutive model for lubrication layer thickness, *i.e.*, $h = \Gamma \Delta P_S$.

Reorganizing the equations given above, we can now rewrite the final results for frictional stress and lubrication layer thickness in a compact form as

$$\begin{cases} \tau_S = \max(0, C_S(P_{S0} - P_L)) \\ h = \max(0, \Gamma(P_L - P_{S0})). \end{cases} \tag{46}$$

Notice that the constants P_{S0} and Γ, related to elastic stress in the fibre plug as $h = 0$ and to rate of change of that stress with respect to h, may depend on flow conditions and not only on fibre properties. In particular, they may depend on the initial turbulent intensity and on the details of turbulence decay and formation of the fibre plug in the developing flow region downstream of the turbulence generator (see Sect. 3.4.3).

Given these basic results we can now find the limiting values of wall stress (pressure gradient) where the fibre plug is first set to motion and where the lubrication layer is first formed. The value τ_{w0} at which the fibre plug starts to move can be solved by setting $v_s = 0$, $\tau_s = C_s P_{s0}$ and $h = 0$ in Eq. (40), and solving for the wall stress. The result is

$$\tau_{w0} = \left(1 - \frac{2}{R}\phi\sqrt{\phi k}\right)^{-1} C_S P_{S0}. \tag{47}$$

When the gradient is below this limit, the fibre plug is stationary, and the mechanical friction τ_s must be calculated from Eq. (40) by setting $v_s = 0$ and $h = 0$. The value

τ_{wl} at which the lubrication layer is created can be found by setting $P_s = 0$ in Eq. (43) to solve for the corresponding plug velocity, and then applying Eq. (40). The result is

$$\tau_{wl} = \left(1 - \frac{2}{R}\phi\sqrt{\phi k}\right)^{-1} \left(\frac{2P_{s0}}{C_L \rho \frac{v^2}{k}}\right)^{1/\beta} \sqrt{\phi}\rho\frac{v^2}{k}. \tag{48}$$

b) Turbulent flow

For the turbulent flow regimes III–V, illustrated in Fig. 48, we have to rely on experimental profile correlations that can be obtained using pulsed ultrasound Doppler velocimetry. Fig. 50 shows the mean velocity profiles of pine fibre suspension of consistency 1% for flow rate ranging from 1.5 l/s to 5 l/s. Due to noise caused by the wall-fluid interface, the velocity measurement by the PUDV method is not accurate below ~1 mm from the wall, and those results are excluded from the profiles shown. A peculiar feature of the measured mean velocity at high flow rates is the S-shaped profile near the wall. (A similar result was obtained recently also by Xu and Aidun for rectangular channels [5].)

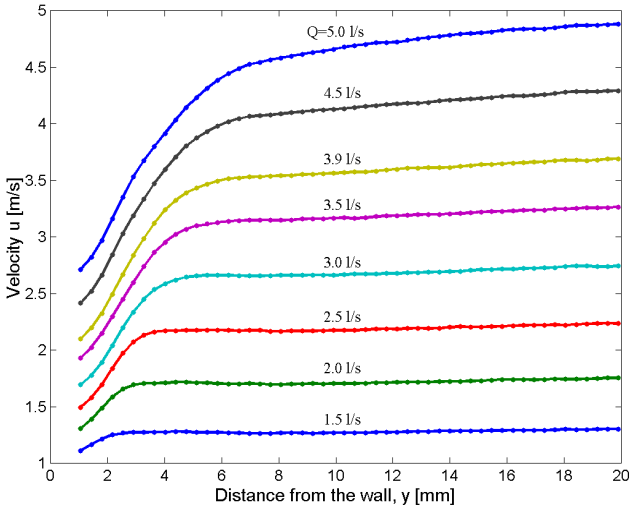

Figure 50. Mean velocity profiles of pine fibre suspension at consistency 1% as a function of distance from the tube wall. Flow rate is varied from 1.5 l/s to 5 l/s where the flow is in the mixed or turbulent flow regimes. The centre line of the acrylic tube is located at y = 20 mm.

As in the case of Newtonian flows, parametrization of turbulent velocity profiles of also fibre suspensions is best done utilizing the standard non-dimensional wall-layer variables defined by

$$u^+ = u/u^*$$
$$y^+ = yu^*/\nu, \tag{49}$$

where $u^* = (\tau_W/\rho)^{1/2}$ is the friction velocity, ρ and ν are the density and the kinematic viscosity of the fluid and τ_W is the wall shear stress obtained from the pressure drop measurements. Fig. 51 shows the same velocity profiles as Fig. 50 but redrawn in the dimensionless variables. Also shown is the standard logarithmic velocity profile for turbulent Newtonian flow, namely:

$$u^+ = \frac{1}{\kappa}\ln\left(y^+\right) + B, \tag{50}$$

where the constants κ and B have the standard values 0.41 and 5.5, respectively [4].

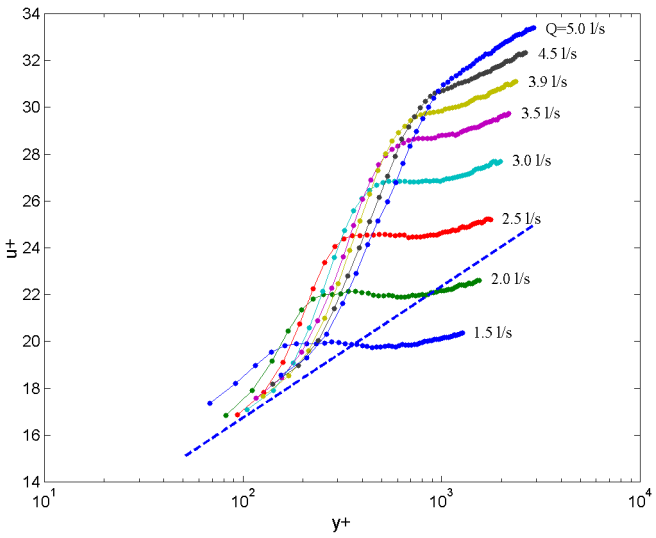

Figure 51. Same as Fig. 50 but for dimensionless velocity and distance from the tube wall, see Eq. (49). The dashed line is the standard logarithmic profile of turbulent Newtonian flow, Eq. (50).

A remarkable feature of the profiles shown in Fig. 51 is that there seems to exist an unique (approximate) envelope curve that corresponds to a limiting velocity profile shape as the flow rate approaches infinity. That envelope curve consists of a logarithmic near wall region where the profile coincides with that of Newtonian flow, a yield region where velocity gradient is higher than that of Newtonian flow, and a core region where the profile again is of the form given by Eq. (50) but with a value of constant B above that of Newtonian flows (*i.e.,* B ~ 5). The near wall region extends up to a distance scale $y_L^+ \sim 10^2$. Correspondingly, the core region starts at a distance scale $y_H^+ \sim 10^3$ and extends up to tube centre at $y^+ = R^+$. The yield region (in very high flow rate limit) is located between y_L^+ and y_H^+.

At finite flow rates the dimensionless velocity profiles seem to be approximately independent of flow rate in the region near the tube wall. At distances $y^+ < y_L^+$ the velocity profiles thus approximately coincide with that of Newtonian flow. Above that point in the yield region, the profiles follow the envelope curve up to a certain point $y_C^+ \le y_H^+$ that depends on flow rate. From that point on, the velocity profiles again become approximately logarithmic with varying slope such that at low flow rates, the slope is zero and approaches the Newtonian profile value ($1/\kappa$ in the logarithmic y^+-scale) as the flow rate increases. The measured profiles can be approximated by a piecewise logarithmic profile of the form.

$$u^+ = \frac{1}{\kappa}\ln\left(y^+\right) + B + \Delta u^+, \tag{51}$$

where

$$\Delta u^+ = \begin{cases} 0 & ; \quad 0 < y^+ \le y_L^+ \\ \dfrac{\alpha}{\kappa}\ln\left(y^+ / y_L^+\right) & ; y_L^+ < y^+ \le y_C^+ \ (\le y_H^+) \\ \Delta u_C^+ - \dfrac{\beta}{\kappa}\ln\left(y^+ / y_C^+\right) & ; y_C^+ < y^+ \le R^+. \end{cases} \tag{52}$$

Here, α and β give the slope (relative to Newtonian profile value) of the envelope curve in the yield region and the core region, respectively, and $\Delta u_C^+ = \dfrac{\alpha}{\kappa}\ln\left(y_C^+ / y_L^+\right)$. Figure 52 illustrates the simplified profile and the meaning of various parameters. Notice, that the quantities y_L^+, y_H^+ and α are constants for a given suspension. Instead, β and y_C^+ depend on flow rate (on τ_W) in a manner that remains to be found.

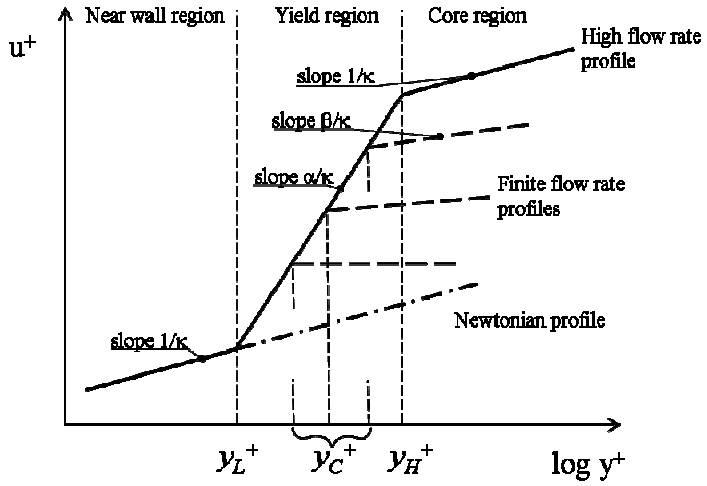

Figure 52. The piecewise logarithmic approximation of measured velocity profiles shown in Fig. 51. The parameters are as in Eqs. (51) and (52).

Within the present parametrization for each velocity profile at a finite flow rate, y_C^+ denotes the point where the profile departs from the high flow rate envelope curve, and the upper limit of the yield region. (At very low flow rates, that point may appear already at the near wall region in which case the yield region does not exist.) Obviously, the flow is turbulent and the fibre phase is fluidized in the near wall and yield regions. The existence of the yield region is most likely related to quenching of wall induced turbulence due to presence of fibres. As a consequence, the rate of turbulent transfer of longitudinal momentum from the core region towards the wall (and thus, the effective eddy viscosity of the suspension) is reduced. The existence of the yield region is thus identified as the primary phenomenon underlying the drag reduction found in the mixed and turbulent flow regions. Indeed, according to the present results, set up of the drag reduction regime takes place at the flow rate regime where the yield region in the velocity profile first appears.

At relatively low flow rates, the velocity profile in the core region is flat indicating existence of a central fibre plug and y_C^+ denotes the position of the plug surface. According to the conventional reasoning, plug rupture takes place at the position where the total stress equals the disruptive shear stress τ_D which, in turn, is a material property of the fibre network. This suggests a correlation for y_C^+ in the form

$$y_C^+ = R^+(1-\tau_D/\tau_W)\,. \tag{53}$$

It appears, however, that this correlation is *not* in accordance with the observed profiles and pressure loss behaviour (see below). As discussed above, the concept of disruptive shear stress as the criterion of plug rupture is somewhat questionable in the case where no actual rupture of once formed fibre network takes place. We assume here, instead, that the existence of fluidized annulus and fibre plug is controlled by a critical turbulent intensity that can prevail in the suspension. Lacking the possibility to measure the absolute values of turbulent intensity we further assume that the turbulent intensity is correlated with the mean flow velocity gradient, instead of total shear stress level. In other words, we assume that the upper limit of the yield region is set by the requirement that the mean velocity gradient is a (material) constant at that location, *i.e.* that

$$\frac{du}{dy}_{|y=y_C} = \Gamma_C = \text{constant.} \tag{54}$$

Converting this equation in dimensionless form, solving for y_C^+ in the yield region and taking into account the limitation $y_C^+ \le y_H^+$ set by the present quite rough parametrization of the profile, leads to the correlation

$$y_C^+ = \min\left(y_H^+, \left(u^* / u_C^*\right)^2 \right), \tag{55}$$

where

$$u_C^* = \sqrt{\frac{\nu \kappa \Gamma_C}{1+\alpha}}\,. \tag{56}$$

Notice that according to Eq. (55), y_C^+ does not depend on tube radius, as it would according to Eq. (53). If necessary, this result can be generalised to other parts of the profile and to more refined profile parametrizations. Finally, examination of the profile data suggests correlating the core region slope parameter β with y_C^+ as

$$\beta = 1 - \left(y_C^+ / y_H^+ \right)^2 . \tag{57}$$

To summarize, the velocity profiles in mixed and fully turbulent flow regimes are parametrized by Eqs. (51) and (52) that include four free parameters: y_L^+, y_H^+, α and u_C^* (or alternatively, Γ_C). Figure 53 shows the measured and fitted profiles for 1% pine and 2% birch (which have approximately the same crowding number) at several flow rates in the mixed and turbulent regions. The fitted parameter values are given in Table 4. Notice however, that for birch suspension, the yield layer seems to be located too close to the wall to be reliably measured by PUDV method for all but the highest flow rates (*i.e.* within the range ~1 mm from the wall). This feature gives rise to some additional uncertainty in the fitted values of profile parameters for 2% birch suspension.

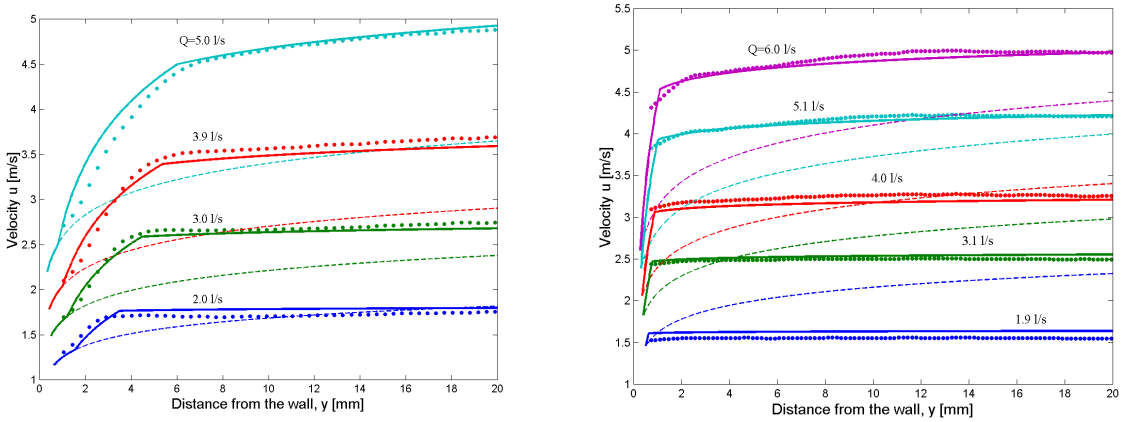

(a) (b)

Figure 53. Measured velocity values (solid symbols) and fitted profiles (solid lines) at different flow rates in mixed and turbulent flow regimes for 1% pine (a) and 2% birch (b). Also shown are the logarithmic Newtonian profiles (dashed lines) corresponding to same values of wall stress (pressure loss) as the measured profiles.

Table 4. Fitted values of turbulent profile parameters for 1% pine and 2% birch fibre suspension. See Eqs. (51) and (52).

Parameter	**Pine 1%**	**Birch 2%**
y_L^+	120	50
y_H^+	880	320
α	1.8	2.4
u_C^* [m/s]	0.0047	0.0125

Given the new profile information obtained by the PUDV method, we can now discuss in more detail the dynamics of the transition from the incipient turbulent regime via mixed flow regime to the fully turbulent regime (regimes III, IV and V in Fig. 48). The incipient turbulence region most likely arises due to growth of the lubrication layer thickness until turbulent fluctuations of the fluid phase can exist between the wall and the fibre plug. The edge of the fibre plug is not sharp, however. Instead, a surface layer exists where the average fibre concentration increases from zero to some constant value within a distance scale set by a structural correlation length of the fibre network (that can be expected to be of the order of fibre length, but may depend on concentration). Due to low fibre concentration near the surface, the fluid phase turbulence is not effectively damped until well inside the plug. Consequently, the flow behaviour is dominated by fluid phase turbulence in a region that starts from the outer edge of the viscous sublayer well inside the fibre free lubrication layer, and extends inside the fibre core a distance of the order of correlation length. This explains the observed behaviour that the velocity profile of fibres approach that of turbulent Newtonian fluid near the wall. Remember that the PUDV techniques could not be applied close enough to the wall such that the linear viscous sublayer could be resolved.

As the flow rate is increased, turbulence production at the wall increases and fluctuations can prevail deeper in the fibre phase core preventing fibres from forming continuous network within some annular region. Well inside the core, fibre concentration is high leading to effective attenuation of turbulent fluctuations. The attenuation is most effective in the size scale of correlation length. On the other hand, the size scale of the largest eddies, that contain most of the turbulent energy and that are most effective in momentum transfer (*i.e.* in generating turbulent friction) is set by the distance from the wall. An immediate consequence of the arguments given above is that at a distance of the order of correlation length from the wall, the largest eddies possible

at that distance, are effectively attenuated by the fibres. Consequently, the turbulent friction is attenuated leading to the yield layer characterized by increasing velocity gradient and the S -shaped profile shown in Fig. 51. (Obviously, this conclusion is based on an assumption that the friction is dominated by turbulence.) The existence of the yield layer, located between y_L^+ and y_C^+ in the schematic illustration of the profile parametrization shown in Fig. 52, is the origin of the drag reduction phenomenon – although within the present reasoning that region could more accurately be described as the 'region of flow enhancement'.

As the flow rate is further increased, the turbulent production still increases and the turbulent annulus can diffuse deeper in the fibre core. Entering further away from the wall leaves space to larger eddies that are *not* anymore attenuated very effectively. As a consequence, the core region can finally remain turbulent due to eddies larger than correlation length. Furthermore, the large scale end of the turbulent spectrum near the tube centre can become similar to that of pure fluid. At very high flow rates the turbulent momentum transfer and consequently the mean velocity gradient approaches that of turbulent Newtonian flow. That would explain the limiting value of slope $1/\kappa$ in the logarithmic y^+-scale in the core region (see Figs. 51 and 52).

To summarize, the present data does not quite support the traditional conception on the transition from mixed to fully turbulent flow according to which the fibre plug core is gradually disrupted by turbulence (or shear stress) starting from its outer edge and continuously proceeding towards the centre until the plug is worn out altogether. According to the present results instead, two mechanisms are effective. First, increase of turbulent intensity near the wall does indeed lead to annulus of disrupted fibre phase and a central fibre plug, the radius of which slowly decreases with flow rate. Second, at high enough flow rates, large scale fluctuations can persist throughout the core and the 'degree of fluidization' gradually increases with flow rate in the entire central core. At very high flow rates the large scale turbulent structure of the core region is similar to that of pure fluid (at the same wall shear stress) indicating 'fully fluidized' state of flow. Notice, however, that the present results are based on measurements in a relatively small diameter tubes. In larger tubes, additional phenomena related to the turbulent diffusion and scales may become important.

3.4.6 Pressure loss correlations

We now turn to the study of loss in turbulent flow, *i.e.* in various flow regimes. The aim is to utilize the modelled velocity profile in the plug flow regime and a simplified parametrization of the measured profile in turbulent regimes, and thereby derive a correlation formula for the pressure loss. The flow rate corresponding to a given friction

velocity/wall stress (that yields the pressure loss) is found simply by integrating the velocity profile over the tube cross section. Notice, that this procedure is analogous with that used already by Prandtl for finding his famous friction factor correlation for Newtonian fluids based on logarithmic velocity profile in smooth pipes [4].

For plug flow regions, integration of the average bulk velocity $\phi v_f + (1-\phi)v_s$ over the cross-section of the pipe using Eqs. (40) and (41) yields

$$Q = 2\pi R \frac{\phi k}{\mu}\left[\tau_s - (1-\phi)\tau_w\right] + \pi R^2 v_s + \frac{\pi R}{\mu}\tau_w h^2 . \tag{58}$$

In dimensionless variables, the corresponding formula reads

$$Q^+ = 2\pi R^+ \phi k^+ \left[\tau_s^+ - (1-\phi)\right] + \pi {R^+}^2 v_s^+ + \pi R^+ {h^+}^2 , \tag{59}$$

where $\tau_s^+ = \tau_s / \tau_w$. Further investigation of Eqs. (58) and (59) reveals that the dominant term on the right hand side is the second one for all values of wall shear within the plug flow regimes, except of those very close to τ_{w0} where the fibre plug starts to move. As a good approximation valid for most practical cases in the plug flow regimes, we can thus write

$$\begin{aligned} Q &\cong \pi R^2 v_s \\ Q^+ &\cong \pi {R^+}^2 v_s^+ \end{aligned} . \tag{60}$$

For mixed and turbulent regions, integration of the velocity profile given by Eqs. (51) and (52) yields

$$Q^+ = Q_0^+ + \Delta Q_1^+ + \Delta Q_2^+ , \tag{61}$$

where

$$\begin{aligned} Q_0^+ &= \pi {R^+}^2 \frac{1}{\kappa}\left[\ln R^+ + B\kappa - \frac{3}{2}\right] \\ \Delta Q_1^+ &= \pi {R^+}^2 \frac{\alpha}{\kappa}\left[\ln\left(\frac{y_C^+}{y_L^+}\right) + \frac{1}{2}\left(\left(\frac{y_C^+}{R^+}\right)^2 - \left(\frac{y_L^+}{R^+}\right)^2\right) - 2\left(\left(\frac{y_C^+}{R^+}\right) - \left(\frac{y_L^+}{R^+}\right)\right)\right] \\ \Delta Q_2^+ &= \pi {R^+}^2 \frac{\beta}{\kappa}\left[\ln\left(\frac{y_C^+}{R^+}\right) + \frac{1}{2}\left(\left(\frac{y_C^+}{R^+}\right) - 3\right)\left(\left(\frac{y_C^+}{R^+}\right) - 1\right)\right]. \end{aligned} \tag{62}$$

Here, the first term Q_0^+ is the contribution of the standard Newtonian profile, the second term ΔQ_1^+ gives the additional flow contribution due to yield region and the constant velocity contribution in the core region. The third term ΔQ_2^+ includes the effect of the non-zero slope in the core region (that becomes significant at high flow rates, see Fig. 52). Finally the flow rate Q in physical dimensions is given in terms of the dimensionless flow rate as

$$Q = \frac{\nu^2}{u_*^*} Q^+ . \tag{63}$$

This equation gives the required correlation between the flow rate and pressure loss. Figure 54 shows the measured pressure loss for 1% pine and 2% birch suspensions together with the correlations given by Eq. (60) and by Eqs. (61)–(62) for plug flow and turbulent regimes, respectively.

The fitted values of the combinations of model parameters that appear in the approximate flow rate equation, Eq. (60) for plug flow regime are given in Table 5. For the turbulent regime, the pressure loss is calculated using the parameter values given in Table 4 as obtained from a fit to profile data. Notice that while knowing the profile parameters y_L^+, y_H^+, α and u_C^* immediately yields an accurate pressure loss correlation, the inverse is not true: knowledge of pressure loss behaviour alone does not yield unique values of profile parameters. Consequently, a direct fit of Eqs. (61)–(62) in the turbulent regime would lead to even closer agreement with the pressure loss data as the one shown in Fig. 54, but with parameter values that do not reproduce good approximation to the measured profiles through Eqs. (51) and (52).

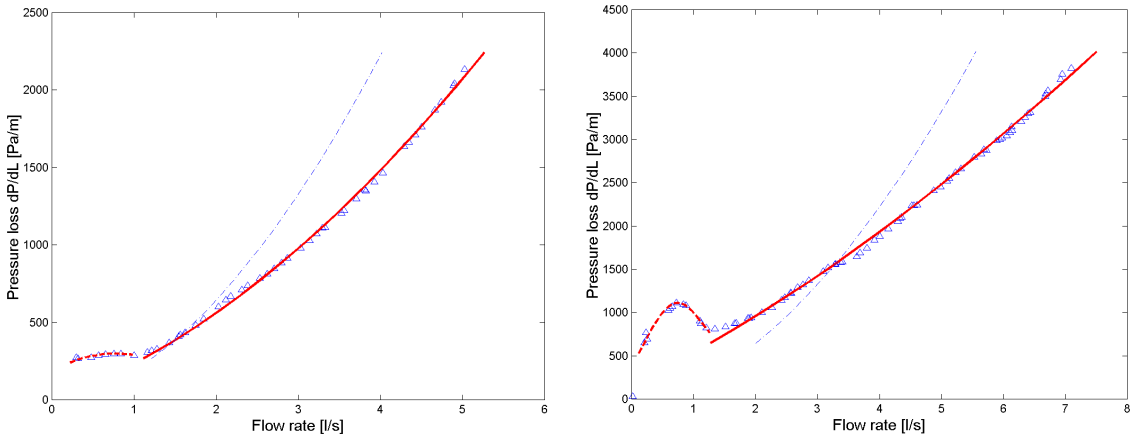

(a) (b)

Figure 54. Measured (symbols) and calculated pressure loss for plug flow (dashed line) and turbulent regime (solid line) as a function of flow rate for 1% pine (a) and 2% birch (b). Also shown is the Newtonian correlation for smooth pipe turbulent flow (dash-dotted line).

Table 5. Values of the relevant combinations of plug flow model parameters fitted for 1% pine and 2% birch fibre suspension loss data. The fit is made using Eq. (60).

Parameter	Pine 1%	Birch 2%
k [10^{-9}m^2]	36	2.0
$C_s C_L$	0.098	0.00024
$C_s P_{s0}$ [N/m^2]	1.7	3.6
Γ / C_s [10^{-6} m^3/N]	68	3.8
β	1.5	3.5

As shown by Fig. 54, the agreement between measured and calculated pressure loss behaviour is very good in the present cases. At the relatively low consistencies considered here, the mixed and turbulent flow regimes are obviously the most important regimes from practical point of view. At those domains, the pressure loss correlation discussed above is based on a somewhat arbitrary and suggestive parametrization of the flow profile, the generality of which can not be assured given the rather small amount of data yet available. However, even more important than the explicit functional form of the pressure loss correlation given by Eqs. (61)–(63), these formulas suggest a certain scaling law of the correlation, namely that

$$Q^+ = Q^+(R^+, u^*/u_C^*), \tag{64}$$

i.e. that the dimensionless flow rate of suspension depends only on two quantities, the dimensionless tube radius R^+ and the ratio u^*/u_C^*, where u_C^* is a material parameter related to the critical turbulent intensity that is sufficient to keep the fibre phase fluidized. Furthermore, it appears that the primary variable here is R^+. Instead, the dependence on u^*/u_C^* is relatively weak and limited to low flow rate end of the mixed flow region. As a good approximation we can then drop the dependence on u^*/u_C^* in Eq. (64). In particular, using Eqs. (61) and (62) in the high shear stress limit, and using the approximation valid for large tubes that $y_L^+, y_H^+ << R^+$ we get.

$$Q^+ \cong Q_0^+ + \Delta Q_\infty^+, \tag{65}$$

where Q_0^+ is given by Eq. (62) and

$$\Delta Q_\infty^+ = \lambda_1 R^+ + \lambda_2 {R^+}^2. \tag{66}$$

Instead of four material parameters for the velocity profiles, we are now left with only two material parameters λ_1 and λ_2 that are related to the original profile parameters as

$$\lambda_1 = 2\pi\frac{\alpha}{\kappa}(y_H^+ - y_L^+)$$
$$\lambda_2 = \pi\frac{\alpha}{\kappa}\ln(y_H^+ / y_L^+). \tag{67}$$

In order to test the scaling law (15), we show in Fig. 55 the pressure loss data measured at VTT flow laboratory for 1% commercial fine, LWC and SC pulps in three different standard steel tube sizes DN100, DN200 and DN300. The measurement was done only in mixed and turbulent regimes where the three pulps show very similar loss behaviour. No profile information is available. Also shown in Fig. 55 are the results obtained by fitting Eqs. (65) and (66) using only the data for the smallest tube size, DN100. The curves for the two larger tubes then ensue purely from the proposed scaling law. The fitted values of the two parameters are λ_1 = 96 600 and λ_2 = 7.33. As discussed above, knowledge of pressure loss behaviour alone does not yield unique values of profile parameters. We have, however verified that plausible values of profile parameters can be chosen such that the loss behaviour shown in Fig. 55 is reproduced also by Eqs (61) and (62).

3.4.7 Conclusions

To conclude, we have used pulsed ultrasound Doppler velocimetry and laser-optical wall layer measurements in an in-depth study of fibre suspension flows in a straight tube downstream of a sudden step expansion. The experimental data result in a refined insight of the developing flow and of various flow regimes in the fully developed flow. Especially, the phenomena related to formation of lubrication layer and to transition from laminar plug flow to mixed and fully turbulent flows are discussed. A two-phase laminar flow model including realistic lubrication layer dynamics is developed for the fully developed plug flow regime. In the turbulent regime the flow is described using a simple velocity parametrization based on direct measurement of the mean velocity profile. These results lead to an empirically motivated new pressure loss correlation that is formally reminiscent of the corresponding scaling law for pure Newtonian flows in turbulent flow. The proposed correlation was successfully applied here to a very limited amount of data. Final verification of and extension of the results to include effects of *e.g.* pulp type and concentration require further measurements that were not possible within the present project.

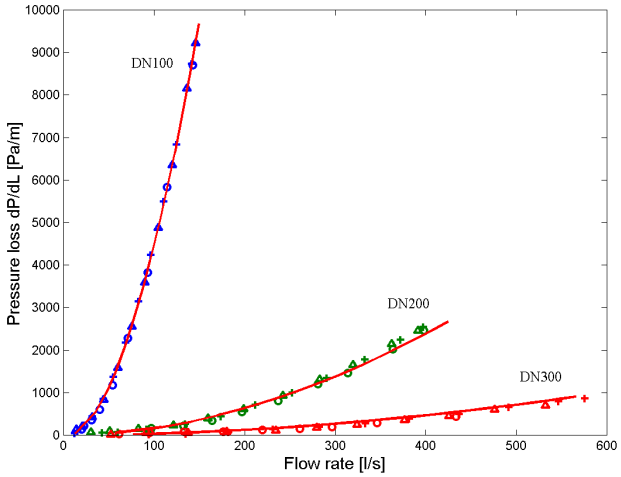

Figure 55. Measured pressure loss as a function of flow rate for 1% commercial fine paper (Δ), LWC (O) and SC (+) pulps (VTT, 1996). The measurement was done for three different standard steel tubes, DN100 (Ø = 110.3 mm), DN200 (Ø = 215.1 mm) and DN300 (Ø = 300 mm). Solid lines show the fitted behaviour according to Eqs. (65) and (66). The fit was done using the data for DN100 tube only.

References

[1] Duffy, G.G. The unique behaviour of wood pulp fibre suspensions. *9th International Conference on Transport and Sedimentation of Solid Particles,* 2–5 September, Cracow, Poland, 1997.

[2] Lee, P.F.W. and Duffy, G.G. An Analysis of the Drag Reducing Regime of Pulp Suspension Flow. *Tappi* **59** (1976), pp. 119–122.

[3] Duffy, G.G. and Titchener, A.L. The disruptive shear stress of pulp networks. *Svensk Papperstid.* **78** (1975), pp. 474–479.

[4] White, F.M. *Fluid Mechanics*. 5th ed. McGraw–Hill, NY, 2003.

[5] Xu, H. and Aidun, C.K. Characteristics of fiber suspension flow in a rectangular channel. *Int. J. Multiphase Flow* **31**, (2005), pp. 318–336.

3.5 Application of ultrasound anemometry for measuring filtration of fibre suspensions: effect of fibre and pulp properties

Sanna Haavisto

VTT, P.O. Box 1603, FI-40101 JYVÄSKYLÄ, Finland

We present here results for filtration experiments with refined and fractionated chemical pulp suspensions. The properties of consolidating fibre network are described in terms of permeability and structural pressure. The main objective of this work was to clarify the effect of fibre and pulp properties on the dynamics of the filtration and on the rheological properties of filtrating fibre network. The relevance of coarseness, average fibre length, fibre length distribution and Canadian Standard Freeness on permeability constant and structural pressure was evaluated. The filtration properties could be correlated with fines fraction and coarseness of fibres.

3.5.1 Filtration device

The filtration device consists of a gravity driven hand-sheet mould equipped with a pulsed ultrasound Doppler anemometer (PUD) for measuring the local time-dependent velocity field of the fibre phase during filtration (see Fig. 56). Simultaneously, the position of the free surface (total flux of the suspension) of the suspension and the fluid pressure at the wire are measured using separate transducers. Based on acquired experimental information, other relevant flow quantities can be computed utilizing the two-phase flow equations appropriate for the system. Detailed description of this device and experimental setup is explained elsewhere [1, 2].

3.5.2 Data analysis

The filtration is driven by gravitational forces. Therefore the process can be described as a 1-D process in the vertical direction (z-direction). A vertical time dependent filtration flow of a suspension containing a continuous fluid phase and a particulate solid phase is governed by the following continuity and momentum equations

$$\frac{\partial}{\partial t}\phi_f + \frac{\partial}{\partial z}\left(\phi_f \tilde{u}_f\right) = 0 \tag{68}$$

$$\frac{\partial}{\partial t}\phi_s + \frac{\partial}{\partial z}\left(\phi_s \tilde{u}_s\right) = 0 \tag{69}$$

$$\phi_f \frac{\partial}{\partial z}\tilde{p}_f = D - \phi_f \tilde{\rho}_f g \tag{70}$$

$$\phi_f \frac{\partial}{\partial z} p_s = -D - \phi_f \phi_s \left(\tilde{\rho}_s - \tilde{\rho}_f\right) g \tag{71}$$

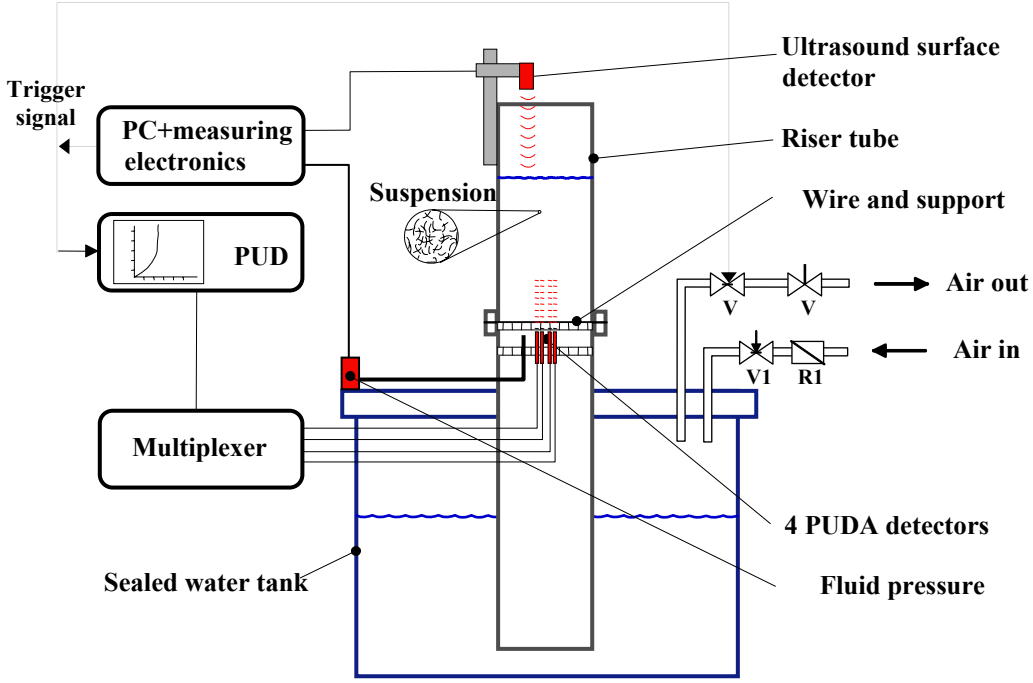

Figure 56. Schematic illustration of the filtration device and measurement setup.

In the equations subscripts *f* and *s* refer to the fluid and solid phase respectively, ϕ_i is the volume fraction, $\tilde{u}_i$ is the flow velocity in z-direction, p_i is the pressure, $\tilde{\rho}_i$ is the density for phase $i = f, s$, D is the momentum transfer term between phases and g is the acceleration due to gravity. The notation $\tilde{x}_i$ denotes an intrinsic average of corresponding quantity, *i.e.* an average taken over the volume occupied by phase in a general averaging volume (such that $\phi_i = \Delta V_i / \Delta V$). Equations (68)–(71) can be derived from the more general flow equations of two phase flow with no mass transfer between phases ignoring inertial, viscous and turbulent terms [1].

The data analysis of the filtration experiments is based on Eqs (68)–(71) with an assumption that the solid velocity field $\tilde{u}_s = \tilde{u}_s(t, z)$ is given by the experiment in the entire flow region above the wire. Conditions for accomplishing the data analysis are the momentum transfer term D and the volume fractions ϕ_i which must be known. It is assumed that the interaction between the phases is given by a Darcy-type drag force density of the form

$$D = -\frac{\mu}{k}\left(\widetilde{u}_f - \widetilde{u}_s\right), \tag{72}$$

where μ is the dynamic viscosity of the fluid phase and k is the permeability coefficient of the fibre network that depends on the volume fractions.

Several permeability functions, applicable for porous materials with qualitatively different structure, can be found in the literature [3]. Here, we shall consider permeability equations by Kuwabara and Kozeny–Carman. The Kuwabara equation of the form

$$\frac{k}{a^2} = \frac{1}{8\phi_s\left(1-\phi_s\right)^2}\left(-\ln\phi_s - \frac{3}{2} + 2\phi_s\right) \tag{73}$$

is especially derived for fibrous structures. The free parameter of Kuwabara equation is the fibre radius a.

Kozeny–Carman equation can be derived analytically for simplified capillary models of porous materials and is of the form

$$\frac{k}{k_0} = \frac{\left(1-\phi_s\right)}{\phi_s^2}. \tag{74}$$

Here, k_0 is the specific permeability constant which includes the specific pore surface area. Kozeny–Carman equation is the most widely used of the expressions relating the permeability in Darcy's law to the properties of the porous material.

The volume fraction of the fibre phase may be related to the mass consistency of dry fibres when density of dry fibres and ratio of bound water mass are known. The density of dry fibres is taken to be $\widetilde{\rho}_c = 1500\,kg/m^3$. The density of wet fibres is calculated to be $\widetilde{\rho}_s \approx 1200\,kg/m^3$ based on the assumption that the ratio of bound water mass to the dry fibre mass is $MR_b = 1.0$.

With these assumptions, we can solve the volume fractions of both phases in the entire flow region. Velocity of fluid phase can be solved using the independent total flux (surface position) measurement. Integrating momentum equations with respect to spatial coordinate z downwards from the measured location of the free surface we find the fluid pressure $\widetilde{p}_f\left(t,z\right)$ and solid pressure $\widetilde{p}_s\left(t,z\right)$ fields and, as a sum of these two, the total pressure $p_T\left(t,z\right)$.

Data analysis is accomplished by fitting the free parameter *a* of Kuwabara permeability equation (k_0 in Kozeny–Carman equation) so that sufficient agreement is achieved among the measured and calculated fluid pressures (see Fig. 57). The fitted value of the permeability constant then serves as one of the key properties in characterising the filtration dynamics of different suspensions.

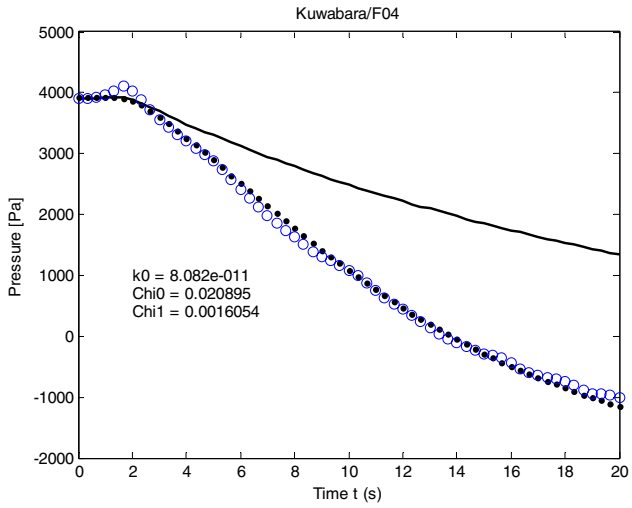

Figure 57. An example of measured and calculated pressures at z = 0. Black solid line is the calculated total pressure. Blue circles show the calculated fluid pressure. Solid symbols are the corresponding measured values of fluid pressure.

3.5.3 Results: Refined softwood

Filtration experiments were performed with pine kraft pulp which was beaten to two different levels. The initial mass consistency of pulp suspensions used in the experiments was 0.2% which corresponds to an amount 16 grams of dry pulp. In each case, the value of free parameter (*a* or k_0) was found by fitting the calculated function $p_f(t, z=0)$ to the measured pressure data. Fitted values and the fit residuals are given in Table 6. A small value of the residual indicates good agreement between measured and calculated pressure values.

Table 6. The fitted values and fit residuals of the free parameters acquired with Kuwabara and Kozeny–Carman models for pine pulp at different refining levels.

Pulp	Refining energy (kWh/t)	KOZENY k_0 (m^2)	Chi^2	KUWABARA 2*a* (µm)	Chi^2
PINE	0	6,33E-13	1,36E-03	13,8	3,10E-03
PINE90	90	1,44E-13	1,57E-02	6,4	8,49E-02
PINE180	180	3,94E-14	8,01E-02	3,4	5,26E-01

The fibre properties of pulp samples were analysed with L&W FiberMaster. Length-weighted average fibre length and coarseness of different fibre samples are shown together with Canadian Standard Freeness values in Table 7. Fig. 58 presents the length-weighted length proportion of different fractions for each sample.

Table 7. CSF and fibre properties of refined pulps measured with L&W FiberMaster image analyser.

Pulp	Av. Fibre length (mm)	Coarseness (mg/m)	CSF (ml)
PINE	2,07	0,201	650
PINE90	1,94	0,187	430
PINE180	1,78	0,179	180

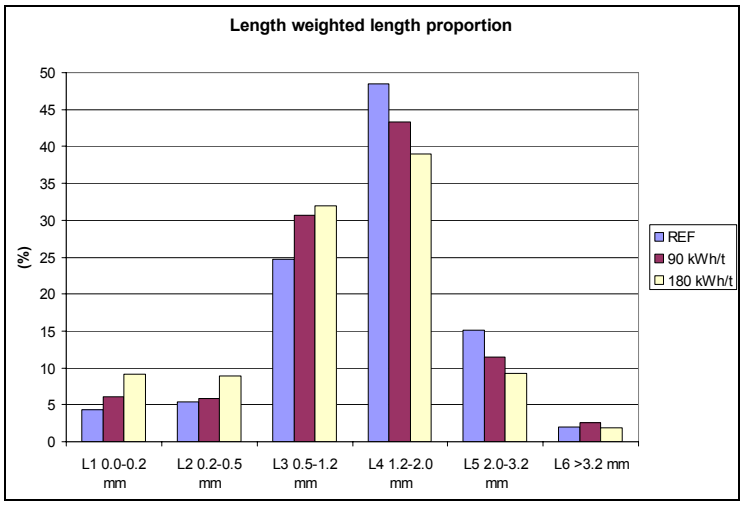

Figure 58. Length distribution for refined pulps. The shortest L1-fraction can be considered as fines fraction.

Increased beating results in decreasing coarseness, CSF, and average fibre length. Beating develops the specific surface area of fibres because of hydration and internal and external fibrillation. This is consistent with the observed reduction in effective fibre diameter as calculated with Kuwabara model.

Beating is also expected to generate fines due to removal of primary wall material from fibres and by fibre cutting. Change in fines content is indicated by the increasing L1-fraction (0.0–0.2 mm) in Figure 58. The production of fines affects the development of fibre network resistance. Fine material seems to decrease the void volume of the network by blocking the available pore area for water flow. This is reflected by the decrease in specific permeability (in Kozeny–Carman relation) which is proportional to the specific pore surface area in the fibre network.

Figure 59 shows the fitted permeability constants as a function of fibre coarseness and Canadian Standard Freeness. According to the results, both Kuwabara and Kozeny–Carman permeability models give a moderate correlation between coarseness and permeability constant.

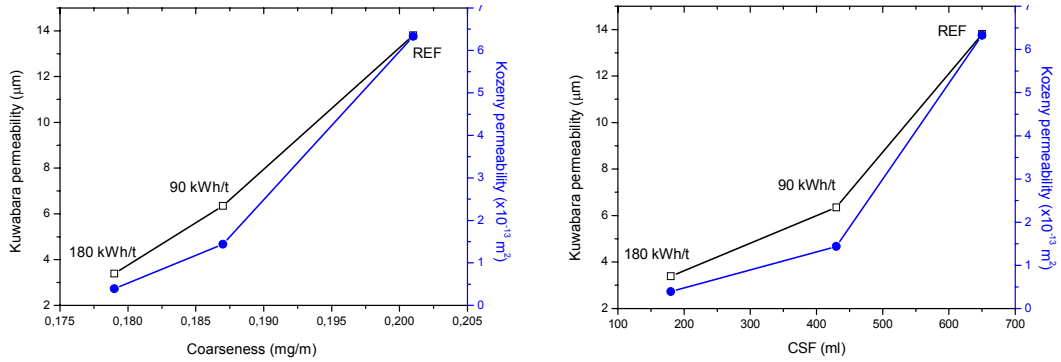

(a) (b)

Figure 59. Fitted permeability constants as a function of a) coarseness and b) CSF. Solid symbols represent the values calculated with model by Kozeny–Carman.

In filtrating suspensions, fibre network stress arises due to resistance of the network to fluid flow. Figure 60 presents the measured dimensionless solid pressure (vertical normal stress) as a function of consistency for unbeaten and beaten pine fibres. The values of solid pressure and consistency are given for a set of fibre layers along their pathlines. Each curve in Fig. 60 thus represents the stress behaviour of a single fibre layer during filtration. As indicated by Fig. 60, fibre network formed by beaten fibres can be perceived softer than that formed by unbeaten pine fibres.

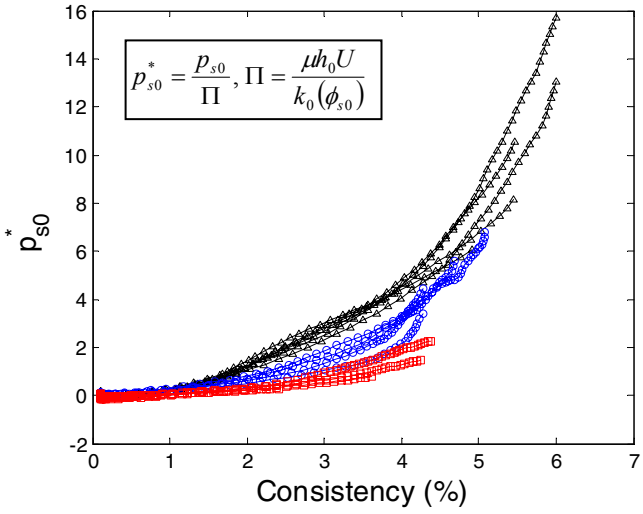

Figure 60. Dimensionless solid pressure as a function of consistency along pathlines for pine fibres. Triangular symbols correspond to the unbeaten fibres. Circles correspond to the beating level of 90 kWh/t and squares to the beating level of 180 kWh/t. The pressure scale is given by Π = 50 Pa.

3.5.4 Results: Fractionated softwood

These filtration experiments were carried out for pine kraft pulp, fractionated with pressure screen to three different fractions. Initial conditions were similar to those in the experiments for beaten pulps (see above). Fitted values and the fit residuals for permeability constants are given in the Table 8.

Table 8. Fitted values of the free parameters and fit residual for Kozeny–Carman and Kuwabara permeability functions for unfractionated and fractionated softwood fibres (LF = long fraction, MF = midde fraction and SF = short fraction). Also shown are the fibre properties measured by FiberLab analyzer.

Pulp	KOZENY k_0 (m^2)	KOZENY Chi^2	KUWABARA 2a (µm)	KUWABARA Chi^2	Av. fibre length (mm)	Coarseness (mg/m)	Width (µm)	CSF (ml)
PINE	6,21E-13	2,32E-03	12,6	4,92E-03	2,03	0,197	20,9	715
PINE LF	9,22E-13	1,55E-03	15,9	8,93E-02	2,65	0,240	30,0	737
PINE MF	3,63E-13	2,20E-02	9,6	1,00E-02	2,09	0,160	22,0	679
PINE SF	2,76E-13	1,64E-02	4,8	8,93E-02	1,65	0,145	18,1	563

In pressure screen fractionation fibres are primarily separated on the basis of fibre length and secondarily on the basis of fibre flexibility [4]. Effects of fibre fractionation were characterized in terms of general changes in the fibre properties and fibre length distribution of the pulp using Kajaani FiberLab analyser. Average fibre length, width and coarseness of different fibre samples together with values of Canadian Standard Freeness are also shown in Table 8. Figure 61 shows the length distribution of the fractionated pulps. Results show that coarseness and length of the fibres is altered considerably in pressure screening. The change in freeness reflects the change in fibre length and alteration in the proportion of fines.

Despite the similarity in average fibre length and length distribution, the filtration properties of the reference pulp and the middle fraction are different. Therefore average fibre length does not explain the observable decrease in permeability constant. Figure 62 shows fitted permeability constants as a function of coarseness and freeness. Increasing coarseness and freeness leads to larger value for permeability constant. Increase in coarseness and fibre width reflects decrease in fibre flexibility. Therefore results indicate that network formed by long and coarse fibres is more open and has lower filtration resistance. The specific permeability predicted by Kozeny–Carman model gives a very good correlation with fibre coarseness.

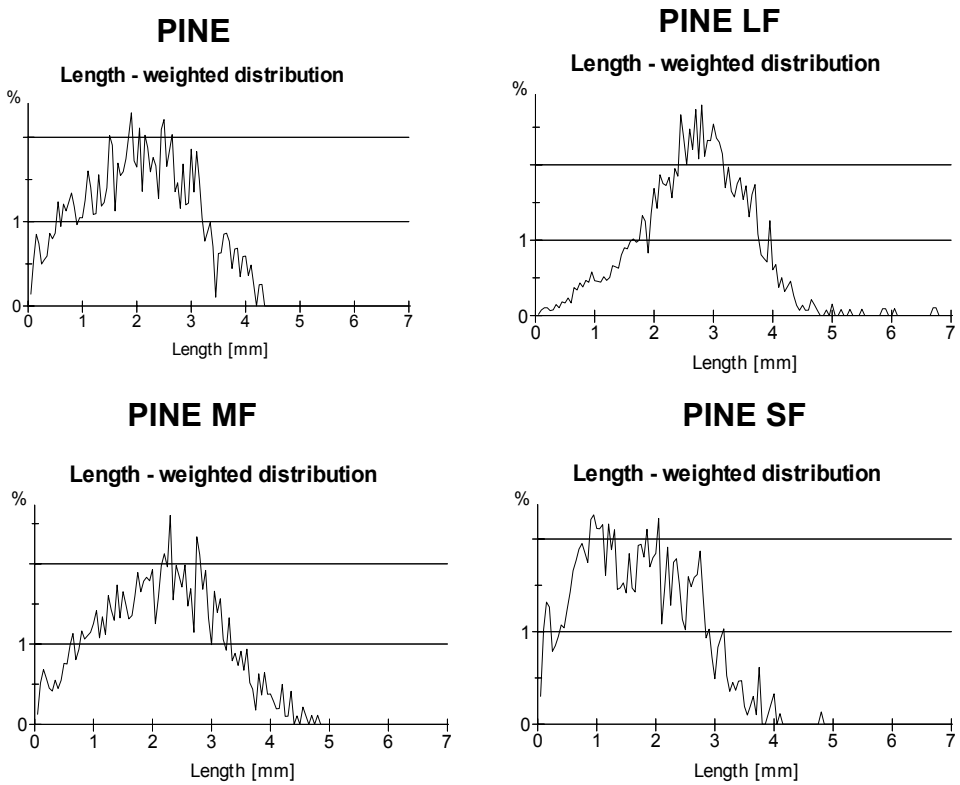

Figure 61. Length distribution of original pine pulp and of different fractions.

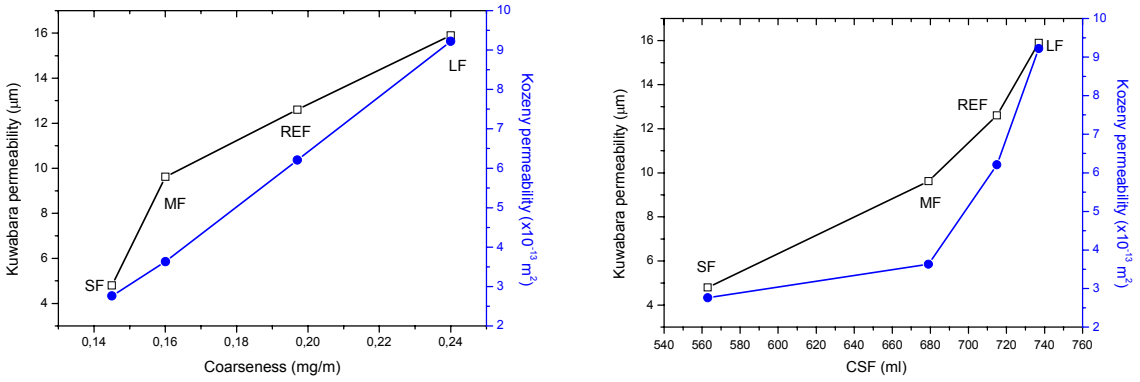

(a) (b)

Figure 62. Fitted permeability constants as a function of a) coarseness and b) CSF. Open and solid symbols represent the values calculated with models by Kuwabara and Kozeny–Carman, respectively

Figure 63 shows the solid pressure as a function of consistency for fractionated pine fibres similarly as for beaten fibres (see Fig. 60). The fibre network formed by coarser and longer fibres can carry higher structural pressure and thus form stiffer structure than the network formed by shorter fractions. Furthermore, clear difference between unfractioned pulp and middle fraction is observed in spite of the fact that the mean fibre

length is similar for these two suspensions. This result clearly demonstrates that not only the mean fibre length but also the length distribution is an important factor affecting stiffness of the consolidating network.

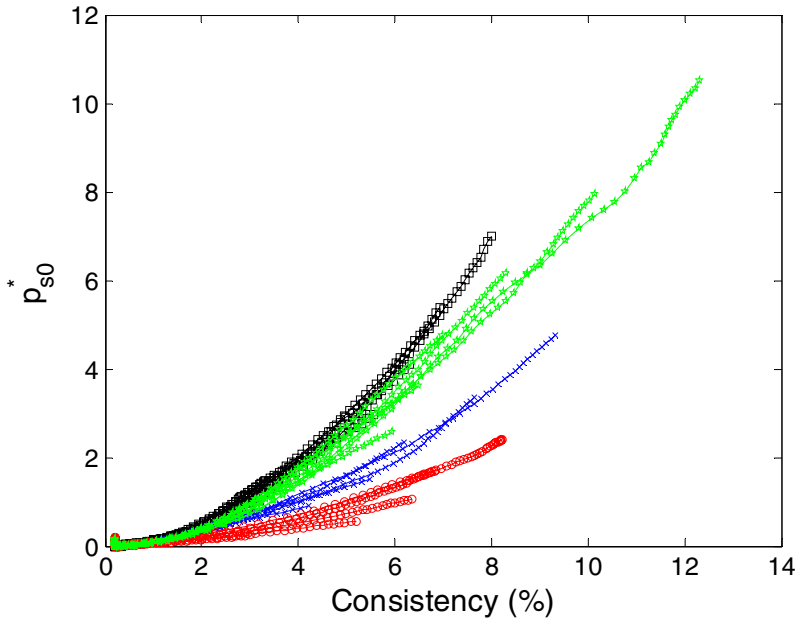

Figure 63. Dimensionless solid pressure as a function of consistency along pathlines for pine fibres. Star-shaped symbols correspond to the unfractioned pine fibres. Squares correspond to the long fraction, crosses to the middle fraction and circles to the short fraction. Absolute pressure scale is approximately 50 Pa.

3.5.5 Conclusions

The physical properties of consolidating fibre network in filtration process were studied together with common pulp and fibre properties. Two methods of pulp preparation, beating and fractionation, were used. Beaten fibres formed a more compact network due to fibre shortening and reduction of fibre stiffness. This was indicated by slower drainage (lower permeability) and decreasing structural pressure as a function of consistency. Dewatering efficiency of pulp was also decreased by the fibre fines which block up the network pores.

Changes in coarseness and fibre length introduced by fractionation were observed to correlate with the permeability constant. Instead, correlation with the average fibre length was not found. Fibre networks formed by fractions with longer and coarser fibres yielded larger structural pressure as a function of consistency. Information on the material properties of the consolidating fibre network acquired from this work can be utilised to extend knowledge on paper forming. We emphasize, that the quantities

related to flow resistance and network stiffness measured with the present method, based on ultrasound-Doppler techniques, are directly related to physical material properties of the forming fibre network. This is not the case with many standard parameters such as Canadian standard freeness, which is a an 'index' that is heavily affected by the particular geometry of the standard device on which the measurement is based. Therefore, the present parameters are directly useable *e.g.* in modelling of forming process in order to fix some of the model parameters by independent measurements, and thereby to improve model reliability.

References

[1] Kataja, M. and Hirsilä, P. Application of ultrasound anemometry for measuring filtration of fibre suspension. The Science of Papermaking. Transactions of the 12th Fundamental Research Symposium. Vol. 1. Baker, C.F. (ed.). Oxford, September 2001. The Pulp and Paper fundamental Research Society, UK, 2001. Pp. 591–604.

[2] Kataja, M. (ed.). Rheological materials in process industry. ReoMaT Project Report 2003. VTT Project Report, 15.3.2004.

[3] Jackson, G.W. and James, D.F. The permeability of fibrous porous media. *Can. J. Chem. Eng.* **64**, (1986), pp. 364–374.

[4] Karnis, A. Pulp fractionation by fiber characteristics. *Paperi & Puu*, Vol. 79, No. 7, (1997), pp. 480–488.

3.6 Lattice-Boltzmann simulations of particle suspension flows

Jari Hyväluoma*, Tomi Kemppinen*, Pasi Raiskinmäki**, Antti Koponen**,
Jussi Timonen* and Markku Kataja*

(*) Department of Physics, P.O. Box 35 (YFL), FI-40014 Universtiy of Jyväskylä, Finland

(**) VTT, P.O. Box 1603, FI-40101 JYVÄSKYLÄ, Finland

We have used the lattice-Boltzmann (LB) simulation code developed earlier [1] to study rheological properties and flow behaviour of liquid-particle suspensions. The code is three dimensional and fully parallellized. It can include particles of different sizes and interactions between the suspended particles (these features are not utilized in this study, however). The advantage of the present method of *direct* numerical simulation is that we can study in detail both the basic particle-scale phenomena and their macroscopic consequences *i.e.* the measurable mean properties of the flow. In particular, we can study the different microscopic phenomena that contribute to the apparent rheological properties of the suspension, namely the momentum transfer due to viscous stress of the carrier fluid, due to elastic stress in particles caused by interactions with fluid and by particle-particle collisions, and due to fluctuating motion of both phases. Similarly, we can study important macroscopic flow phenomena such as mean flow profile, slip at the tube wall and formation of concentration gradients due to migration of particles. The results are particularly useful in analysing the experimental results obtained by rheological measurements of particulate suspensions and thereby in gaining better understanding of the actual material properties of the suspension. This information is essential in *e.g.* developing numerical models for processes involving flow of such suspensions.

Here, we demonstrate the use of the LB method starting from a study of very basic particle scale phenomena that contribute to the observed shear thickening of non-colloidal particulate suspensions in simple shear flow, namely the effect of a single suspended particle and the effect of a single chain-like cluster of suspended particles. By a cluster we mean here a compact group of particles, formed as a result of hydrodynamic forces that bring suspended particles to close contact with each other. Short-range lubrication forces between these particles are then responsible for binding together such otherwise temporary aggregates. We then calculate the dependence on particle concentration of the apparent viscosity of the suspension. Since this dependence is well known from earlier theoretical and experimental studies, this results gives an excellent benchmarking test for the method used here. Another benchmarking case is provided by the study of strain hardening, for which we find good qualitative agreement with the data found in the literature. These results are reported in more detail in

references [2–3]. Finally, we apply the the method in analysing the flow in capillary viscometer and compare the numerical results with measured data, and thereby seek to use the method as an advanced data-analysis tools for the experiments.

3.6.1 Shear flow of particle suspensions

In order to better understand the origin of the shear-thickening behavior observed in particulate suspensions, we consider here two simplified cases. First, a single suspended particle is shown to increase the effective viscosity under shear flow of this simple suspension for particle Reynolds numbers above unity, due to inertial effects that change the flow configuration around the particle. Second, a chain-like cluster of suspended particles is shown to increase the momentum transfer in a shear flow between channel walls, and thereby the effective viscosity of the suspension in comparison with random configurations of particles. These elementary mechanisms are expected to carry over to large-scale particle-fluid suspensions that are considered in later sections.

All simulations presented here were performed in a plane Couette geometry for non-Brownian spherical particles. Suspensions were confined between parallel plates, and a shear flow was created by moving the plates in opposite directions with equal speeds. Periodic boundary conditions were imposed in the other two directions.

As the first example we consider the shear-thickening behavior of a simplest possible suspension consisting of only one particle in the middle of the system. (Notice, however, that there are periodic boundaries.) Due to its initial position, the particle does not move during the simulation, but it can rotate. The size of the system is 50 x 50 x 50 lattice units and the diameter of the particle is 22 lattice units. Simulations were done by using a fixed value for the viscosity and increasing the shear rate. The results are shown in Fig. 64 where a small but detectable shear thickening is seen even in this very simple system, when the particle shear Reynolds number exceeds unity. On the other hand, in simulations with inertial effects ignored (i.e. Stokes flow), this effect is absent. Stress analysis in the middle plane shows that the observed shear thickening mainly results from increased particle stress due to pressure forces.

Simultaneously with shear thickening, a change in the flow field around the particle is also found. For small shear rates fluid flows smoothly through the gaps between the particle and the walls. When the shear rate increases, streamlines begin to increasingly bend in front of (and behind) the particle, finally making a complete 'U-turn'. This behavior leads to a situation in which the fluid speed in the gaps is (relatively) decreased, and the angular velocity of the particle is also reduced (see Fig. 64). Similar

observations for a single suspended particle have been made in two dimensions by solving the Navier-Stokes equation with a finite element method [4]. Notice also that in two-dimensional LB simulations, a reduction in the angular velocity of particle clusters has been observed to be connected with the shear thickening of the suspension [5].

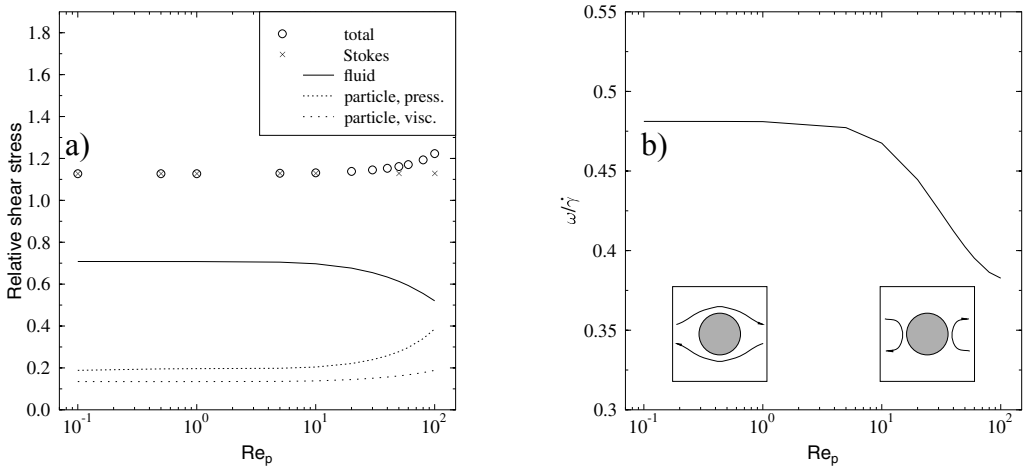

(a) (b)

Figure 64. a) The relative shear stress of the suspension as a function of particle Reynolds number $\mathrm{Re_p} = \dot{\gamma}\,\mathrm{d}^2/\nu$*, where* $\dot{\gamma}$ *is the shear rate, d is the particle diameter and* ν *is the kimematic viscosity of the fluid. Also shown are the results for the Stokes flow simulations and the different components of the stress in the middle horizontal plane of the system. b) The angular velocity of the suspended particle scaled with the shear rate as a function of particle Reynolds number. The insets in the right panel show schematically the change in the flow field as* $\mathrm{Re_p}$ *increases.*

An important phenomenon related to microstructural changes of particle aggregation is the formation of chain-like clusters of particles, which rotate while being advected in the shear flow [5]. We now demonstrate the effect on the total shear stress of an idealized rotating chain-like cluster. The artificial cluster considered consists of seven spherical particles as shown in Fig. 65. The size of the calculational grid is 160 x 111 x 50 (flow, gradient and vorticity directions, respectively). The diameter of the particles is 14 lattice units and the wall speed is 0.003 in lattice units. After the particles are placed in their initial positions their motions are determined by the hydrodynamic forces excerted on them by the flowing carrier fluid (see Ref. [2] for details). As the model suspension is sheared, the chain-like array of particles rotates, and the shear forces acting on the particles bring them closer together when the orientation of the array changes from horizontal to vertical (see Fig. 65). Thereafter interparticle distances begin to increase when the array continues to rotate further, and the cluster may eventually break up. During this process, the relative shear stress stays clearly above that for a random configuration of the same particles. This stress increase results from increased internal stresses of the particles and the high fluid stresses created between them (see

Figs 65 and 66). We expect that a qualitatively similar mechanism is behind strain hardening (see the next Section) and shear-thickening behavior of many real suspensions.

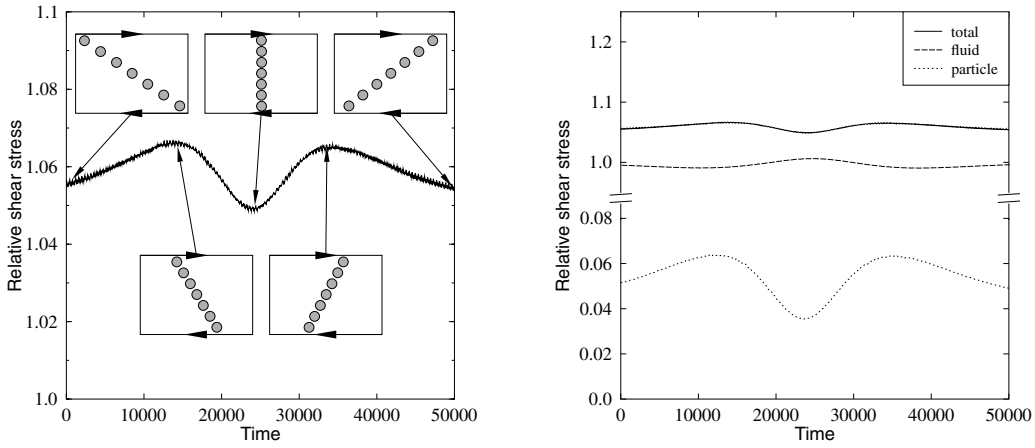

Figure 65. a) The relative wall stress as a function of time for an idealised cluster of suspended particles. The average relative shear stress for a random configurations of the same particles is 1.03. The insets show the orientation of the cluster at different instants of time. b) The shear stress of the fluid and of the particle in the middle plane of the system is shown.

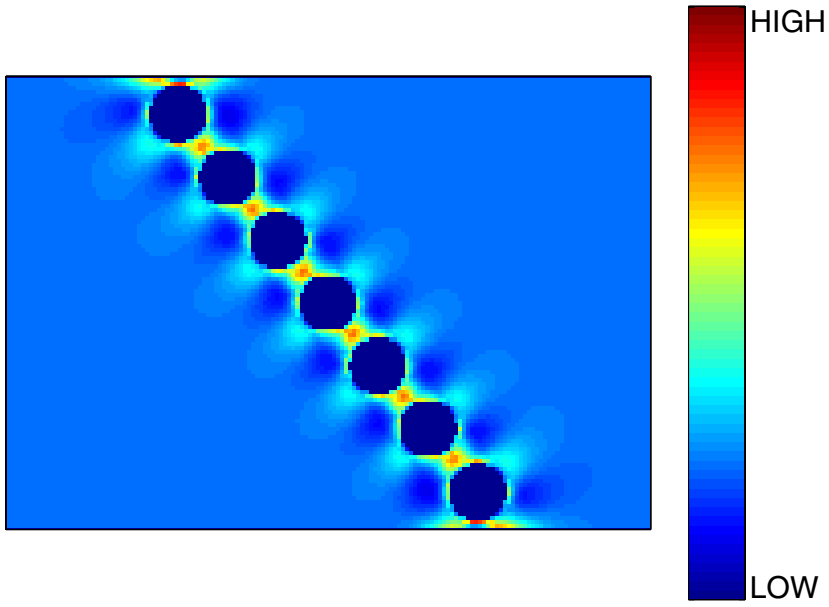

Figure 66. Instantaneous fluid shear stresses in a planar cross section of the system with an idealized cluster.

Finally, we utilize the numerical LB method in computing the relative viscosity of the suspension as a function of the solid volume fraction. These simulations were

performed in the Stokes regime, and the number of simulated particles (diameter 12 lattice units) varied from 200 to 2000 depending on the solid-volume fraction. As is evident from Fig. 67, the result is in excellent agreement with the semi-empirical Krieger–Dougherty relation [6] for this system. This result can be considered as a positive validation of the numerical method and code used in this work. Notice that the simulated results shown in Fig. 67 are obtained from the computed total shear stress and mean shear rate as given by the numerical method and that there are no adjustable parameters involved.

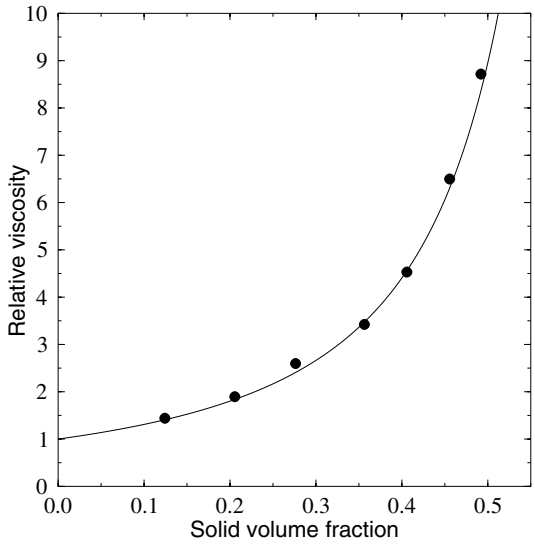

Figure 67. Relative viscosity of a Stokesian suspension of spherical particles as a function of solid-volume fraction. Circles denote the simulated data and the solid line is the Krieger–Dougherty relation [6].

3.6.2 Strain hardening

There is increasing evidence that many phenomena exhibited by liquid-particle suspensions, which cannot be explained by effects produced by non-interacting suspended particles, are related to their microstructure, *i.e.*, to spatial correlations of these particles. One form of spatial correlation is formation of clusters of suspended particles, which we already know [5] to have significant influence on the rheological properties of the suspension, although direct experimental demonstration of this influence has proved to be rather difficult.

A particularly interesting phenomenon observed in liquid-particle suspensions, which is related to shear thickening and has recently received experimental attention, is the so-called strain-hardening effect: A significant and abrupt rise in viscosity is observed when an initially immobile suspension is induced to sheared motion. The prevailing

belief is that also this phenomenon results from formation of particle clusters although no direct evidence of such clustering has so far been found. The strain-hardening phenomenon is present even in the simplest possible liquid-particle suspension, namely in that consisting of a Newtonian carrier fluid and non-Brownian and non-colloidal spherical particles. This kind of simple suspension was very recently analyzed in the detailed experiments by Carreau and Cotton [7]. It is evident that in strain hardening some of the mechanisms responsible for increased viscosity in concentrated suspensions are expected to come into operation. Therefore, a more detailed understanding of the underlying mechanism behind strain hardening may also shed new light into structural issues that are more generally related to formation of viscosity in liquid-particle suspensions. Such information may also be valuable in design of new suspensions for industrial use, *e.g.* paper coating materials with engineered properties.

Strain hardening simulations were done in a plane Couette geometry in which the suspension is confined between two parallel plates. A shear flow was introduced by moving the plates in opposite directions with equal speed. The size of the system was (L_x x L_y x L_z) = (260 x 158 x 90) lattice units, where x is the flow direction and y is the direction in which the velocity gradient was introduced; z is often called the vorticity direction. The simulated suspension consisted of spherical monodispersed particles with a diameter of d = 12 lattice units. The solid volume fraction of the suspension varied between 0.41 and 0.56, and the number of particles between 1655 and 2270, respectively. A more comprehensive description of the simulation techniques and numerical details is given in Ref. [3]. The initial set-up of simulation for solid volume fraction 0.41 is shown in Fig. 68. An instantaneous velocity field and a random particle distribution used as the initial condition is shown in Fig. 69 for a x-y cross section of the simulation volume.

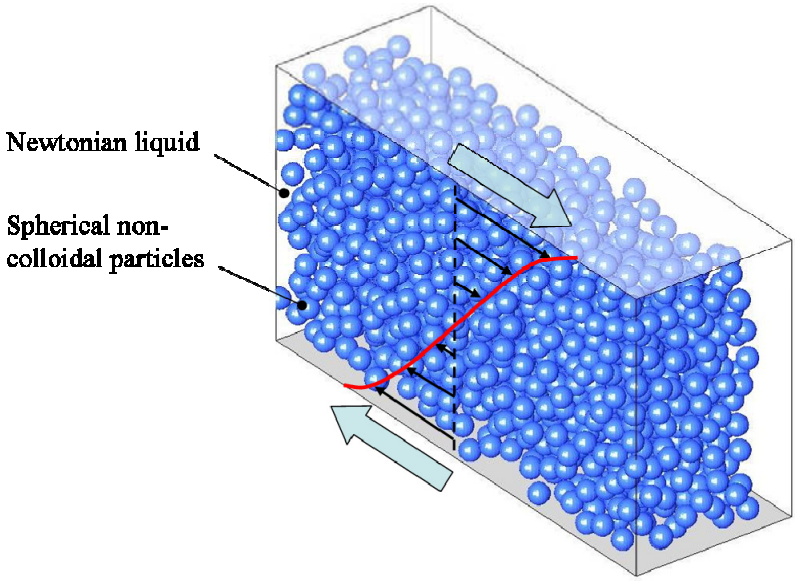

Figure 68. Set-up for shear driven Couette flow simulations of particulate suspension.

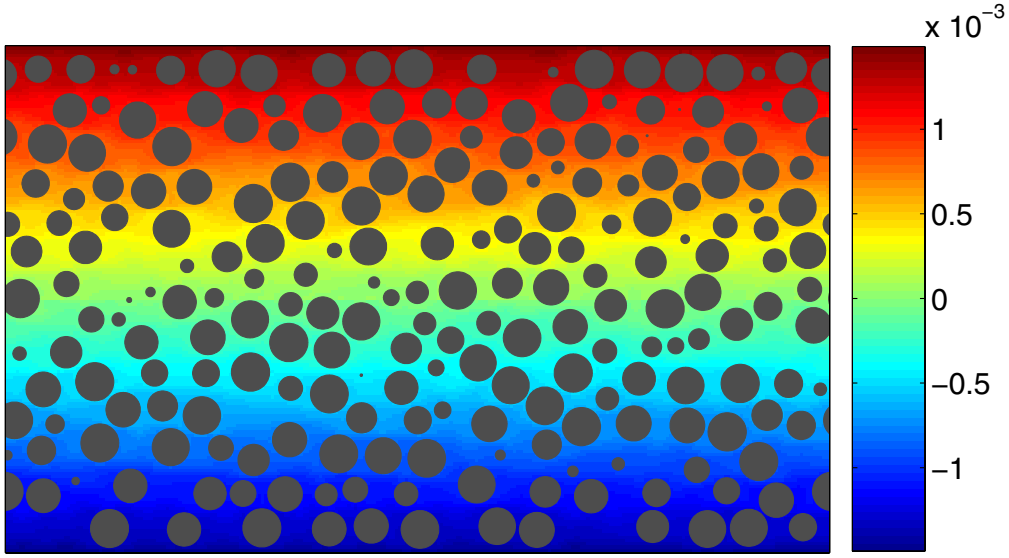

Figure 69. A cross section of the initial velocity field (color coded) and particle distribution for the suspension with the solid volume fraction 0.41. Notice, that the suspension is monodisperse and the apparent variation of particle size in the x-y plane shown is due to their different position in the z-direction.

The measurements reported in Ref. [7] were done at extremely low shear flow. The restrictions set simply by the CPU time available made simulations for such low shear values impossible. Also, the system size in our simulations was smaller than that of Ref. [7] in which the distance between the plates was 100 particle diameters, whereas in our case it was about 13 particle diameters. Thus we cannot expect an exact reproduction of the experimental results in our simulations, but this does not prevent us from semi-quantitative comparison of the results, and from analyzing in particular the microscopic mechanism behind the strain-hardening phenomenon.

In Fig. 70 we show the viscosities obtained from four start-up tests in which the solid-volume fractions were 0.41, 0.46, 0.51, and 0.56. Viscosity was determined from the shear forces acting on the plates by assuming a linear velocity profile between the plates in analogy with the experimental procedure. The results of these start-up tests displayed strain-hardening behavior qualitatively similar to that observed in Ref. [7] *i.e.*, a significant rise in viscosity was observed when the strain (*i.e.* the maximal horizontal displacement of the fluid per unit height) reached a value of about 0.1. For decreasing solid-volume fraction the rise in the viscosity was also decreased, and it appeared at a somewhat lower strain. Fluctuations in the upper viscosity plateau were comparatively large due to the fairly small size of the simulated system.

We now demonstrate that the strain-hardening phenomenon results from changes in the microstructure of the suspension, which mainly appear as formation of particle clusters. We define a cluster such that particle i is considered to be in a cluster if in the same

cluster there is a particle j such that $\left|\vec{r}_i - \vec{r}_j\right| - a_i - a_j < \delta_c$, where $\vec{r}_i$ and a_i are the position and radius of the i:th particle and δ_c is a predefined treshold value for largest allowed distance between the nearest-neighbor particles in a cluster. In the present analysis the threshold value was δ_c = 0.1 lattice units. A rather strict definition for a cluster is needed due to the high solid volume fractions used in the simulations. However, a small variation in the threshold value would not change the qualitative behavior.

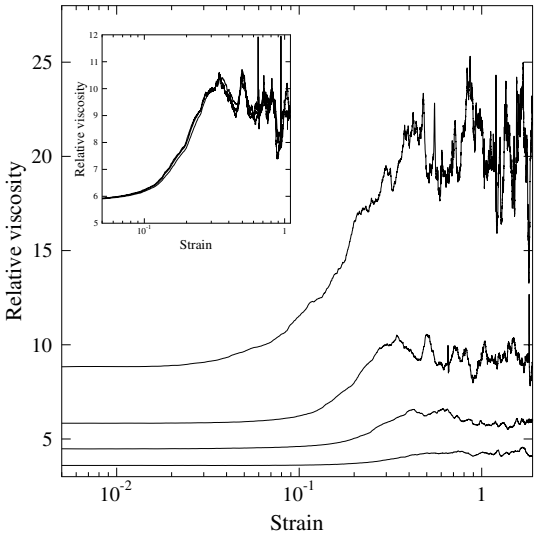

Figure 70. Relative viscosity as a function of strain: simulation results for solid-volume fractions 0.41, 0.46, 0.51, 0.56. The lowest (highest) curve is related to the lowest (highest) volume fraction of the suspension. In the inset shown is the relative viscosity of a suspension with the solid volume fraction 0.51 for three different shear rates.

We now demonstrate that the strain-hardening phenomenon results from changes in the microstructure of the suspension, which mainly appear as formation of particle clusters. We define a cluster such that particle i is considered to be in a cluster if in the same cluster there is a particle j such that $\left|\vec{r}_i - \vec{r}_j\right| - a_i - a_j < \delta_c$, where $\vec{r}_i$ and a_i are the position and radius of the i:th particle and δ_c is a predefined treshold value for largest allowed distance between the nearest-neighbor particles in a cluster. In the present analysis the threshold value was δ_c = 0.1 lattice units. A rather strict definition for a cluster is needed due to the high solid volume fractions used in the simulations. However, a small variation in the threshold value would not change the qualitative behavior.

We define the clustering ratio as the proportion of the particles that belong to any of the clusters. This quantity does not describe all aspects of clustering and its effect on the apparent viscosity of the suspension: Also the size, shape, and orientation of the clusters may affect the viscosity. Clustering ratio will, however, give a qualitative picture of the

clustering process. In Fig. 71 we show the number of clustered particles as a function of strain for the same simulations for which the viscosities were shown in Fig. 70. It is evident that clustering ratio behaves similarly to viscosity. When the solid-volume fraction of the suspension is increased, clustering and the rise in viscosity both appear at a smaller value of strain. It is evident that for increasing concentration the mean interparticle distance becomes smaller, which enhances clustering. Experiments indicate that the viscosity of the suspension is independent of the shear rate in the regime of very low rates. We therefore considered the behavior of our model suspension with a solid-volume fraction of 0.51 for three different shear rates. Notice that in all these simulations exactly the same initial configuration of particles was used. We found that the behavior of viscosity was almost identical for the three shear rates (c.f. the inset in Fig. 70). This indicates that strain hardening is indeed connected to the microstructure of the suspension.

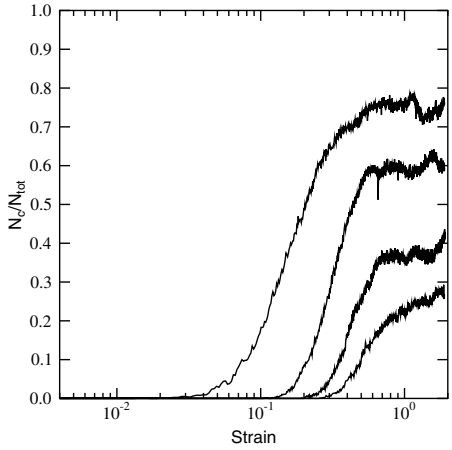

Figure 71. Number of clustered particles as a function of strain for the same simulations as those shown in Fig. 70. N_c is the number of clustered particles and N_{tot} is the total number of particles.

Consider now momentum transfer in the above suspensions. The lattice-Boltzmann method is ideal for this kind of analysis since the stress tensor can be calculated locally from the non-equilibrium part of the distribution function, and no approximation is needed for derivatives of the local velocity. The stresses that originate from the fluid and the solid phase can be determined separately, and we did so in each plane parallel to the moving plates. We thus determined the proportion of viscosity that results from momentum transfer through the fluid phase, averaged over all planes. The rest of the viscosity results from the internal stresses of the particles since the convective stresses were found to be insignificant in both the fluid and the solid phase. Results of this stress analysis is shown in Fig. 72. It is evident from this figure that the observed increase in viscosity, *i.e.*, the strain-hardening effect, is caused by enhanced momentum transfer via the solid phase.

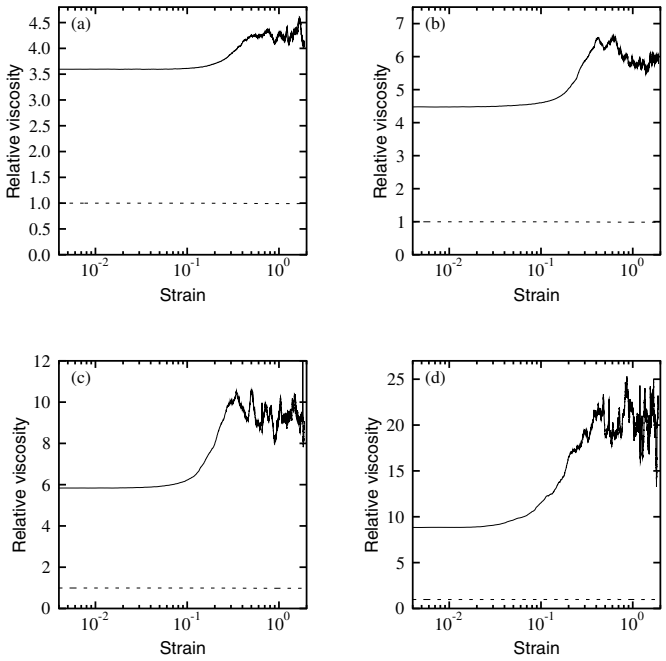

Figure 72. Relative viscosity as a function of strain for solid volume fractions (a) $\phi = 0.41$, (b) $\phi = 0.46$, (c) $\phi = 0.51$, and (d) $\phi = 0.56$. Dotted lines indicate the proportion of viscosity that results from fluid stress.

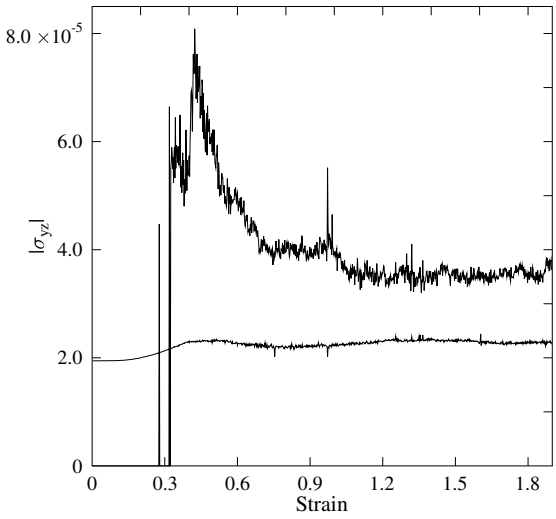

Figure 73. Mean internal stress of clustered (upper curve) and non-clustered particles (lower curve) for solid volume fraction 0.41. Notice that there were no clustered particles initially.

We still need to verify that the enhanced momentum transfer via the solid phase is indeed dominated by clusters of particles. To this end we determined the mean internal stress for each individual particle. This was done by integrating the forces acting on the surfaces of the particles [3]. This force is directly obtained from the fluid-solid

boundary condition imposed. Since we know from the cluster analysis which particles belong to clusters, we can determine the average internal shear stresses in clustered and non-clustered particles using the stresses of individual particles. As shown in Fig. 73 the stresses in the clustered particles are considerably higher than those in the non-clustered particles. We can thus conclude that formation of particle clusters is indeed responsible for the strain-hardening phenomenon.

3.6.3 Particle migration effects in capillary viscometric flows

Capillary viscometers are widely used in industry to study the properties of various non-Newtonian fluids such as polymer melts and particulate suspensions under high shear flow conditions. The results thus obtained are useful in quality control, materials testing and process control purposes. The basic purpose of such testing may be *e.g.* to monitor uniformity of a product or to find experimental correlations between the measured rheological properties of a fluid and the behaviour of a process involving flow of the fluid. For coating process of paper *e.g.*, general guidelines can be given for selecting optimal coating materials and/or for identifying possible problems that can be anticipated for a certain material – on the basis of capillary viscometric measurement of the coating pigment suspension. While such results are based on extensive amount of carefully correlated data and are very useful for many practical purposes, they are limited to the particular measuring set-up and coating process for which the correlation was originally found. Instead, such results may not be very helpful *e.g.* in predicting the behaviour of a coating material in an other type of coating device – perhaps in one that is still to be designed.

It is well known that the rheoloical behaviour – or more specifically, the dependence of viscosity on shear rate – of a particulate suspension as measured using capillary viscometer can not be considered as a general material property of the suspension. The basic reason for this is that while only the total pressure loss and flow rate through the capillary tube are measured, the actual velocity profile in the tube is not known. Instead, an *assumed* profile is used in analysing the result and calculating the value of apparent shear rate and apparent viscosity at the tube wall. It is also well known, that the assumptions made at this point (often realized in terms of various standard 'corrections' to the original result) are not on a very solid foundation and may lead to significant misinterpretation of the data. Of special importance here is the apparent slip that typically occurs at the tube wall for particulate suspension flows. This phenomenon is known to result from migration of particles away from the wall. Unlike for many types of polymer-based non-Newtonian fluids, there seems to be no reliable correction method available that could account for wall slip effect for particulate suspensions. Here, we will combine experimental capillary viscometry and the numerical LB method

in order to study the underlying microscopic mechanisms that lead to wall slip and thereby effort in developing effective ways for experimental data analysis to probe true material properties of liquid particle suspensions.

The experimental and numerical set-ups studied here both consist of non-colloidal and non-Brownian suspension of spherical particles suspended in Newtonian fluid. In experimental set-up, the flow channel is a capillary tube of circular cross section whereas in numerical simulation, flow between parallel plates is considered. The channel width to particle diameter ratio varies roughly between 30 and 75 in the experiments and is 13 in numerical simulations. The ranges of particle Reynolds number obtained in experiments and in numerical simulations just barely overlap. Furthermore, the particles used in numerical simulation are elastic, whereas the class particles used in experiments may have some weak short range interactions. Although complete similitude between experimental and numerical set-up could thus not be achieved due to technical limitations in both methods, the systems studied experimentally and numerically are qualitatively quite similar. We can therefore anticipate only qualitatively similar results but obviously not exact quantitative match of the results.

Experimental procedure and results

Capillary rheometer measurements were carried out for a non-colloidal suspension of solid glass spheres ($d = 10\ \mu m$, $\rho = 2.5\ g/cm^3$) and a low viscosity Newtonian oil ($\eta_0 = 0.094$ Pa·s, $\rho = 0.940\ g/cm^3$). The diameter of capillaries used were 0.735 mm, 0.525 mm and 0.292 mm. Length and diameter ratios (l/d) were approximately 170, 120 and 95, respectively. Maximum shear rate was of the order of 10^6 1/s at maximum pressure of 200 bar. Three values of volume fraction of particles were used, namely $\phi = 0.20$, 0.35 and 0.45. Measurement temperature was approximately 20°C. Figure 74 shows the measured (uncorrected) results for relative viscosity η/η_0 measured using a capillary of length $l = 49.9$ mm and diameter $d = 0.292$ mm. Notice, that the viscosity η_0 of the carrier fluid was measured using the same capillary viscometer. The results show strong shear thinning behaviour that is typical to also many industrial suspensions such as paper coating materials in the range of the apparent shear rate used in this experiment.

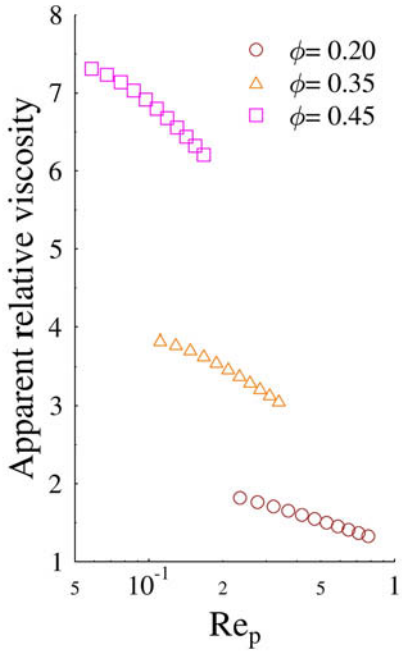

Figure 74. Apparent (uncorrected) relative viscosity of a model suspension (class spheres of diameter 10 μm suspended in oil with viscosity 0.094 Pa·s) at various values of particle volume fraction as measured using capillary viscometer. The length and diameter of the capillary was 49.9 mm and 0.292 mm, respectively.

Numerical set-up

The numerical procedure used in this study is similar to that used above in the strain hardening simulations – a plane geometry with suspension is confined between two parallel plates. In this case, however, we consider pressure-driven Poiseuille flow with fixed channel walls. The size of the basic system was (L_x x L_y x L_z) = (300 x 162 x 80), The simulated suspension consisted of spherical monodispersed particles with a diameter of $d = 12$ lattice units. Here we only considered one mean solid volume fraction of 0.35. The number of particles was 1438. Otherwise, the used method and numerical details were the same as those used in the previous section (see also Ref. [3]).

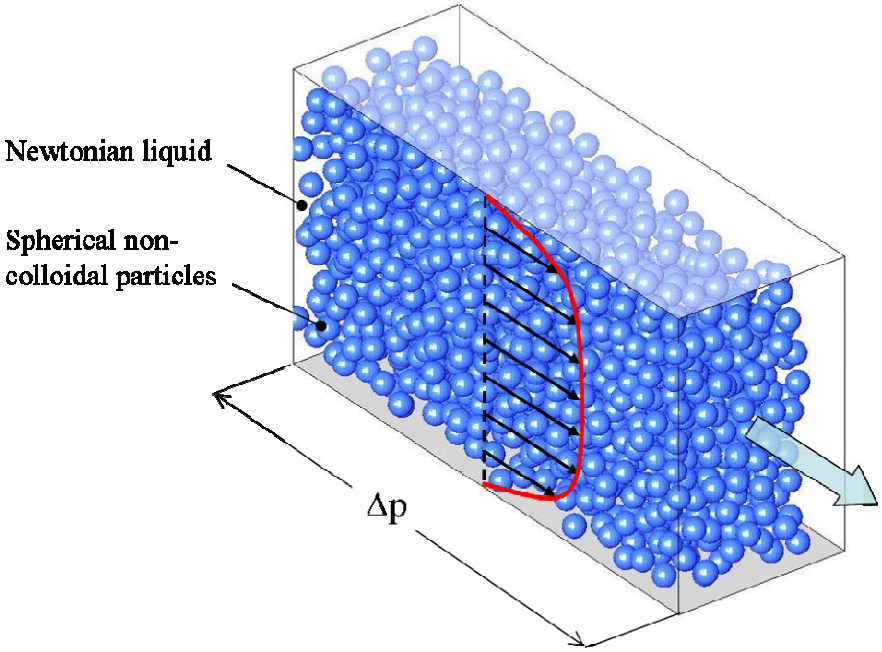

Figure 75. Set-up for pressure driven Poiseuille flow simulations of particulate suspension.

In order to directly compare the numerical results with experimental data, and to gain at least qualitative understanding on the microscopic mechanisms that underlie the observed behaviour, we analyse the numerical results in two different ways. First, we ignore the actual velocity profile that is known from numerical solution and calculate the 'apparent viscosity' in exactly the same manner as is done in the experimental rheology, *i.e.* using only the computed total flow rate and pressure loss and assuming Newtonian profile. In addition, we apply the conventional corrections due to non-Newtonian profile, again exactly the same manner to the numerical data and and to the measured results. Second, we utilize the computed velocity profile and calculate the 'intrinsic viscosity' using local values of shear stress and shear rate. As will be shown, the two approaches lead to quite different results. Notice however, that the latter method of finding the local value of viscosity, based on actual (computed) velocity profile, is free from any assumptions concerning the flow profile or boundary condition and therefore does not need any 'corrections'. We thus expect the intrinsic viscosity to reflect the material properties of the model suspension more directly than the apparent viscosity which may be strongly affected by the properties of the flow and not just of the material.

Results

Figure 76 shows the experimental and numerical results for apparent relative viscosity as a function of shear rate and of particle Reynolds number (dimensionless shear rate) defined as

$$\mathrm{Re}_p = \frac{d^2 \dot{\gamma}_W}{\upsilon}, \tag{75}$$

where d is the particle diameter, $\dot{\gamma}_W$ is the apparent shear rate at the tube wall and υ is the kinematic viscosity of the fluid. Also shown are the values of viscosity with the appropriate corrections applied. The results for a single solid volume fraction $\phi = 0.35$.

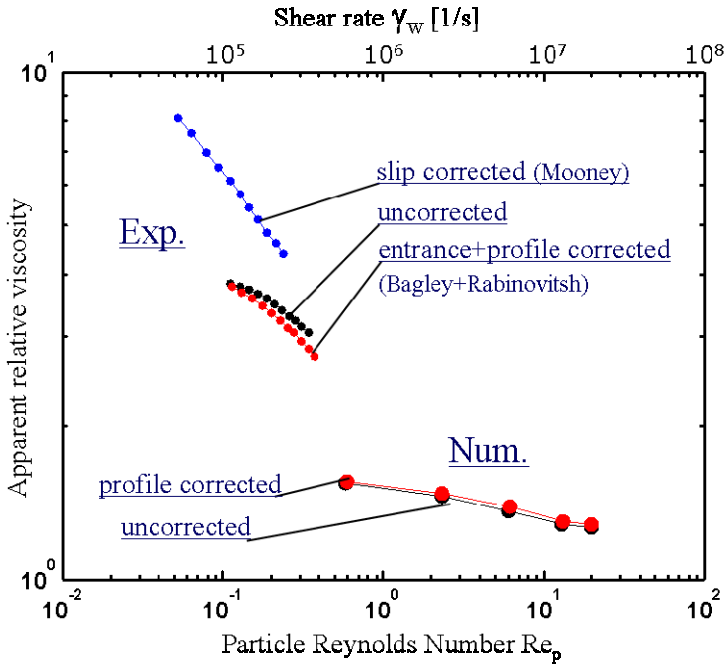

Figure 76. Experimental and numerically computed values of apparent relative viscosity of particulate suspensions as a function of particle Reynolds number and shear rate (top axis). The solid volume fraction is 0.35. Also shown are values of viscosity with standard corrections applied in a similar manner to experimental and numerical results.

Notice, that since the suspension and the flow conditions used in the experiment are not exactly the same as in the numerical simulation, we can not expect quantitative match of the results. In particular, due to limitations in both capillary viscometric and LB numerical techniques used, the shear rate range available for the two methods do not coincide. We can, however, make a resonable qualitative comparison of the results.

As shown by Fig. 76, both experimental and numerical results show clear shear thinning behaviour of the suspension. Notice, that the shear thinning is usually associated with Brownian motion present in colloidal suspensions. In this case, however, the actual suspension used in the experiments was clearly non-colloidal and no Brownian motion was implemented in the numerical simulations. Furthermore, the results are not qualitatively changed by taking into account the standard corrections – in particular, not even by the usual Mooney correction due to wall slip. In this respect, the experimental and numerical results are in qualitative agreement.

We now turn to more detailed analysis based on computed flow profiles across the channel. Figure 77 shows the calculated mean profiles of the flow for particle volume fraction 0.35 and for various flow rates. The mean velocity is defined here as the volume fraction weighed time average of the two phases. Also shown in Fig. 77 are the parabolic flow profile (assumed in the previous analysis of apparent uncorrected viscosity) and the profile of shear stress. All profiles are normalized by the maximum value. We first observe, that the actual mean velocity profiles deviate drastically from the parabolic profile. Although not shown here, even the profiles obtained by applying the standard Rabinowich correction for a non-Newtonian profile are quite different from the computed profiles. Utilizing the computed profiles, we can now calculate local values of shear rate, shear stress and consequently, of viscosity across the channel (see Fig. 77). We call the (position dependent) viscosity thus calculated as the 'intrinsic viscosity'.

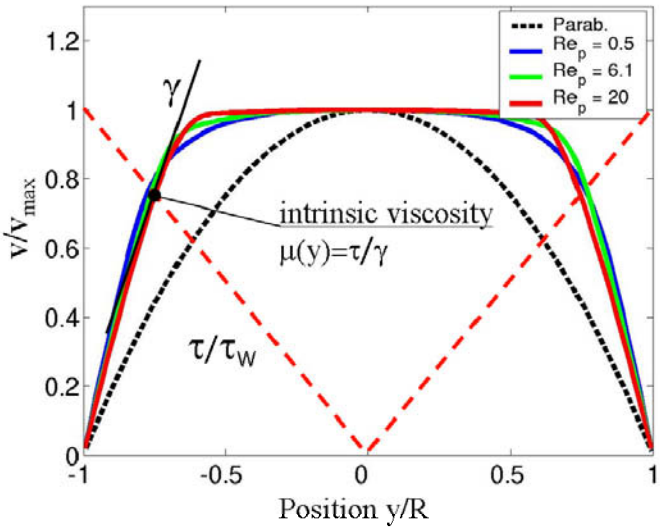

Figure 77. Numerically computed normalized values of mean flow velocity as a function of position across the channel for different flow rates. The solid volume fraction is 0.35. Also shown are the Newtonian (parabolic) flow profile and the distribution of shear stress across the channel. Also shown is the definition of the intrinsic viscosity as calculated using the local values of shear rate and shear stress.

A more detailed analysis of the flow behaviour in the channel reveals that the high shear rate regions near the walls is associated with development of concentration profile in the cannel, in particular, with migration of particles away from the walls. This phenomenon is known as the 'tubular pinch effect' and has been found experimentally by Segre and Silberberg [8]. Figure 78 shows the calculated mean solid volume fraction profiles across the channel for various total flow rates. As can be seen in the figure, a particle free depeletion layer is developed near the walls and the thickness of that layer increases with increasing flow rate. This layer is well known to be the origin of the apparent wall

slip phenomenon. Furthermore, in addition to different values of shear rate, the values of viscosity computed at different locations also correspond to different values of concentration. Figure 79 shows the computed intrinsic relalative viscosity as a function of the volume fraction. Notice, that every computed point in the figure corresponds to the local value of intrinsic viscosity as a function of the local value of concentration (both calculated at the same point y), and that results from all total flow rates used in simulations are used here. An excellent agreement between the computed results and the semiempirical result by Krieger and Dougherty, also shown in Fig. 79, is found.

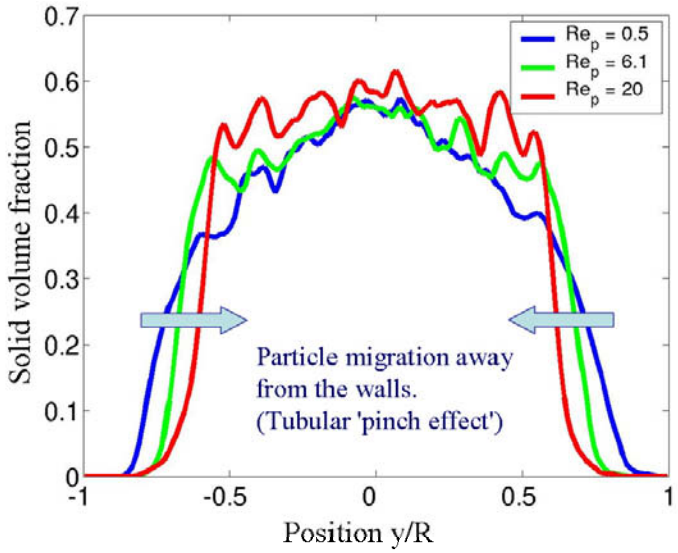

Figure 78. Numerically computed solid volume fraction profiles as a function of position across the channel for different flow rates. The mean solid volume fraction is 0.35.

In order to find the behaviour of the suspension at fixed particle consistency, we show in Fig. 80 the intrinsic relative viscosity as a function of particle reynolds number at a constant solid volume fraction of $\phi = 0.25$. Thus, the values of viscosity and particle reynolds number shown in Fig. 80 are picked from profiles computed at different total flow rates at y-locations where $\phi(y) = 0.25$. For other values of ϕ, the result is similar, but scales according to Krieger–Dougherty result at each given shear rate. The result shows shear thickening behaviour and is thus qualitatively different from the apparent viscosity result shown in Fig. 76. We emphasise that the result shown in Fig. 80 is based on direct numerical simulation where no arbitrary assumptions or adujstable parameters are used. Therefore, as the computational model suspension is considered, the actual material property of the suspension at a constant consistency is shear thickening as indicated in Fig. 80. The apparent shear thinning behaviour found in Fig. 76, where the conventional experimental method of analysis was applied in the present numerical simulations, is due to misinterpretation of wall slip as shear thinning. The wall slip, in turn, appears due to particle migration in the transverse direction leading to particle depletition region near the walls. The resulting viscosity profile across the channel, with

low viscosity region near the wall, is fully explained by the Krieger–Dougherty relation. Notice, that this result, including the discrepancy between the rheological character of the suspension as determined on the basis of apparent viscosity, *i.e.* analogously with the standard experimental procedure, and on the basis of intrinsic viscosity, which utilizes the actual computed behaviour, only applies to numerical model suspension. Given the good qualitative agreement of the results between the LB numerical method and all experimental data available, it is highly possible that similar phenomena (and the related misinterpretation of data) indeed take place in the experiments as well. In the absence of measured velocity profile in the capillary viscometric experiments, it is however impossible to unambiquously verify this statement.

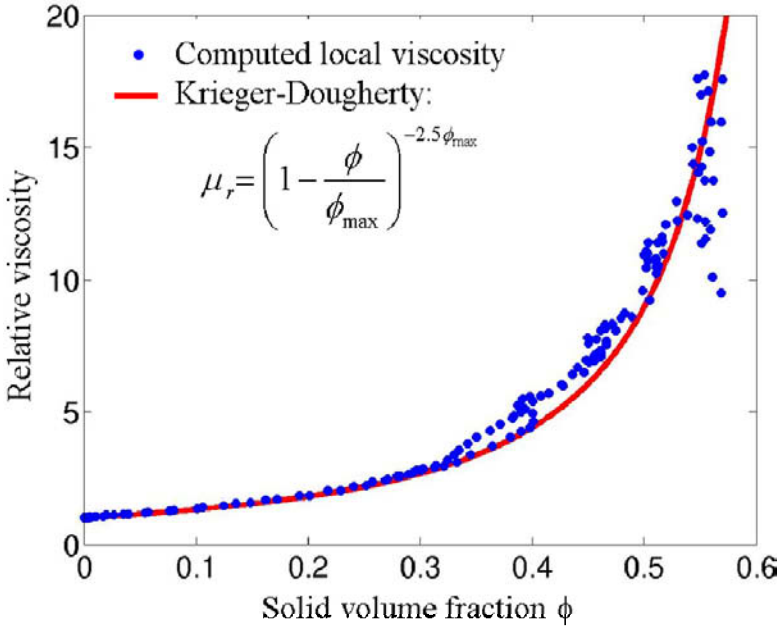

Figure 79. Numerically computed intrinsic relative viscosity as a function of (local) solid volume fraction for all the flow rates used in simulations. Also shown is the semiempirical Krieger–Dougherty correlation with the maximum packing ratio parameter $\phi_{max} = 0.7$.

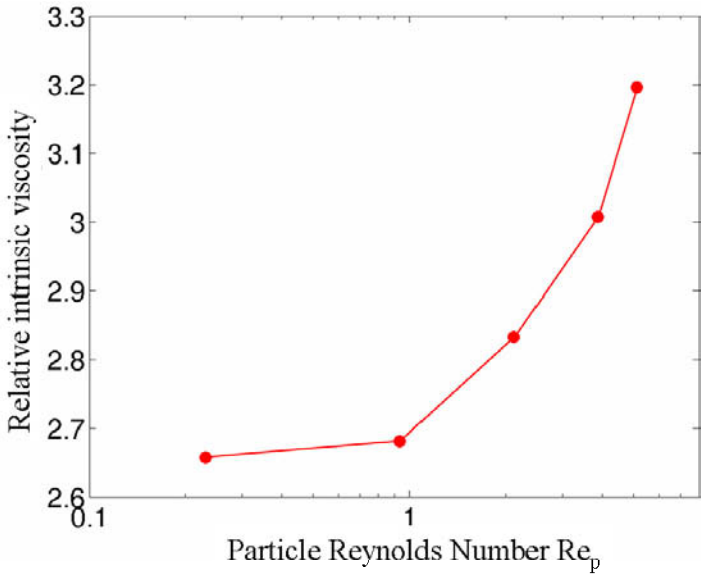

Figure 80. Numerically computed intrinsic relative viscosity as function of (local) solid volume fraction for all the flow rates used in simulations. Also shown is the semiempirical Krieger–Dougherty correlation with the maximum packing ratio parameter ϕ_{max} = 0.7. (dimensionless shear rate, defined by Eq. (75) except that the shear rate at the wall $\dot{\gamma}_W$ is replaced by the local shear rate $\dot{\gamma}(y)$) at fixed

3.6.4 Non-Newtonian lattice-Boltzmann model

Non-Newtonian fluids are present in a broad range of discplines in engineering and science. One interesting system containing such fluids is a particle suspension where solid particles are suspended in a non-Newtonian liquid. In this section we present a lattice-Boltzmann model that was developed in order to simulate flow of suspensions with non-Newtonian carrier liquid.

One form of a non-Newtonian fluid is a fluid whose deviatoric stress tensor is related to the shear-rate tensor by equation

$$\sigma'_{\alpha\beta} = 2\mu_{eff}(\dot{\gamma})\gamma_{\alpha\beta}. \tag{76}$$

Above $\dot{\gamma}_{\alpha\beta}$ is the shear-rate tensor, the $\dot{\gamma}$ shear rate, and μ_{eff} the effective (dynamic) viscosity. For Newtonian fluids μ_{eff} is constant as a function of shear rate. Non-Newtonian fluids can be modelled by choosing a specific form for the effective viscosity.

We added non-Newtonian behaviour to the lattice-Boltzmann model by varying viscosity locally as the function of shear rate. This kind of approach is well suited for

lattice-Boltzmann since in this method shear-rate tensor can be obtained efficiently and locally from some intrinsic quantities of the lattice-Boltzmann method without numerical differentiation of the velocity field. We have tested so-called power-law model for non-Newtonian fluid but we also stress that our code is by no means restricted to simulations of power-law fluids but easily copes with other types of models for the effective viscosity. For the power-law fluids viscosity is given by equation

$$\mu_{eff} \propto \dot{\gamma}^{n-1}, \tag{77}$$

where n is a (positive) power-law index. This effective viscosity describes a shear-thinning fluid if $n<1$, a shear-thickening fluid if $n>1$, and a Newtonian fluid if $n = 1$.

We tested our implementation by simulating pressure-driven channel flow of the power-law fluid for which the analytical steady-state velocity profiles are known and given by

$$\frac{u(x)}{u_m} = \frac{2n+1}{n+1}\left[1-\left(\frac{2|x|}{w}\right)^{1+1/n}\right]. \tag{78}$$

Above w is the width of the channel and u_m is the mean velocity. In Fig. 81 we show the results obtained by lattice-Boltzmann method and compare these to corresponding analytical profiles. A good agreement between simulated and analytical profiles is found. We also combined the non-Newtonian lattice-Boltzmann model with the model for suspended particles and the resulting method appeared to be numerically stable.

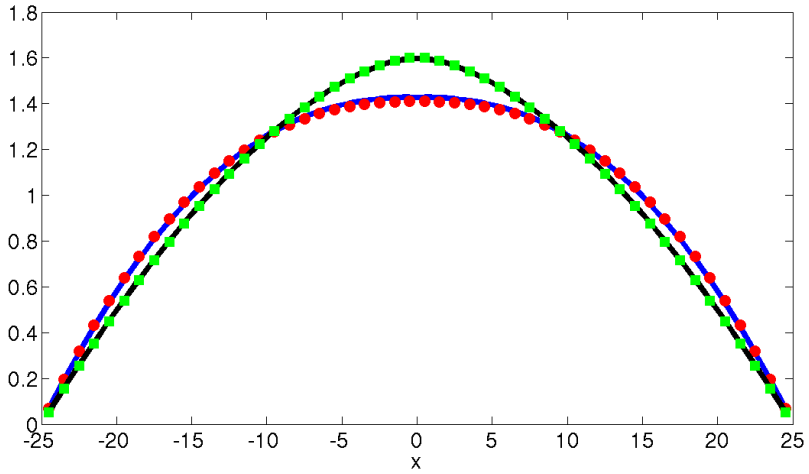

Figure 81. Velocity profiles for pressure-driven channel flow for power-law fluids. Simulation results are shown by the dots and the solid lines are for analytical profiles. Both shear-thickening (green) and shear-thinning (red) fluids were simulated and the values of the power-law index were n = 1.5 and n = 0.75, respectively.

3.6.5 Conclusions

In this work we simulated the behaviour of a liquid-particle suspension with non-colloidal and non-Brownian solid particles using the LB method. The strength of computer simulations in studying correlated structures inside suspensions, which may significantly affect their rheological behaviour, is that simulations make it possible to analyze in detail the microscopic structure of the suspension. They thus provide direct information that would be difficult to obtain by experimental techniques. In addition to the structural information, the LB method enables computation of the internal stresses of individual particles as well as the local components of the stress tensor in the fluid. These features of the method enable, *e.g.*, an exact analysis of various momentum transfer mechanisms that are responsible for changes in the viscosity of the suspension.

We demonstrate, in terms of two simple examples, how the LB method in combination with detailed stress analysis can be used to effectively study the origin of the observed non-Newtonian behaviour of non-Brownian particulate suspensions. First we considered a very simple system of periodic suspension, and found that inertial effects that become detectable for particle Reynolds numbers above unity, change the flow field around the particle so as to increase the shear stress of the system. Next, we considered the effect of a single artificial cluster of suspended particles on the solid volume fraction dependence of the viscosity of this suspension. A chain-like cluster of suspended particles rotating in the shear flow was found to increase the momentum transfer between the channel walls in comparison with random configurations of particles. This behaviour indicates that increased formation of particle clusters for increasing solid-volume fraction of the suspension will contribute to the related increase in its viscosity. We then simulated the shear flow of a non-Brownian suspension in Couette geometry and found that, as a function of the solid volume fraction, in the Stokes regime the simulated viscosity of the suspension agrees well with the semi-empirical Krieger–Dougherty relation. This result can be considered as a positive validation of the method used.

In the second part of this work, we analyzed the viscosity of a liquid-particle suspension that is immobile initially but is then induced to sheared motion. At the early phases of the process, the viscosity of the suspension stayed almost constant, but increased then fairly rapidly to a clearly higher level. We showed that this rise in viscosity is accompanied by formation of clusters of suspended particles. A detailed analysis of momentum transfer in the system revealed that increasing viscosity is caused by increasing momentum transfer via suspended particles. Finally we demonstrated that momentum transfer is dominated by particles that belong to clusters. We could thereby explain the mechanism that creates the so-called strain-hardening phenomenon observed earlier in detailed small-strain experiments on liquid-particle suspensions [7]. It is evident that the clustering tendency of suspended particles, shown here to be

responsible for the strain-hardening phenomenon, is also more generally a mechanism that causes the viscosity of the suspension to increase for increasing shear-Reynolds number, before inertial effects begin to play a dominant role.

In the third part of the work we study the flow of a particulate suspension in capillary rheometer in an effort to gain understanding on the various effects that may hamper the interpretation of experimental data, effects of wall slip and non-Newtonian profile, in particular. We analyse the numerical data on capillary flow of suspension in two different ways. Firstly, we only utilize the computed pressure difference and total flow rate in the capillary and analyse the results in the same manner as the corresponding experimental results are analysed – including various standard corrections. Comparison with actual experimental results shows good qualitative agreement and unambiguously indicate shear thinning behaviour. Next, we utilize the calculated profiles of velocity, particle consistency and shear stress. Based on this more detailed information we calculate the intrinsic viscosity which is not subject to any additional assumptions and can be considered as an actual material property of the model suspension. This analysis verifies that the apparent shear thinning observed experimentally (and numerically, if the numerical results are analysed analogously with experimental results) indeed arises from migration of particles away from the walls, and the resulting concentration gradient across the capillary. The thin layer near the wall completely depleted from particles leads to apparent wall slip (of the solid phase). The intrinsic viscosity of the suspension depends on local particle concentration according to the Krieger–Dougherty correlation. Furthermore, analysing the intrinsic viscosity in a constant particle consistency reveals the actual material property of the model suspension to be shear thickening and not shear thinning. The results thus obtained help to understand the underlying flow dynamics in capillary viscometer and especially the subtleties involved in interpretation of the data. The standard corrections applied to capillary viscometric results, the slip correction, in particular, were not found to yield correct rheological material property of the model suspension studied here. The results also demonstrate the need of further research in the topic.

In the last part of the work we report results from implementing a non-Newtonian LB model. The model is successfully validated for a simple Poiseuille flow of both shear thinning and shear thickening fluids with power law dependence of viscosity on shear rate. The model is applicable in simulating flows of particulate suspensions with non-Newtonian carrier fluid.

References

[1] Kataja, M. (ed.). Rheological materials in process industry. ReoMaT Project Report 2003. VTT Project Report, 15.3.2004.

[2] Hyväluoma, J., Raiskinmäki, P., Koponen, A., Kataja, M. and Timonen, J. Lattice Boltzmann Simulation of Particle Suspensions in Shear Flow. *J. Stat. Phys*. **21** (2005), pp. 149–161.

[3] Hyväluoma, J., Raiskinmäki, P., Koponen, A., Kataja, M. and Timonen, J. Strain hardening in liquid-particle suspensions. *Phys. Rev.* **E72**, 061402 (2005).

[4] Patankar, N.A. and Hu, H.H. Finite Reynolds number effect on the rheology of a dilute suspension of neutrally buoyant circular particles in a Newtonian fluid. *Int. J. Multiphase Flow* **28** (2002), pp. 409–425.

[5] Raiskinmäki, P. Dynamics of multiphase flows: liquid-particle suspensions and droplet spreading. PhD Thesis, University of Jyväskylä, 2004.

[6] Krieger, I.M. and Dougherty, T.J. A Mechanism for Non-Newtonian Flow in Suspensions of Rigid Spheres. *Trans. Soc. Rheol.* **3** (1959), pp. 137–152.

[7] Carreau, P.J. and Cotton, F. In Transport processes in bubbles, drops, and particles. 2nd ed. Ed. by De Kee, D. and Chabra, R.P. Taylor & Francis, New York, 2002.

[8] Segre, G. and Silberberg, A. Behaviour of macroscopic rigid spheres in Poiseuille flow. Part 2. Experimental results and interpretation. *J. Fluid. Mech.* **14**, (1962), pp. 136–157.

3.7 Validation of lattice-Boltzmann numerical simulation for fluid flow through compressed paper board samples

Viivi Koivu*, Tuomas Turpeinen, Markko Myllys and Markku Kataja

Department of Physics, P.O. Box 35 (YFL), FI-40014 Universtiy of Jyväskylä, Finland

We have continued the study of fluid flow properties of fibrous porous materials using direct numerical simulations and high-precision X-ray tomographic images. The main results were given earlier in Ref. [1]. Here, we report the latest results from experimental validation of the lattice-Boltzmann numerical simulation method used in computing the flow permeability of compressed paper board samples. The samples were imaged under varying degree of compression at European Synchrotron Radiation Facility (ESRF) in Grenoble. The resulting 3D pore structure were then used in numerical flow simulation to find the computed value of flow permeability. The results were compared with experimental values obtained using the permeability cell at University of Jyväskylä.

3.7.1 Experimental procedure and numerics

Samples of layered cardboard of basis weight 225 g/m^2 and size 2 x 2 mm^2 were imaged at ESRF X-ray tomographic facility ID19 using plastic sample holders specifically constructed to allow samples to be held in a compressed state during imaging (see Fig. 82). The imaging was made in absorption mode with resolution 0.7 μm. Altogether four sets of images were taken, each set containing three individual 3D images. Two of the sets contained three images of different physical samples held at different levels of compression. The remaining two sets contained three images of a same physical sample but the degree of compression increased between exposures. All eight physical samples thus needed were taken out of the same cardboard sheet. The raw images were filtered to remove excess noise and ring artifacts inherent of the imaging method.

The permeability of the cardboard samples for air flow was measured as a function of degree of compression using the permeability cell shown in Fig. 83. To measure permeability, a circular sample of diameter of 90 mm, taken from a sheet macroscopically identical with that used in tomographic imaging, was placed in the permeability cell between two smooth sintered compression plates and the air flow was directed through the system. Pressure loss was measured as a function of flow rate first with no mechanical pressure load. Then the sample was compressed between sintered plates with hydraulic pump and the permeability was measured as a function of the sample thickness at a constant flow rate. Measurements were carried out at loading

force up to 50 kN with intervals of 1 kN. The maximum mechanical pressure applied to the sample was thus approximately 7.9 MPa. The measurement was done in the viscous creeping flow regime where Darcy's law applies.

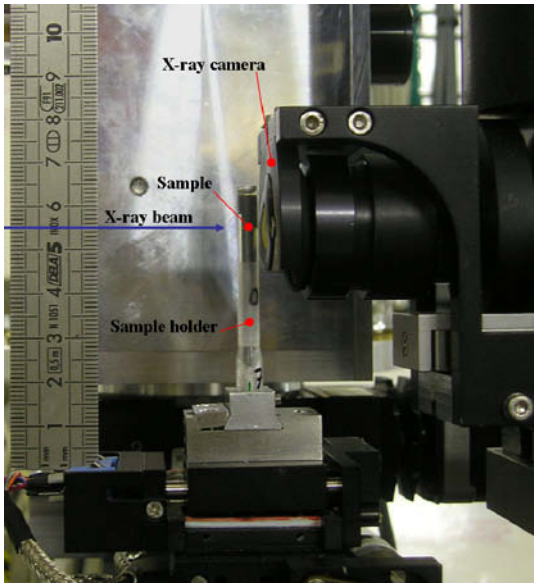

Figure 82. The acrylic sample holder mounted in the manipulator device in front of the X-ray camera optics at ESRF tomographic imaging laboratory ID19. The cardboard sample (not visible) is located in the middle part of the tubular holder. Compression of the sample is provided by a piston operated by a screw in the bottom part of the holder.

Figure 83. Permeability cell used to measure the flow resistance of card board samples under compression.

3.7.2 Results

Fig. 84 shows 2D cross sections of the original 3D tomographic images of card board samples compressed at three different values of thickness. In Fig. 85 shown is the numerically solved flow field of a viscous fluid on a 2D cross section of one of the samples. The flow is induced by a vertical pressure gradient across the sample. Integration of the flow field yields the total flow rate. The permeability of the sample is then be calculated using Darcy's law.

The calculated and measured results for permeability as a function of thickness of the cardboard sample are shown in Fig. 86. Due to structural limitations of the permeability cell, the degree of compression available in experiments is less than that obtained by the sample holder used in tomographic imaging. This is simply due to very different size of the samples used in these two experiments: the area of the tomographic sample is approximately 4 mm^2 whereas the area of the sample in permeability experiment is three orders of magnitude higher. The total force required to compress the sample in the permeability cell to the same minimum thickness easily obtained in the tomographic sample holder would have caused permanent deformations of the permeability cell structure. Another consequence of the small sample size used in tomographic imaging and computation is large scatter of the results. In spite of these shorcomings, it is clear from Fig. 86 that the agreement between computed and measured results is very good. We consider this as a positive validation of the computational method based on high resolution tomographic imaging and lattice-Boltzmann numerical flow simulation methods. These methods have already been successfully applied also in computing structural and flow resistance properties of other porous materials such as paper making fabrics. In that case, the accuracy is even better since the structure of the fabrics is much simpler than that of paper. Consequently, tomographic images obtained also by the state of the art table top scanners, instead of the large scale synchrotron device, are sufficently good to yield reliable flow simulation results.

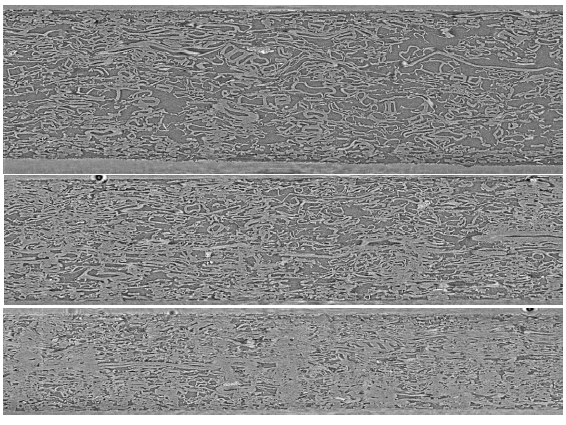

Figure 84. 2D cross sections of tomographic images of three cardboard samples compressed to different levels.

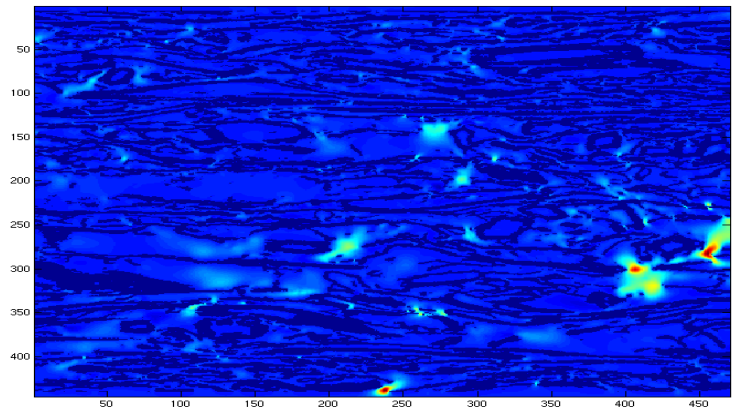

Figure 85. Numerically solved flow velocity field on a 2D slice of tomographic image of a compressed cardboard sample. The dark blue color shows the fibre structure (the thresholded tomographic image). Blue color indicates low velocity and light and red colors indicate high flow velocity in the pore space between and inside the fibres. The direction of pressure gradient and mean flow is from top to bottom.

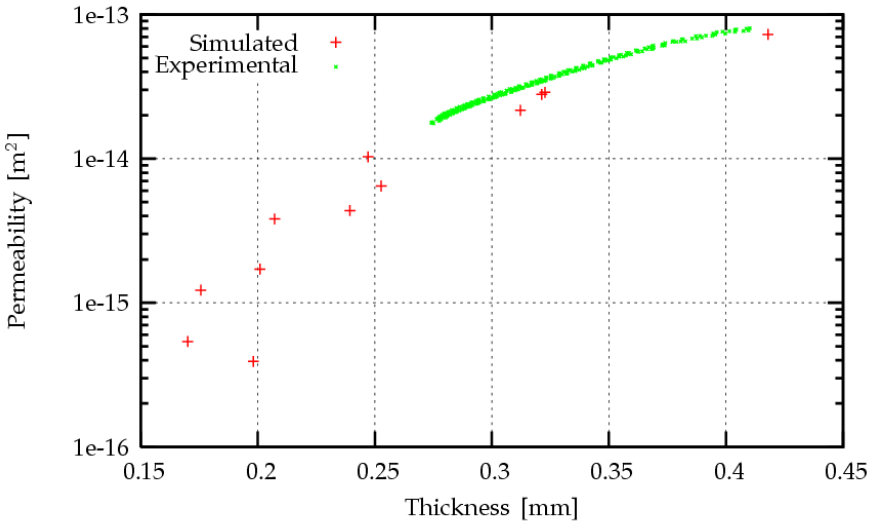

Figure 86. Measured and computed values of permeability for compressed card board as a function of the thickness of the sample.

Reference

[1] Kataja, M. (ed.). Rheological materials in process industry. ReoMaT Project Report 2003. VTT Project Report, 15.3.2004.

3.8 Rheology of consolidating fibre network

Elias Retulainen, Kristian Salminen, Tero Ponkkala and Vesa Kunnari

VTT Technical Research Centre of Finland, Papermaking processes, P.O. Box 1603, FI-40101 JYVÄSKYLÄ, Finland

3.8.1 Background

In paper machine after the wire section the web is wet and weak. In spite of that it is subject to considerable dynamic stresses due to wet pressing, web transfer and drying. As dryness increases also the temperature, structure and mechanical properties of the web are changed. Main changes are related to the reduction of water. Water is located inside the fibre walls and in the pores between fibres. The amount of water contributes to the forces affecting between and within fibres. The properties of wet web are assumed to be affected by the properties of fibres, the interaction forces between fibres and the properties of water used in furnish preparation. Fines have been found to have a considerable effect on mechanical and optical properties of dry paper [1]. It is thus reasonable to expect that fines also modify the behaviour of wet fibre network.

In papermaking and converting processes paper is subject also to stresses in out-of plane direction. Typically wet pressing, size pressing, calendering, reeling, winding and printing operations cause considerable dynamic out-of-plane stresses and deformations in paper. Theses processes are dynamic and so the testing method must take place under dynamic conditions. It is important to understand the resulting thickness change, the contact area between paper and the cylinder surface and the final irreversible deformation and how they depend on the shape and extent of the press pulse, and on the temperature – humidity conditions. Paper structure is one factor in determining the compressive deformation of paper. Paper structure is changed by the raw material composition and wet stretching/drying history and material distribution in z-direction.

3.8.2 Objectives

3.8.2.1 In-plane rheology of wet paper

The main objective in this experimental subproject was to determine the time and temperature dependent properties of consolidating, wet fibre network and their connection to the geometrical and surface chemical properties of fibre furnish, and to the properties of water locating within and between fibres.

The study was divided to three main phases:

- to determine the role of chemical and mechanical pulp fines and fibres on the properties of wet fibre network.
- to determine the possibilities of using suitable dry strength chemicals for improving the wet web strength and affect its rheology.
- to make a check-out how the properties of white water and the chemicals it contains affect the rheology of the wet web.

3.8.2.2 Rheological properties in out-of-plane direction

In this experimental part the z-directional deformation behaviour of fibre networks under varying compression conditions (temperature- moisture, time and strain rate) is studied. The main objective is to find the connection between deformation behaviour, z-directional structure and the stresses that the wet web has been subject to during drying and wet pressing

The objective was to determine the basic rheological characteristics of paper structure under compressive stresses during short time scales. First task was to modify and tune the dynamic compression tester for different dynamic loading modes under wider temperature/moisture conditions and determine the key parameters.

3.8.3 In-plane rheology

3.8.3.1 Effects of furnish composition on mechanical properties of wet web

Abstract

Fines are known to have significant effect on mechanical properties of dry paper. There is much less information of their effect on wet web properties, and especially on its dynamic strength and relaxation characteristics. Additionally, the relative importance of fines fraction when combined with different fibre fractions is also unknown. In this study fines from mechanical and chemical pulps were added to long fibre fractions of mechanical and chemical pulps. The dynamic tensile and relaxation properties were measured with a special test rig using strain rate of 1 m/s.

The results showed that both chemical and mechanical pulp fines significantly consolidate the wet web. The pure long fibre fraction of chemical pulp gave significantly higher tensile strength and tension after relaxation than TMP fibre fraction. The addition

of chemical pulp fines to fibre fractions of mechanical and chemical pulps improved wet web tensile strength (at specified dryness) significantly more than addition of TMP fines. While tensile strength was strongly dependent on the quality of fines, the residual tension was mainly determined by the amount of fines. Chemical pulp fines added to TMP fibre fraction gave remarkably higher residual tension than when added to kraft fibres. This shows the high strength potential of stiff TMP fibres that is realised only when the inter-fibre connections of wet paper are strengthened sufficiently.

Introduction

Fines are flexible, highly swollen and they have great effect on wet end chemistry, water removal and mechanical properties of web [1]. The effect of fines is mainly due to their ability to increase density and bonded area in sheet, but they are known to have only a minor effect in specific bond strength [2]. Wet web is held together by friction forces between fibres and surface tension of water. Fines fill interfibre space during sheet dewatering and increase the amount of fibre-air-water interactions [3]. Even though fines are known to reduce water removal after press section it also known that fines carry nearly twice the amount of water per unit dry mass than fibres [3]. This means that removal of free water in wet web occurs at lower dryness levels.

There are many ways to classify fines. They are traditionally divided into primary and secondary fines. Sometimes fines from broke, fillers etc. are considered as tertiary fines. Especially for chemical pulps, primary fines affect less to tensile properties of dry and wet web and water removal than secondary fines [4].

Another way to divide fines is according to their physical properties, weather they are flake-like or fibrillar. This division is quite rough. For chemical pulps almost all fines are more or less fibrillar. For mechanical pulp the amount of fibrillar fines i.e. fibrillar content is one of the key parameters determining mechanical properties of paper. Fibrillar content is increased with increasing refining energy. This is because flake-like fines are mainly formed from lignin rich middle lamella and primary wall, whereas fibrills are formed mainly when refining secondary wall [5]. Fibrillar fines are known to give high tensile properties for dry and wet web, while flake-like fines give high light scattering values. Sheets made from chemical pulp fines (mainly fibrillar fines) give high density to sheet, typically between 1100–1200 kg/m^3 while TMP fines gives density of 450–500 kg/m^3.

The effect of fines on dry paper mechanical properties is well known. There is less information is about their effect on wet web dynamic tensile and relaxation properties.

Experimental

Pulps and fractionation

The pulps used in the experiment were bleached softwood kraft pulp and TMP pulp, both pulps from Finland. The bleached kraft pulp was beaten in Valley beater to 500 CSF (25 SR). After beating the pulp was fractionated. The long fibre fractions were separated with Bauer McNett apparatus (R16 + R25). Fines were separated from the pulps manually using a 200 mesh screen.

Handsheets

Handsheets of 60 g/m^2 were formed using white water circulation. Sheets were formed according to SCAN-standard, except the wet sheets for strength and relaxation testing were pressed on two different pressure levels (50 kPa and 350 kPa) in order to reach two different dry solids content levels. Wet samples were stored at +7 °C temperature. From wet and dry handsheets, samples having length of 100 mm were prepared. Dry samples having width of 15 mm and wet samples having width of 20 mm were used in this study.

Results

Sheet density was strongly affected by the type of fibres and fines as can be seen in Figure 87. Density of handsheets made from kraft pulp long fibre fractions were 570 kg/m^3 and 290 kg/m^3 for TMP long fibre fraction. The addition of kraft fines to TMP and kraft fibres reduced the difference in density values. The addition of kraft fines into TMP long fibre fraction increased density significantly more than the addition of TMP fines. This shows the high capacity of kraft fines to increase the cohesion forces in wet paper and densify the sheet. By adding 20% TMP fines to TMP long fibres only a minor change took place in density. The density level of the blend of TMP Fines and fibers was significantly lower than that of unfractioned TMP pulp. This means that middle fraction of TMP pulp plays an essential role in consolidation.

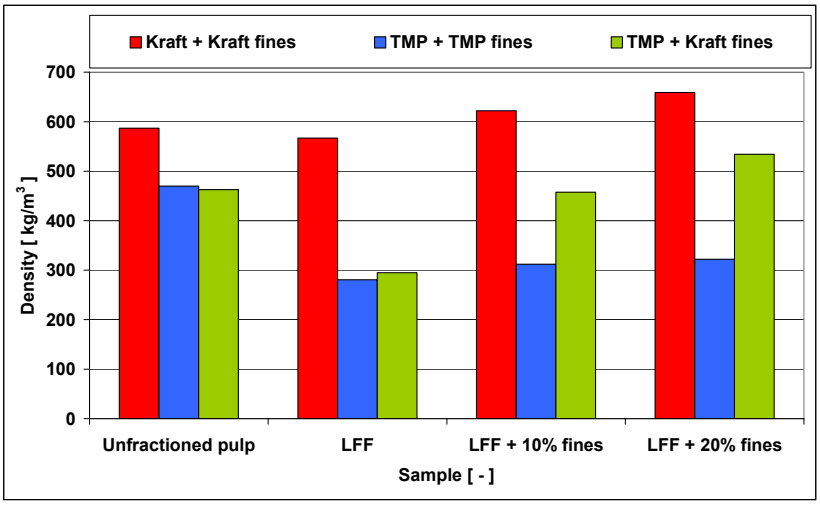

Figure 87. Effect of TMP and kraft fines on the density of kraft and TMP handsheets.

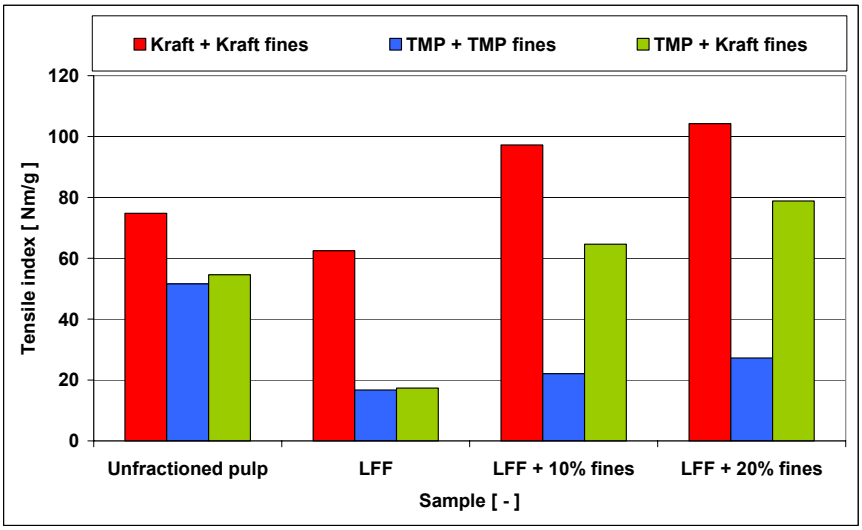

Figure 88. The effect of TMP and kraft fibres and fines on the tensile index of handsheets.

Figure 88 shows the effect of different fines and fibres on tensile index of handsheets. Tensile index of unfractioned kraft pulp was 75 Nm/g while the tensile indexes of unfractioned TMP pulps were 51 and 53 N m/g. The aim was to use TMP at same tensile index level. This carried of well. Handsheets made from TMP and kraft long fibres gave tensile index values of 17 Nm/g and 63 Nm/g respectively. These results showed that for TMP the middle fraction and fines played an essential role in strengthening the dry paper, while the tensile index of kraft was strongly determined by long fibre fraction. When fines were increased into long fibre fractions, the kraft fines increased significantly more tensile index for TMP long fibres than TMP fines did. Increase of 20% kraft fines content in TMP long fibre fraction decreased significantly the difference between the gap to kraft long fibre based pulp. TMP long fibres and the pulp added with fines increased relatively more density than tensile index (compare to Fig. 87).

The effect of TMP and kraft fibres and fines on strain at break was similar to density as Fig. 89 shows. It become clear that for TMP middle fraction has a great effect on stress-strain properties, whereas fines and long fibres determines mainly the mechanical properties of dry woodfree papers. Kraft fines increased strain at break significantly more than TMP fines.

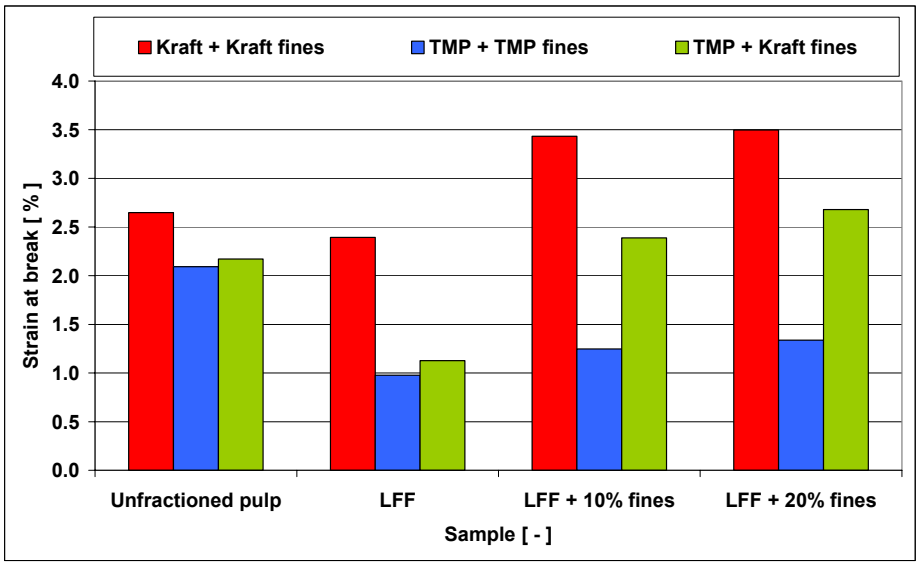

Figure 89. The effect of TMP and kraft fibres and fines on the strain at break of handsheets.

The shrinkage potential of handsheets was measured as the change of circumference while they were dried freely after 350 kPa wet pressing (Fig. 90). Shrinkage potential is affected by the shrinking force of network which is greatly related to bonding and the axial stiffness of network that prevents the transformation of web. Handsheets made from stiff TMP long fibre fraction had shrinkage value in average 0.55% while it was 2.1% for handsheets made from kraft long fibre fraction. This could partly be explained by the fact that chemical pulp long fibres are more swollen and they have lower axial stiffness. Addition of kraft fines increased shrinkage significantly more than increase of TMP fines into TMP long fibres. When reflecting the results as a function of density (Figure 91), it became clear that the increase of density affects more to the shrinkage of kraft paper than paper made from TMP long fibres. This also indicated that axial stiffness of TMP long fibres prevents the web from shrinking more than kraft long fibres.

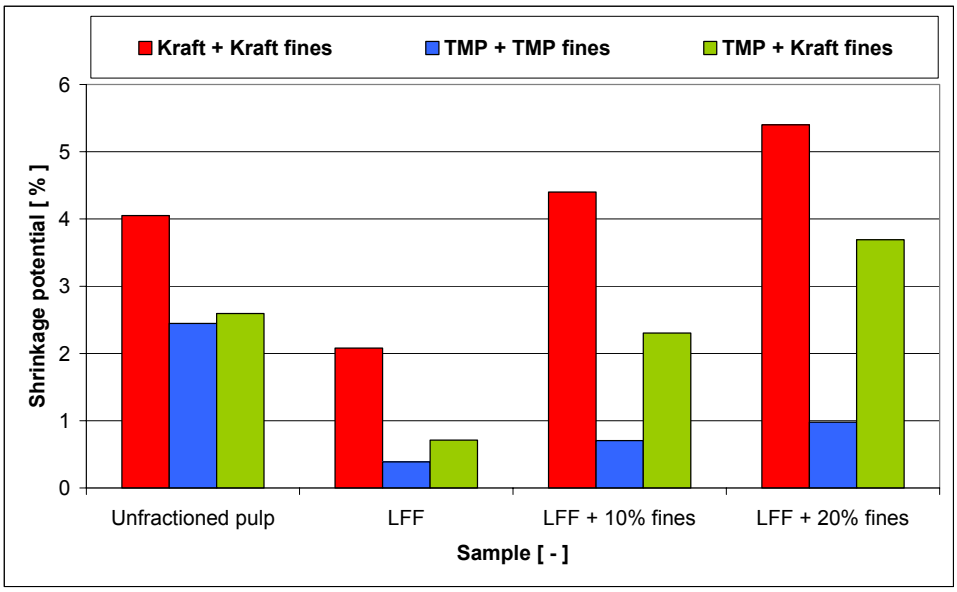

Figure 90. The effect of TMP and kraft fibres and fines on the shrinkage potential of handsheets.

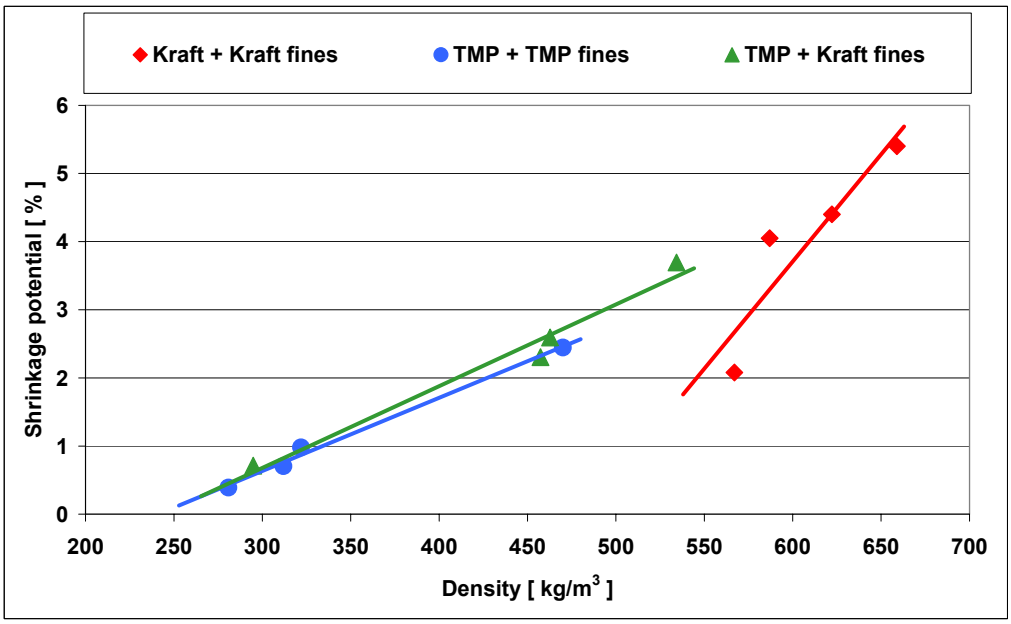

Figure 91. The effect of TMP and kraft fibres and fines on the strain at break of handsheets as a function of density.

The mechanical properties of wet samples are presented here as a function of dry solids content. Tensile and relaxation properties are known to have strong dependence on dry solids content between dry solids contents 30–90% [1, 2, 3]. Thus, wet paper properties in this chapter are presented with exponential or power fit to describe effect of dry solids content.

The effect of kraft and TMP fines on TMP long fibres on initial wet web tensile strength is presented in Fig. 92. Addition of kraft pulp fines increased clearly more the wet web tensile strength than addition of TMP fines did. This can be explained by the fact that kraft fines had significantly higher surface area than TMP fines in average. Surprisingly, addition TMP fines had only a minor effect on dryness after wet pressing, while addition of kraft fines decreased dryness remarkably. Unfractioned TMP pulp had significantly higher wet web tensile strength than TMP long fibres with fines. Unfractioned pulp had also significantly lower dryness after wet pressing. The tensile strength of wet samples (dry solids content 50%) was approximately 10% of the strength of dry paper.

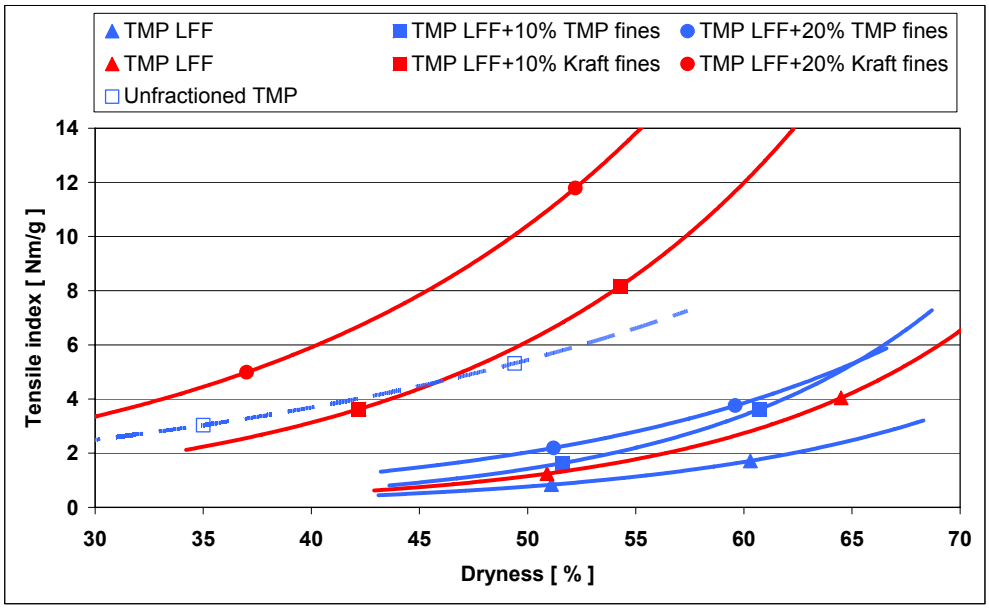

Figure 92. The effect of kraft and TMP fines on TMP long fibres on initial wet web tensile strength.

The effect of kraft fines on TMP and kraft long fibres on initial wet web tensile strength is presented in Fig. 93. Flexible kraft long fibres gave higher wet web tensile strength than stiff TMP fibres. The addition of kraft fines decreased dry solids content after wet pressing for both pulps, but at the same time the tensile strength was increased. When comparing the results in fixed dryness it seems that by adding 20% of fines content, the wet web strength is almost equal with both long fibre types.

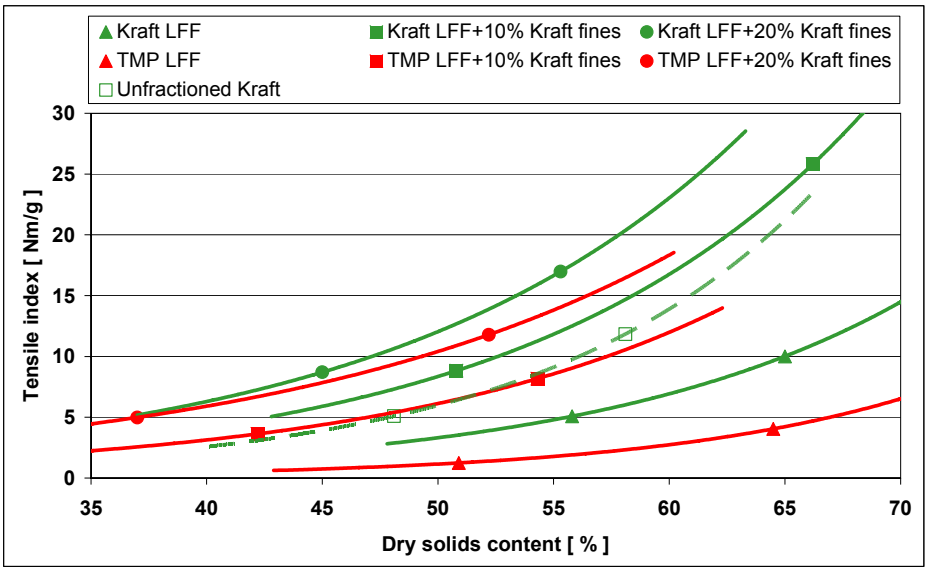

Figure 93. The effect of kraft fines on TMP and kraft long fibres on initial wet web tensile strength.

Fig. 94 shows the effect of TMP and kraft fines and TMP long fibres on dynamic modulus of wet samples. There was no significant difference in dynamic modules of TMP and kraft long fibres. The adding of TMP fines on TMP long fibres lowered slightly dynamic modulus of samples. The addition of kraft fines increased dynamic modulus significantly at fixed dryness. Dynamic modulus is greatly dryness dependent. At constant dryness the elastic modulus of unfractioned TMP was twice as high as for TMP long fibres added with 20% fines. But when comparing the absolute values after wet pressing the results are vice versa.

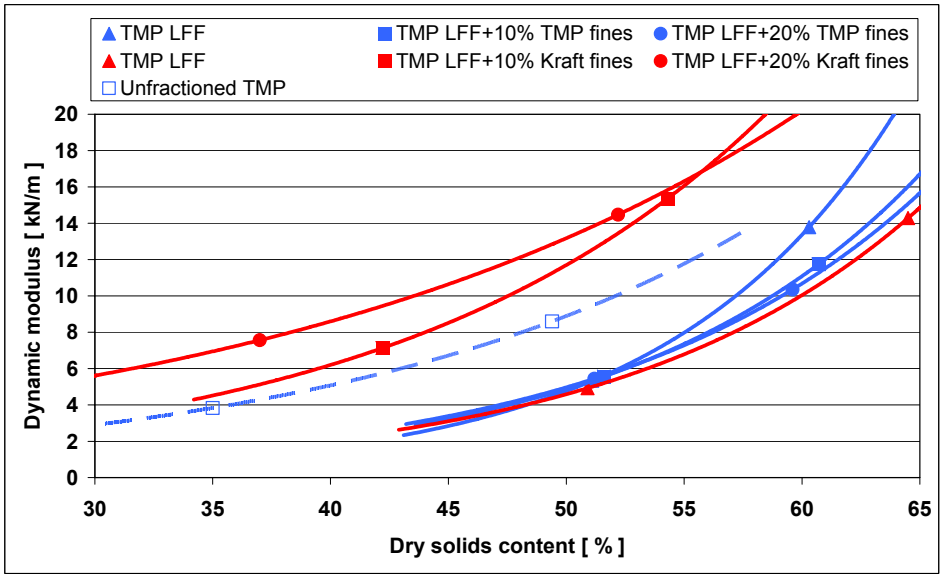

Figure 94. The effect of TMP and kraft fines and TMP long fibres on dynamic modulus of wet samples.

Fig. 95 shows the effect of kraft fines and long fibres of kraft and TMP long fibres on dynamic modulus of wet samples. The dynamic modulus of wet samples is more dependent of fibre-fibre contacts than fibre properties. The dynamic modulus is greatly affected by amount of fines, but there was only a minor difference between samples having different long fibre types. When adding kraft fines the dynamic modulus is increased.

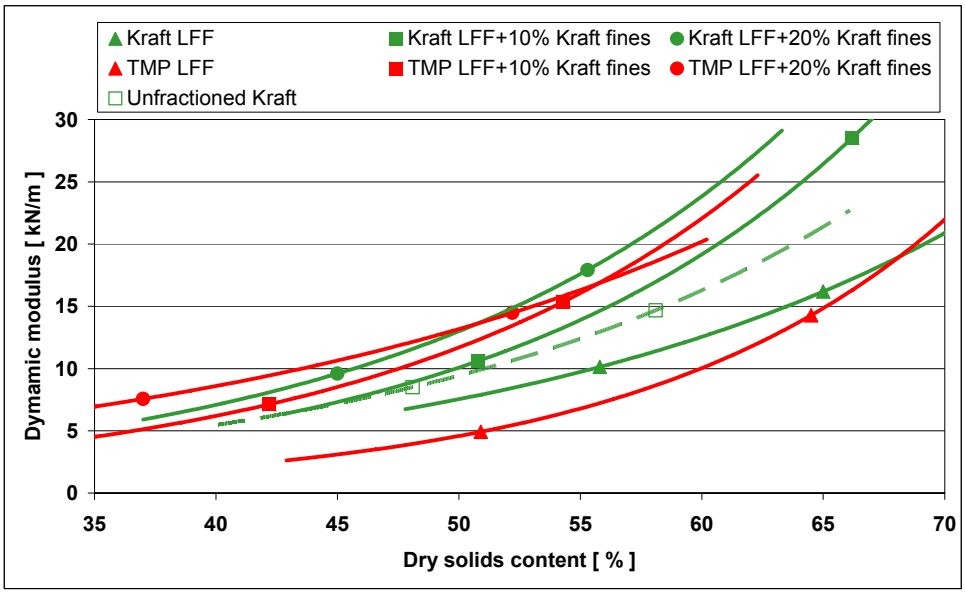

Figure 95. The effect of kraft fines and long fibres of kraft and TMP long fibres on dynamic modulus of wet samples.

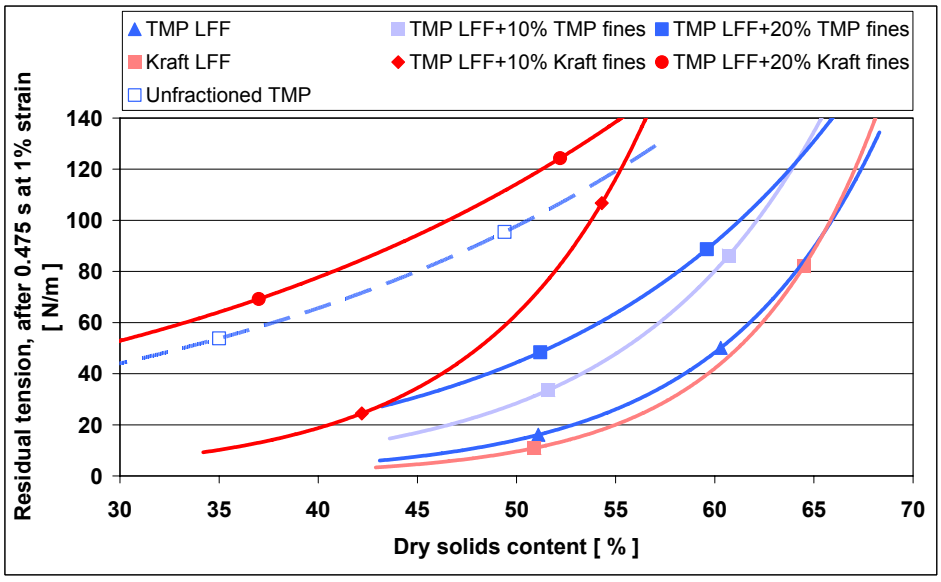

Figure 96. Figure effect of TMP and kraft fines and TMP long fibres on residual tension of wet samples.

Fig. 96 shows the effect of TMP and kraft fines and TMP long fibres on residual tension of wet samples. Addition of kraft and TMP fines into TMP long fibres increased residual tension considerably at a constant dryness level. Adding of kraft fines on TMP long fibres had bigger effect on residual tension than adding of TMP fines, especially when comparing the results at constant dry solids content level. Unfractionated TMP had two times higher residual tension than TMP long fibres with 20% fines when the comparison is made at constant dryness level. This shows that the middle fraction and the synergy of fractions had great significance on wet web relaxation properties.

Fig. 97 shows that residual tension was not only strongly fines dependent, but also greatly dependent on the types of long fibres. At constant drybess of 50%, the addition of 20% kraft fines into TMP long fibres gave residual tension value of 110 N/m, while it was only 60 N/m when adding 20% of kraft fines into kraft long fibres. The addition of fines content from 10% to 20% on kraft based pulp increased residual tension only by approximately 10 N/m at fixed dryness level of 50%.

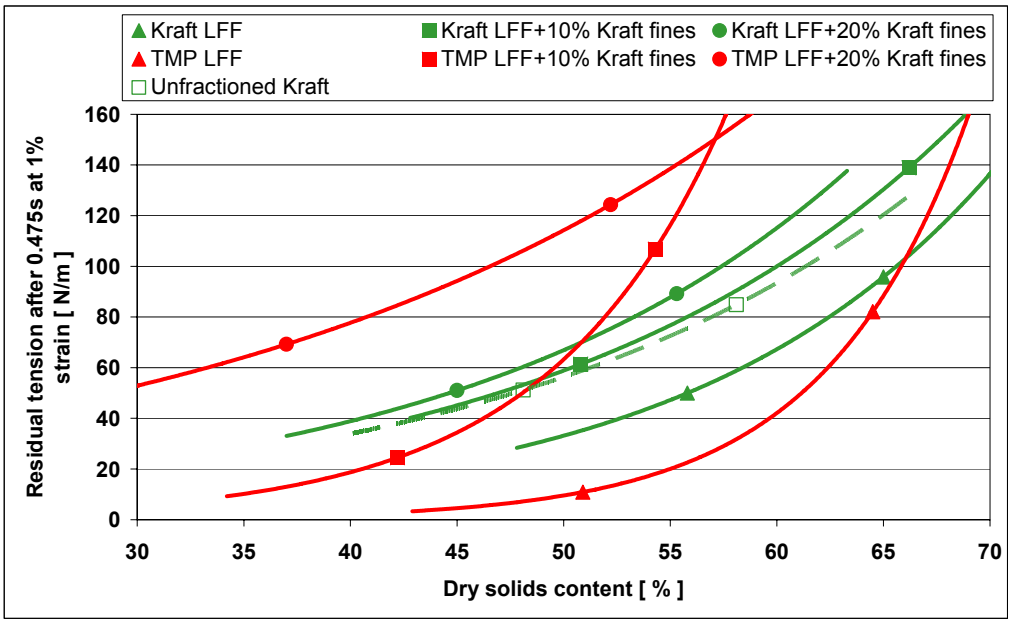

Figure 97. The effect of kraft fines and long fibres of kraft and TMP long fibres on residual tension of wet samples.

The relative amount of relaxation can be calculated with Equation (79).

$$R = \frac{T_{\max} - T_{res}}{T_{\max}}, \tag{79}$$

where R is the relative amount of relaxation, T_{max} is maximum tension and T_{res} is residual tension after 0,475 seconds.

The bigger the amount of relaxation, the more tension is lost during relaxation. The smaller the relative amount of relaxation, the smaller is the loss of tension after straining. Relative amount of relaxation is useful when pulp relaxation tendency is evaluated. Figure 98 shows the effect of TMP and kraft fines and TMP long fibres on residual tension of wet samples. The R-value of TMP long fibre based pulps is strongly dependent on dry solids content and the amount of fines. At constant dryness the quality of fines (at 10% or 20% fines level) had no significant effect on the amount of relaxation.

Figure 99 shows that the R-value of kraft long fibres based pulps was not as strongly dryness or fines dependent than TMP based pulps. At 50% dry solids content the R-value of unfractioned pulps were similar. Samples made from pure TMP and kraft long fibres lost approximately 80% and 60% of tension respectively. This result showed that the R-value is strongly dependent on fibre-fibre interactions.

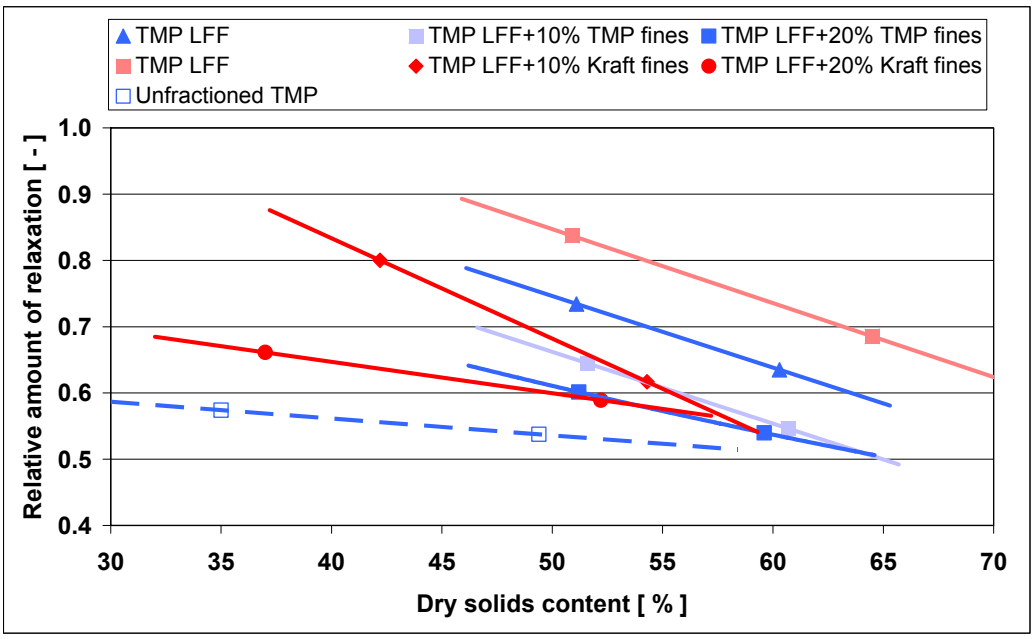

Figure 98. Figure effect of TMP and kraft fines and TMP long fibres on relative amount of relaxation of wet samples.

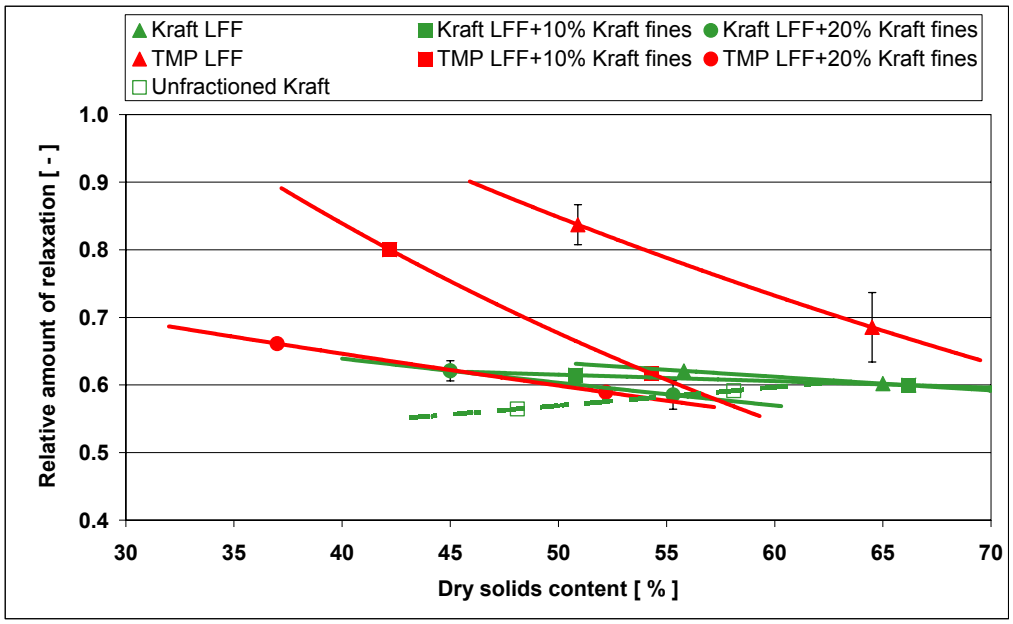

Figure 99. The effect of kraft fines and long fibres of kraft and TMP long fibres on relative amount of relaxation of wet samples.

Conclusions

Tensile and relaxation properties of dry and wet web are strongly dependent on the amount and quality of fines material.

Addition of kraft fines increased tensile strength and stiffness of wet and dry web significantly more than the addition of TMP fines.

TMP fines had no significant effect on water removal rate while kraft fines slowed the water removal rate significantly.

Fibre-fibre interactions and axial stiffness of fibres (long fibre type) seemed to determine the wet web stiffness and drying shrinkage potential.

Addition of TMP fines gave relatively higher improvements on residual tension than on tensile strength of wet web.

The relative amount of relaxation was found to be mainly depend on the amount and quality of fines and dryness. The dependence was stronger with TMP based pulps than with kraft based pulps.

As the fines strengthens the interaction between fibres, also the fiber properties become important. Mechanical pulp fibres offer higher potential for improving the residual tension of wet web whereas the wet web strength is better with kraft fibers.

References

[1] Peterson, D., Zhang, S., Qi, J. and Cameron, J. An Effective Method to Produce High Quality Fiber Fines. *Progress in Paper Recycling,* 10(2001)3.

[2] Retulainen, E., Luukko, K., Nieminen K., Pere, J., Laine J. and Paulapuro, H. Papermaking quality of fines from different pulps – the effect of size, shape and chemical composition. 55th Appita Annual Conference, Hobart, Australia 30.4.–2.5.2001.

[3] Seth, R.S. The measurement and significance of fines. *Pulp & Paper Canada* 104:2(2003)3.

[4] Corson, S.R. Influence of fibre and fines fractions on thermomechanical pulp properties. Doctoral Thesis. Trondheim, Norway, 1979.

[5] Luukko, K. Characterization and properties of Mechanical Pulp Fines. Doctoral Thesis. Espoo, Finland, 1999.

[6] Kurki, M., Kekko, P., Kouko, J. and Saari, T. Laboratory scale measurement procedure of paper machine wet web runnability, Part 1. *Paper and Timber,* 86(4) 2004, pp. 256–262.

[7] Brecht, W. and Erfurt, H. Wet-Web strength of Mechanical and Chemical Pulps of Different Form Composition. *Tappi,* 12(12) December 1959, pp. 959–968.

[8] Shallhorn, P.M. Effect of Moisture Content on Wet-Web Tensile Properties. *Journal of Pulp and Paper Science*, 28(11) November 2002, pp. 384–387.

3.8.3.2 Effect of white water properties on mechanical properties of wet web

Introduction

Paper machine production speed is often limited by open draws, especially in the press-to-dryer transfer area. At this location the dry solids content of wet web varies typically between 40–50%, which means that the tensile strength is only 10–15% of the strength of dry paper. For wet web (dryness below 60%) surface tension is assumed to play an essential role in holding the web together. While dry solids content increases the importance of surface tension decreases [1].

In order to maintain a stable run through the dryer section a certain tension is needed in the web. Due to the low tensile stiffness of wet web a considerable amount of strain is needed to create sufficient tension. However, more than 50% of this tension is lost in 0.5 seconds due to relaxation. The remaining tension, the residual tension after relaxation, is a parameter found to predict the wet web runnability in dryer section [2].

In this paper, the objective was to identify the effect of different dissolved and colloidal substances in white water, on surface tension and especially on wet web rheological properties. Since surface tension is known to contribute to inter-fibre bonding [3], a special attention was given to examine the correlation between surface tension and tensile properties of dry and wet paper.

Experimental

Handsheets

Handsheets of 60 g/m^2 were formed using white water circulation from bleached pine softwood kraft pulp beaten to 500 CSF in a Valley beater. Sheets were formed according to SCAN-standard, exept the wet sheets for strength and relaxation testing were pressed on two different excess pressure levels (50 kPa and 350 kPa) in order to reach two different dry solids content levels. Wet samples were stored at +7 °C temperature. The drainage time of sheets were measured during the moulding. The adding of different substances was made during the forming of sheets.

Samples:

Deionized water

TMP filtrate after peroxide bleaching (UPM Kymmene Jämsänkoski mills), pulp diluted in deionized water in 1:6 ratio

100 ppm surfactant Liptol S-100, (Brenntag Nordic Oy)

100 ppm oleic acid ($C_{18}H_{34}O_2$) Sigma-Aldrich 75093

100 ppm defoamer De-Airex 7061, (Hercules).

Water surface tension measurement

The measurements were made by KRÜSS K9 -surface tension measurement device. The method utilizes the principle of the du Noüy ring method, measuring the necessary force to pull a platinum ring a precisely known dimension free from the surface film of the water sample. Surface tension was measured from white water after 15 handsheets were formed. The possible solid particles were not removed from the white water in order to simulate the actual situation in forming.

Fast tensile and relaxation measurements

Dynamic tensile strength and relaxation properties of samples were measured with "IMPACT", fast tensile strength testing rig. The basic idea was to create a sudden strain

increase to paper sample. IMPACT created an average velocity of 1 m/s (while in standard tensile strength test the velocity is 22 mm/min = 0.00037 m/s). In this experiment paper sample having length of 100 mm were used, meaning that the strain velocity was 1000%/s.

The relaxation properties (maximum tension and residual tension) were measured at 1% strain for dry samples and at 1% and 2% strains for wet samples. The relaxation time used for dry samples was 9.5 s. For wet samples the relaxation time used was 0.475 s. The dynamic strength, breaking strain and dynamic elastic modulus were determined while straining samples to the breakpoint. Fast tensile test rig IMPACT is presented in Fig. 100.

Figure 100. Fast tensile test rig IMPACT.

Results

The dry solids content, drainage time of sheets and surface tension of white water are presented in Table 9.

Table 9. The dry solids content, drainage time of handsheets and surface tension of white water.

	Added chemical [ppm]	Surface tension [mN/m]	Drainage time [s]	Dry solids content [%] 50 kPa	350 kPa	Dry	Grammage [g/m^2]
Deionized water	-	54	4.5	48	62	92	57.8
TMP filtrate	-	44	6.7	53	63	93	58.2
Surfactant	100	42	5.1	58	65	93	63.7
Oleic acid	100	41	5	53	63	93	59.2
Defoamer	100	49	4.5	49	61	93	59.0

The surface tension of deionized water was originally 72 mN/m and it was reduced to 54 mN/m during the white water circulation. The lowering derived from the dissolving substances from bleached pulp. TMP filtrate, surfactant or oleic acid lowered the surface tension further by 10 units or more.

The drainage time of handsheets varied between 4.5–6.7 s. The drainage was slowest when using TMP filtrate which is a caused by the fines particles. No significant correlation between the drainage time and surface tension was found.

The dry solids content of 50 kPa pressed handsheets varied considerably. While making the sheets with white water containing TMP-filtrate or adding, surfactant or oleic acid the dry solids content increased compared to deionized water. The increase was greatest with surfactant. It is evident that the decrement of surface tension increases the water removal of sheets. It is also known that different contaminants affect the hydrophilicity / hydrophobicity of fibre surfaces at different ways. This might explain why the surfactant gives higher dryness than oleic acid. The differences between dry solids content levels of different trial points after 50 kPa wet pressing seemed to be larger than after 350 kPa pressing.

The tensile strength of dry samples is presented in Fig. 101. The tensile strength is greatest with samples made with deionized water. While forming the handsheets with water from TMP mill or with white water containing surfactant the tensile strength was decreased 12–17%. Addition of oleic acid or defoamer had only a minor effect on tensile strength (less than 5%). Lowered surface tension decreased the tensile strength of dry paper. The results show that different substances were inhibiting the forming of bonds. The correlation between surface tension and tensile strength of dry samples is presented in Fig. 102.

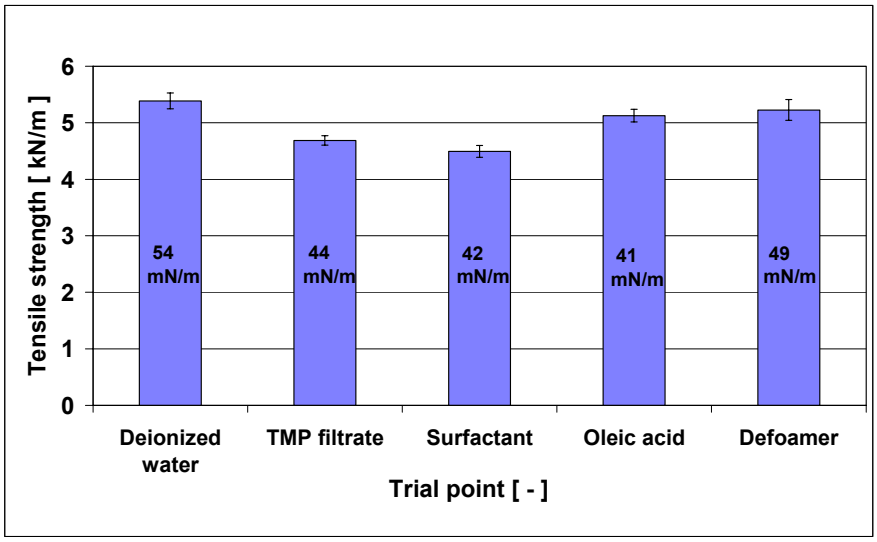

Figure 101. The dynamical tensile strength of dry samples. The surface tension of white water after forming of 15 balance handsheets is marked on the bars.

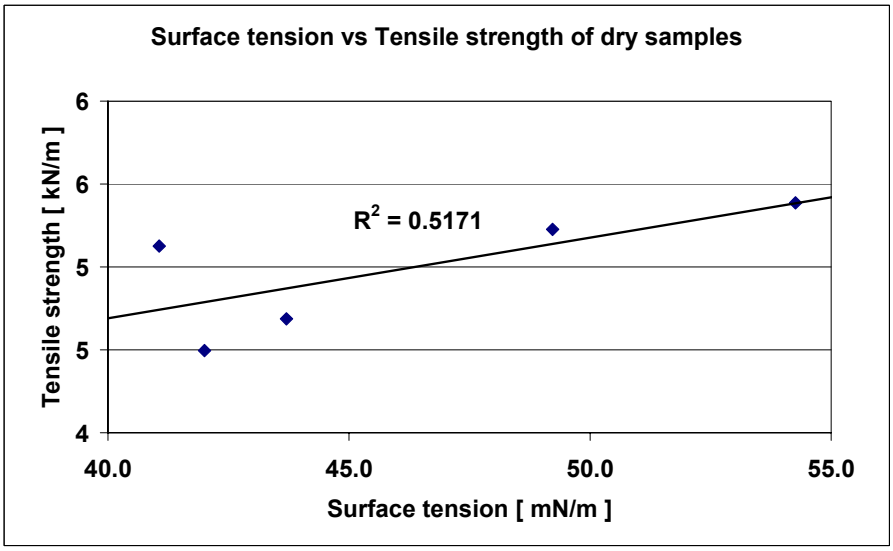

Figure 102. The correlation between surface tension and tensile strength of dry samples.

The tensile strength of wet samples refers to the maximum tension that a wet web can bear without breaking. The wet tensile strength has been used as an indicator of runnability and maximum production speed of PM in several publications [4, 5]. The tensile strength of wet samples as a function of dry solids content is presented in Figure 103.

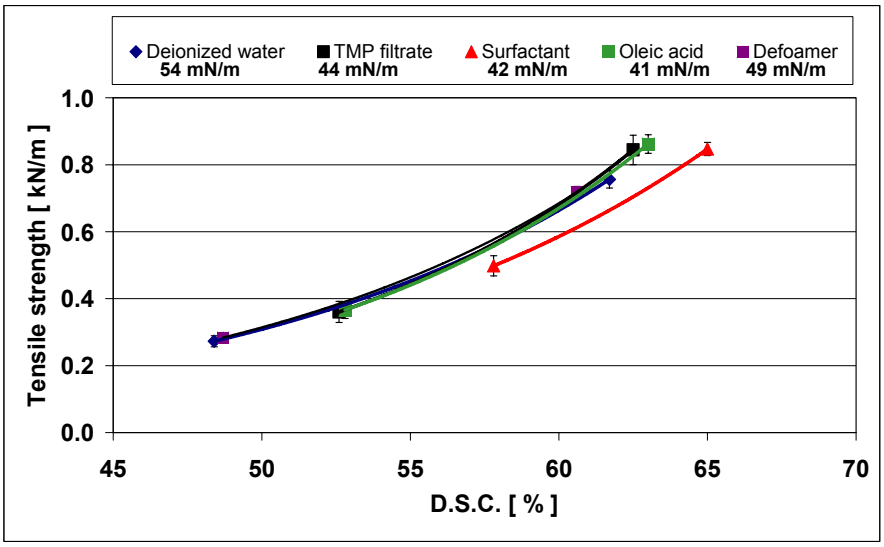

Figure 103. The tensile strength of wet samples as a function of dry solids content.

It is well known that tensile strength of wet paper increases exponentially when the dryness of web increases. Therefore an exponential curve has been fitted to the data. At constant dryness level, the surfactant point has the lowest tensile strength, while other trial points seem to be at quite similar level (in order to approximate the tensile properties and the performance of wet web at paper machine, especially in open draws, it is essential to take into account the dry solids content level due to pressing). The increment of dry solids content after adding surfactant was remarkable. In comparison to handsheet made from deionized water, the increase of dryness after 50 kPa wet pressing was approximately 10% and after 350 kPa approximately 3%. Therefore this trial point gave the highest tensile strength values on a constant wet pressure level. The lowest tensile strength values at constant pressure were gained by using deionized water or by adding defoamer. These results indicate that lowering surface tension may improve give higher tensile strength of wet paper after the press section at PM (where the dryness varies typically between 40–50%). The correlation between the surface tension and the average dry solids content of wet pressed handsheets is presented in Fig. 104.

In open draw tension is created to the web by the elongation caused by speed difference of press-section and the beginning of dryer section. This tension relaxes rapidly due to time-dependent viscoplastic properties of paper. In order to prevent fluttering, wrinkling and bagging after the open draw a certain web tension is needed. A higher tension is needed with increased PM production speed mainly due to increasing of centrifugal and dynamic pressure forces [6]. The residual tension of press dry hand sheets measured by IMPACT at two different straining levels (1% and 2%) is presented in Fig. 105.

On fixed dryness level the trial points made with white water containing deionized water and added defoamer gave the highest residual tension values and highest surface

tension. A 100 ppm addition of surfactant into water lowered considerably residual tension at a constant dryness level, but greatly enhanced water removal after wet pressing. The absolute values after wet pressing (especially after 50 kPa pressure) are due to good water removal significantly higher than for trial points with high surface tension. When comparing the values on average dryness level, surfactant gave more than 20% higher residual tension values in comparison to trial point made from deionized water. Increasing the amount of straining from 1% to 2% increased the residual tension on average by 75%. This means than in order to reach similar tension to with lower dryness nearly 1.3 times greater strain is needed. High strain rate increases porosity of web and lowers the strain at break of dry paper, which is needed especially for good runnability at the press room. The correlation between surface tension and residual tension on a constant dryness level (55%) is presented in Fig. 106.

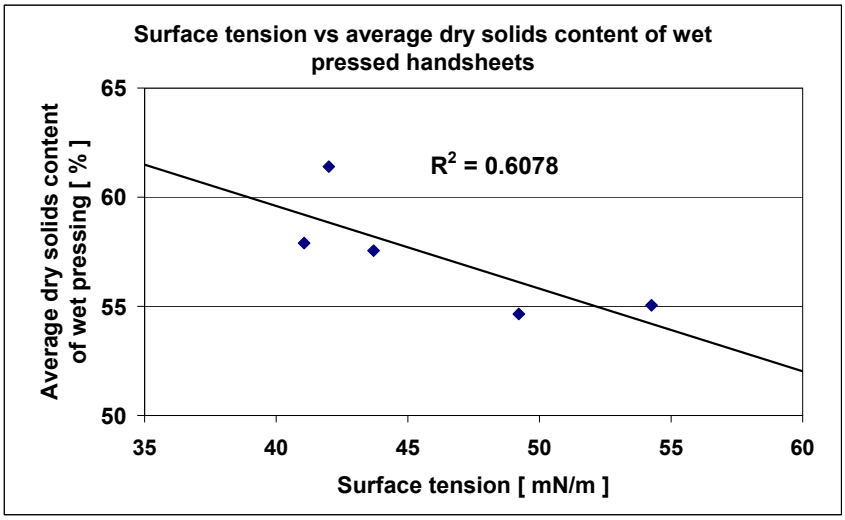

Figure 104. The correlation between the average dry solids content of wet pressed handsheets.

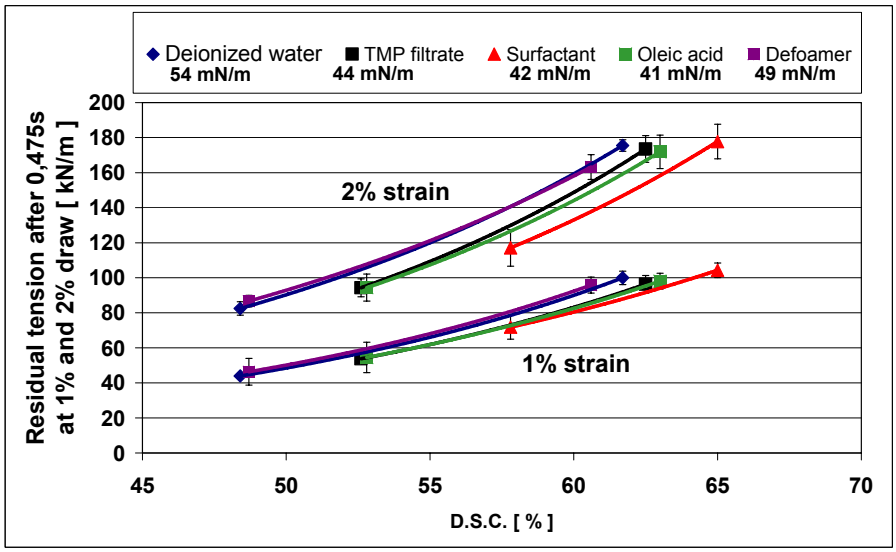

Figure 105. Residual tension of press dried handsheets at two different straining levels.

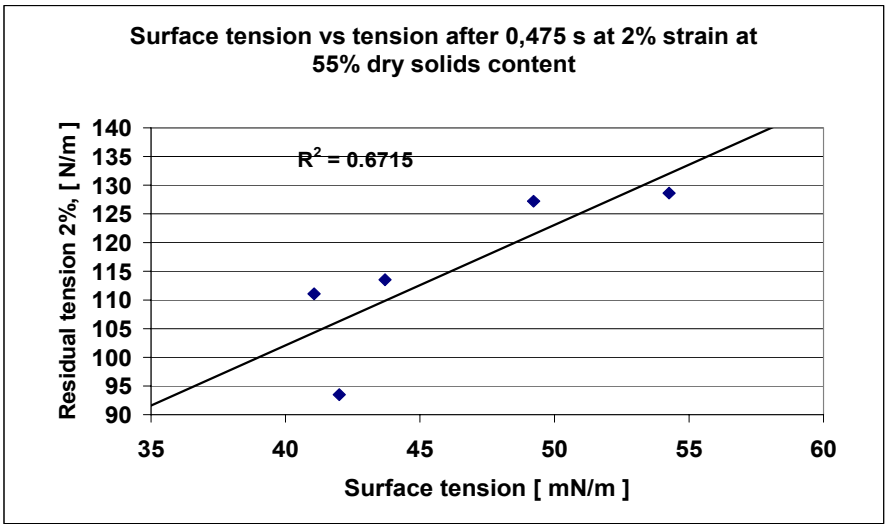

Figure 106. The correlation between surface tension and residual tension at a constant dryness level of 55%.

Conclusions

The dissolved and colloidal substances present in white water affect the wet web strength extensional stiffness and tension after relaxation i.e. tension holding capacity. This predicts that they also have definite effect on wet web runnability.

The decrease of surface tension at certain solids content was accompanied by a decrease of tensile strength of dry paper and reduction in wet web strength, tensile stiffness and residual tension.

Reduced surface tension, however, could also result in increased solids content after wet pressing which could override the negative effect on wet web strength.

Surface tension of white water is one factor contributing to the wet web strength and relaxation but does not alone explain the results.

Also the absorption of certain white water components onto fiber surfaces and desorption from fibre surfaces affects the strength properties of wet and dry paper.

References

[1] Lyne, L.M. and Galley, W. Measurement of wet web strength. *Tappi* 12(1954)37, pp. 694–704.

[2] Kurki, M., Kouko, J., Kekko, P. and Saari, T. Laboratory scale measurement procedure of paper machine wet web runnability: Part 1. *Paperi ja Puu* 4(2004), pp. 256–262.

[3] Kokko, S., Niinimäki, J., Zabihian, M. and Sundberg, A. Effects of white water treatment on the paper properties of mechanical pulp – A laboratory study. *Nordic pulp and paper research journal* 3(2004)19, pp. 386–391.

[4] Jantunen, J. Runnability and mechancial properties of paper. Helsinki 1989, INSKO, Publication 93–89, Fiber and paper physics. 30 p. (In Finnish.)

[5] Wahren, D. Wet webs in open draws. *Tappi* 3(1981)64, pp. 694–704.

[6] Kurki, M., Pakarinen, P., Juppi, K. and Martikainen, P. Web handling, In: Papermaking. Part 2. Drying, Ed. by Karlsson, M. Papermaking science and technology, Jyväskylä, 2000. Pp. 374–431.

3.8.3.3 Effect of dry strength additives on the rheology of wet web

Introduction and objectives

There is very little information how dry strength additives affect the rheology of wet paper. Some literature data indicate that the wet web strength is reduced by adding conventional starch, and improved by some modified starches and chitosan /1–4/. But how they affect the tension holding capability (residual tension) of wet web under dynamic conditions is not known.

The objective of this experimental part was to find out how a conventional cationic starch and different starch modifications affect the wet and dry paper sheet and especially how these chemicals contribute to runnability factors. Previous studies have shown that modified starch improves the strength of dry paper but how they affect the wet web strength is hardly analyzed.

The secondary objective was to find out the possibilities to improve rheological properties of paper sheet in laboratory scale by spraying chemicals. In measurements different starch modifications were used as additives and the differences in paper properties were measured. The focus was to investigate if chemicals, which chemical structure includes modified D-glucose particles, were able to build linkages even if the dry content of paper would be under 50%. The rheological properties such as tensile

strength, relaxation, drying stress and potential shrinkage were measured and the results were studied from the runnability point of view. All chemicals were added by spraying, which is quite unusual way to add chemicals and sizing agents, but in this experiment the only way to reach a sufficient retention with nonionic and anionic compounds.

Materials and methods

Pulp and chemicals

Bleached pine kraft pulp (Akipine, Botnia) was beaten to 25 ºSR at HUT with a hollander. Five modified starches were used as additives in this work. Starches were cooked for one hour and diluted to 0,5% consistency before spraying. The experimental starched used were slightly anionic and spray addition was used. The sprayed amount of starch was 1%. In some cases also 2% addition was used, but due to the high amount of water, the amount retained in the sheet could not be controlled. The wet pressing at standard pressure was applied after the spraying.

The following six cases were tested:

REF	reference sheets
CAT	commercial cationic starch (Raibond 15)
EXP1	experimental oxidised starch
EXP2	experimental oxidised starch
DAS1	experimental dialdehyde starch (molecular weight 545 700 g/mol)
DAS2	experimental dialdehyde starch (molecular weight 21 100 g/mol).

Spraying unit

Spraying instrument was functioning with compressed air. Paper sheet was placed on the wire, which area was about 20 × 30 cm. Through the wire, there was aspiration in such a way, that between the sheet and the wire there was vacuum. With help of vacuum it was easier to hold the sheet stable on the wire during spraying operation. On the other hand chemicals were sprayed and thus with help of vacuum it was easier to increase retention of chemicals. The wire and the sheet were on a sledge, which ran with a constant speed through an aerosol spout. Distance between sledge and spout was 40 cm. Standard wet pressing procedure was applied after spraying. The chemical amount was 1%, of which part may have migrated to the blotters during wet pressing.

Figure 107. Spraying equipment.

Drying stress analyser

Drying stress was analyzed with Lloyd LR10k instrument and breadth of paper sheet, which was used in this instrument, was 45 mm. Distance between jaws was 100 mm and the jaws were stationary during measurements. Round the jaws there was a cubicle made of plastic, wherein hot air dried was used to dry the paper sheet. When hot air was bnlown onto paper, the sheet tries to shrink and create a drying stress.

Infra red light streamed through the paper sheet and measured chances in dry content by absorption. Lloyd instrument measured drying stress and information was transferred to computer. During measuring process there was also another computer, which was used. Computer number 2 was connected to the IR-instrument and measured the changes in voltages. With help of voltage levels it was possible to follow changes in dry solids content, because dry content was correlated with voltage levels.

The results were handled with help of computer macro program, which counted the drying stress as a function of dry solids content.

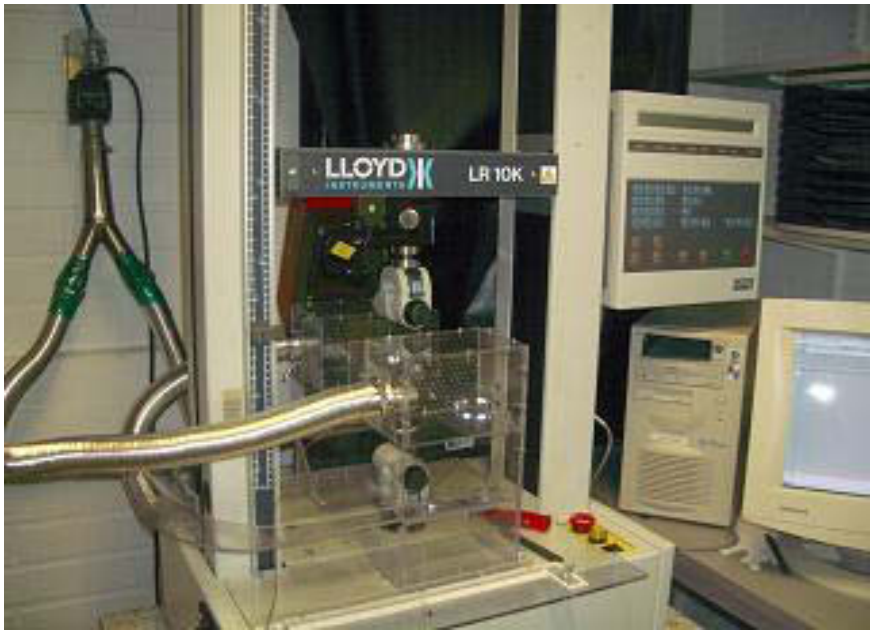

Figure 108. Equipment used in drying stress measurements.

Results

Wet web tensile strength was affected by the added starch. The added amount was 1%. The cationic starch reduced the wet strength, but the EXP1 and DAS2 improved the wet strength (Fig. 109). We can assume that wet strength depends mainly on the forces affecting at the contact points of fibers. The cationic starch, although known to improve the dry strength by increasing the hydrogen bonding between fibers, here seems to reduce the interaction between fibers.

Also the residual tension measurements show similar results as the wet strength (Fig. 110). Cationic starch reduced the residual tension, the EXP1, DAS1 and DAS2 improve the tension. Here the effect is more distinct than with wet tensile strength. When the results are compared at constant dry matter content of 50% the DAS2 increased the residual tension by 30% compared to the reference, and 46% compared to the cationic starch case. The latter is a relevant reference point in the case when dry strength additive is used anyway.

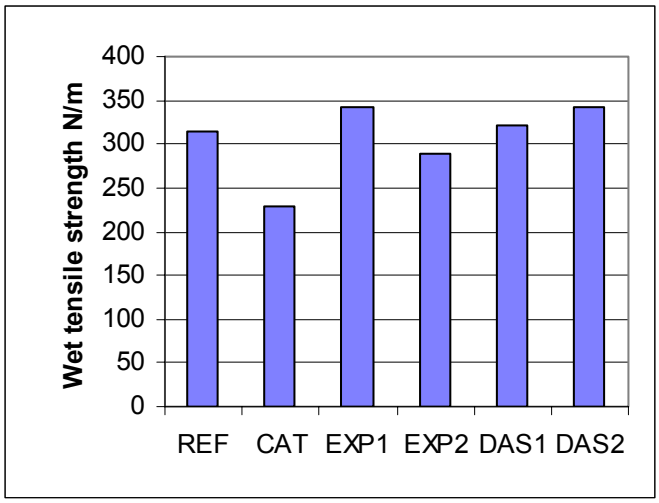

Figure 109. Initial wet strength of handsheets with different starch types.

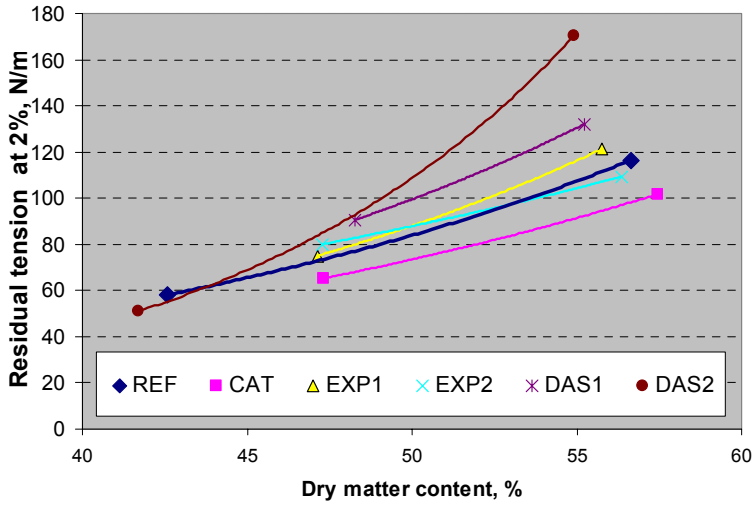

Figure 110. The residual tension at 2% strain after 0.5 s relaxation when different starch types have been sprayed onto the sheet.

The drying stress created during drying was also measured, and the results indicate some differences between starches. Fig. 111 shows that the drying stress is increased at a slower pace when the cationic starch is present than in the case of reference ('no chemicals'). However, when the dry matter content is over 90% the stress is increased faster reaching the same drying stress as the reference. The DAS1 shows a highest drying stress all the time. But the drying stress of DAS2 does not develop as fast as with DAS1 when the dry matter content is over 83%, is gives actually a lower stress that cationic starch.

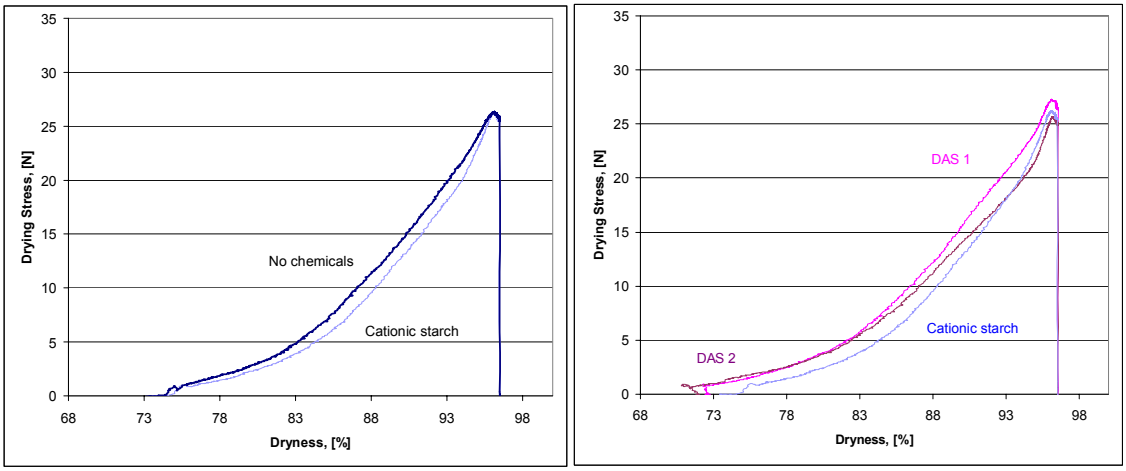

Figure 111. The development of drying stress with reference and cationic starch (left); and dialdehyde starches (right) compared with the cationic starch.

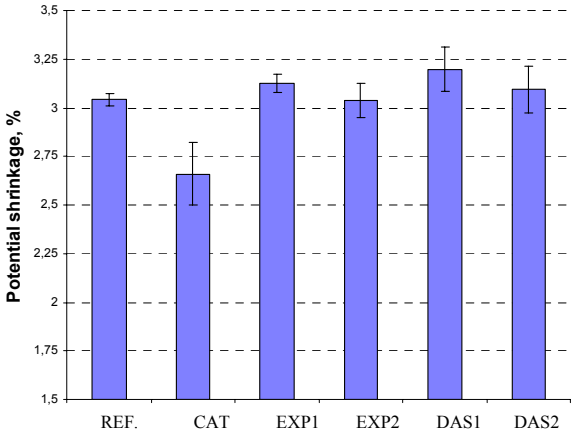

Figure 112. Effect of the added starches on the potential shrinkage (free shrinkage) of the sheets.

Also the potential shrinkage (free shrinkage) of DAS1 is higher that with the reference (Fig. 112). And the lowest shrinkage takes place with cationic starch. Also this result suggest that the cationic starch reduces the drying shrinkage of the web. The shrinkage of fibers is probably not affected by starch but the fiber shrinkage is not transmitted to network shrinkage in the same degree as with other cases. The cationic starch may affect fibre surface properties and reduce the fiber-fiber friction.

The shrinkage tendency and drying stress of the sheet are known to be related to the activation of the fibers to bear load in tensile test. The lower shrinkage and drying stress during the first part of the drying phase result also to a lower tensile stiffness for the cationic starch containing sheet (Fig. 113). The tensile strength on the other hand is not only affected by the load-bearing activity of the structure but also the strength of the

inter-fiber bonds. The all the starches seem to improve the inter-fiber bonding strength that results in higher tensile strength.

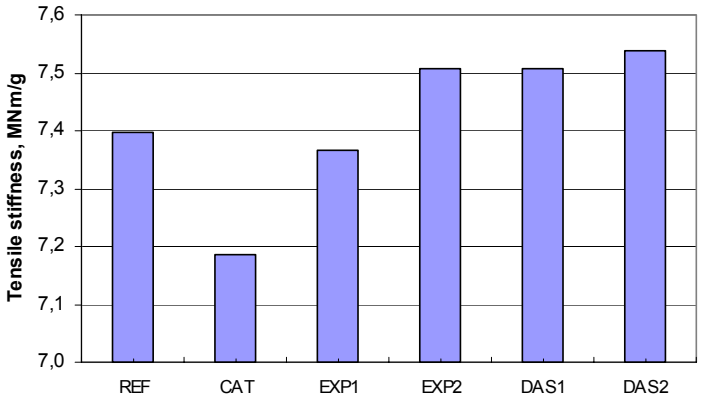

Figure 113. Effect of the added starched on the tensile stiffness of the sheets.

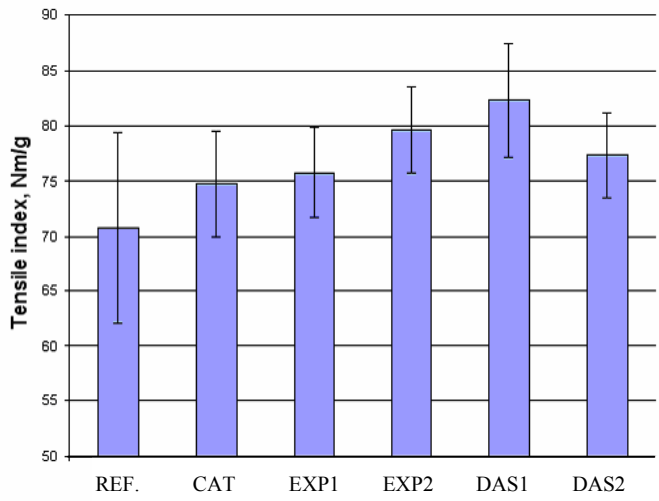

Figure 114. The effect of different starches on the tensile strength.

Conclusions

The effect of starch on the wet web strength, shrinkage, drying stress and strength of dry paper was studied. The conventional cationic starch improves tensile strength of dry paper but reduced tensile stiffness, wet web strength and tension after relaxation. It also reduced the extent of free shrinkage of the sheet. The dialdehyde starches on the other hand improved the wet web strength and tension after relaxation, and additionally gave a good dry strength.

The development of the drying stress indicated that conventional starch does not contribute to drying stress when the web is wet, but it has a strong impact when the web

reaches the final dryness. The dialdehyde starch on the other hand seems to be able to increase the drying stress of wet web. The final stress, however, is not necessary affected. These results suggest that cationic starch reduces the friction or inter fiber contact strength in wet web, but dialdehyde starch is able to form some permanent bonds at rather low solids content.

These results show that the chemical additives can have an important role in the runnability, shrinkage and strength properties of wet and dry paper.

References

[1] Laleg, M., Ono, H., Barbe, MC. and Pikulik, I.I. The effect of starch on properties of groundwood furnishes and paper. *Tappi Papermakers Conference*, Atlanta, April 1990.

[2] Laleg, M. and Pikulik, I.I. Modified starches for increasing paper strength. *CPPA 78th Annual meeting – Technical section*, Montreal, Jan. 1992.

[3] Allan, G.G., Fox, J.R., Crosby, G.D. and Sarkanen, K.V. Chitosan, a mediator for fibre-water interactions in paper. *FPRC Trans. VIth. Fund. Res. Symposium*, Oxford, 1977.

[4] Laleg, M. and Pikulik, I.I. Unconventional strength additives. *Nordic Pulp and Paper Research Journal* 8(1993)1, pp. 41–47.

3.8.4 Out-of-plane rheology

3.8.4.1 The test instrument

A compression tester was used in this sub-study. The instrument is specillay designed and built for short time scale testing of compressive properties of paper. The first target in the out-of-plane direction study was to update the existing compression device. The operation principle of the device is similar to that of typical platen press testers. The material to be examined is placed between two press plates to a specified preload. The compression pulse is applied to the sample and the compressive force and compression of the sample are measured at the same time. With separate climate chamber, the conditions of the test cell area can be adjusted. The tester is computer controlled (for more detailed information on tester, see www.paperrc.com.).

Based on accumulated knowledge of using the device, following improvements were made: redesigning the force measurement, automation of the pre-stress mechanism, enabling closed-loop feedback system for force signal and checking out the operation of the device after renewals. Benefit, cost and future needs were considered when making decisions regarding update.

The improvements made for the compression device offers ways to understand better out-of-plane compression behaviour of paper in both empirical and fundamental meaning. Until now, studies related to out-of-plane compression are mainly made at static conditions in testing room climate with fixed temperature and humidity. In relation to dynamic tests and elevated moisture and temperature levels which are interesting in practical applications, there are not many studies available in the public literature. Many challenges are yet to overcome also in modelling of paper compressibility.

3.8.4.2 Characteristics of out-of-plane rheological behaviour of paper

Abstract

Paper experiences z-directional compressive strains in several papermaking and converting processes. The rheological response of paper generally depends on the humidity, temperature, structure and composition of paper. In this experimental study the dynamic strain behaviour of paper under z-directional compressive forces was investigated using a novel custom made laboratory testing rig.

Laboratory hand sheets with same basis weights but different raw material composition were used. Compressive stress level and dwell time were main external variables. The

applied dwell times ranged from a few milliseconds to several hundred milliseconds. The stress levels were varied from a few megapascals to tens of megapascals. The temperature and moisture of the samples were constant. The plastic, elastic and creep components of strain caused by increasing stress and dwell time were determined and analysed. The results show that the logarithmic strain varied non-linearly with increasing stress level. The plastic deformation was causing the increase of the logarithmic strain. The increasing dwell time at constant stress caused also non-linear increase in strain. This was due to both increase in plastic component and decrease in the elastic component. The results also revealed significant differences between mechanical and chemical pulp samples in both time and stress-dependent behaviour of strain probably due to the difference in the network structure. Large deformations occurred already in short time-scales.

Approach

In papermaking and converting processes paper is subject to stresses in out-of plane direction. Typically wet pressing, size pressing, calendering, reeling, winding, printing and cutting operations cause considerable dynamic out-of-plane stresses and deformations in paper. It is important to understand the resulting thickness change, the contact area between paper and the cylinder surface and the final irreversible deformation and how they depend on the shape and extent of the press pulse, and on the temperature – humidity conditions. Paper structure is one factor determining the compressive deformation of paper. Structure is changed by the furnish composition and wet stretching/drying history and material distribution in z-direction.

The effects of main external variables on paper compressibility have been recognized for several decades [1, 2, 3, 4]. However, there are still some shortcomings in the present knowledge. First of all, most of the studies are made using static or quasi-static compression pulses, which are outside the time-scales of actual process. Fewer studies are made near process time-scales. The effects of conditioning of paper samples, i.e. elevations in temperature and moisture content, on compressibility are not fully examined as well. The reason for these shortcomings has been in the limited capacities of the experimental set-ups.

In this study, the objective was to determine basic reological characteristics of paper under compressive stresses during short times scale. The interest was in examining how handsheets made of pure pulp components differ in compressibility behaviour when stress magnitude and stress dwell time are varied. The compressibility of pulp mixes and the effect of elevated moisture content will be the subject of further studies.

Materials and methods

Materials

Handsheets were made from mechanical and chemical pulp according to SCAN-C 26:76 apart from the following exception: the normal drying plates were replaced by blotters in order to avoid two sidedness created by conventional drying plates. This method allows the hand sheets to shrink modestly during drying.

The pulps used were obtained from Finnish pulp mills. Chemical pulp was Aki Botnia pine bleached sulphate softwood pulp from Äänekoski mill beaten to 500 ml CSF with a Valley laboratory hollander. Mechanical pulp was unbleached softwood SC TMP pulp with 50 CSF from Jämsänkoski mill. The handsheet grammage was 60-g/m^2 and average thicknesses of chemical and mechanical pulp sheets were 105 μm and 150 μm, respectively. Conventional tests were conducted under standard climate (23 ^oC and 50% RH). Some relevant handsheet properties are listed in Table 10.

Table 10. Basic properties of tested hand sheet samples.

Property		Chemical pulp	Mechanical pulp
Caliber/sheet	μm	105	150
Density	kg/m^3	571	400
Basis Weight	g/m^2	60	60
Paper moisture at 50% RH	%	91.1	89.9
PPS roughness	μm	8.4	7.7

Testing equipment and methods

A dynamic compression test rig with press platens was used in the measurements. The tester is called AKTU and it is developed in the laboratory of VTT Processes in Jyväskylä [5]. The basic idea behind this device is similar to that of a typical uniaxial compression tester. The material to be examined is placed between two press plates under a certain initial preload. A compression pulse is applied to the sample and the resulting compressive force and deformation are measured at the same time. The force is measured above the sample with a quartz crystal force gauge and the compressive pressure is specified as the force divided by the surface area of the sample. Compressive deformation is measured with three eddy-current distance sensors and is defined as the average change in distance between the press platens. The tester is capable of producing controlled pressure loading pulses with duration about 1 millisecond and dynamic force up to 5 kN, depending on required speed and displacement. Moreover, testing conditions (temperature and humidity) can be varied by using a climate chamber. The temperature in the climate chamber can be adjusted from 20°C to 80°C and moisture from 5% RH to 60–90% RH, the upper limit depending on the temperature. A computer with special

data acquisition software and a data acquisition board is used for recording the measurements. The experimental equipment is shown in Figure 115.

Experiments

Compression tests were made on one sample sheet using single rectangular shaped stress pulse with constant rise rate. Both pulse dwell time and stress level were changed independently. Dwell time was varied from 4 to 512 ms under given 10 MPa stress and stress level was increased from 2MPa to the highest level, while the 128 ms dwell time was kept constant. The highest stress levels were 36 MPa for mechanical pulp and 49 MPa for chemical pulp determined by the limited force-motion relation of the actuator. The round pressing area had 10 mm diameter. Static prestress of 100 kPa was used to make sure that there is a good initial contact between the sample and the press plates right from the beginning. Tests were repeated five or more times for every trial point and the shown results are averages of those measurements. In addition, the effect of machine compliance under load was eliminated from the results.

Data analysis

Force (F), compressive deformation (Δl) and time (t) data are recorded in compression tests. The compression stress, σ applied to the sample is calculated from the compression force and nominal area under compression (A). Absolute compressive deformation can be used to describe the response of material to applied stress, but it is dependent on material dimensions, especially thickness. Strain, on the other hand, is a property of material itself independent of dimensions and is therefore preferred for comparison of different samples. The logarithmic or true strain ε of sample caused by applied stress is defined through the equation: $\varepsilon = -\ln(l / l_o)$, where l and l_o are current and initial thicknesses of sample. Because the sample weight is not affected by the compression process and there is no essential variations in plane directional dimensions during compression in the case of paper, the change in sample thickness is in practise equal to the change of sample density and therefore the strain can also be expressed as: $\varepsilon = -\ln(\rho_o / \rho)$, where ρ and ρ_o are current and initial density of sample. The logarithms are negative valued due to thickness reduction (and density increase) and the minus signs have been added because the convenience of using positive values.

In the analysis, the total strain ε_t is divided into subcomponents including instant elastic strain ε_i and creep strain ε_c which are obtained from rising part of the strain curve and to elastic ε_e and plastic strain ε_p found from the post peak or decaying part of the strain curve. The delayed elastic (viscoelastic) component is not separated from the total strain but it is included in elastic strain. Different strain components are located by utilising the peaks of first derivate of strain. The components are linked to each other by following equations: $\varepsilon_t = \varepsilon_i + \varepsilon_c$, $\varepsilon_t = \varepsilon_e + \varepsilon_p$.

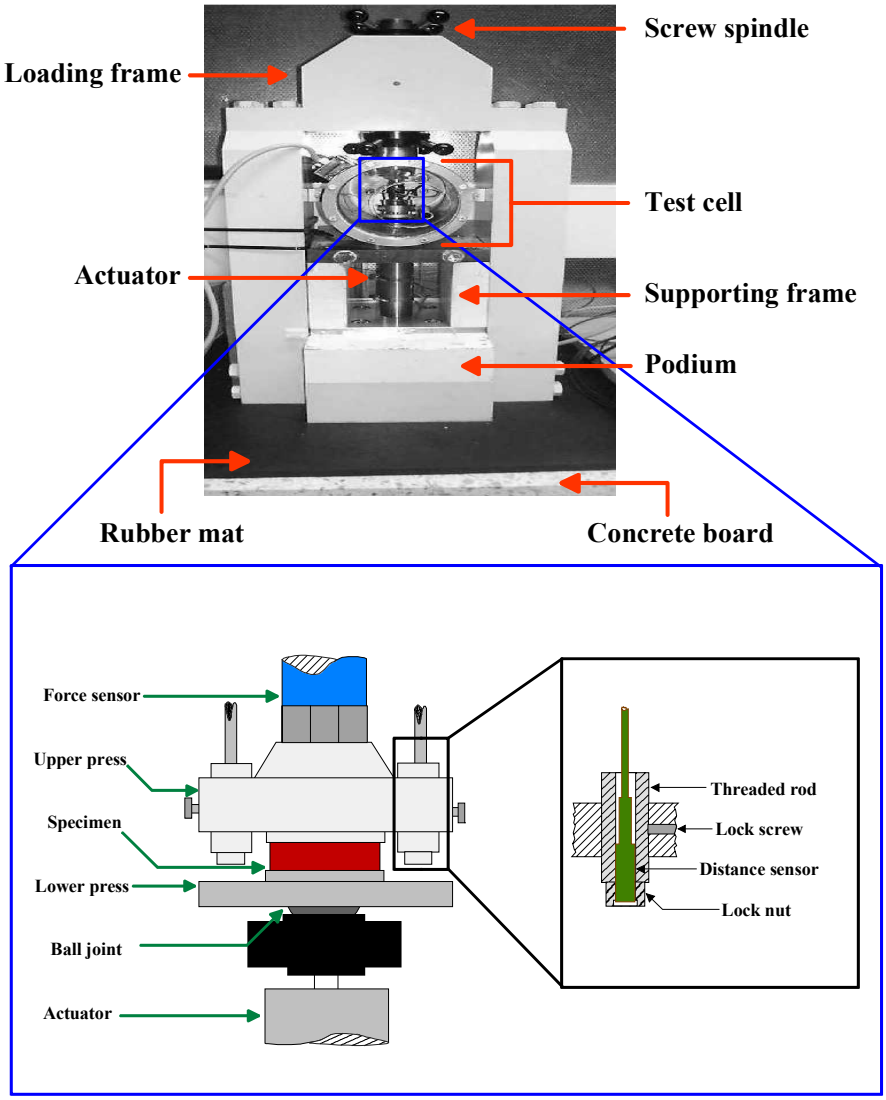

Figure 115. General view of the test rig (upper figure) and detailed side view of the test cell area (expanded view).

A logarithmic function $\varepsilon = a + b\ln(x)^c$, (*where x is time or stress*) with three free parameters a, b and c was fitted to strain-time and strain-stress data. Parameter values of the function were evaluated using Matlab based fitting program. As can be seen from the results, this function describes well the strain-time and strain-stress behaviour in the measured range. However, logarithm has a negative infinite value at the origin, which gives a non-physical value for strain at zero time and stress. This is the main drawback of using a logarithmic function.

Results

The experimental results are shown in Figures 116 and 117. The values of the fitted parameters in the logarithmic function and the coefficients of determination are listed in Table 11. All the plots are presented in log-linear format.

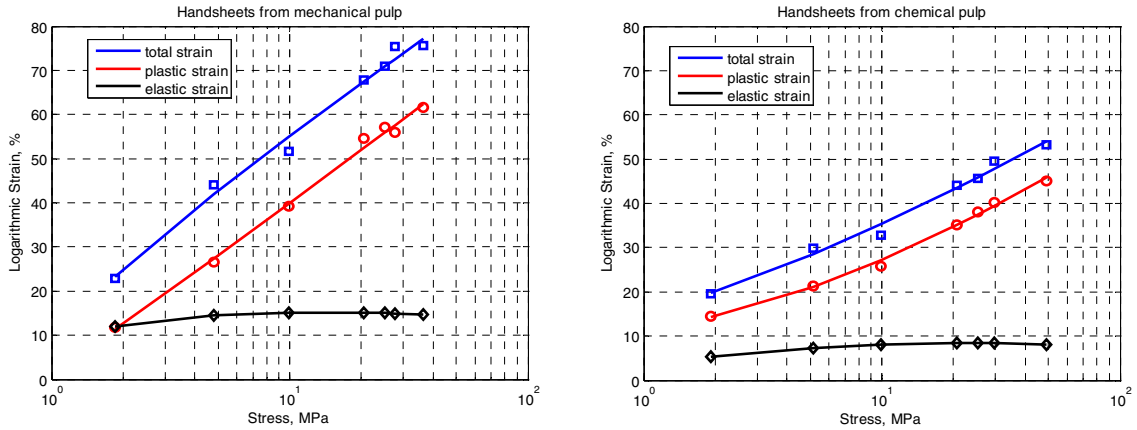

Figure 116. Different strain components versus stress with varying magnitude and constant duration (128 ms) for hand sheets made of chemical (left) and mechanical pulp (right). The solid lines are the predictions of the logarithmic model.

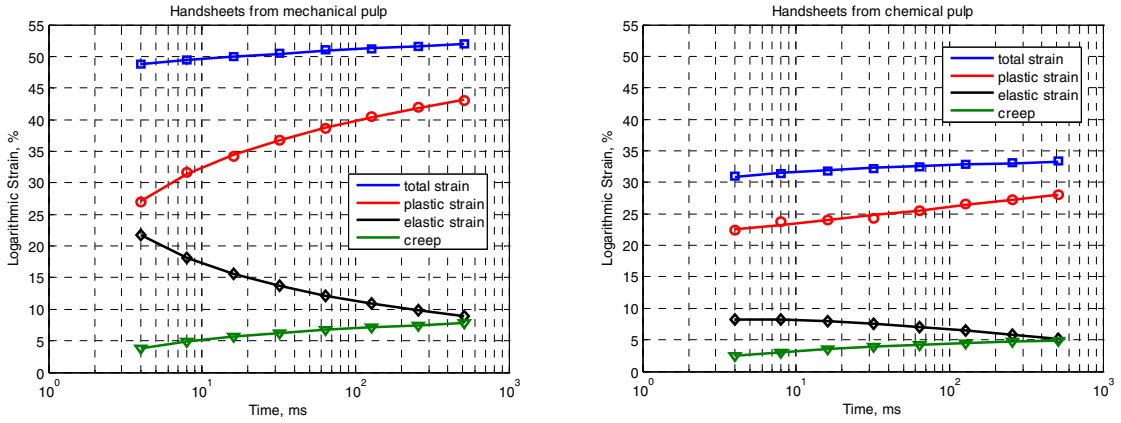

Figure 117. The effect of loading time on strain components under given (10 MPa) stress. The solid lines are the predictions of the logarithmic model.

Increasing compressive stress (Fig. 116) causes an apparently linear increase (in log-linear diagram) in the logarithmic strain with both furnishes. The elastic strain stays nearly constant and the increased deformation is mainly due to plastic strain component. The total deformation and the total strain is higher with the mechanical pulp sheets, and also the elastic strain component is higher with mechanical pulp than chemical pulp handsheets.

Increasing holding time at constant stress (Fig. 117) increases the total strain almost linearly in log-linear frame. However, the elastic strain is decreased and plastic strain is increased with increasing time but the creep strain is increased very little. This suggests that the creep strain is only partially responsible for the increased plastic strain, but also part of the elastic strain is converted into plastic strain. These changes are greater in short time scale.

Conclusions

The results show that the novel compression test equipment is suitable for studying short time scale rheological phenomena of paper. The response of logarithmic strain to increased compressive stress is apparently linear in log-linear scale and is mainly due to increased plastic deformation. Increasing dwell time under constant stress increases the logarithmic strain also linearly in log-linear scale. On the contrary to the effect of compressive stress, the strain increase in time is due to nonlinear response of plastic and elastic strains.

Mechanical pulp sheets show larger deformations under compressive stress, and also a larger part of this deformation is elastic than with chemical pulp sheets.

Table 11. Identified parameter values of used logarithmic function for different strain components.[*)]

Development of strain components under various stress magnitudes with given dwell time				
Strain component	a	b	c	r^2
total strain, mech.	8.6030	22.4474	0.8737	0.9892
plastic strain, mech.	1.5184	16.2315	1.0344	0.9951
elastic strain, mech.	---	---	---	---
total strain, chem.	15.9671	6.6080	1.2884	0.9851
plastic strain, chem.	12.1989	4.1380	1.5429	0.9951
elastic strain, chem.	---	---	---	---
Development of strain components at various dwell times of given stress magnitude				
total strain, mech.	45.6965	2.6357	0.4744	0.9957
plastic strain, mech.	-437.7703	461.4103	0.0226	0.9993
elastic strain, mech.	---	---	---	---
creep strain, mech.	$-7.0625 \cdot 10^5$	$7.0625 \cdot 10^5$	$3.7445 \cdot 10^{-6}$	0.9537
total strain, chem.	$5.8441 \cdot 10^5$	$-5.8438 \cdot 10^5$	$-2.7195 \cdot 10^{-6}$	0.9749
plastic strain, chem.	21.5210	0.7270	1.2015	0.9797
elastic strain, chem.	---	---	---	---
creep strain, chem.	-8.2798	10.2657	0.1376	0.9806

[*)] r^2 is a square of Pearson's correlation coefficient. Elastic strain is obtained by subtracting the plastic strain from the total strain. Therefore the data of elastic strain is not fitted to the model and the parameters are missing from the table.

References

[1] Jackson, M. and Ekström, L. Studies concerning the compressibility of paper. *Svensk Papperstidning* 67(2)1964, pp. 807–821.

[2] Chapman, D.L.T. and Peel, J.D. Calandering processes and the compressibility of paper, Part 1. *Paper Technology* 10(2)1969, p. 116.

[3] Colley, J. and Peel, J.D. Calandering processes and the compressibility of paper, Part 2. The effects of moisture content and temperature on the compressive creep behaviour of paper. *Paper Technology* 13(5)1972, p. 350.

[4] Rättö, P. On the compression properties of paper – implications for calandering. PhD thesis, Department of Paper Technology, KTH, Stockholm, Sweden, 2001.

[5] www.paperrc.com (know-how-menu → pressing/drying-submenu → compressibility).

3.8.4.3 Out-of-plane rheological behaviour of paper: the effect of furnish composition, basis weight and drying shrinkage

Abstract

The effect of amplitude and duration of compression pulse on strain response of paper was studied over a wide range: time duration varied from 4 to 512 ms and stress amplitude from 2 to 35 MPa. Hand sheets made of mechanical and chemical pulp and their blends were used. The behaviour of surface and bulk structures on compressive stress was studied by varying the basis weight of the sheets. Additionally, the effect of drying shrinkage on compressive strain behaviour was examined. The results indicated that large differences occur between pulps in both time and stress-dependent response of compressive strain. Additionally, drying shrinkage and basis weight had also significant impact on strain behaviour.

Introduction

Basic building elements of paper sheet are typically wood fibres, which are composed of same basic polymers – cellulose, hemicelluloses and lignin – despite of large variety of wood species used in papermaking. In fine structure of wood fibre several concentric layers can be detected, see Fig. 118. In pulping process the adjacent fibers in wood are separated and the outermost layers (ML, P, S1) of fibre are usually removed at the same time. Secondary wall is composed of three sublayers (S1, S2, S3). The cell wall layers the both amorphous and branched hemicelluloses together with amorphous lignin form a matrix (glue), which is reinforced by highly crystalline fibrils that are composed of

bundles of cellulose molecule chains. Fibrils, especially in the thickest layer S2 form helically wound spirals around the fiber axis. The fibril angle, in which fibril spirals around the fibre is important factor determining the strength of fibre. [2, 3, 4]

Significant differences in fiber morphology (length, diameter, wall thickness) and physical properties (coarseness, basis weight) exist between wood species (hardwood, softwood) but also within same tree (early wood, late wood).

Fibres are separated from each other either mechanically or chemically in the pulping process. Although there are a set of different choices in both pulping techniques, the most significant differences are the results of the chemical composition and mechanical structure of pulps. The chemical composition is conserved in mechanical pulping whereas in chemical pulping the lignin is mostly dissolved from the fibre walls. The consequence is that mechanically pulped fibres are stiff and rigid while chemically pulped fibre are soft and flexible. These basic fibre properties have strong effect on the mechanical behaviour of paper prepared from them.

In papermaking process, a suspension composed of water and 0.5–1.0% pulp fibers is evenly distributed to a moving porous fabric through which excess water is drained. In some phase of dewatering, surface tension forces between fibers start to interact and weak inter-fiber bonds are created. During drying process, the bonds gain more strength and finally a porous fiber network is formed. The porous volume of dry paper (before calendering) is usually more than 50% of the total volume. [5, 6, 7, 9]

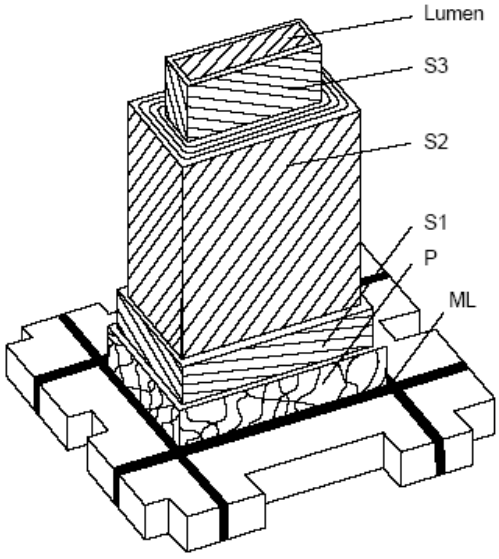

Figure 118. The simplified fine structure of cell wall in wood fibre is shown. Cell wall is built up by middle lamella (ML), primary wall (P) and secondary walls (S1, S2, and S3). The middlemost hollow is called lumen (the figure is from Paper Physics, K. Niskanen (1998), Fapet Oy).

How paper structure behaves under out-of-plane compressive stress and what provides the resistance is also considered in previous studies. According to these works, a following summary can be drawn: first, at small loads, the collapse of the large interfibre pore structure begins. This phase probably involves bending of more flexible fibres, fibre slippage and shear deformation and also collapse of individual thin walled fibres. Second, at intermediate loads, the structure is more packed and the collapse of intra fiber pore structure takes place. Local stress peaks may cause fracture of some rigid and brittle mechanical fibers. In addition, some interfiber bond breakage may occur. Finally, at large loads, the paper sheet is fully densificated and fiber fracture begins. In examination of paper behaviour under compressive stress SEM and CLSM has been utilized [5, 7, 8, 9, 10].

The above-described compression behaviour of paper is common for cellular materials. The presence and importance of paper compressive strain behaviour in papermaking and converting processes are discussed by authors recently. [1]

In the current work the primary interest was in clarifying some of the fundamental factors behind paper compression behaviour under dynamic stress. To fill that purpose, furnish composition, basis weight, stretching/drying history and forming method (layered/conventional) were varied in preparing the hand sheets for the tests. In the compression tests conducted under laboratory environment, amplitude and dwell time of single and cyclic stress pulses were changed.

Experimental

Materials

A set of laboratory hand sheets with different furnish compositions were manufactured for the tests. Hand sheets were chosen due to their isotropic structure. This selection enables comparative study of compression behaviour of sheets made of different pulps without the effect of machine and cross-machine directions or other factors not known with commercial papers. Sheets were prepared from mechanical and chemical pulp according to SCAN-C 26:76 apart from the following exception: the drying plates were replaced by blotters in order to avoid two sideness. This choice allows the hand sheets to shrink modestly during drying. In one separate experiment, drying shrinkage was varied in order to study its effect on paper compressive behaviour.

The pulps used were obtained from Finnish pulp mills. Chemical pulp (CHEM) was Aki Botnia pine (bleached sulphate softwood pulp) from Äänekoski mill beaten to 500 ml CSF with a Valley laboratory hollander. Mechanical pulp was unbleached softwood SC TMP pulp with 60 ml CSF from Jämsänkoski mill. Sheets were made both from pure

pulps and blends. Also three-layer sheets were made with 40 g/m^2 TMP in the middle layer and 20 g/m^2 CHEM at the surfaces. The pulp percentual portion in the sheet is shown in short notation of the sheet, which is used hereafter. Notations are TMP100, CHEM100, TMP80CHEM20, conventional and layered TMP50CHEM50.

Tests were conducted under controlled conditions: temperature 23^{o}C and humidity 50%RH. The samples were conditioned at least 24 h before testing. Some hand sheet properties which have influence on compression behaviour are summarized in Table 12. Round sample of 10 mm in diameter was used in testing the compressive behaviour.

Table 12. Basic properties of tested hand sheets.

Property	**TMP100**	**TMP80CHEM20**	**TMP50CHEM50**	**TMP50CHEM50, layered**	**CHEM100**
Caliper/sheet	150 µm	138 µm	124 µm	155 µm	106 µm
Density	412 kg/m^3	443 kg/m^3	497 kg/m^3	506 kg/m^3	580 kg/m^3
Basis weight	60 gsm	60 gsm	60 gsm	80 gsm [c)]	60 gsm
Moisture [a)]	9,7%	10%	8,9%	9,7%	8,4%
Bendtsen [b)]	68 ml/min	74 ml/min	83 ml/min	100 ml/min	185 ml/min
Roughness [d)]	1204 ml/min	1222 ml/min	1180 ml/min	1735 ml/min	1538 ml/min
Scott bond	220 J/m^2	239 J/m^2	257 J/m^2	---	431 J/m^2

a) Hand sheet moisture at 23 ^{o}C, 50% RH, b) Air permeability measurement (SCAN-P 26:78), 10cm^2, c) Three-layer hand sheet with 20gsm chemical pulp at surfaces and 40gsm mechanical pulp in the middle, d) Average Bendtsen roughness of both surfaces, samples were too rough for PPS measurement.

In addition, samples were manufactured to study the effect of surface roughness on compressive strain. For that purpose, a basis weight series was prepared where the basis weight was changed from 40 to 120 gsm in steps of 20 gsm. Table 13 demonstrates the variation of some hand sheet properties with grammage for TMP50CHEM50 sample. Basis weight series were manufactured earlier also from TMP100 and CHEM100, but other properties besides grammage and thickness were not measured from those sheets.

Table 13. Basic properties of TMP50CHEM50 hand sheets with different grammages.

Property	**Unit**	**40 gsm**	**60 gsm**	**80 gsm**	**100 gsm**	**120 gsm**
Caliper/sheet	µm	90	123	154	187	218
Density	kg/m^3	442	500	525	542	561
Bendtsen [b)]	ml/min	124	79	62	56	44
Roughness [d)]	ml/min	1033	1161	1476	2005	2080
Scott bond	J/m^2	270	260	283	285	313

Testing equipment

Compression experiments were performed using a novel platen-press tester presented in previous work. [1] Briefly, the sample is placed between two platens under predetermined load. Electromechanically actuated cylinder generates the compression pulse applied to the sample. Both compressive force and thickness change are recorded simultaneously. For that purpose, test-rig is instrumented with three eddy-current distance sensors and a quartz crystal force gauge. Thickness change is defined as the average change in distance between the platens. All sensors are located in the fixed upper platen. Available performance range depends on the relation between force, displacement and speed, but compressive forces up to 5 kN with duration even down to 1 millisecond can be produced. Due to the actuator, stroke length is limited to 160 µm, which is yet enough for dry paper testing. Test cell area including platens and sensors can be surrounded with special climate chamber where testing conditions can be varied: temperature is adjustable from 20 to 80 °C and relative humidity from 5 to 50–90%RH, the upper limit depending on temperature. Measurements are run under computer control, using special data acquisition software operating in conjunction with data acquisition board.

Experiments

Series of compression tests were made on one sample sheet using either single or cyclic stress pulses with rectangular shape and constant rise rate. Both holding time and stress amplitude were changed independently. With single pulse, holding time was varied from 4 to 512 ms under given 10 MPa stress. In cyclic tests, stress peak amplitude was increased from around 2MPa to 35 MPa, while the 64 ms holding time and 32 ms relaxation time between pulses was fixed, see Fig. 119. Before testing, sample was positioned to 100 kPa static offset-load to make sure that there is an adequate initial contact between the sample and the press plates right from the beginning. Offset load was kept on for a while after stress release of single stress pulse and between stress pulses in case of cyclic loading. Tests were repeated five or more times for every trial point and the shown results are averages of those measurements. In addition, the effect of machine compliance under load was eliminated from the results.

In the analysis, logarithmic strain is used due to high strain levels. The total strain (ε_t) is divided into subcomponents including instant elastic strain (ε_i) and creep strain (ε_c) which are obtained from loading phase of the strain curve and to elastic (ε_e) and plastic strain (ε_p) found from the post peak or unloading phase of the strain curve. The delayed elastic (viscoelastic) component is not separated from the total strain but it is included in elastic strain. Different strain components are located by utilising the peaks of first derivate of strain. The strain components are linked to each other by following equations: $\varepsilon_t = \varepsilon_i + \varepsilon_c$, $\varepsilon_t = \varepsilon_e + \varepsilon_p$.

In sequential loading tests, sample permanent density is different between single pulses. At the beginning of certain pulse, density is a combination of initial density and permanent strain gained in previous pulse. This relation is utilized in defining the ratio of incremental strain components as function of density (Fig. 122).

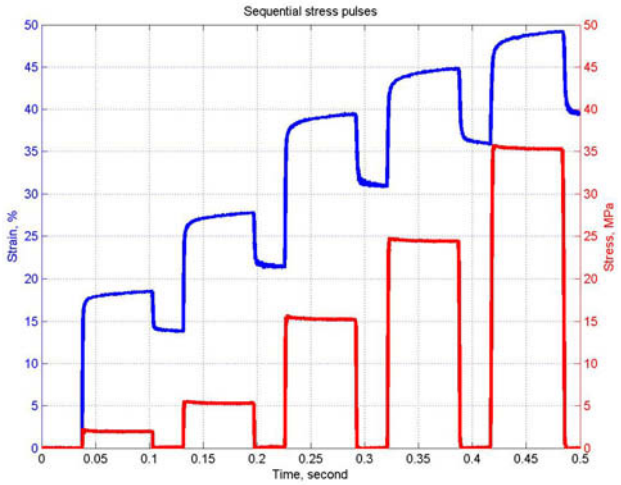

Figure 119. An example of sequential loading (lower curve) and the corresponding strain response of uncalandered handsheet sample. Pulse duration was 64 ms and relaxation time between pulses was 32 ms.

Results and discussion

First some comments on the measured basic properties. For handsheets made of mechanical dominated pulp the initial density and the average roughness is clearly smaller when compared to sheets made of chemical pulp. Differences of physical properties originate from used fibres and how they form the network. Fines properties are also important. Typically rigid mechanical fibres form sparse network with rough surface, which can be smoothened by fines whereas flexible chemical fibres form compact network with smoother surface. Equilibrium moisture content is larger for mechanical pulp sheets. Basis weight has significant effect on most physical properties as well.

Single pulse loading

It was investigated how the paper compressive strain changes under constant load. Samples were loaded over a different periods of time ranging from 4 to 512 ms using single rectangular shaped stress pulses with 10 MPa amplitude and constant rise rate. The behaviour of different strain parameters was extracted from the test data. Fig. 120 shows results of this parameter-time behaviour from which following observations can be made:

– Increasing holding time from 4 ms to 512 ms has a rather moderate effect on total strain.

– Instant compressive strains have good correlation with initial sheet densities: mechanical pulp dominated sheets have much higher compressive strains than sheets containing more chemical pulp.

– Although a larger part of the total strain is elastic in mechanical pulp dominated sheets, elastic strain decreases and turns into plastic faster with time.

– Surprisingly, there is no difference in compression behaviour between conventional and layered three-ply samples.

– Compressive behaviour of pulp blends seems to be clearly additive with chemical pulp content.

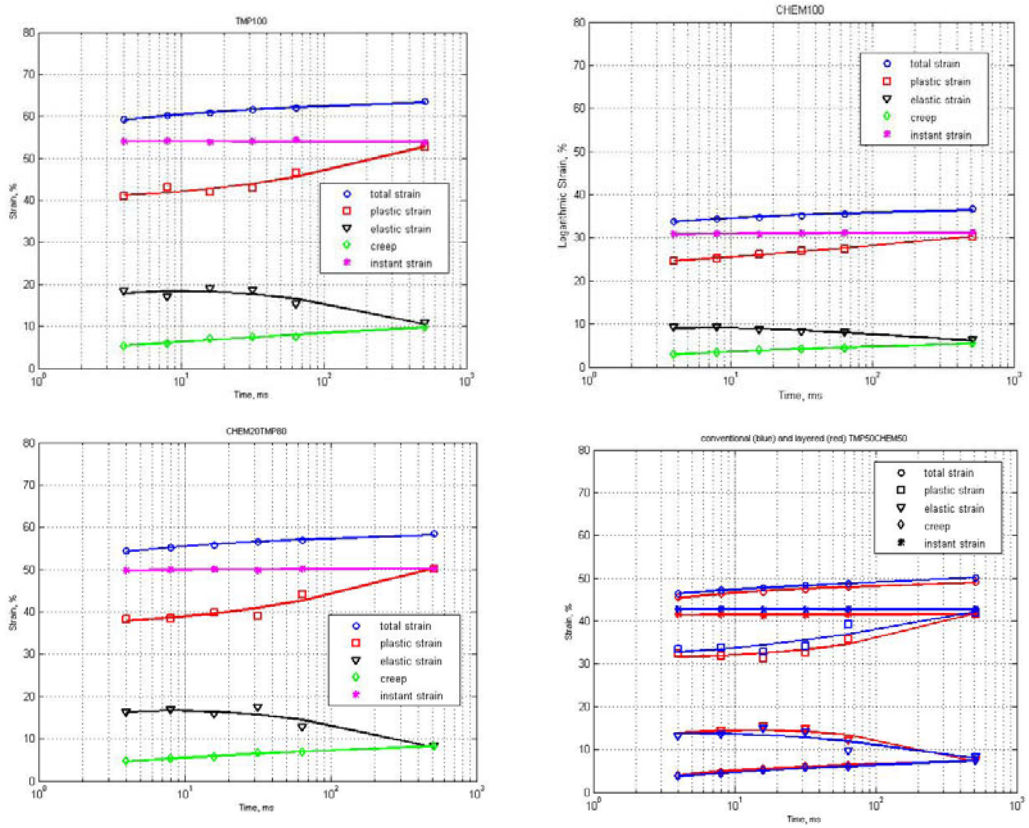

Figure 120. Strain vs. time for different samples: hand sheets made of both pure mechanical pulp (TMP100) (top left) and pure chemical pulp (CHEM100) (top right) and hand sheets made of pulp blends CHEM20TMP80 (bottom left), conventional pulp blend and layered three-ply sheet TMP50CHEM50 (bottom right).

Cyclic loading

The effect of stress level on compressive strain of paper was studied using sequential stress pulses with constant dwell time and increasing amplitude. Characteristic stress and strain data for the tests are shown in Fig. 119. In this type of cyclic loading, paper behaves differently in every single stress pulse. Behaviour is primarily dominated by

paper density. For uncalandered handsheet, the initial density is low and the sheet does not return to its original shape after single stress pulse but a permanent strain remains. How permanent strain and other strain components behave with increasing stress is plotted in Fig. 121. The increment of permanent strain in relation to increment of total strain changes as densification proceeds: larger part of total strain increment recovers and paper turns from elasto-plastic into nearly elastic material. How the plastic-elastic transfer takes place in two extreme cases, the strain ratio of increments – increment of plastic strain to increment of total strain- is plotted against density for sheets made of pure pulps in Fig. 122. Similarly, the growth of total strain with stress slows down with increasing density.

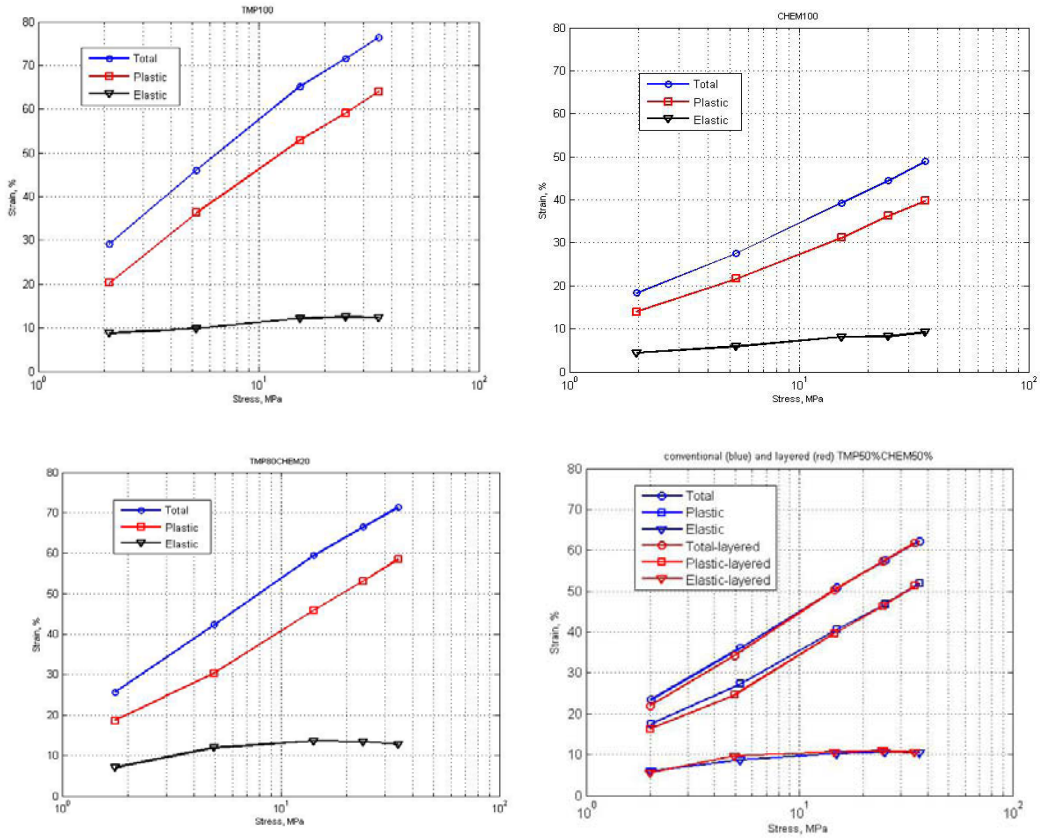

Figure 121. The behaviour of total strain and its components as a function of stress for same hand sheets as in Fig. 120.

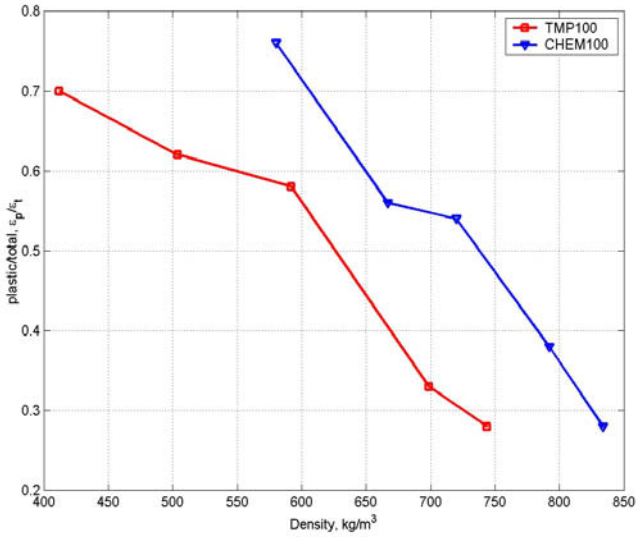

Figure 122. The ratio between increments of plastic and total strain with density in cyclic loading with increasing amplitude is shown.

Findings from experiments with different loading amplitudes:

- Stress level has a significant impact on paper strain and resulting density.
- The part of permanent strain from total strain increases with increasing stress for all samples, when the strains are related to initial density, see Fig. 121.
- Chemical pulp containing sheet is clearly more plastic when the ratio between increments of plastic and total strains of pulps are compared in same density, see Fig. 122.
- Stress amplitude was raised using cyclic loading, but the results are in practice identical with the ones made earlier using single pulse loading [1].

Drying shrinkage

Measurements were made to demonstrate the effect of drying induced shrinkage on paper compressive strain. Three separate shrinkage levels were allowed. First, the wet samples were uniaxially strained 2% in-plane direction with shrinkage restricted during subsequent drying. Second, the shrinkage was fully restricted, but no strain was applied. Third, the samples were dried without restriction. These tests were made using custom-made experimental set-up build in Lloyd universal test machine (type LR 10K). The increase in solid content was monitored continuously during drying and three different samples were tested: CHEM100, TMP100 and TMP80CHEM20. Samples for compression tests were taken from the middle region of the hand sheet. Compression tests were carried out using single rectangular shaped stress pulses with 10 MPa amplitude and 64 ms duration.

Fig. 123 shows the compression behaviour with drying shrinkage. For both chemical pulp sheet and pulp mixture sheet total and plastic compression increases when it is switched from restricted to free shrinkage drying. Mechanical pulp sheet has different behavior: largest total and plastic strains are gained when paper is stretched during drying. Free shrinkage produces still a bit higher total strain than pure restricted drying.

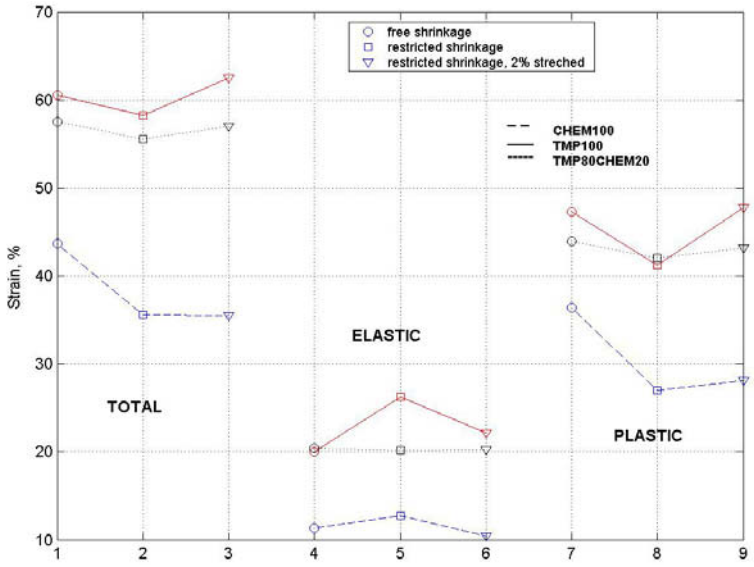

Figure 123. Variations in paper strain components resulting from drying induced shrinkage.

Elastic strain has different behaviour than those of plastic and total strains. Biggest changes are in pure pulp sheets whereas pulp mixture sheet has not notable changes. Restricted shrinkage produces largest elastic strains.

Basis weight

Strain behaviour of paper surface and internal structure was investigated by varying the basis weight of samples. Sometimes paper is understood as a structure formed by internal layer and two surfaces. How to distinguish the surface and internal strain behaviour from each other is the key question.

It was measured that paper thickness increases linearly with basis weight, see upper plot in Fig. 124. Based on this known connection, it has been previously proposed[2] that internal layer increases with basis weight according to the product of basis weight and some constant slope but no changes happen in surfaces, which are responsible of the non-zero constant in linear relationship.

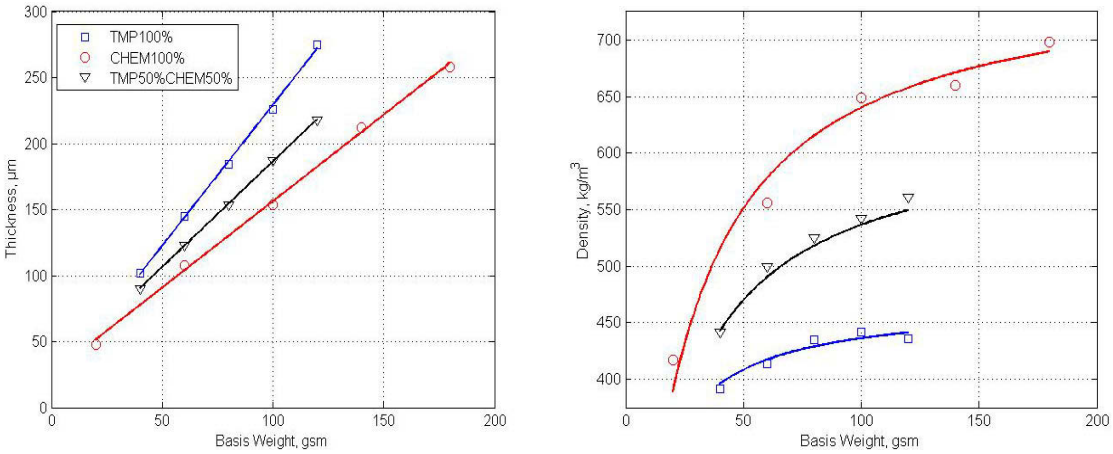

Figure 124. Basis weight dependence of measured thickness (left) and density for different pulps (right) is presented.

Due to this thickness – basis weight behaviour, paper density has nonlinear (hyperbolic) relation with basis weight, see lower plot in Fig. 124. Density approaches to its limiting value at high basis weight levels, in which point internal structure dominates the surfaces and the density is same as internal layer density.

Despite the good fitting results, there are some shortcomings in the linear proposition. For instance, at the limit of zero basis weight, when internal structure has disappeared and the upper and lower surfaces locate on top of each other, thickness reaches a nonzero value, which is arising from the surfaces. To avoid this non-physical behaviour at zero basis weight, also the surface thickness portion in thickness model should depend on basis weight somehow. Another indication of connection between basis weight and surface thickness is the increase of roughness values with basis weight (see Table 13).

To fulfil the shortcomings of linear relationship, the constant value of surface thickness was rejected and an assumption of power law behaviour between surface thickness and basis weight was made. This nonlinear thickness model was consistent with the linear model at measured dataset, showing apparently linear behaviour. Although excellent correlation was gained in comparison of data with the nonlinear thickness model, the reliability of the fitted parameters suffered from too few data points. The model still followed the first impression of the expected behaviour better than linear model.

How the above-described density variation with basis weight affect compressive strain is shown in Fig. 125. The examination is shown for TMP50CHEM50, from which the basic properties were known (see Table 13).

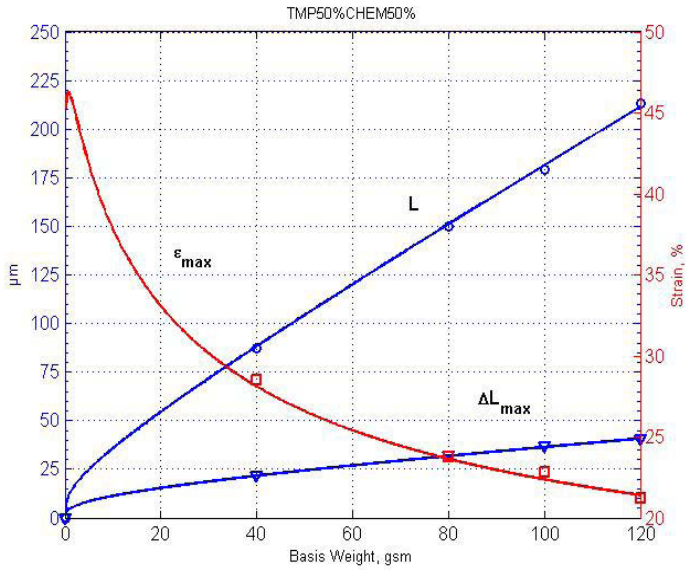

Figure 125. Thickness L, maximum compression ΔL_{max} and strain ε_{max} are plotted against basis weight. The few data points have markers but the lines are predicted through the models for thickness, maximum compression and strain.

According to Fig. 125 the difference between maximum compression and thickness increases strongly with basis weight and this is seen also in maximum strain. The maximum (instant) compressive strain of examined papers can be explained purely by basis weight and applied stress.

Conclusions

This study considered compressive strain behaviour of hand sheets made of both pure pulps and mixed blends.

Significant differences were seen in compressive strain between samples. Duration of compression pulse had small effect on total strain in the tested time range, but the remaining plastic strain increased and the elastic strain decreased notably with time for mechanical pulp dominated sheets. Similar but lot smaller effect was seen for chemical pulp sheet, which is an interesting result.

Stress on the other hand had large effect on all strain components. The portions of elastic and plastic parts of total strain at same density depended on pulp type: chemical pulp sheet is evidently more plastic than mechanical pulp sheet. At high stress levels, total densities approach each other regardless of pulp and the elastic nature takes over. Although density is a major factor in paper strain behaviour, it does not explain by itself the whole behaviour, which can be concluded from these results.

In drying induced shrinkage tests, chemical pulp sheet showed large differences in plastic and total strains when shrinkage was allowed during drying compared to situations where shrinkage was restricted. This behaviour was most likely resulting from differences in sample densities due to drying method. Pulp mixture sheet had similar behaviour with pure chemical pulp sheet, but mechanical pulp sheet behaved differently: restricted shrinkage together with stretching under drying produced largest compressive strains for mechanical pulp sheet. This outcome is not explained with density differences.

In tests with different basis weights, where only paper surface/bulk relation was assumed to vary, big differences were found in paper compression behaviour. The apparent thickness, density and compression behaviour of chemical pulp sheet was more sensitive to basis weight than that of mechanical pulp sheet. This is due to the fact that surface roughness or thickness was not independent of basis weight but changed considerably with it. At high basis weights surface thickness looses its effect. Therefore, heavier basis weights had smaller strain, which is controlled by bulk structure, whereas for lighter basis weights surfaces dominate the compression behaviour. According to the analysis made, total strain in single compression pulse can be explained by applied stress and basis weight for studied samples.

References

[1] Ponkkala, T., Kunnari V. and Retulainen, E. Characteristics of out-of-plane rheological behaviour of paper. *Annual Transactions of Nordic Rheology Society* 2005, Vol. 13, pp. 263–268.

[2] Niskanen, K. Paper Physics. Papermaking Science and Technology, Fapet Oy, Helsinki, 1998. Pp. 55–87.

[3] Scott, W.E. Principles of Wet End Chemistry. Tappi Press, Atlanta, 1996. Pp.10–14.

[4] Sjöström, E. Wood Chemistry: fundamentals and appkications. Academic Press, Inc., London, 1993. Pp.1–20.

[5] Feygin, V.B. Modelling paper strain in a calender nip. *Tappi Journal* 1999, Vol. 82, No. 8, pp. 183–188.

[6] Pawlak, J.J. and Keller, D.S. The compressive response of a stratified fibrous structure. *Mechanics of Materials* 2005, 37, pp. 1132–1142.

[7] Pawlak, J.J. and Keller, D.S. Relationships between the local sheet structure and z-direction compressive characteristics of paper. *Journal of pulp and paper science* 2004, Vol. 30, No. 9, pp. 256–262.

[8] Browne, T.C., Crotogino, R.H. and Douglas, W.J.M. The effect of paper structure on behaviour in a calender nip. *Journal of pulp and paper science* 1995, Vol. 21, No. 10, pp. 343–347.

[9] Haslach, H.W. A model for drying-induced microcompressions in paper: buckling in the interfiber bonds. *Composites Part B* 1996, Vol. 27B, No. 1, pp. 25–33.

[10] Retulainen, E., Moss, P. and Nieminen, K. Effect of calendering and wetting on paper properties. *Journal of Pulp and Paper Science* 1997, Vol. 23, No 1, pp. 34–39.

4. Publications, reports and dissertations

1. Kataja, M. (ed.). Rheological materials in process industry. ReoMaT Project Report 2003. VTT Project Report, 15.3.2004.

2. Aho, J. and Syrjälä, S. Evaluation of pressure dependence of viscosity for some polymers using capillary rheometer. *Annual Transactions of the Nordic Rheology Society* 2005, 13, pp. 55–59.

3. Aho, J. and Syrjälä, S. Determination of the entrance pressure drop in capillary rheometry using Bagley correction and zero-length capillary. *Annual Transactions of the Nordic Rheology Society* 2006, 14, pp. 143–147.

4. Aho, J. and Syrjälä, S. Pressure dependence of viscosity of polymer melts. Submitted for publication in *Polymer Testing*.

5. Ponkkala, T., Kunnari, V. and Retulainen, E. Characteristics of out-of-plane rheological behavior of paper. Poster presented at the 14th Nordic Rheology Conference 2005, 1–3 June 2005, Tampere, Finland. *Annual Transactions of the Nordic Rheology Society,* 2005, Vol. 13.

6. Salminen, K. and Retulainen, E. Effects of white water composition on strength and runnability of wet paper. Poster presented at ABTCP-PI 2005 Congress; 38 CONGRESSO E EXPOSIÇÃO INTERNACIONAL DE CELULOSE E PAPEL 17.–20.10.2005 Sao Paulo, Brazil.

7. Ponkkala, T., Kunnari, V. and Retulainen, E. Out-of-plane rheological behaviour of paper: the effect of furnish composition, basis weight and drying shrinkage. Paper presented at the the 15th Nordic Rheology Conference 2005, 1–3 June 2005, Stockholm Sweden. *Annual Transactions of the Nordic Rheology Society*, 2006, Vol. 13.

8. Salminen, K. and Retulainen, E. Effects of furnish composition on mechanical properties of wet web. Paper presented at the Progress in Paper Physics Seminar, 1–5 October, 2006, Oxford, Ohio.

9. Hyväluoma, J., Raiskinmäki, P., Koponen, A., Kataja, M. and Timonen, J. Lattice Boltzmann Simulation of Particle Suspensions in Shear Flow. *J. Stat. Phys.* 2005, 21, pp. 149–161.

10. Hyväluoma, J., Raiskinmäki, P., Koponen, A., Kataja, M. and Timonen, J. Strain hardening in liquid-particle suspensions. *Phys. Rev. E72*, 061402 (2005).

11. Aaltosalmi, U., Kataja, M., Koponen, A., Timonen, J., Goel, A., Lee, G. and Ramaswamy, S. Numerical analysis of fluid flow through fibrous porous materials. *J. Pulp and Paper Sci*. 2004, 30, 9, pp. 251–255.

12. Hyväluoma, J., Raiskinmäki, P., Koponen, A., Kataja M. and Timonen, J. Lattice-Boltzmann simulation of particle suspensions in shear flow. *J. Stat. Phys*. 2005, 121, 1/2, pp. 149–161.

13. Hyväluoma, J., Raiskinmäki, P., Jäsberg, A., Koponen, A., Kataja, M. and Timonen, J. Simulation of liquid penetration in paper. *Phys. Rev. E* 2006, 73, Issue 3.

14. Hyväluoma, J., Raiskinmäki, P., Koponen, A., Kataja, M. and Timonen, J. Strain hardening in liquid-particle suspensions, International Conference for Mesoscopic Methods in Engineering and Science, Braunschweig, Germany, 26–30 Jul 2004.

15. Raiskinmäki, P. and Kataja, M. Rheological measurements of fibre suspension using ultrasound Doppler techniques. *Transactions of the Nordic Rheology Society*, Vol. 13, Tampere, Finland, 1–3 June 2005.

16. Raiskinmäki, P. Dynamics of multiphase flows: liquid-particle suspensions and droplet spreading. PhD Thesis, JYFL Research Report 7/2004. University of Jyväskylä, 2004.

17. Aaltosalmi, U. Fluid flow in porous media with the lattice-Boltzmann method. PhD Thesis, JYFL Research Report 3/2005, University of Jyväskylä, 2005.

18. Koivu, V. Paperin permeabiliteetin mittaamismenetelmä. Pro gradu, Department of Physics, University of Jyväskylä, August 2004.

19. Gustafsson, J., Toivakka, M. and Koskinen, K.K. Rheology of strongly sedimenting magnetite suspensions. *Annual Transactions of the Nordic Rheology Society* 2005, Vol. 13.

Series title, number and
report code of publication

VTT Research Notes 2428
VTT-TIED-2428

Author(s)
Kataja, Markku (ed.)

Title

Rheological materials in process industry
ReoMaT Final Report

Abstract

'Rheological materials in process industry (ReoMaT)', was a three-year research project started 1.2.2003 and funded mainly by Tekes and industry. It was carried out as a joint effort of five research groups from VTT, University of Jyväskylä, Tampere University of Technology and Åbo Akademi University. The participating companies were Metso Paper Oy, Outokumpu Research Oy, M-real Oyj, Stora Enso Oyj, Kemira Chemicals Oy and Premix Oy. The project was devoted to the study of properties and dynamics of rheological and porous materials found in industrial processes. The general goal of the project part was to support the related industrial research by methods development, research networking and technology transfer. The research included three main topical areas: experimental rheology, development of experimental techniques and numerical analysis. In addition to conventional methods, the projected research utilized several novel techniques, both experimental and numerical, that have only recently become available in other disciplines of materials science and flow mechanics. The results of the first project year were reported separately in: *M. Kataja (ed.), Rheological materials in process industry. ReoMaT Project Report 2003, VTT Project Report, 15.3.2004*. This reports covers the results of ReoMaT consortium for its latter two-year funding period 1.1.2004–30.4.2006.

The results of the project are prolific ranging from direct numerical simulation results on elementary dynamics of momentum transfer in particulate suspensions to new semiempirical pressure loss correlations in fibre suspension flows, rheological characterization of polymer-based and fibrous materials, and to new measurement methods for sedimenting suspensions. Results of general interest have been published in international conferences and journals.

The main results of the project, readily applicable in industrial research and development are:

- A new measurement technique based on helical-flow modified rotational rheometer was developed. The measurement allows for characterization of strongly sedimenting suspensions, which has not been possible previously. The measurement will be offered to industry as a research service.
- The research has enabled to better identify and account for various factors related to the rheometry of polymer melts. The consequent improved accuracy of the rheological characterization of polymeric materials is of great practical importance for example when solving the processability problems in existing processes or when developing new materials.
- The research has led to several new innovations in experimental techniques for finding the relevant material properties of liquid-particle suspensions. In particular, methods based on ultrasound Doppler velocimetry are now being utilized in industrial research by the participating groups. Further development and possible commercialisation of some of the methods is projected.
- New improved semiempirical correlation model for estimating losses for fibre suspension flows was developed. The model and the related measurement techniques is adopted by the participating research groups as a new supplement in their research service potential, and is thereby available for the industry.
- New research method based on using x-ray tomography and numerical lattice-Boltzmann flow simulation has been employed and validated. The techniques is now available for the industry and has already been used in analysing *e.g.* structure and transport properties of paper-making fabrics.
- The in-plane mechanical properties of wet web were found to be strongly affected by furnish, chemicals and DCSs (dissolved and colloidal substances). This offers new possibilities for controlling rheology, stiffness and runnability of wet webs. The results have led to applications and applied research projects in the industry.
- The improved z-directional compression tester proved to be a valuable tool in studying the out-of-plane behaviour of paper under short compressive pulses. The instrument and the generated knowledge is applicable, and has been applied, in industrial cases for solving problems related to paper deformations and processability under z directional stresses.

Many of these results now make an important contribution to the present capabilities of the participating groups and have already been successfully utilized in industrial research carried out parallel to the present project. Some of the results are expected to make similar contribution and benefit research and applications in the near future.

Based on the results and their estimated impact, we conclude that the general goal of the ReoMaT project, namely "to support the related industrial research by methods development, research networking and technology transfer", has been met.

ISBN
978-951-38-7200-1 (soft back ed.)
978-951-38-7201-4 (URL: http://www.vtt.fi/publications/index.jsp)

Series title and ISSN	Project number
VTT Tiedotteita – Research Notes 1235-0605 (soft back ed.) 1455-0865 (URL: http://www.vtt.fi/publications/index.jsp)	25680

Date	Language	Pages
September 2008	English	172 p.

Name of project	Commissioned by
51REOMAT2	Tekes, industry

Keywords	Publisher
rheology, rheological materials, rheometry, porous material, particulate suspension, momentum transfer, fibre suspension, pressure loss, polymers, fibrous materials, x-ray tomography, lattice-Boltzmann flow simulation, ultrasound Doppler velocimetry	VTT Technical Research Centre of Finland P.O. Box 1000, FI-02044 VTT, Finland Phone internat. +358 20 722 4520 Fax +358 20 722 4374

'Rheological materials in process industry (ReoMaT)', was a three-year research project started 1.2.2003 and funded mainly by Tekes and industry. It was carried out as a joint effort of five research groups from VTT, University of Jyväskylä Tampere University of Technology and Åbo Akademi University. The project was devoted to the study of properties and dynamics of rheological and porous materials found in industrial processes. The research included three main topical areas: experimental rheology, development of experimental techniques and numerical analysis. In addition to conventional methods, the projected research utilized several novel techniques, both experimental and numerical, that have only recently become available in other disciplines of materials science and flow mechanics. The results of the project are prolific ranging from direct numerical simulation results on elementary dynamics of momentum transfer in particulate suspensions to new semiempirical pressure loss correlations in fibre suspension flows, rheological characterization of polymer-based and fibrous materials, and to new measurement methods for sedimenting suspensions.

Julkaisu on saatavana	Publikationen distribueras av	This publication is available from
VTT PL 1000 02044 VTT Puh. 020 722 4520 http://www.vtt.fi	VTT PB 1000 02044 VTT Tel. 020 722 4520 http://www.vtt.fi	VTT P.O. Box 1000 FI-02044 VTT, Finland Phone internat. + 358 20 722 4520 http://www.vtt.fi

ISBN 978-951-38-7200-1 (nid.)
ISSN 1235-0605 (nid.)
ISBN 978-951-38-7201-4 (URL: http://www.vtt.fi/publications/index.jsp)
ISSN 1455-0865 (URL: http://www.vtt.fi/publications/index.jsp)